Advances in Polymer Technology

Applications of Fiber Reinforced Polymer Composites in Civil Engineering

Lead Guest Editor: Tianyu Xie
Guest Editors: Guangming Chen, Mohamed A. Sadakkathulla, Mohamed Elchalakani, and Jinjun Xu

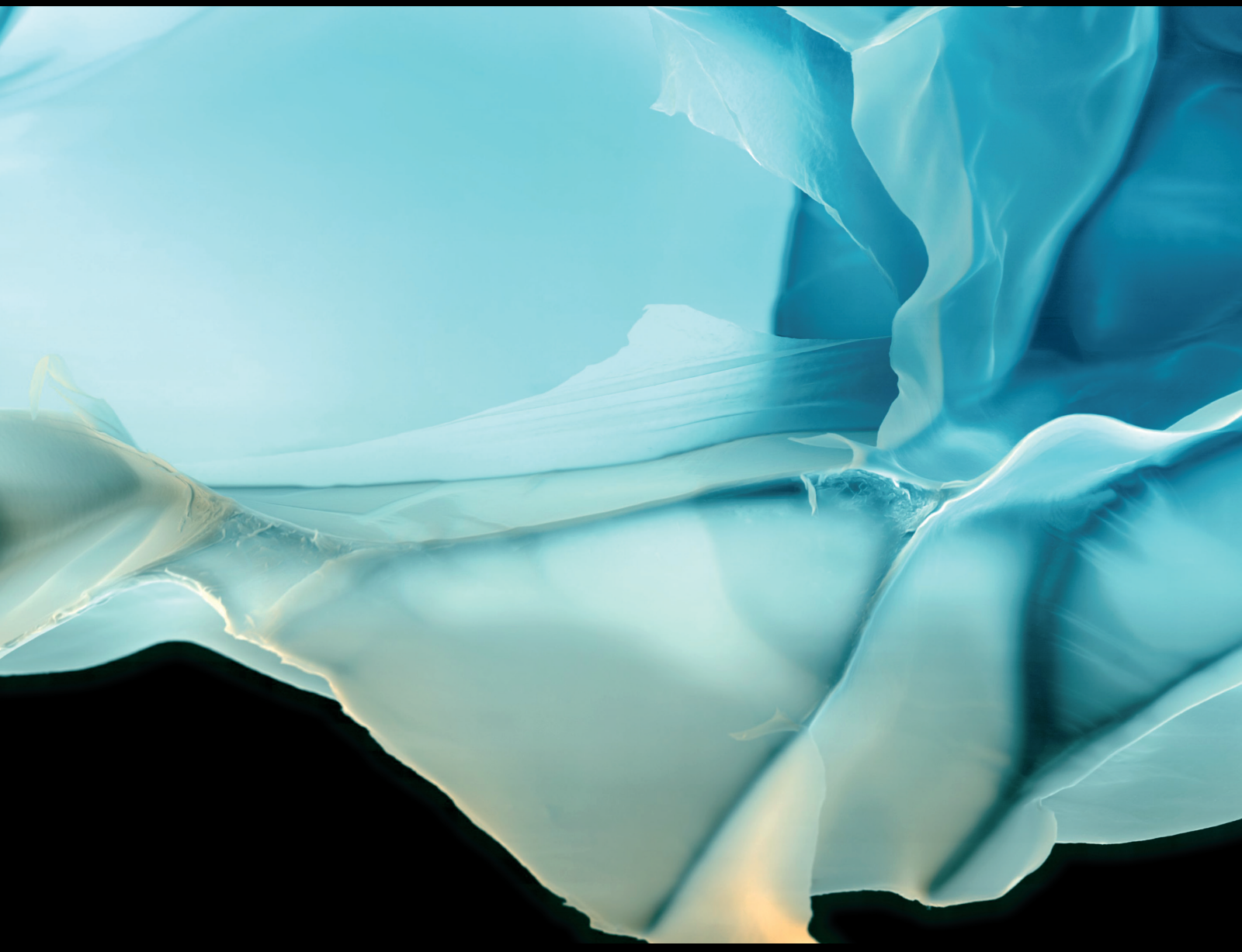

Applications of Fiber Reinforced Polymer Composites in Civil Engineering

Advances in Polymer Technology

Applications of Fiber Reinforced Polymer Composites in Civil Engineering

Lead Guest Editor: Tianyu Xie
Guest Editors: Guangming Chen, Mohamed A. Sadakkathulla, Mohamed Elchalakani, and Jinjun Xu

Contents

Hindawi
Advances in Polymer Technology
Volume 2020, Article ID 2809302, 12 pages
https://doi.org/10.1155/2020/2809302

Research Article

Finite Element Failure Analysis of GFRP Laminates in Plate-Cone Reticulated Shell

Xing Wang,[1] Yu Jiang,[1] Yonghui Huang ,[2] Yue Huang ,[2,3] and Fan Wang[4]

[1]*School of Civil Engineering, Guangzhou University, Guangzhou 510006, China*
[2]*Guangzhou University-Tamkang University Joint Research Center for Engineering Structure Disaster Prevention and Control, Guangzhou University, Guangzhou 510006, China*
[3]*School of Civil Engineering, Qingdao University of Technology, Qingdao 266033, China*
[4]*Guangzhou University Library, Guangzhou University, Guangzhou 510006, China*

Correspondence should be addressed to Yonghui Huang; huangyh@gzhu.edu.cn and Yue Huang; jeff.yue.huang@gmail.com

Received 28 October 2019; Accepted 29 February 2020; Published 19 June 2020

Guest Editor: Guangming Chen

Plate-cone reticulated shell is a new type of spatial structures with good mechanical behavior, technical economy, and architectural appearance. In this paper, using ANSYS software, the strength failure analysis model of composite laminates is established in cooperation with the Strength Criterion of Hoffman. The effects of layer number, laying direction, and thickness of laminates on the ultimate strength of laminates are studied by detailed parametric analysis, which provides a theoretical basis for the design of composite plate-cone reticulated shell and GFRP laminated plates. Some important conclusions are obtained and can be applied to engineering practice.

1. Introduction

Plate-cone reticulated shell is an emerging spatial structure in recent years, which is developed based on Kaiser aluminum stressed-skin dome. The structure is assembled with cone elements and truss members, which are connected at the joints using bolts [1] as shown in Figures 1 and 2. Plate-cone reticulated shell is a special type stress-skin structures of half continuity and half lattice since ventral members (also ventral members and bottom members) of common double-layer reticulated shell are replaced by cone elements. The cone plates can be made of conventional materials such as aluminum alloy, and steel or light composite materials such as carbon fiber reinforced polymer (CFRP) or glass fiber reinforced polymer (GFRP). Plate-cone reticulated shell is an effective structure that can make full use of the strength and stiffness of the plates. At the same time, it integrates load-bearing, enclosure and decoration into a whole. Because of the high strength-to-weight ratio, good technical and economic benefits, and distinctive architectural visual effect, the plate-cone reticulated shell has been widely used as a long-span spatial structure [2, 3]. The idea of plate-cone reticulated shell was originated from the Kaiser aluminum stressed-skin dome. The first Kaiser aluminum stressed-skin dome was built on the Hawaiian village of Honolulu, USA, in 1957 with a span of 44.2 m [4]. To date, there are many other aluminum stressed-skin domes which have been built in schools, banks, city centers, conference halls etc., such as three Temcor aluminum dome stadiums with 71 m span on Elmira College, New York, and the airlines dome with 60 m span on Schipol Airport of Amsterdam, Holland [1]. Since the 1990s, composite materials such as FRP have been increasingly used in civil engineering [5]. Because FRP is much lighter and stronger than ordinary steel and aluminum alloy, it is more preferred to be used as the prefabricated cone element in plate-cone reticulated shells.

Many studies have been carried out in relation to conventional single-layer or double-layer reticulated dome. Among them, Fan et al. [6] studied the elasto-plastic stability of seven types of commonly used single-layer reticulated shells. Xiong et al. [7] investigated the elasto-plastic stability of single-layer latticed shells with aluminum alloy gusset joints. Hiyama et al. [8] investigated the global buckling behaviors of an aluminum alloy double-layer spatial latticed

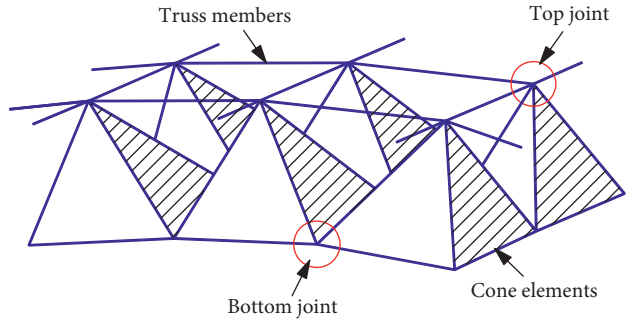

Figure 1: Segment of the plate-cone reticulated shell.

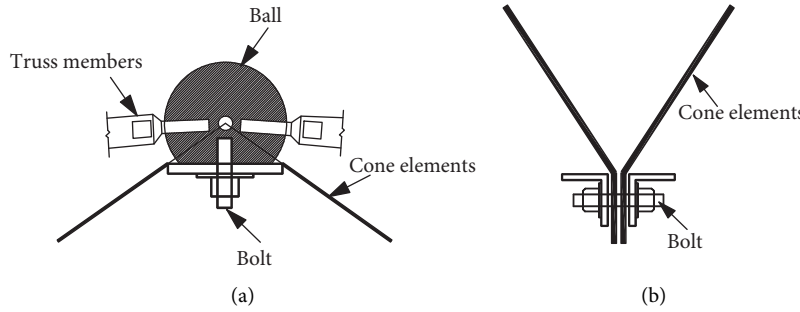

Figure 2: Sketch of connecting joints: (a) top joint and (b) bottom joint.

structure with tubular pipes, ball connections, and joining bolts via experimentation and analysis. Xie and Li [9] studied the natural vibration characteristics of an aluminum alloy double-layer reticulated shell with various structural dimensions. Zhi et al. [10] examined the failure mechanisms of single-layer reticulated domes subjected to seismic loads. Zhai et al. [11] carried out the dynamic response analysis of the reticulated domes under blast loading using the finite element (FE) software ANSYS/LS-DYNA for studying damage model and damage assessment. Lin et al. [12] studied the failure modes of a reticulated dome in a small airplane.

Most of the aforementioned studies are focused on the structural behavior of reticulated domes of homogeneous materials. In contrast, the studies on the GFRP laminates in plate-cone reticulated shell are limited, among which Robak [13] studied the structural use of plastics pyramids in double-layer space grids, Wang and Wang [14] researched the preliminary application of GFRP on plate-cone reticulated shells and analyzed the plate-cone reticulated shell as a whole, material design and structure design have not been done. Composite materials possess some distinct mechanical properties, such as anisotropy, nonhomogeneity, low interlaminar shear modulus and low interlaminar shear tensile strength, geometric nonlinearity, and material nonlinearity. These mechanical characteristics make the problem more complicated and challenging than the conventional materials that is homogeneous, continuous, linear elastic, and isotropic. Hence, it is necessary to investigate the behavior and strength of the composite plate-cone reticulated shell with FRP laminates.

In this paper, based on the composite mechanics and the theory of plate and shell, the elastic stress in the principal direction of single-layer plate of plate-cone reticulated shell is calculated by using finite element analysis. Then, the ultimate strength of each layer under each load step is obtained by the Strength Criterion of Hoffman, and the failure load of the first failed layer of laminated plate (defined as the first layer strength) and the failure load of the last failed layer (defined as the last layer strength) are obtained and evaluated. The strength and main influencing factors of composite laminates are studied comprehensively and deeply which provides theoretical foundation for the design of composite plate-cone reticulated shells with laminated plates.

2. Failure Analysis of GFRP Composite Laminates

Generally, in composite laminates, the fiber orientation in each layer is different. In some cases, even the material properties and thickness at different layers are different. Hence, the resistance of each layer of fibers to external load is different. It is highly unlikely for all layers of fibers to reach the ultimate strength and fail at the same time under certain external loads. Instead, the failure of the laminates often initiates from the weakest layer and propagate layer by layer.

The different strength criteria of single-layer composite plate has been proposed for the different situations. Strength Criteria of Tsai–Hill did not consider the influence of difference with tensile strength and compressive strength on material failure. Hoffman considered the factor of difference

with tensile strength and compressive strength and supplied some linear terms shown as follows [15]:

$$C_1(\sigma_2-\sigma_3)^2 + C_2(\sigma_3-\sigma_1)^2 + C_3(\sigma_1-\sigma_2)^2 + C_4\sigma_1 + C_5\sigma_2 + C_6\sigma_3 + C_7\tau_{23}^2 + C_8\tau_{31}^2 + C_9\tau_{12}^2 < 1. \quad (1)$$

Considering the orthotropy and plane stress state of the single-layer plate, the Strength Criteria of Robert [15] which is shown in equation (2) was derived from equation (1):

$$F = \frac{\sigma_1^2 - \sigma_1\sigma_2}{X_tX_c} + \frac{\sigma_2^2}{Y_tY_c} + \frac{X_c - X_t}{X_tX_c}\sigma_1 + \frac{Y_c - Y_t}{Y_tY_c}\sigma_2 + \frac{\tau_{12}^2}{S^2} < 1, \quad (2)$$

where F is the failure value and $F \geq 1.0$ means material failure occurs. X_t, X_c, Y_t, Y_c, and S are the basic strength of the single-layer FRP laminate which can be obtained from the material property test, σ_1 and σ_2 are the principal stresses along the principal directions, and τ_{12} is the maximum shear stress.

To perform the failure analysis, the normal stress $\{\sigma_x, \sigma_y, \tau_{xy}\}$ of each layer of laminates along the reference axis of element's coordinate x, y, and z are calculated firstly. Because the layering angle of each layer is different, the calculated normal stress of each layer may not follow the principal direction of elasticity. In order to carry out strength failure analysis, the normal stress $\{\sigma_x, \sigma_y, \tau_{xy}\}$ of laminates under the element's coordinate system should be transformed into the principal stress $\{\sigma_1, \sigma_2, \tau_{12}\}$ along the principal direction of elasticity of the layer by using equation (3). Then, the strength of each layer is calculated according to the Strength Criterion of Hoffman which is shown in equation (2).

$$\begin{Bmatrix} \sigma_1 \\ \sigma_2 \\ \tau_{12} \end{Bmatrix} = \begin{bmatrix} \cos^2\theta & \sin^2\theta & 2\sin\theta\cos\theta \\ \sin^2\theta & \cos^2\theta & -2\sin\theta\cos\theta \\ -\sin\theta\cos\theta & \sin\theta\cos\theta & \cos^2\theta - \sin^2\theta \end{bmatrix} \begin{Bmatrix} \sigma_x \\ \sigma_y \\ \tau_{xy} \end{Bmatrix}. \quad (3)$$

In order to obtain the normal stress of each layer of laminates, nonlinear static analysis of the plate-cone reticulated shell under step-by-step loading was carried out using commercial finite element software ANSYS. Then, the principal stress of the single-layer plate is obtained according to equation (3). The ultimate strength of each layer at each load step is obtained by Strength Criterion of Hoffman, and the ultimate strength of the first failed layer (defined as the first layer strength) and the ultimate strength of the last failed layer (defined as the last layer strength) are analyzed and evaluated.

It should be point out that the strength of the first failed layer is generally considered as the ultimate strength of the composite laminates in engineering design, so the stiffness reduction of the laminate plate caused by the failure of a certain layer is generally not considered in the structural analysis. Nevertheless, the ultimate strength of the last failed layer of the laminate is also calculated in this paper in order to evaluate the interval between the ultimate strength of the first layer and that of the last layer. This is critical and essential to identify a reasonable design of the laminate composite, which is characterized by the full use of the potential of composite materials.

3. Finite Element Analysis

3.1. Geometry and Material Properties of the Model. A plate-cone cylindrical reticulated shell with quadrangular pyramids is studied using finite element analysis, as shown in Figure 3. The span of structure $S = 30$ m, length $L = 45$ m, vector height $F = 10$ m, and thickness $h = 1.5$ m. The top connecting truss members are steel pipes of $\Phi 108 \times 5.0$ mm, and the triangle plates of cones are orthogonal symmetric GFRP laminated plates that consist of four layers of laminates with total thickness equal to 8 mm. The matrix of each layer is composed of glass/epoxy resin, and the laying mode of laminated plates is $[0/90]^\circ_S$, i.e., the orientation of fibers are 0° in the first and the fourth layers and 90° in the second and the third layers. The material properties of the GFRP plates are listed in Table 1. The steel pipes are considered as ideal elastic plastic material with elastic modulus $E = 206$ GPa, yield strength $f_y = 235$ MPa, and Poisson ratio $\mu = 0.3$.

3.2. Finite Element Model. For the composite plate-cone reticulated shell, the FEM analysis model only with the top member, without bottom members and middle members, is adopted in this paper. The model considers the joints of the top members as hinged and the bottom joints as rigid (as shown in Figure 2). In the ANSYS model, the spatial truss element Link8 with 2 nodes and 6 degrees of freedom is used to model the top truss members, and the finite strain shell element Shell181 with 4 nodes and 24 degrees of freedom is used to model the triangular plate elements. This element type was demonstrated to suit for analyzing layered composite structures where material properties were varied at different layers [16–18].

The translational displacements of bottom nodes along two longitudinal edges are restricted in three directions. Uniformly distributed vertical loads of 2 kN/m^2 is applied perpendicular to the shell surface. Self-weight of the structure is also considered. Figure 4 shows the finite element model of the plate-cone cylindrical reticulated shell, which contains 326 nodes, 600 shell elements, and 275 link elements.

3.3. Numerical Results. The displacements and internal forces of the plate-cone cylindrical reticulated shell are

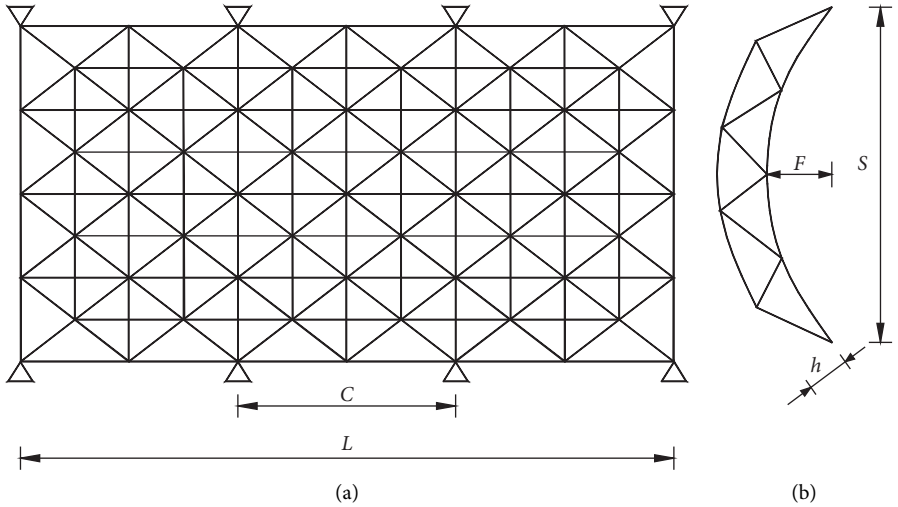

Figure 3: Geometric parameters of the plate-cone cylindrical reticulated shell.

Table 1: Material properties of the GFRP laminate.

E_X (GPa)	$E_Y = E_Z$ (GPa)	$G_{XY} = G_{XZ}$ (GPa)	G_{YZ} (GPa)	$PR_{XY} = PR_{XZ}$
53.74	17.95	8.63	5.98	0.25
PR_{YZ}	$X_t = X_c$ (GPa)	Y_t (GPa)	Y_c (GPa)	S (GPa)
0.49	1.034	0.027	0.138	0.041

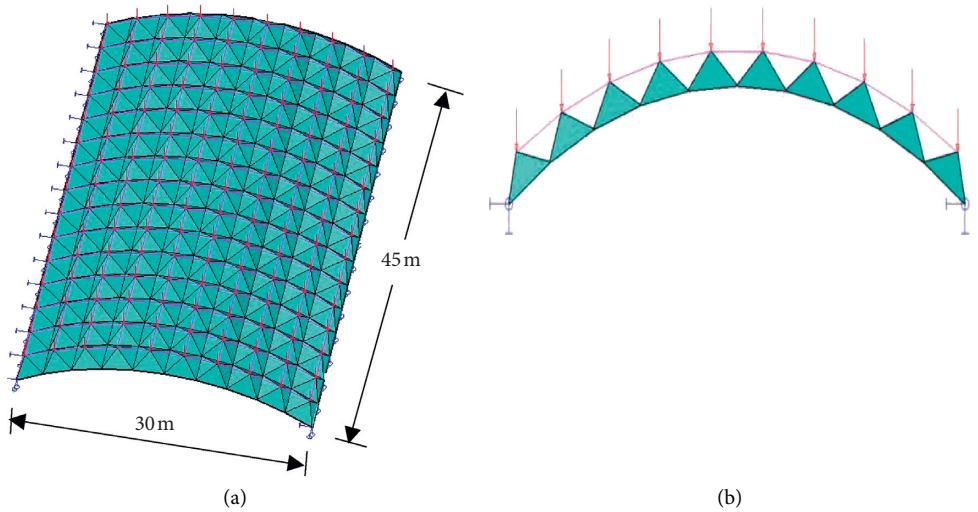

Figure 4: FE model of the plate-cone cylindrical reticulated shell.

obtained. Figure 5 shows the vertical displacement of the plate-cone reticulated shell. Figures 6 and 7 present the axial force of the top member and the laminates. Figures 8 and 9 show the stresses in each layer of laminates.

From Figure 5, it can be seen that the maximum displacement of the plate-cone reticulated shell is 6.18 mm. The ratio of the maximum displacement to the span of the structure is 1/4854, which reveals that the composite plate-cone reticulated shell has large stiffness similar to the conventional steel plate-cone reticulated shell.

From Figures 6 and 7, it can be seen that the composite plate-cone reticulated shell has the same rules for static internal force distribution as the common steel plate-cone reticulated shell [19, 20]. The maximum axial compression force of top members is −32.732 kN, and the maximum axial compression force of plates is -51.055 kN. The strength of each layer of laminates was calculated according to equations (2) and (3)fd2. The results show that the strength of the first and fourth layer of composite laminates is 0.007029, and the strength of the second and third layer of composite

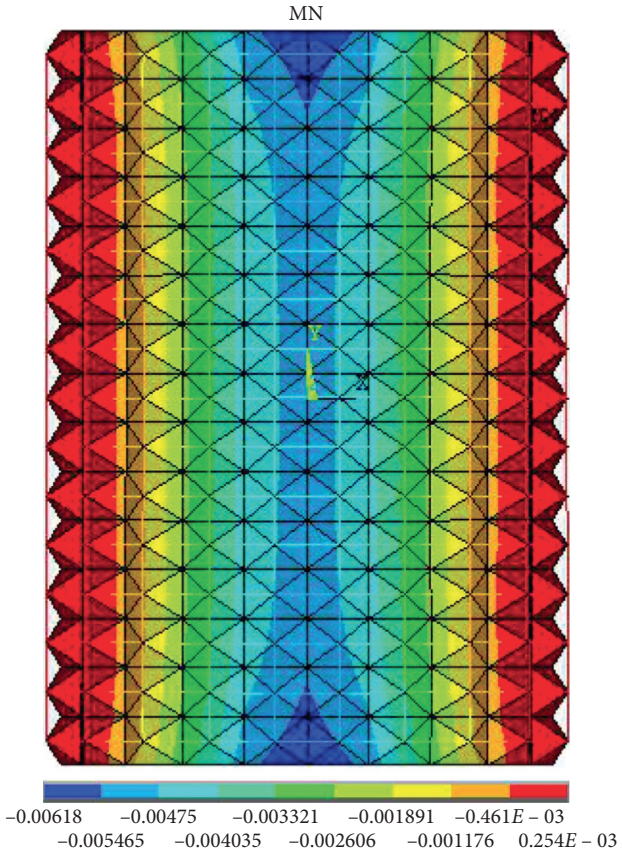

Figure 5: Vertical displacement of the plate-cone reticulated shell (m).

laminates is 0.071455. Therefore, the composite plate-cone reticulated shell has notable residual strength. However, the internal force distribution is not uniform among layers of laminates, so it is necessary to analyze the reasonable laying design for laminates of the composite plate-cone reticulated shell.

4. Parametric Analysis

4.1. Effect of the Number of Laminate Layers. In order to evaluate the effects of various design parameters on the behavior of the GFRP laminates, a parametric analysis is conducted using the FE model established above. Firstly, the effect of the number of laminate layers on the strength of each layer is studied. There are two groups of laying mode used in this plate-cone cylindrical reticulated shell. The first group is composed of laminates with fibers oriented in 90° and 0°: [90/0/90] (mode 1), $[90/0]^{\circ}_{S}$ (mode 2), [90/0/90/0/90] (mode 3), $[90/0/90]^{\circ}_{S}$ (mode 4), and the number of the laminate layers for modes 1 to 4 is 3 to 6, respectively. The second group is composed of laminates with fibers oriented in −45° and +45°: [−45/+45/−45] (mode 5), $[-45/+45]^{\circ}_{S}$ (mode 6), [−45/+45/−45/+45/−45] (mode 7), and $[+45/-45/+45]^{\circ}_{S}$ (mode 8), and the number of laminate layers for modes 5 to 8 is also 3 to 6, respectively. A schematic diagram showing the different modes is presented in Figure 10. The total thickness of the composite laminates is 8 mm in all cases, and the thickness of each layer is equal.

Figures 11 and 12 show the ultimate strength of the reticulated shell composed with the first group (modes 1~4) and the second group (modes 5~8) of laminates, respectively.

It can be seen from the figures that the number of laminate layers has insignificant effect on the failure load of the composite plate-cone reticulated shells with quadrangular cones for the same laying mode and total thickness. Taking the first group as an example, it is found that the first failed layer of laminates is the layer with fibers oriented in 90° occurring in the direction of 90° fibers, while the failure of the last layer occurs in the direction of 0° fibers. The first layer strength and the last layer strength are almost the same even though the number of layers is different. The first layer strength and the last layer strength for the mode with four layers of laminates (i.e., laying mode 2) are only 8.16% and 4.75% greater than that of the mode with three layers of laminates (i.e., laying mode 1), respectively. Therefore, it can be concluded that the influence of the number of layers on the ultimate strength and failure sequence of each layer of laminates can be ignored if the total thickness of the GFRP laminates is the same. Considering the material cost and time consumption, it is recommended that the layer number of laminates should not be too much, and the total layer number of laminates is suitable to be 4 layers.

4.2. Effect of Laying Direction. The laying direction of laminates is another critical parameter of laminates. Because the laying structures are different, that is to say, if the order of each layer in the laminate is different, the ultimate strength of the laminate may be totally different even for the same material system. Therefore, for the composite plate-cone reticulated shell, studying the influence of laying direction on the strength of the laminate is very necessary and of significant importance in practice.

In order to discuss the influence of laying direction on the strength of the structure, the mechanical properties of eight kinds of laying directions (total thickness is 8 mm, and the thickness of each layer is uniform) are calculated using finite element analysis. Combining with the Strength Criterion of Hoffman, the ultimate strength and the failure sequence of layers of laminates are obtained. The detailed results are shown in Table 2.

It can be found from Table 2 that the laying direction of the laminate has significant influence on the strength of the structure. It can also be observed that

(1) The ultimate strength of the plate-cone reticulated shell with different laying modes are different. The first layer strength of laminates with laying mode of $[0/90]^{\circ}_{S}$ and $[90/0]^{\circ}_{S}$ are 26.6 kN/m^2, while the last layer strength is about 130 kN/m^2. However, for laminates with laying modes of $[-45/+45]^{\circ}_{S}$ and $[+45/-45]^{\circ}_{S}$, all of four layers almost fail concurrently, and the failure load is about 44.5 kN/m^2.

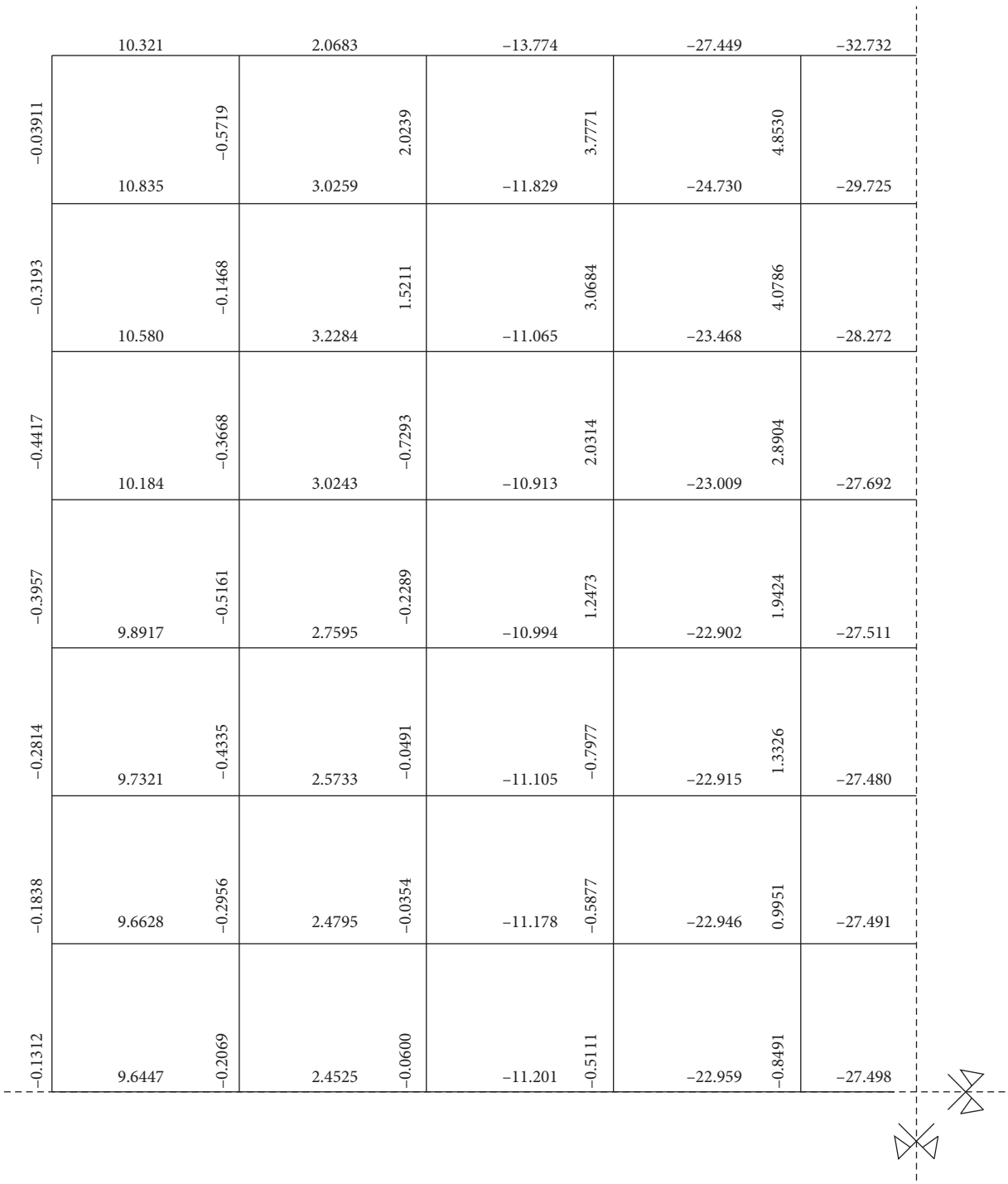

Figure 6: Axial force of top members of the plate-cone reticulated shell (kN).

(2) The failure sequence of layers is also different. The first failed layers of laminates with laying modes of $[90/0]^{\circ}_{S}$, $[+45/0]^{\circ}_{S}$, and $[90/+45]^{\circ}_{S}$ are the first and fourth layers, while the last failed layers are the second and third layers. However, for laminates with laying modes of $[0/90]^{\circ}_{S}$, $[0/-45]^{\circ}_{S}$, and $[+45/0]^{\circ}_{S}$, the failure sequence of layers are just the opposite, that is, the first failed layers are the second and third layers, and the last failed layers are the first and fourth layers. For laminates with laying modes of $[-45/+45]^{\circ}_{S}$ and $[+45/-45]^{\circ}_{S}$, all four layers failed simultaneously.

(3) The strength interval between the first layer strength and the last layer strength is also different. For laminates with laying modes of $[0/90]^{\circ}_{S}$ and $[90/0]^{\circ}_{S}$, there is the largest strength interval between the first

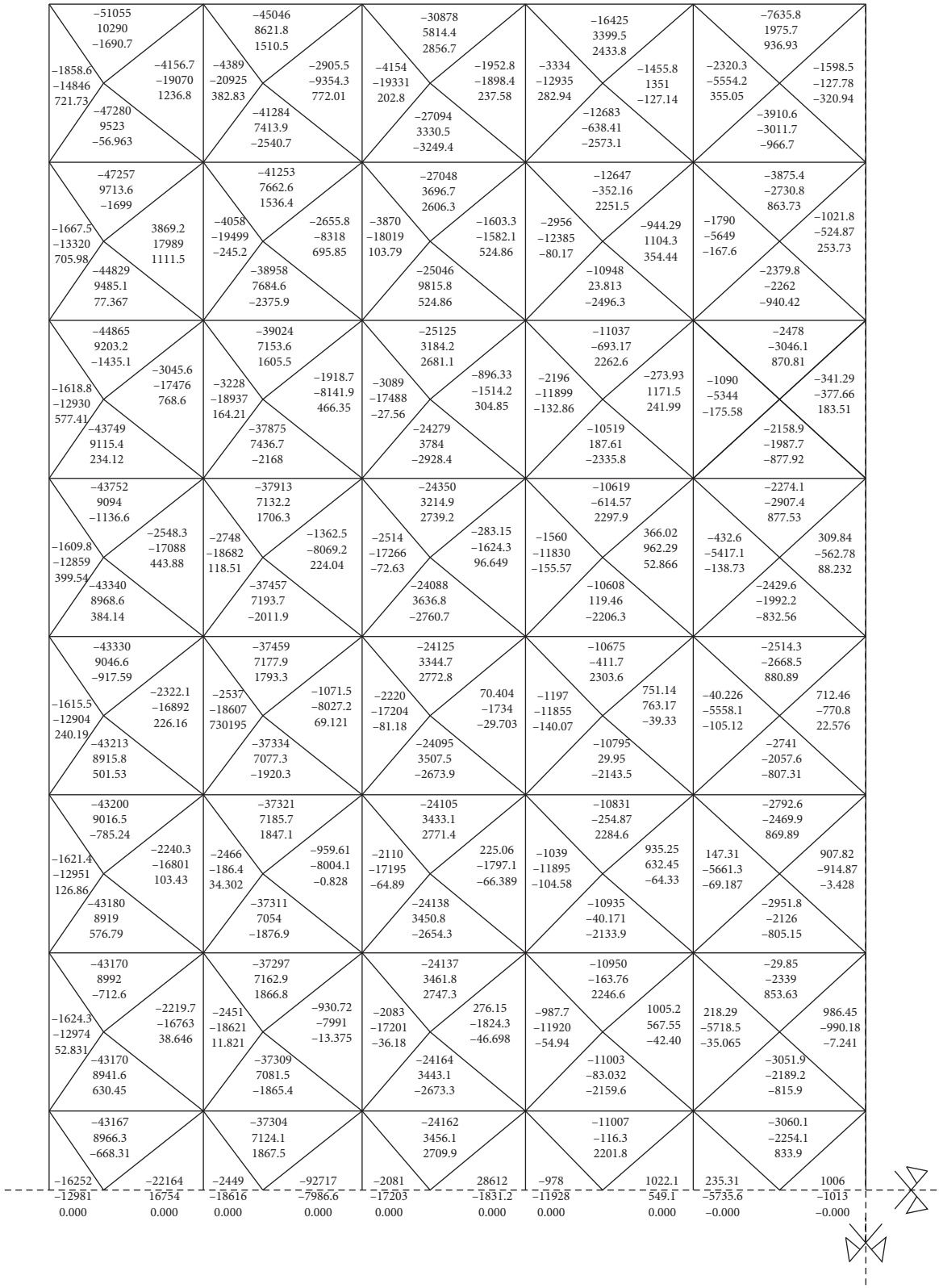

Figure 7: Axial force of laminates of the plate-cone reticulated shell (N).

strength and the last strength. The ratio between the last layer strength and the first layer strength for laminates with laying modes of $[0/90]^{\circ}_{S}$ and $[90/0]^{\circ}_{S}$, $[+45/90]^{\circ}_{S}$ and $[+90/+45]^{\circ}_{S}$, and $[+45/0]^{\circ}_{S}$ and $[+0/+45]^{\circ}_{S}$ are 4.89, 2.95, and 1.27, respectively. And for laminates with laying modes of $[-45/+45]^{\circ}_{S}$ and

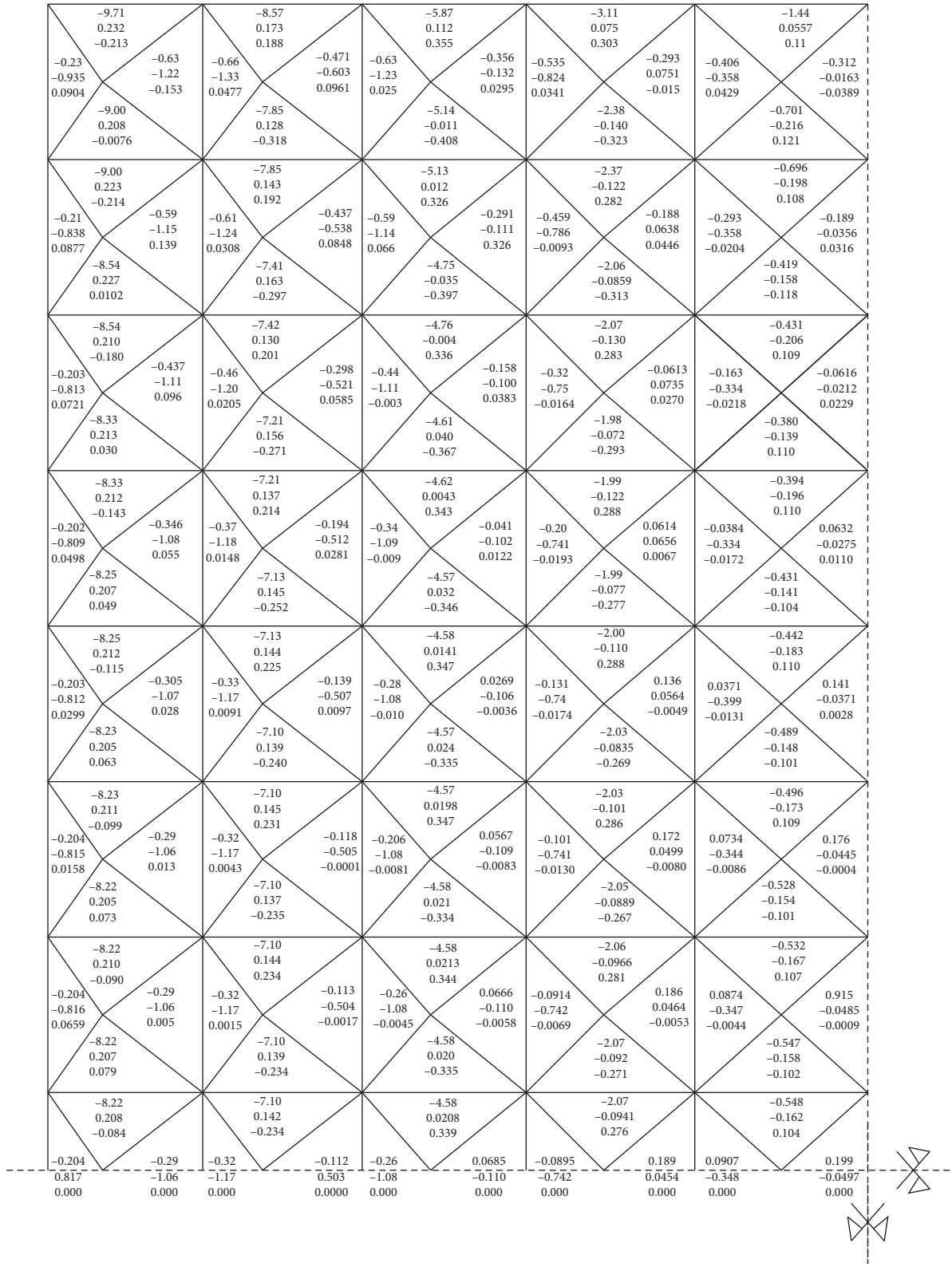

Figure 8: Normal and shear stress (σ_x, σ_y, τ_{xy}) of the first and fourth layers of laminates (MPa).

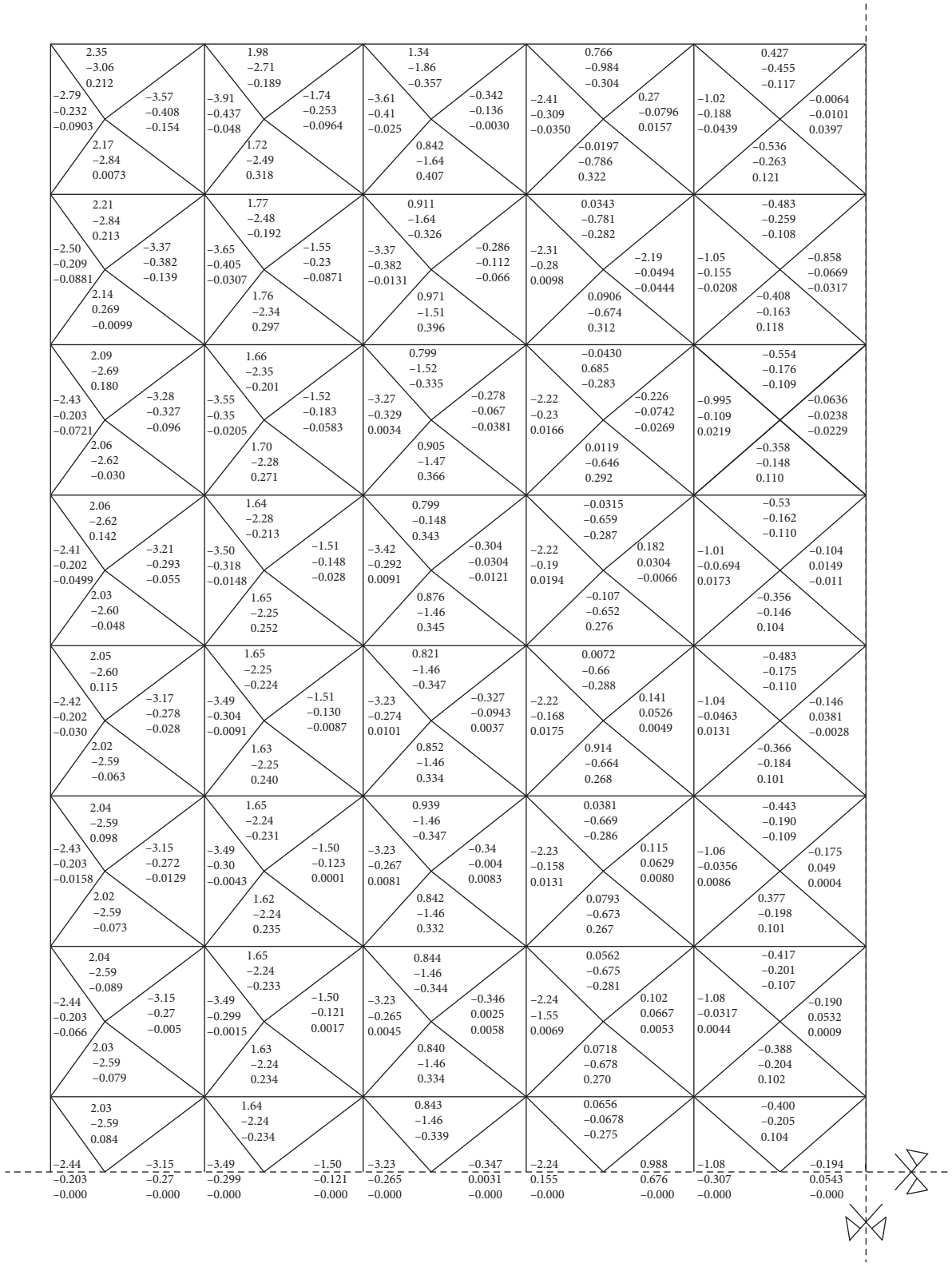

Figure 9: Normal and shear stress (σ_x, σ_y, τ_{xy}) of the second and third layers of laminates (MPa).

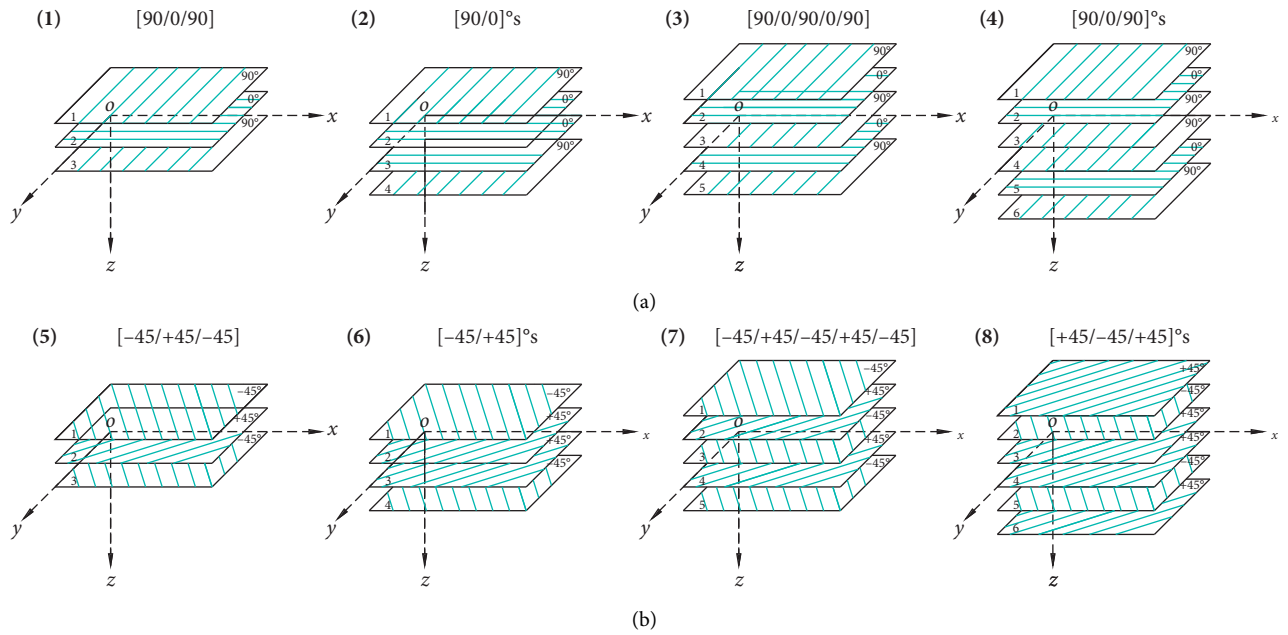

Figure 10: Composition of FRP laminates with fibers oriented in different directions. (a) Group 1. (b) Group 2.

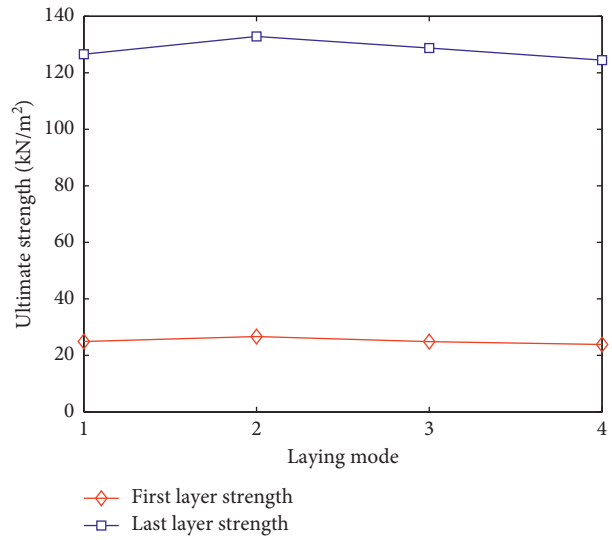

Figure 11: Ultimate strength of the reticulated shell composed with first group laminates.

$[+45/-45]^{\circ}_{S}$, all four layers fail at the same time, so there is no strength interval between the last layer strength and the first layer strength.

Based on the above analysis, it can be concluded that the laying direction of laminate is a key factor affecting the ultimate strength of GFRP laminate of the composite plate-cone reticulated shell.

4.3. Effect of Thickness of Laminate. In order to study the influence of the thickness of laminates on the ultimate strength of laminates, the parametric analysis for laminates with different total thickness and different thickness of individual layer is conducted. The triangular plates of cone elements are adopted with different laying design, i.e., the laying directions are all $[90/0]^{\circ}_{S}$, but the total thickness of the laminates and the thickness of each layer are different. In this paper, the mechanical properties of six kinds of laminates with different laying modes (seen in Table 3) are calculated, and the ultimate strength of the structure under uniformly distributed loads are obtained by combining the Strength Criterion of Hoffman; more detailed results are shown in Table 3.

From Table 3, it can be seen that the thickness of composite laminates has a significant effect on the ultimate strength of laminates in plate-cone reticulated shells. With

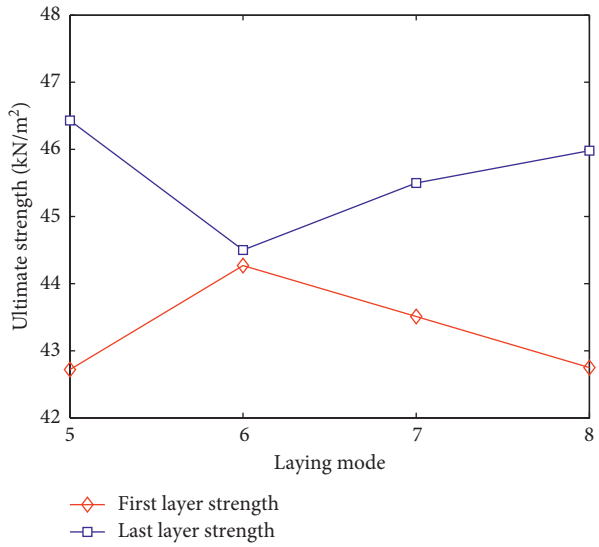

Figure 12: Ultimate strength of the reticulated shell composed with second group laminates.

Table 2: Uniformly distributed load when layer-by-layer failure of laminated plates.

Laying mode	First layer strength (kN/m^2)	Layers failed at first	Last layer strength (kN/m^2)	Layers failed at last
$[0/90]^\circ_S$	26.6	2nd and 3rd layers	130.0	1st and 4th layers
$[90/0]^\circ_S$	26.5	1st and 4th layers	132.3	2nd and 3rd layers
$[-45/+45]^\circ_S$	44.5	All of four layers	44.5	All of four layers
$[+45/-45]^\circ_S$	44.4	All of four layers	44.5	All of four layers
$[+45/0]^\circ_S$	65.4	1st and 4th layers	83.0	2nd and 3rd layers
$[0/+45]^\circ_S$	65.5	2nd and 3rd layers	83.0	1st and 4th layers
$[+45/90]^\circ_S$	14.8	2nd and 3rd layers	43.6	1st and 4th layers
$[90/+45]^\circ_S$	14.8	1st and 4th layers	43.8	2nd and 3rd layers

Table 3: Comparison of ultimate strength of laminated plates with different thicknesses.

Thickness of each layer	Total thickness (mm)	First layer strength Q_1 (kN/m^2)	Last layer strength Q_2 (kN/m^2)	Q_2/Q_1
[2 mm/2 mm] $_S$	8	26.6	132.3	4.99
[1 mm/1 mm] $_S$	4	14.0	76.8	5.48
[3 mm/1 mm] $_S$	8	23.2	121.3	5.23
[1 mm/3 mm] $_S$	8	28.8	134.0	4.66
[2 mm/1 mm] $_S$	6	18.5	100.0	5.40
[1 mm/2 mm] $_S$	6	21.7	108.5	5.01

Note: [3 mm/1 mm] $_S$ indicates that the thickness of the first and fourth layers is 3 mm, and that of the second and third layers is 1 mm.

the change of the thickness of each layer, the first layer strength and last layer strength of the structure vary remarkably. Generally, the first layer and last layer strengths will increase with the increase of the total thickness and the thickness of the second and fourth layers. It can also be found that with the change of total thickness, the strength interval between the first layer strength and last layer strength of the laminates changes slightly. The ratios between the last layer ultimate strength Q2 and the first layer ultimate strength Q1 are about 5.

5. Conclusions

The strength of each layer in FRP laminate is one of the main controlling factors in the design of composite plate-cone reticulated shell. In this paper, using ANSYS software, a strength model of composite laminate is established using the Strength Criterion of Hoffman without considering the stiffness degradation of laminates. The effects of number of layers, laying direction, and thickness of laminates on the ultimate strength of laminates are studied in the parametric analysis. Based on the results of the numerical analysis, the following conclusions can be drawn:

(1) In the composite plate-cone reticulated shell, the influence of the number of laminate layers on the ultimate strength and failure sequence of each layer of laminated plates is negligible. Taking into account other factors, such as material cost and time consumption, the total layer number of laminate is recommended as four layers.

(2) The laying direction is one of the key factors affecting the ultimate strength of the composite laminate in the plate-cone reticulated shell. The influence of laying direction on the ultimate strength and strength interval is significant. It should be fully used in design of practical engineering to achieve reasonable strength interval of laminate, for making full use of potential and advantages of composite material.

(3) The influence of the thickness of composite laminate on the ultimate strength of laminate is significant. The first layer strength and last layer strength will increase with the total thickness increase, and the thickness of the second and fourth layers increase. But the influence of the total thickness on the strength interval is negligible.

Data Availability

The data used to support the findings of this study are included within the article.

Conflicts of Interest

The authors declare there are no conflicts of interest.

Acknowledgments

Financial support from the National Natural Science Foundation of China is gratefully acknowledged. This research was funded by the National Natural Science Foundation of China, grant nos. 51678313 and 51608135, and Taishan Scholars Program of Shandong Province, China, grant no. tsqn201909127.

References

[1] Z. S. Makowski, *Analysis, Design, and Construction of Braced Domes*, Nichols Publication Company, New York, NY, USA, 1984.

[2] K. Parsa and L. Hollaway, "Application of advanced composites to a double layer stressed skin roof structure," *International Journal of Space Structures*, vol. 12, no. 2, pp. 69–80, 1997.

[3] S. Halliwell, "In-service performance of glass reinforced plastic composites in Building," *Proceeding of the Institution of Civil Engineers: Structures and Buildings*, vol. 17, no. 1, pp. 99–104, 2004.

[4] W. Morgan, *The Elements of Structure, Pitman*, University of Auckland, New Zealand, Oceania, 2nd edition, 1981.

[5] C. E. Bakis, L. C. Bank, V. L. Brown et al., "Fiber-reinforced polymer composites for construction-state-of-the-art review," *Journal of Composites for Construction*, vol. 6, no. 2, pp. 73–87, 2002.

[6] F. Fan, Z. Cao, and S. Shen, "Elasto-plastic stability of single-layer reticulated shells," *Thin-Walled Structures*, vol. 48, no. 10-11, pp. 827–836, 2010.

[7] Z. Xiong, X. Guo, Y. Luo, and S. Zhu, "Elasto-plastic stability of single-layer reticulated shells with aluminium alloy gusset joints," *Thin-Walled Structures*, vol. 115, pp. 163–175, 2017.

[8] Y. Hiyama, K. Ishikawa, S. Kato, and S. Okubo, "Experiments and analysis of the post-buckling behaviors of aluminum alloy double layer space grids applying ball joints," *Structural Engineering and Mechanics*, vol. 9, no. 3, pp. 289–304, 2000.

[9] Z. H. Xie and L. J. Li, "Earthquake resistant capability analysis of aluminium alloy double layer reticulated shell structure," *Journal South China University Technology*, vol. 3, no. 1, pp. 127–129, 2003.

[10] X. D. Zhi, F. Fan, and S. Z. Shen, "Failure mechanisms of single layer reticulated domes subjected to earthquake," *Journal of the International Association for Shell and Spatial Structures*, vol. 48, no. 1, pp. 29–44, 2007.

[11] X. Zhai, Y. Wang, and Z. Sun, "Damage model and damage assessment for single-layer reticulated domes under exterior blast load," *Mechanics Based Design of Structures and Machines*, vol. 47, no. 3, pp. 319–338, 2019.

[12] L. Lin, Y. X. Ren, M. Y. Huang, X. D. Zhi, and D. Z. Wang, "Failure modes of a reticulated dome in a small airplane crash," *Advances in Civil Engineering*, vol. 2019, Article ID 5025637, , 2019.

[13] D. Robak, "The structural use of plastics pyramids in double-layer space grids," in *Proceeding of the IASS Symposium on Membrane Structures and Space Frames*, pp. 105–112, Osaka, Japan, September 1986.

[14] X. Wang and F. Wang, "Application of composite materials in plate-cone reticulated shells," *Journal of Zhejiang University of Technology*, vol. 31, no. 2, pp. 124–128, 2003.

[15] M. J. Robert, *Mechanics of Composite Materials*, Taylor & Francis Group, New York, NY, USA, 2nd edition, 1999.

[16] Z. Yang, Y. Huang, A. Liu, J. Fu, and D. Wu, "Nonlinear in-plane buckling of fixed shallow functionally graded graphene reinforced composite arches subjected to mechanical and thermal loading," *Applied Mathematical Modelling*, vol. 70, pp. 315–327, 2019.

[17] Z. X. Zhang, A. R. Liu, J. Yang et al., "Nonlinear in-plane elastic buckling of a laminated circular shallow arch subjected to a central concentrated load," *International Journal of Mechanical Sciences*, vol. 2019, pp. 161-162, 2019.

[18] Y. H. Huang, Z. C. Yang, A. R. Liu, and J. Y. Fu, "Nonlinear buckling analysis of functionally graded graphene reinforced composite shallow arches with elastic rotational constraints under uniform radial load," *Materials*, vol. 11, no. 6, p. 910, 2018.

[19] X. Wang and S. L. Dong, "A study on static characteristics for plate-cone reticulated shell," *Building Structure*, vol. 30, no. 9, pp. 28–30, 2000.

[20] X. Wang and S. L. Dong, *Composite Structures FEM Analysis for Plate-Cone Reticulated Shell, ISSEYE-6*, Yunnan Science and Technology Press, Kunming, China, 2000.

Hindawi
Advances in Polymer Technology
Volume 2020, Article ID 6029047, 9 pages
https://doi.org/10.1155/2020/6029047

Research Article

Dynamic Characteristics and Chloride Resistance of Basalt and Polypropylene Fibers Reinforced Recycled Aggregate Concrete

Dong Lu,[1,2] **Hui Cao**,[3] **Qiangru Shen**,[3] **Yue Gong**,[4] **Cheng Zhao**,[1] **and Xiaohui Yan**[1]

[1]*School of Materials Science and Engineering, Chang'an University, Xi'an 710064, China*
[2]*School of Civil Engineering, Harbin Institute of Technology, Harbin 150000, China*
[3]*School of Transportation and Civil Engineering, Nantong University, Nantong, Jiangsu 226019, China*
[4]*State Key Laboratory of Metal Matrix Composites, Shanghai Jiao Tong University, Shanghai 200240, China*

Correspondence should be addressed to Hui Cao; caohui03@ntu.edu.cn

Received 11 October 2019; Revised 30 December 2019; Accepted 9 January 2020; Published 2 June 2020

Guest Editor: Jinjun Xu

Fiber polymer has been extensively used to improve the mechanical properties and durability of concrete. However, the studies of the effect of fiber polymer on the dynamic performance of recycled aggregate concrete (RAC) is still very limited. In this study, we prepared two types of RAC formulations: RAC reinforced with basalt fibers (BFs) and RAC reinforced with polypropylene fibers (PPs), and compared the effects of fiber types and contents on the air void content, workability (slump), mechanical properties (compressive and flexural strength), dynamic characteristics (dynamic modulus of elasticity and damping ratio), and chloride resistance of RAC. The experimental results showed that the air void content and slump value decreased with the increase of replacement percentage of RCA and fiber contents. Adding PPs provided a more negative effect on the slump of RAC than BFs. The mixtures containing 0.2% PPs and BFs both obtained the highest flexural strength. The addition of PPs was more effective than BFs in improving the damping ratio of RAC, and the mixtures containing 0.3% PPs and BFs both obtained the highest damping ratio. Compared to the RAC without addition of fiber, the charge passed of specimen with addition of PPs approximately increased by 45%, while the specimen with addition of BFs approximately increased by 30%, when the fiber content was 0.3%. This study demonstrates the potential of using fiber to promote the dynamic properties of RAC.

1. Introduction

Over the past several decades, with the rapid development of the infrastructure industry, especially in developing countries, a large amount of construction and demolition waste (C&DW) generated [1–4], which not only causes serious pollution to the environment but also leads to waste of nonrenewable resources [5, 6]. Thus, several researches have begun to investigate and indicate that the application of RCA in RAC is an effective way to reuse C&DW [7, 8]. Previous reports showed that the mechanical properties and durability of RAC are generally worse than natural aggregate concrete (NAC) [9, 10]; this mainly attributes to the microcrack [11] and adhered old mortar that exist in RCA [12, 13]. In addition, several studies found that the performance of RAC is related to the replacement percentage [14], type [11, 15], size [13] of RCA, properties of interface transition zone (ITZ) [16], admixtures [17], etc. These characteristics of RCA and RAC all hinder its application in some areas.

To address this issue and improve the properties of RAC, several methods were applied to improve the properties of RAC these days [1, 17–19], for instance, strengthening or removing the adhered old mortar of RCA [15, 20], applying a two-stage mixing approach, and introducing some mineral admixtures [17, 20]. However, removing the adhered old mortar from RCA may cause microcracks, the enhancing effectiveness of adhered old. Fiber polymer has a super aspect ratio and can form bridge action when adding to concrete, which makes it possible to improve the properties of RAC [21–23].

These days, a large number of reports have confirmed that the addition of fiber is an effective tool to improve the properties of RAC [22, 24–26]. Niu et al. [21] investigated

Table 1: Properties of cement.

Chemical composition (mass%)				Physical properties		Flexural strength (MPa)		Compressive strength (MPa)	
SiO_2	Al_2O_3	FeO	CaO	Specific gravity (kg/m^3)	Specific surface (m^2/kg)	3 d	28 d	3 d	28 d
18.7	5.9	3.4	61.9	3170.0	360.0	7.5	8.7	44.7	50.1

the effect of BFs on the compressive strength of concrete (C30, C40, and C50) and found that the maximum increment in compressive strength was 9.18% (C30), 5.06% (C40), and 7.13% (C50), respectively. Caetano et al. [25] carried out an experiment to study the flexural strength of a high strength steel fiber concrete; results showed that the addition of steel fibers improving the fracture energy of concrete increases its ultimate flexural strength. Grzymski et al. [22] found that the concrete prepared with recycled steel fiber showed about six times lower efficiency in absorbing the energy after concrete matrix cracking, compared with a typical steel fiber-modified concrete. Similar conclusion was also reported by Akça et al. [23]. To date, the studies of the effect of fiber on the properties of RAC mainly involve the mechanical properties and durability, while the effect of fiber on dynamic properties and chloride resistance of RAC is still limited. Steel fiber, as the most commonly used fiber to reinforce RAC, has a high bulk density and increases the self-weight of concrete structure [25]. Furthermore, steel fiber is susceptible to corrosion. These drawbacks all limit its application in some areas with requirements of antivibration and chloride corrosion resistance [25].

Damping is the ability to convert the vibration energy into other forms of energy during the vibration process [26, 27]. Previous investigations indicated the weak bond strength between the BFs and cement mortar in concrete; this characteristic may increase the energy dispersion [28]. Therefore, several studies investigated the dynamic characteristics of BF-reinforced RAC and pointed that the fiber-reinforced RAC leads to a higher damping ratio than that of the NAC, while adding BFs significantly reduced the mechanical performance of RAC [27]. PP has a higher elongation at break, approximately increased by 5-6 times than that of the BFs, which has potential possibilities to increase the dynamic properties of concrete [27]. Nowadays, the increasing application of various types of fibers in concrete makes the dynamic behavior of RAC even more complex. To date, the studies of the effect of PPs on the dynamic properties of RAC are still limited, especially in the comparative study of the dynamic characteristics of RAC modified with PPs and BFs.

In this study, for the first time, we compared the effects of fiber contents/types on the air void content, workability (slump), mechanical performance (compressive and flexural strength), dynamic characteristics (dynamic modulus of elasticity and damping ratio), and chloride resistance of RAC. Two types of RAC formulations were prepared: RAC reinforced with BFs and RAC reinforced with PPs. The experimental results showed the potential of using fiber to promote the damping ratio and flexible strength of RAC. It is greatly significant to further apply fiber in RAC.

Table 2: Properties of FA.

Chemical composition (mass%)				Physical properties (%)		Activity index (%)	
CaO	SiO_2	Al_2O_3	Fe_2O_3	Fineness	Loss	7 d	28 d
49.7	31.1	6.0	3.8	25.3	4.5	97.2	101.3

2. Materials and Experiments

2.1. Materials

2.1.1. Cementitious Materials. Portland cement (P·O 42.5) and fly ash (FA) are used in this study. Tables 1 and 2 present the properties of cement and FA, respectively. Which complied with the requirements of the Chinese National Standards GB175-2007 [29] and GB/T 1596-2005 [30], respectively.

2.1.2. Aggregates. Crushed limestone with a continuous grading is used as coarse aggregate (Figure 1) in this study. The aggregate has the maximum size of 19 mm, and Table 3 presents the properties of coarse aggregate. The fine aggregate used was river sand. It has a water absorption of 1.14% and fineness modulus of 2.60, respectively. The properties of corsage and fine aggregate complied with the Chinese National Standards GB/T 14685-2011 [31] and GB/T14684-2011 [32], respectively.

2.1.3. Fiber Polymer and Additive. The PPs and BFs were used to improve the dynamic properties of RAC. Table 4 presents the properties of fiber. Polycarboxylate-based superplasticizer (SP) was used in this study, and the solid content and water-reducing ratio of the SP is 35% and 28%, respectively.

2.2. Mixture Proportions. To compare the effects of fiber contents/types and replacement percentage of RCA on the air void content, workability, mechanical properties, dynamic characteristics, and chloride resistance of RAC. Nine different mix proportions were considered in this study.

Tables 5 and 6 show the mix proportions of the reference concrete and RAC, respectively. The addition of fiber polymer was at volume content of 0.0-0.3%, respectively. The mixtures were named as follow: take the 50RAC-PP-0.1 for instance, 50RAC refers to the replacement percentage of RAC which is 50.0%, and the PP-0.1 refers to the amount of PPs which is 0.1%. The tap water consists of two parts: the water consumption of ordinary concrete mix design and the additional water. It should be noted that the additional water does not change the effective water-to-binder ratio of the mixture.

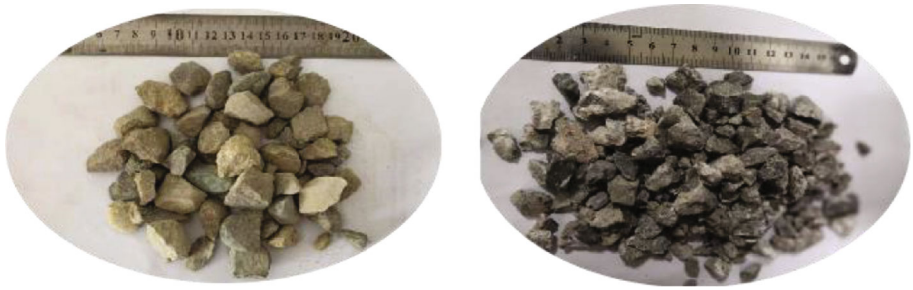

Figure 1: Coarse aggregate used in this study: NCA and RCA.

Table 3: Properties of RCA and NCA.

Type	Crushing value index (%)	Apparent density (kg/m^3)	Bulk density (kg/m^3)	Water absorption (%)
NCA	9.8	2561.0	1380.0	1.1
RCA	15.7	2509.0	1253.0	5.5

Table 4: Properties of PPs and BFs.

Laber	Diameter (μm)	Density (kg/m^3)	Elastic modulus (GPa)	Elongation (%)	Tensile strength (MPa)
PP	32.0	920.0	3.8	20.0	450.5
BF	17.0	2590.0	89.1	2.9	2670.0

Table 5: Mix proportion of reference concrete (kg/m^3).

Cement	Fly ash	River sand	Natural aggregate	Water	Additive
425.0	75.0	700.0	1050.0	165.0	5.0

Table 6: Mix proportions of reference concrete and RAC.

Concrete ID	Volume content of fiber (%)		Coarse aggregate (%)		Water (kg)
	PP	BF	NA	RA	
R	0.0	0.0	0.0	0.0	165 (0)
50RAC	0.0	0.0	50.0	50.0	165 (23.2)
100RAC	0.0	0.0	100.0	100.0	165 (46.4)
50RAC-PP-0.1	0.1	0.0	50.0	50.0	165 (23.2)
50RAC-PP-0.2	0.2	0.0	50.0	50.0	165 (23.2)
50RAC-PP-0.3	0.3	0.0	50.0	50.0	165 (23.2)
50RAC-BF-0.1	0.0	0.1	50.0	50.0	165 (23.2)
50RAC-BF-0.2	0.0	0.2	50.0	50.0	165 (23.2)
50RAC-BF-0.3	0.0	0.3	50.0	50.0	165 (23.2)

2.3. Test Methods

2.3.1. Air Void Content. A concrete air void content measuring instrument (LC 61-7L) was used to test the air void content of fresh concrete according to the Chinese National Standard GB/T 50080-2016 [33].

2.3.2. Workability. The slump value was applied to measure workability of fresh RAC according to the Chinese National Standard GB/T 50080-2016 [33].

2.3.3. Mechanical Performance. For the compressive and flexural strength test, the cubic specimens with a dimension of 150 mm × 150 mm × 150 mm and prismatic specimens with a dimension of 100 mm × 100 mm × 400 mm were used, respectively. After 24 hours from the initial casting, the samples were demolded and then kept for 7 and 28 days at a curing room (20 ± 1°C, ≥95% RH) until the day of the test, in accordance with the Chinese National Standard GB/T 50081-2002 [34].

2.3.4. Dynamic Properties. For the dynamic modulus of the elasticity test, samples with a dimension of 100 mm × 100 mm × 400 mm were used after 28 days of curing according to the Chinese National Standard GB/T 50082-2009 [35], which were obtained by the transverse resonant frequent method and the result obtained by the average three individual test results, which were calculated by

$$E_d = 13.244 \times 10^{-4} \times \frac{WL^3 f^2}{\alpha^4}, \quad (1)$$

where E_d is the dynamic modulus of elasticity of concrete, MPa; W is the weight of sample, kg; L is the length of test sample, mm; f is the transverse frequency of the specimen, Hz; α is the side length of square cross-section sample, mm.

The damping ratio was used to define the damping capacity of concrete. A free-free beam vibration and pulse hardware/software (Brüel & Kjær) were used to test the damping ratio of concrete according to Tian et al. [26]. Figures 2 and 3 show the acceleration history of free vibration of the RAC and the resonance curves, respectively. All specimens for the damping ratio test were after 28 days of curing, and the samples with the dimension of 100 mm × 100 mm

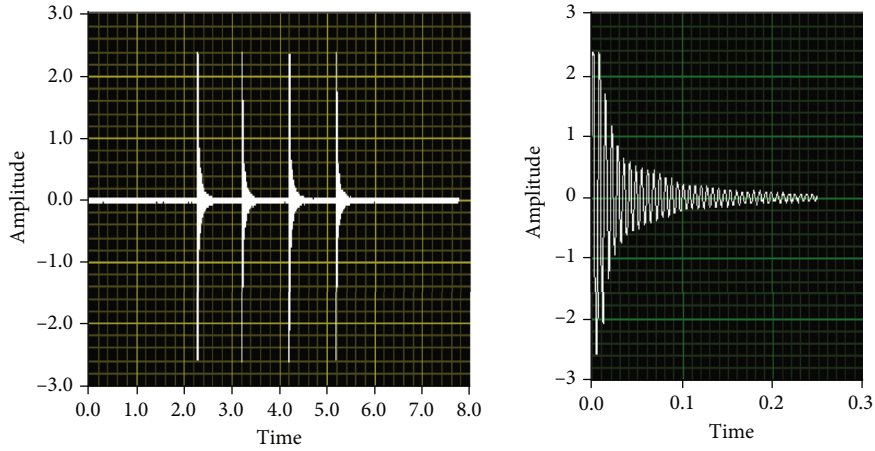

Figure 2: Acceleration response signals as time magnitude.

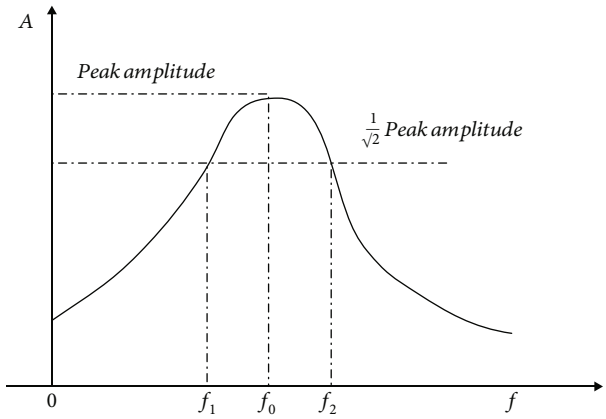

Figure 3: The half-power bandwidth method for the estimation damping ratio of concrete [26].

× 400 mm. The damping ratio of concrete was calculated by the half-power bandwidth method, which was calculated by

$$\xi = \frac{(f_1 - f_2)}{2f_0}, \quad (2)$$

where ζ represents the damping ratio of RAC, %; f_1 and f_2 represent the frequencies corresponding to an amplitude of $f_0/\sqrt{2}$, Hz; f_0 represents the resonant frequency of RAC, Hz.

2.3.5. Chloride Resistance. The rapid chloride migration method (RCM) was applied to evaluate the chloride resistance of concrete after 28 days of curing according to the Chinese National Standard GB/T 50082-2009 [35]. Figure 4 presents the test process of chloride resistance of concrete.

2.3.6. Microstructure Characterizations. The microstructure of concrete was characterized by a S-4800 environmental scanning electron microscope (ESEM). After 28 days of curing, the specimens were broken into small pieces and selected for sample preparation. It should be noted that the surface of specimens was coated by gold before testing.

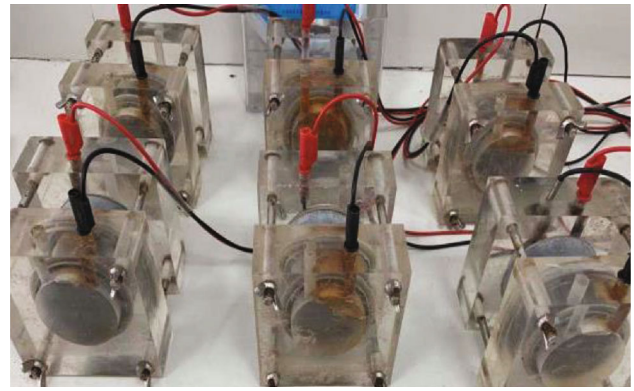

Figure 4: Test process of the chloride resistance of concrete.

3. Results and Discussion

3.1. Air Void Content. Figure 5 shows the air void content value of fresh concrete. It can be observed that the addition of fiber had a significant influence on the air void content of RAC. The air void content of RAC slightly decreased by 15.8% (50RAC-PP-0.1), 21.1% (50RAC-PP-0.2), 5.3% (50RAC-BF-0.1), 15.8% (50RAC-BF-0.2), and 21.1% (50RAC-BF-0.3) in each case, compared with 50RAC. Only the mixture 50RAC-PP-0.3 containing 0.3% PPs significantly reduced by 31.6%.

The addition of RCA had no significant influence on air void content when replacement percentage of RCA is less than 50%, while a sharp reduction of air void content could be found at 100% RCA mixture (100RAC). Compared to the reference concrete, the air void content value of fresh RAC decreased by 17.4% (50RAC) and 26.1% (100RAC), respectively. It can be obtained that the addition of RAC in reducing the air void content of RAC was more obvious than that of the addition of fiber.

3.2. Workability. From Figure 6, it can be observed that the slump value decreased by 16.7% (50RAC) and 41.7% (100RAC), respectively, compared with the reference concrete. Further, the mixtures with the addition of PPs

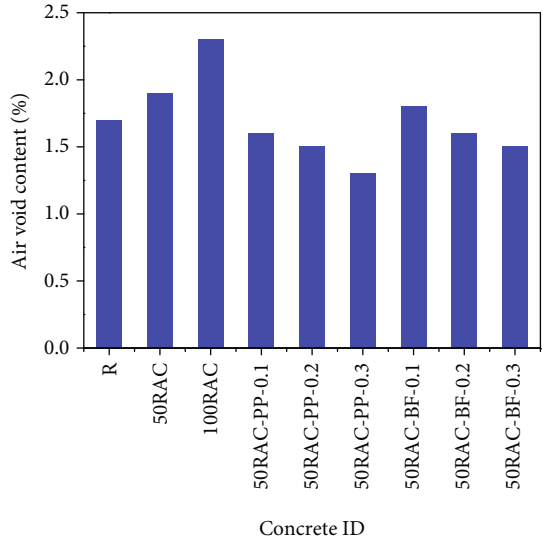

Figure 5: Air void content value of fresh concrete.

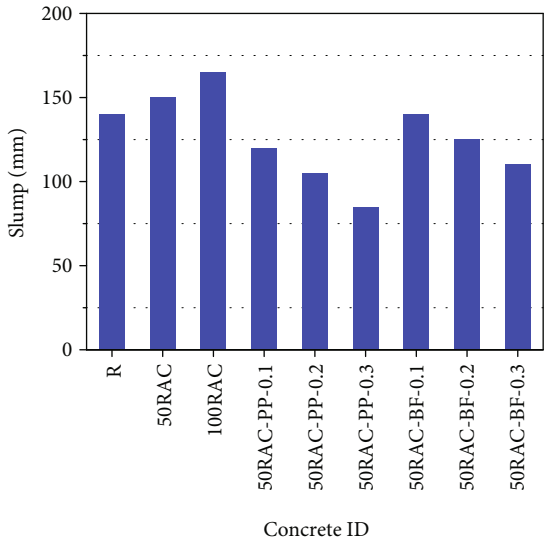

Figure 6: Slump of fresh concrete.

(50RAC-PP-0.1, 50RAC-PP-0.2, and 50RAC-PP-0.3) obtained the relative lower slump value. In addition, the slump value of RAC decreased with the increase of PP or BF content. There is no significant influence when the PP or BF content less than 0.2%, while a significant reduction of slump could be observed on the mixture with 0.3% fiber. The slump value of mixtures 50RAC-PP-0.3 and 50RAC-BF-0.3 decreased by 43.3% and 26.7%, respectively, compared to 50RAC. This is mainly attributed to the fiber that has a high surface area with a high water absorption rate [36, 37], increasing the viscosity of fresh concrete. Therefore, the recommended dosage of fiber is below 0.2% to obtain a relatively good workability of mixture. Further, results indicated that the addition PPs provided a more negative effect on the slump of RAC than that of the BFs.

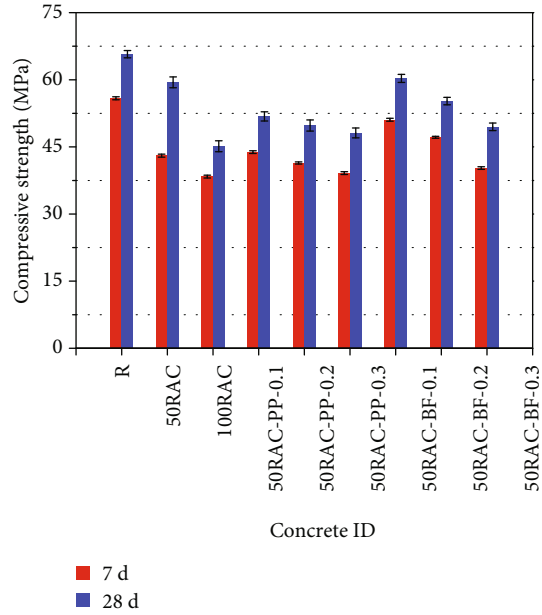

Figure 7: Compressive strength of concrete.

3.3. Mechanical Properties. From Figure 7, it can be obtained that the compressive strength of specimens decreased by 9.6% (50RAC) and 31.2% (100RAC), respectively, after 28 days of curing, compared with the reference concrete. This could be attributed to the adhered old mortar on RCA which has a large number of pores and microcracks [13], resulting in a poor properties of RCA than that of the NCA (as seen in Table 3). It needed to be highlighted that the increment of the replacement percentage of RCA could consequently increase the number of pores and cracks; thus, the compressive strength of RAC decreased with the increase of replacement percentage of RCA [16]. Similar conclusion has been reported by Wijayasundara et al. [3].

The compressive strength of RAC significantly decreased by 12.9% (50RAC-PP-0.1), 16.2% (50RAC-PP-0.2), 5.3% (50RAC-PP-0.3), 19.4% (50RAC-BF-0.2), and 15.9% (50RAC-BF-0.3) in each case compared to that of 50RAC. Only the compressive strength of mixture 50RAC-BF-0.1 slightly increased by 1.5% after 28 days of curing. The results were consistent with the previous reports [36]. The reduction of compressive could be summarized as follows: (1) the addition of fiber brings many defects, such as bubbles, voids, and loose matrix [13]. These defects form a weak ITZ between fiber and mortar and have high porosity and a large number of microcracks [13, 36]; (2) the addition of fiber may be agglomerated when it appears to uneven dispersion, and then, it could form a defect and reduce the compressive strength of RAC [13]; (3) the addition of fiber can form a dimensional network structure; it can dissipate stress and overcome the relative slip between the particles [13]; and (4) the addition of fibers play a role in bridge action, which can prevent the propagation of microcracks [36]. Based on the above, the compressive strength of RAC reinforced with fiber showed a slight reduction or increment, compared to the reference concrete. The weak ITZ between fiber and

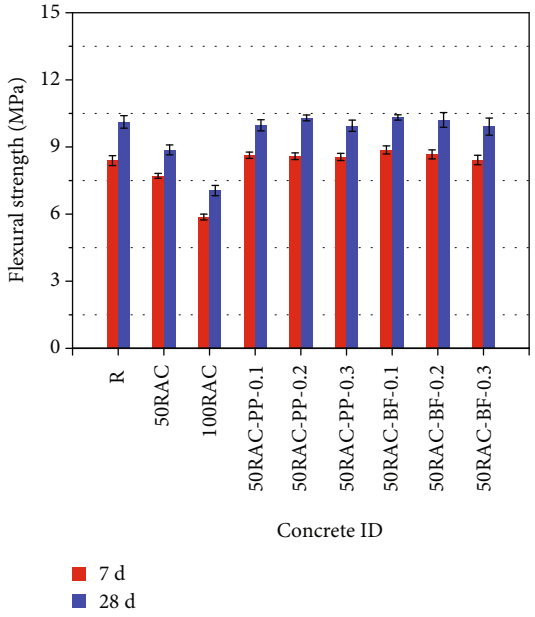

Figure 8: Flexural strength of concrete.

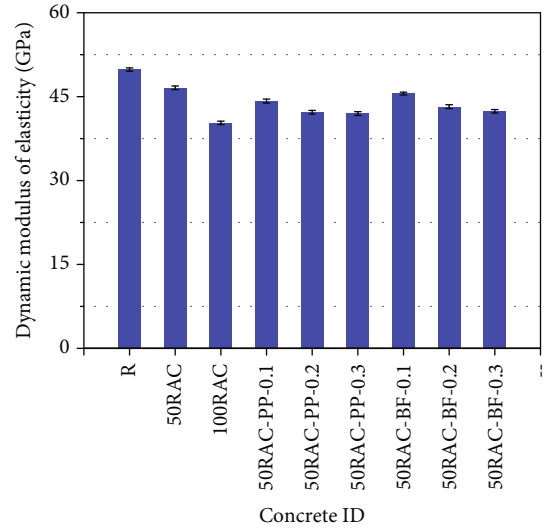

Figure 9: Dynamic modulus of elasticity of concrete.

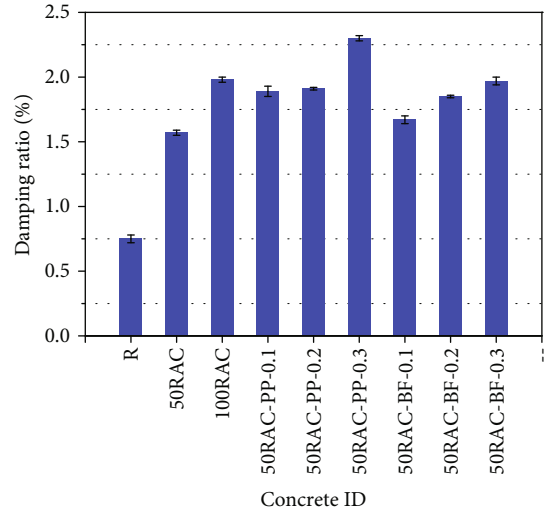

Figure 10: Damping ratio of concrete.

mortar, bubbles, voids, and loose matrix due to the addition of fiber had the potential to increase the damping ratio of RAC with the addition of fiber; this will be discussed in Section 3.4.

The effect of addition of fibers or RCA on the flexural strength of RAC was obvious. Compared to the reference concrete after 28 days of curing, the flexural strength of mixtures 50RAC and 100RAC decreased by 12.4% and 30.1%, respectively, as seen in Figure 8. It also can be observed that the flexural strength of RAC increased by 11.9% (50RAC-PP-0.1), 16.1% (50RAC-PP-0.2), and 12.2% (50RAC-PP-0.3) in each case compared to that of the 50RAC. And the mixtures containing 0.1%, 0.2%, and 0.3% BFs, the flexural strength of concretes increased by 15.1%, 16.4%, and 11.7%, respectively. That is to say, the mixtures containing 0.2% PPs and BFs both obtained the highest flexural strength. This result was consistent with the previous reports [36]. This could be attributed to the bridge action of fiber [36]. Therefore, the recommended dosage of fiber is 0.2% to obtain the highest flexural strength.

3.4. Dynamic Characteristics

3.4.1. Dynamic Modulus of Elasticity. Figure 9 shows the dynamic modulus of elasticity of concrete; it can be observed that the dynamic modulus of elasticity of the specimens 50RAC and 100RAC decreased by 6.6% and 19.1%, respectively, compared to that of the reference concrete after 28 days of curing.

The dynamic modulus of elasticity of RAC reinforced with PPs decreased by 5.1% (50RAC-PP-0.1), 9.3% (50RAC-PP-0.2), and 9.9% (50RAC-PP-0.3) in each case compared to that of the 50RAC, as seen in Figure 9, while the dynamic modulus of elasticity of BF-reinforced RAC decreased by 2.2% (50RAC-BF-0.1), 7.3% (50RAC-BF-0.2), and 9.1% (50RAC-BF-0.3), respectively. The effect of fiber on the dynamic modulus of elasticity of RAC was similar to that of the compressive strength. It can be concluded that the addition of BFs was more effective than that of PPs for increasing the dynamic modulus of elasticity of concrete.

3.4.2. Damping Ratio. From Figure 10, it can be observed that the damping ratio of mixtures (50RAC and 100RAC) after 28 days of curing increased to 1.6% and 2.0%, respectively. That is, the damping ratio of RAC increased by 109.3% (50RAC) and 164.0% (100RAC), respectively, compared to that of the reference concrete. Results showed that the damping ratio of RAC (50RAC and 100RAC) approximately increased by 1.5-2.0 times than that of the reference concrete.

The improvement in the damping ratio of the fiber-reinforced RAC can be summarized as follows: (1) the adhered old mortar of RCA and the ITZs (old and new ITZ) exists substantial number of voids [13, 38], as shown

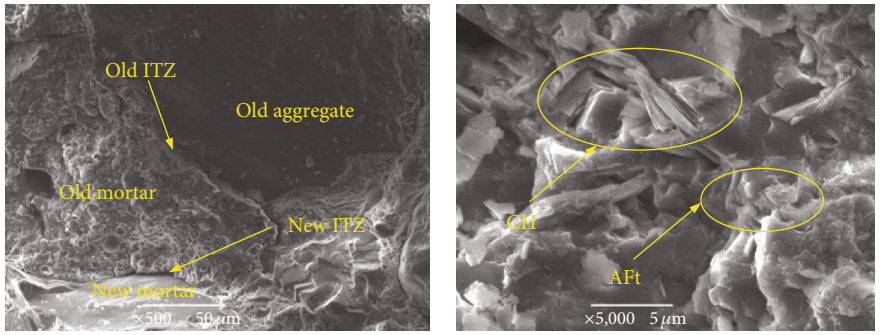

(a) (b)

Figure 11: Microstructure of RAC: (a) classification ITZs of RAC and (b) hydration products.

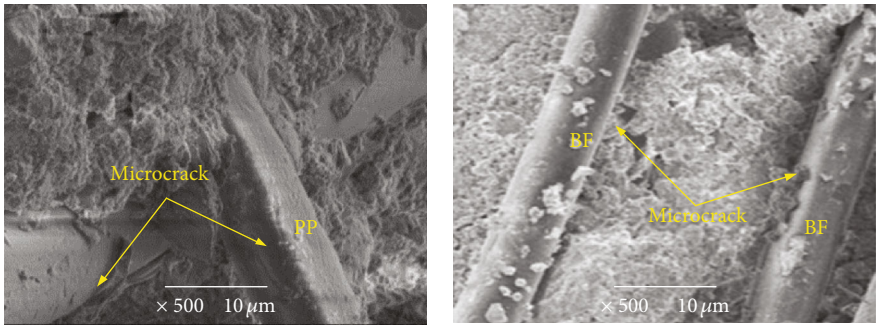

(a) (b)

Figure 12: ITZ between the fiber-mortar (a) PP-mortar and (b) BF-mortar.

in Figure 11, the expansion and contraction of the air in voids conducive to the energy dissipation in RAC [13]; (2) the disperse energy by the friction of microcracks exists in ITZs; additionally, the porous ITZs have a large number of hydration products (CH crystals and AFt), leading to a high porosity and looser microstructure, which provided a positive influence on the energy dissipation of concrete [16, 39]; (3) the existence of old mortar (Figure 11) is conducive to energy dissipation due to the sliding friction between the old and new mortar [13]; and (4) the sliding friction between the fiber and the mortar. Therefore, the damping ratio of RAC increased with the increase of the replacement ratio of RCA. Correspondingly, the characteristics of weaken ITZ have a negative effect on the mechanical properties of RAC, as illustrated in Section 3.3.

The damping ratio of concretes increased by 152.04% (50RAC-PP-0.1), 154.7% (50RAC-PP-0.2), and 206.7% (50RAC-PP-0.3), respectively, while increased by 122.7% (50RAC-BF-0.1), 146.7% (50RAC-BF-0.2), and 162.7% (50RAC-BF-0.3), respectively, compared to that of the 50RAC, as seen in Figure 10. Results indicated that the addition of fibers had a positive effect on the damping ratio of RAC, especially the addition of PPs; this could be attributed to the weak ITZ between fiber and mortar (Figure 12). Therefore, the recommended dosage of fiber was 0.3% to obtain the highest damping ratio. Further, results indicated that the addition of PPs was more effective than that of BFs in improving the damping ratio of RAC.

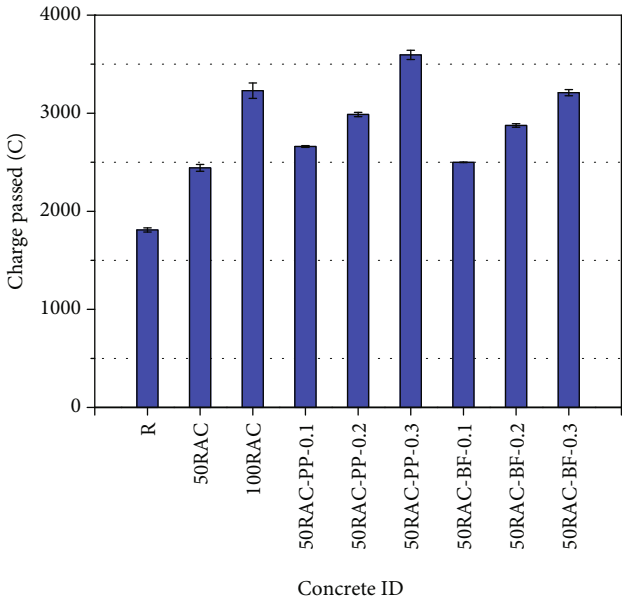

Figure 13: Charge passed of concrete after 28 days of curing.

3.5. Chloride Resistance. From Figure 13, it can be seen that the charge passed increased with the increase of replacement rate of RCA; the charge passed of concrete was 2443.0 C and 3230.3 C, respectively. The maximum charge passed of

mixture belonged to the specimen containing 100% RCA (100RAC).

Compared to the 50RAC after 28 days of curing, the charge passed of RAC with the addition of PPs with 0.1-0.3% contents approximately increased by 8.9-47.2%, while the addition of BFs with 0.1-0.3% contents increased by 2.3-31.4%. The observation was well agreed by the previous studies [23, 25, 36]. The increment in charge passed of RAC reinforced with PPs and BFs could be attributed to the defects in concrete (ITZ between the fiber-mortar and voids) [40]. Further, the charge passed of specimens with the addition of PPs was greater than that of the specimens with the addition of BFs.

4. Conclusions

In this paper, we prepared two types of RAC formulations: RAC reinforced with BFs and RAC reinforced with PPs, and compared the effects of fiber types and contents on the air void content, workability (slump), mechanical properties (compressive and flexural strength), dynamic characteristics (dynamic modulus of elasticity and damping ratio), and chloride resistance of RAC. With the test results presented in this study, the following conclusions can be drawn:

(1) The addition of fiber leads to a reduction of air void content and slump of RAC. The air void content decreased by 15.8% (50RAC-PP-0.1), 21.1% (50RAC-PP-0.2), 5.3% (50RAC-BF-0.1), 15.8% (50RAC-BF-0.2), and 21.1% (50RAC-BF-0.3) in each case, compared with 50RAC. The addition of PPs provided a more negative effect on the slump than that of the BFs; the slump of mixtures 50RAC-PP-0.3 and 50RAC-BF-0.3 decreased by 43.3% and 26.7%, respectively

(2) The contents and types of fiber here had marginal effects on the compressive strength of concrete, while the flexural strength of RAC had been significantly influenced. The flexural strength of RAC increased by 11.9% (50RAC-PP-0.1), 16.1% (50RAC-PP-0.2), and 12.2% (50RAC-PP-0.3) in each case compared to that of the 50RAC. And the mixtures containing 0.1%, 0.2%, and 0.3% BFs, the flexural strength of concretes increased by 15.1%, 16.4%, and 11.7%, respectively. The recommended dosage of fiber is 0.2% to obtain the highest flexural strength

(3) The damping ratio of concretes (50RAC and 100RAC) approximately increased by 1.5-2.0 times than that of the reference concrete. The addition of PPs was more effective than that of BFs in improving the damping ratio of RAC, and the specimens containing 0.3% fiber obtained the highest damping ratio value; the damping ratio of concretes increased by 206.7% (50RAC-PP-0.3) and 162.7% (50RAC-BF-0.3), respectively, compared to that of the 50RAC

(4) The charge passed of specimens with the addition of PPs was greater than that of the specimens with the addition of BFs. Compared to the 50RAC after 28 days of curing, the charge passed of specimen addition of PPs approximately increased by 45%, while the specimen addition of BFs approximately increased by 30%, when the fiber content was 0.3%

Data Availability

The data used to support the findings of this study are included within the article.

Conflicts of Interest

The authors declare that they have no conflicts of interest.

Acknowledgments

This research was supported by the 2018 Nantong Basic Science Research Project (JC2018096) and the Natural Science Fund for Colleges and Universities in Jiangsu Province (17KJB580009).

Supplementary Materials

Table 1 Air void content and slump value of concrete. Table 2 Mechanical properties of concrete. Table 3 Dynamic properties of concrete. Table 4 Charge passed of concrete. *(Supplementary Materials)*

References

[1] V. W. Y. Tam, A. Butera, and K. N. Le, "Carbon-conditioned recycled aggregate in concrete production," *Journal of Cleaner Production*, vol. 133, pp. 672–680, 2016.

[2] J. J. Xu, Z. P. Chen, T. Ozbakkaloglu, X. Y. Zhao, and C. Demartino, "A critical assessment of the compressive behavior of reinforced recycled aggregate concrete columns," *Engineering Structures*, vol. 161, pp. 161–175, 2018.

[3] M. Wijayasundara, R. H. Crawford, and P. Mendis, "Comparative assessment of embodied energy of recycled aggregate concrete," *Journal of Cleaner Production*, vol. 152, pp. 406–419, 2017.

[4] Y. L. Chen, Z. P. Chen, J. J. Xu, E. M. Lui, and B. Wu, "Performance evaluation of recycled aggregate concrete under multiaxial compression," *Construction and Building Materials*, vol. 229, article 116935, 2019.

[5] B. Qi, J. Gao, F. Chen, and D. Shen, "Evaluation of the damage process of recycled aggregate concrete under sulfate attack and wetting-drying cycles," *Construction and Building Materials*, vol. 138, pp. 254–262, 2017.

[6] N. K. Bui, T. Satomi, and H. Takahashi, "Improvement of mechanical properties of recycled aggregate concrete basing on a new combination method between recycled aggregate and natural aggregate," *Construction and Building Materials*, vol. 148, pp. 376–385, 2017.

[7] R. L. Al-Mufti and A. N. Fried, "Improving the strength properties of recycled asphalt aggregate concrete," *Construction and Building Materials*, vol. 149, pp. 45–52, 2017.

[8] A. Koper, W. Koper, and M. Koper, "Influence of raw concrete material quality on selected properties of recycled concrete aggregates," *Process Engineering*, vol. 172, pp. 536–543, 2017.

[9] J. Wang, B. Vandevyvere, S. Vanhessche, J. Schoon, N. Boon, and N. De Belie, "Microbial carbonate precipitation for the improvement of quality of recycled aggregates," *Journal of Cleaner Production*, vol. 156, pp. 355–366, 2017.

[10] M. Wijayasundara, P. Mendis, and R. H. Crawford, "Methodology for the integrated assessment on the use of recycled concrete aggregate replacing natural aggregate in structural concrete," *Journal of Cleaner Production*, vol. 166, pp. 321–334, 2017.

[11] E. Vázquez, M. Barra, D. Aponte, C. Jiménez, and S. Valls, "Improvement of the durability of concrete with recycled aggregates in chloride exposed environment," *Construction and Building Materials*, vol. 67, pp. 61–67, 2014.

[12] D. Xuan, B. Zhan, and C. S. Poon, "Durability of recycled aggregate concrete prepared with carbonated recycled concrete aggregates," *Cement and Concrete Composites*, vol. 84, pp. 214–221, 2017.

[13] C. Liang, T. Liu, J. Xiao, D. Zou, and Q. Yang, "The damping property of recycled aggregate concrete," *Construction and Building Materials*, vol. 102, pp. 834–842, 2016.

[14] C. Zhou and Z. Chen, "Mechanical properties of recycled concrete made with different types of coarse aggregate," *Construction and Building Materials*, vol. 134, pp. 497–506, 2017.

[15] L. Li, C. S. Poon, J. Xiao, and D. Xuan, "Effect of carbonated recycled coarse aggregate on the dynamic compressive behavior of recycled aggregate concrete," *Construction and Building Materials*, vol. 151, pp. 52–62, 2017.

[16] K. Liao, P. Chang, Y. Peng, and C. Yang, "A study on characteristics of interfacial transition zone in concrete," *Cement and Concrete Research*, vol. 34, no. 6, pp. 977–989, 2004.

[17] Z. Tahar, T. Ngo, E. H. Kadri, A. Bouvet, F. Debieb, and S. Aggoun, "Effect of cement and admixture on the utilization of recycled aggregates in concrete," *Construction and Building Materials*, vol. 149, pp. 91–102, 2017.

[18] D. Lu, Z. Tang, L. Zhang et al., "Effects of combined usage of supplementary cementitious materials on the thermal properties and microstructure of high-performance concrete at high temperatures," *Materials*, vol. 13, no. 8, p. 1833, 2020.

[19] T. Y. Xie, G. S. Yang, X. Y. Zhao, J. J. Xu, and C. F. Fang, "A unified model for predicting the compressive strength of recycled aggregate concrete containing supplementary cementitious materials," *Journal of Cleaner Production*, vol. 251, article 119752, 2020.

[20] K. Pandurangan, A. Dayanithy, and S. Om Prakash, "Influence of treatment methods on the bond strength of recycled aggregate concrete," *Construction and Building Materials*, vol. 120, pp. 212–221, 2016.

[21] D. Niu, D. Huang, and Q. Fu, "Experimental investigation on compressive strength and chloride permeability of fiber-reinforced concrete with basalt-polypropylene fibers," *Advances in Structural Engineering*, vol. 22, no. 10, pp. 2278–2288, 2019.

[22] F. Grzymski, M. Musiał, and T. Trapko, "Mechanical properties of fibre reinforced concrete with recycled fibres," *Construction and Building Materials*, vol. 198, pp. 323–331, 2019.

[23] K. R. Akça, Ö. Çakır, and M. İpek, "Properties of polypropylene fiber reinforced concrete using recycled aggregates," *Construction and Building Materials*, vol. 98, pp. 620–630, 2015.

[24] V. T. Giner, S. Ivorra, F. J. Baeza, E. Zornoza, and B. Ferrer, "Silica fume admixture effect on the dynamic properties of concrete," *Construction and Building Materials*, vol. 25, no. 8, pp. 3272–3277, 2011.

[25] H. Caetano, J. P. C. Rodrigues, and P. Pimienta, "Flexural strength at high temperatures of a high strength steel and polypropylene fibre concrete," *Construction and Building Materials*, vol. 227, p. 116721, 2019.

[26] Y. Tian, S. Shi, K. Jia, and S. Hu, "Mechanical and dynamic properties of high strength concrete modified with lightweight aggregates presaturated polymer emulsion," *Construction and Building Materials*, vol. 93, pp. 1151–1156, 2015.

[27] T. Li, J. Xiao, T. Sui, C. Liang, and L. Li, "Effect of recycled coarse aggregate to damping variation of concrete," *Construction and Building Materials*, vol. 178, pp. 445–452, 2018.

[28] F. Abed and A. R. Alhafiz, "Effect of basalt fibers on the flexural behavior of concrete beams reinforced with BFRP bars," *Composite Structures*, vol. 215, pp. 23–34, 2019.

[29] Ministry of Housing and Urban-Rural Development of the People's Republic of China, *Common Portland cement (GB175-2007)*, China Architecture and Building Press, Beijing, 2007.

[30] Ministry of Housing and Urban-Rural Development of the People's Republic of China, *Fly ash used for cement and concrete (GB/T1596-2005)*, China Architecture and Building Press, Beijing, 2005.

[31] Ministry of Housing and Urban-Rural Development of the People's Republic of China, *Pebble and crushed stone for construction (GB/T14685-2011)*, China Architecture and Building Press, Beijing, 2011.

[32] Ministry of Housing and Urban-Rural Development of the People's Republic of China, *Sand for construction (GB/T 14684-2011)*, China Architecture and Building Press, Beijing, 2011.

[33] Ministry of Housing and Urban-Rural Development of the People's Republic of China, *Standard for test method of performance on ordinary fresh concrete (GB/T 50080-2016)*, China Architecture and Building Press, Beijing, 2016.

[34] Ministry of Housing and Urban-Rural Development of the People's Republic of China, *Standard for test method of mechanical properties on ordinary concrete (GB/T 50081-2002)*, China Architecture and Building Press, Beijing, 2002.

[35] Ministry of Housing and Urban-Rural Development of the People's Republic of China, *Standard for test method of long-term performance and durability of ordinary concrete (GB/T 50082-2009)*, China Architecture and Building Press, Beijing, 2009.

[36] X. Hu, Y. Guo, J. Lv, and J. Mao, "The mechanical properties and chloride resistance of concrete reinforced with hybrid polypropylene and basalt fibres," *Materials*, vol. 12, no. 15, article 2371, 2019.

[37] O. H. Wallevik and J. E. Wallevik, "Rheology as a tool in concrete science: the use of rheographs and workability boxes," *Cement and Concrete Research*, vol. 41, no. 12, pp. 1279–1288, 2011.

[38] K. S. Lee, J. Choi, S. Kim, B. Lee, J. Hwang, and B. Y. Lee, "Damping and mechanical properties of composite composed of polyurethane matrix and preplaced aggregates," *Construction and Building Materials*, vol. 145, pp. 68–75, 2017.

[39] A. Parghi and M. S. Alam, "A review on the application of sprayed-FRP composites for strengthening of concrete and masonry structures in the construction sector," *Composite Structures*, vol. 187, pp. 518–534, 2018.

[40] J. J. Xu, Z. P. Chen, Y. Xiao, C. Demartino, and J. H. Wang, "Recycled aggregate concrete in FRP-confined columns: a review of experimental results," *Composite Structures*, vol. 174, pp. 277–291, 2017.

Hindawi
Advances in Polymer Technology
Volume 2020, Article ID 1349034, 15 pages
https://doi.org/10.1155/2020/1349034

Research Article

Effect of Cross-Sectional Aspect Ratio on Rectangular FRP-Concrete-Steel Double-Skin Tubular Columns under Axial Compression

Bing Zhang,[1,2] **Xia-Min Hu**,[2] **Wei Wei**,[2,3] **Qian-Biao Zhang**,[2] **Ning-Yuan Zhang**,[2] **and Yi-Jie Zhang**[2]

[1]*School of Civil and Environmental Engineering, Harbin Institute of Technology (Shenzhen), Shenzhen, China*
[2]*College of Civil Engineering, Nanjing Tech University, Nanjing, China*
[3]*Powerchina Real Estate Group Ltd., Beijing, China*

Correspondence should be addressed to Bing Zhang; zhangb@njtech.edu.cn

Received 23 October 2019; Accepted 12 March 2020; Published 27 May 2020

Guest Editor: Tianyu Xie

Hybrid FRP-concrete-steel double-skin tubular columns (hybrid DSTCs) are novel hollow columns consisting of an outer FRP tube, an inner steel tube, and the concrete between the two tubes. Hybrid DSTCs possess important advantages, such as excellent corrosion resistance as well as remarkable seismic resistance. However, existing studies are mainly focused on hybrid DSTCs with a circular cross section or a square cross section. When a column is subjected to different load levels in the two horizontal directions, a rectangular column is preferred as it can provide different bending stiffness and moment capacity around its two axes of symmetry. This paper presents an experimental study on rectangular DSTCs with a particular focus on the effect of the cross-sectional aspect ratio (i.e., the ratio of the breadth to the width of the rectangular cross section). The effect of the cross-sectional shape of the inner steel tube (i.e., both elliptical and rectangular inner steel tubes were used) and the effect of FRP tube thickness were also investigated experimentally. Experimental results show that a larger aspect ratio will have no negative effect on the confinement effect in rectangular DSTCs; a rectangular DSTC with a larger aspect ratio generally has a larger ultimate axial strain and a higher axial stress at the ultimate axial strain; rectangular DSTCs with an elliptical steel tube generally have better performance than corresponding specimens with a rectangular steel tube. An existing model, which was developed based on a model for rectangular FRP-confined concrete columns and a model for circular DSTCs, is verified using the test results of the present study. The model generally provides close predictions for the peak axial stress of the confined concrete but yields conservative predictions for the ultimate axial strain for rectangular DSTCs.

1. Introduction

In the field of civil engineering, FRP composites have found increasing applications for the retrofitting of existing structures as well as the construction of new structures [1–3]. FRP composites are particularly attractive for use in combination with traditional construction materials (i.e., concrete, steel, and timber) to create novel hybrid structures [4]. Hybrid FRP-concrete-steel double-skin tubular columns (hybrid DSTCs) are novel hollow columns that combine concrete, steel, and FRP together in an optimal manner [5]. Hybrid DSTCs have an outer FRP tube, an inner steel tube, and a layer of concrete between the two tubes (Figure 1). The inner steel tube is the primary longitudinal reinforcement, whereas the outer FRP tube provides confinement to the concrete. The two tubes could be used as the in situ formwork for the concrete casting, thus saving the construction cost and advancing the construction schedule. Hybrid DSTCs are quite suitable for structural members in harsh environments due to their excellent corrosion resistance, which is enabled by the use of the outer FRP tube. Hybrid DSTCs are also particularly attractive for use in seismic regions due to their excellent energy dissipation ability under earthquake loading [6, 7].

Teng et al. [5] presented the first-ever experimental study on hybrid DSTCs under axial compression to explain the

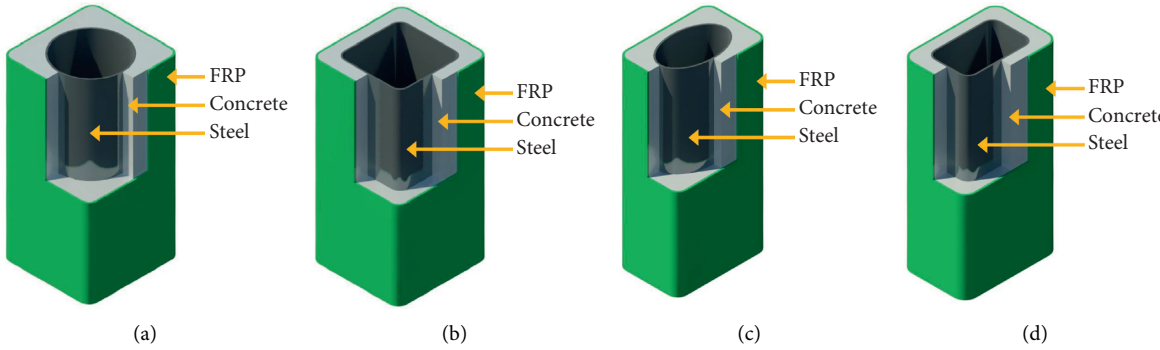

Figure 1: Cross section of square and rectangular DSTCs. (a) Square DSTCs with a circular steel tube, (b) square DSTCs with a square steel tube, (c) rectangular DSTCs with an elliptical steel tube, and (d) rectangular DSTCs with a rectangular steel tube.

rationale of hybrid DSTCs and to demonstrate their advantages. Han et al. [8] commented that this new member form "combines the advantages of all three constituent materials and those of the structural form of double-skin tubular columns." Hollaway [9] introduced this new form of hybrid members in detail in his review paper and commented that it "is relatively easy to construct and is highly resistant to corrosion and earthquakes." In recent years, hybrid DSTCs have already received extensive research attention. Existing studies are mainly focused on hybrid DSTCs under loading conditions as follows: (1) monotonic axial compression [5, 10–12], which confirms that the concrete is confined effectively by the steel tube and the FRP tube, leading to a ductile behavior; (2) cyclic axial compression [13, 14], which shows that the loading history has an accumulative effect on the stress-strain response of repeated unloading/reloading cycles; (3) eccentric compression [15, 16], which indicates that the axial load capacity decreases with the increase of load eccentricity; (4) combined axial compression and cyclic lateral loading [6, 7], which demonstrates that hybrid DSTCs possess excellent ductility under cyclic lateral loading; and (5) impact loading [17, 18], which displays the excellent energy dissipation ability of hybrid DSTCs. Existing studies, however, are mostly focused on hybrid DSTCs with a circular cross section (i.e., the cross section of the outer FRP tube is circular); [5, 8–18] and hybrid DSTCs with a square cross section (i.e., the cross section of the outer FRP tube is square) [6, 19–22]. Although circular columns and square columns are attractive as bridge piers, rectangular columns are preferred if such columns are subjected to different load levels in the two horizontal directions (Figure 1). Rectangular DSTCs could be designed to provide different bending stiffness and moment capacity around the two axes of symmetry according to the engineering requirements [23]. Rectangular FRP-confined concrete columns have received extensive research attention in the last decade [24–30], but experimental research on rectangular DSTCs is rather rare. To the best knowledge of the authors, there is only one experimental study on rectangular DSTCs subjected to axial compression. In Cavill and Yu's [31] study, the effect of the aspect ratio of the rectangular cross section was not investigated. All rectangular DSTCs had a breadth of 185 mm, a width of 105 mm, and a height of 370 mm, and two circular steel tubes were used for each specimen. Cavill and Yu [31] confirmed the concrete in rectangular DSTCs was effectively confined by the FRP tube and the steel tube, leading to a very ductile response.

The present study extends the existing work to rectangular DSTCs subjected to axial compression with a particular focus on the effect of the aspect ratio, which is the ratio of the breadth (the longer side) to the width (the shorter side) of the rectangular cross section. The effect of the cross-sectional shape of the inner steel tube (i.e., both rectangular and elliptical inner steel tubes were used) and the effect of the FRP tube thickness are also investigated experimentally. Rectangular FRP-confined solid concrete columns are fabricated and tested for comparison with rectangular DSTCs.

2. Experimental Program

2.1. Specimen Details. In the present study, rectangular specimens with four types of cross-sectional aspect ratios were fabricated and tested. These specimens all had a height of 600 mm and a corner radius of 30 mm on the outer rectangular cross section. Specimen details are summarized in Table 1, and the cross-sectional configurations are shown in Figure 2. For all specimens, the breadth l of the outer rectangular cross section was 300 mm, while the width w was 300 mm, 250 mm, 200 mm, or 150 mm, leading to four different cross-sectional aspect ratios l/w (i.e., 1.0, 1.2, 1.5, or 2.0). These specimens with an aspect ratio l/w of 1.0 are square DTSCs. As shown in Table 1 and Figure 2, these specimens could be divided into three groups based on their cross-sectional configurations: (1) group 1, rectangular DSTCs with an elliptical inner steel tube (referred to as RE-DSTCs); (2) group 2, rectangular DSTCs with a rectangular inner steel tube (referred to as RR-DSTCs); and (3) group 3, rectangular FRP-confined solid concrete columns (referred to as R-CFFTs). For RE-DSTCs in group-1, four types of elliptical steel tubes were used, which had the same major axis $2a_s$ (i.e., 204 mm), but four different minor axes $2b_s$ (i.e., 204 mm, 170 mm, 136 mm, and 102 mm) (Table 2 and Figures 2 and 3). For RR-DSTCs in group 2, four types of rectangular steel tubes were used, which had the same corner radius of 20 mm and the same breadth l_s for the steel

Table 1: Specimen details.

Specimen type	Specimen name	Sectional dimensions			Steel tube type	FRP layers/thickness (mm)
		l (mm)	w (mm)	l/w		
RE-DSTCs	RC1-ec1-F6	300	300	1.0	ec1	6 layers/2.10
	RC2-ec2-F3	300	250	1.2	ec2	3 layers/1.05
	RC2-ec2-F6	300	250	1.2	ec2	6 layers/2.10
	RC3-ec3-F3	300	200	1.5	ec3	3 layers/1.05
	RC3-ec3-F6	300	200	1.5	ec3	6 layers/2.10
	RC4-ec4-F6	300	150	2.0	ec4	6 layers/2.10
RR-DSTCs	RC1-rc1-F6	300	300	1.0	rc1	6 layers/2.10
	RC2-rc2-F3	300	250	1.2	rc2	3 layers/1.05
	RC2-rc2-F6	300	250	1.2	rc2	6 layers/2.10
	RC3-rc3-F3	300	200	1.5	rc3	3 layers/1.05
	RC3-rc3-F6	300	200	1.5	rc3	6 layers/2.10
	RC4-rc4-F6	300	150	2.0	rc4	6 layers/2.10
R-CFFTs	RC1-F6	300	300	1.0	—	6 layers/2.10
	RC2-F3	300	250	1.2	—	3 layer/1.05
	RC2-F6	300	250	1.2	—	6 layers/2.10
	RC3-F3	300	200	1.5	—	3 layers/1.05
	RC3-F6	300	200	1.5	—	6 layers/2.10
	RC4-F6	300	150	2.0	—	6 layers/2.10

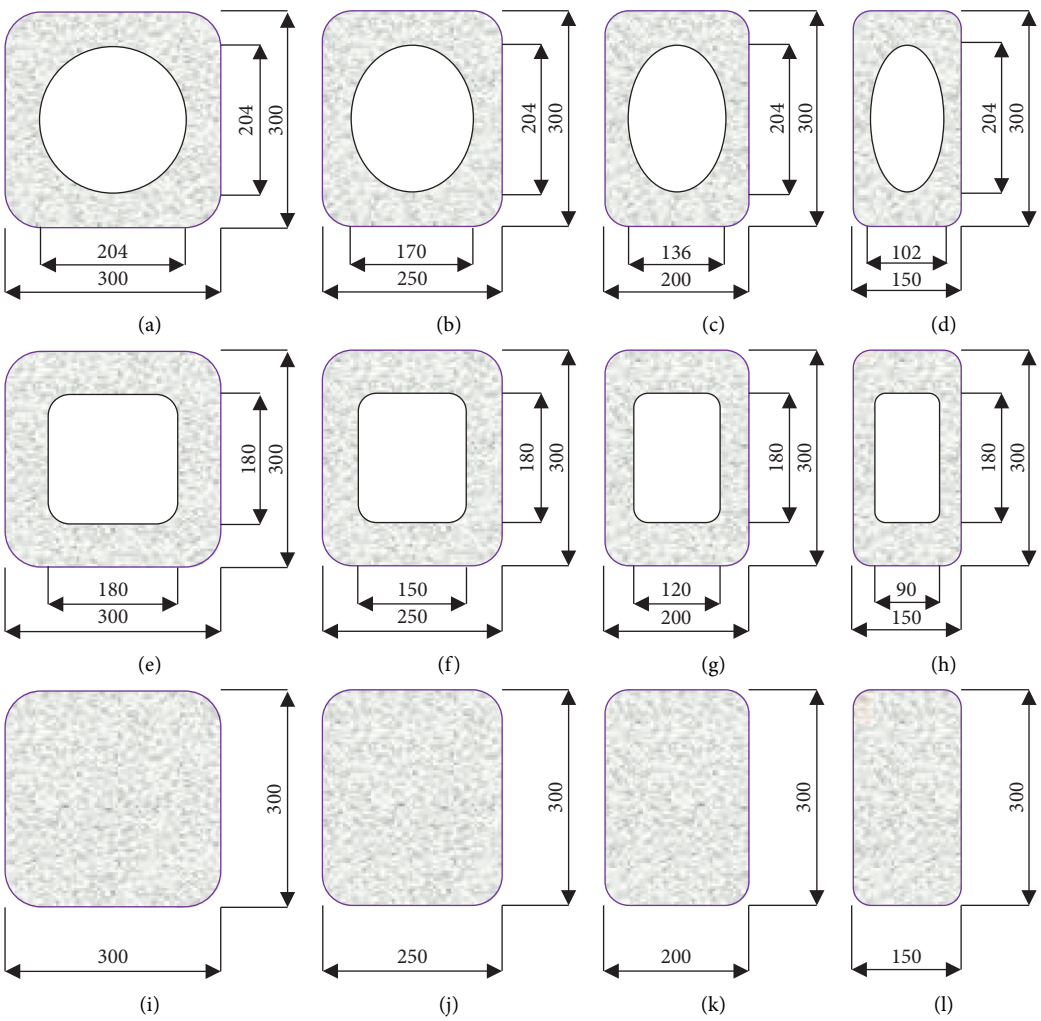

Figure 2: Cross-sectional configurations. (a) RC1-ec1-F6, (b) RC2-ec2-F6 RC2-ec2-F3, (c) RC3-ec3-F6 RC3-ec3-F3, (d) RC4-ec4-F6, (e) RC1-rc1-F6, (f) RC2-rc2-F6 RC2-rc2-F3, (g) RC3-rc3-F6 RC3-rc3-F3, (h) RC4-rc4-F6, (i) RC1-F6, (j) RC2-F6 RC2-F3, (k) RC3-F6 RC3-F3, and (l) RC4-F6.

Table 2: Details of elliptical steel tubes.

Type of steel tube	$2a_s$ (mm)	$2b_s$ (mm)	a_s/b_s	f_y (MPa)	E_s (GPa)	f_u (MPa)
ec1	204	204	1.0	302.6	201.0	441
ec2	204	170	1.2			
ec3	204	136	1.5			
ec4	204	102	2.0			

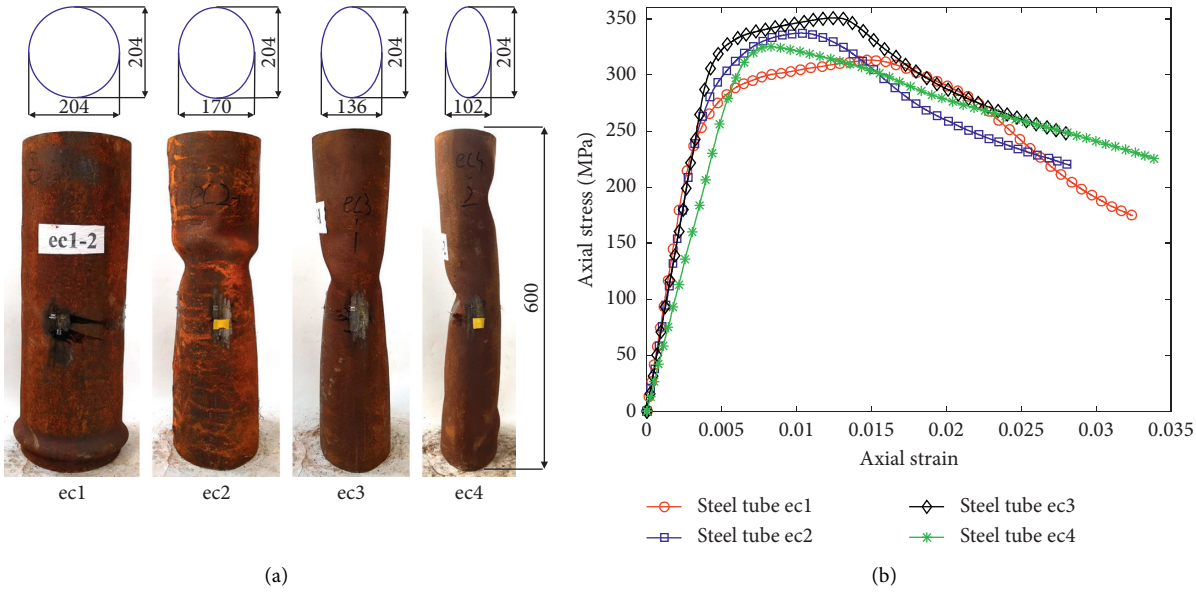

Figure 3: Axial compression test of elliptical hollow steel tubes. (a) Elliptical hollow steel tubes and (b) axial stress-axial strain curves.

rectangular cross section (i.e., 180 mm) but four different widths w_s (i.e., 180 mm, 150 mm, 120 mm, and 90 mm) (Table 3 and Figures 2 and 4). Compared with R-CFFTs, rectangular DSTCs can save concrete significantly due to the inner void, which could be indicated by the void area ratio (i.e., the ratio of the concrete void area to the area of the gross rectangular concrete section). These rectangular DSTCs were designed to have the same void area ratio of 0.46, thus saving around 46% concrete compared with rectangular R-CFFTs in the present study.

As shown in Table 1, each specimen was given a name for ease of reference: (1) "RC1," "RC2," "RC3," and "RC4" are used to indicate the cross-sectional aspect ratio to be "1.0," "1.2," "1.5," and "2.0," respectively; (2) "ec" or "rc" is used to represent the cross section of the inner steel tube to be elliptical or rectangular, followed by a digit to indicate the type of the steel tube as shown in Tables 2 and 3; (3) the letter "F" and one digit are representing the fiber sheet layers of the FRP tube. The nominal thickness of each layer fiber sheet was 0.35 mm, leading to two FRP tube thicknesses for the present study (i.e., 3-layer FRP tube with a nominal thickness of 1.05 mm and 6-layer FRP tube with a nominal thickness of 2.10 mm) (Table 1). For each rectangular DSTC with a rectangular inner steel tube, there was a corresponding rectangular DSTC with an elliptical inner steel tube for comparison, which had the same FRP tube thickness and the same void area ratio as the former one (e.g., RC2-rc2-F6 and RC2-ec2-F6 are a pair of rectangular DSTCs for comparison). All steel tubes in the present study had the same thickness (i.e., 4.5 mm). The FRP tube of all specimens was formed by wrapping continuous unidirectional glass/epoxy laminates on the hardened concrete surface with the fibers oriented in the hoop direction. For each FRP tube, there was an overlapping zone spanning a circumferential distance of around 150 mm along the longer side of the rectangular cross section (Figure 5). Additional FRP strips with a width of 40 mm were provided near the two ends of the specimens to prevent premature failure there. A thin layer of high-strength plaster was used for capping to achieve a flat end before the compressive test.

2.2. Material Properties

2.2.1. Concrete. In order to guarantee the casting quality of the concrete, self-compacting concrete (SCC) was adopted for the present study. Plain concrete cylinders with a height of 300 mm and a diameter of 150 mm were tested following ASTM C39/C39M [32]. A displacement-controlled loading rate of 0.18 mm/min was adopted for the testing of concrete cylinders. The elastic modulus E_c, the peak stress f'_{co}, and the axial strain at the peak stress ε_{co} averaged from these concrete cylinder tests are 33.6 GPa, 50.4 MPa, and 0.26%, respectively.

2.2.2. FRP. Tensile tests were conducted on flat coupons following ASTM D3039 [33] to obtain the material

Table 3: Details of rectangular steel tubes.

Type of steel tube	l_s (mm)	w_s (mm)	l_s/w_s	f_y (MPa)	E_s (GPa)	f_u (MPa)
rc1	180	180	1.0	308.0	200.3	459
rc2	180	150	1.2			
rc3	180	120	1.5			
rc4	180	90	2.0			

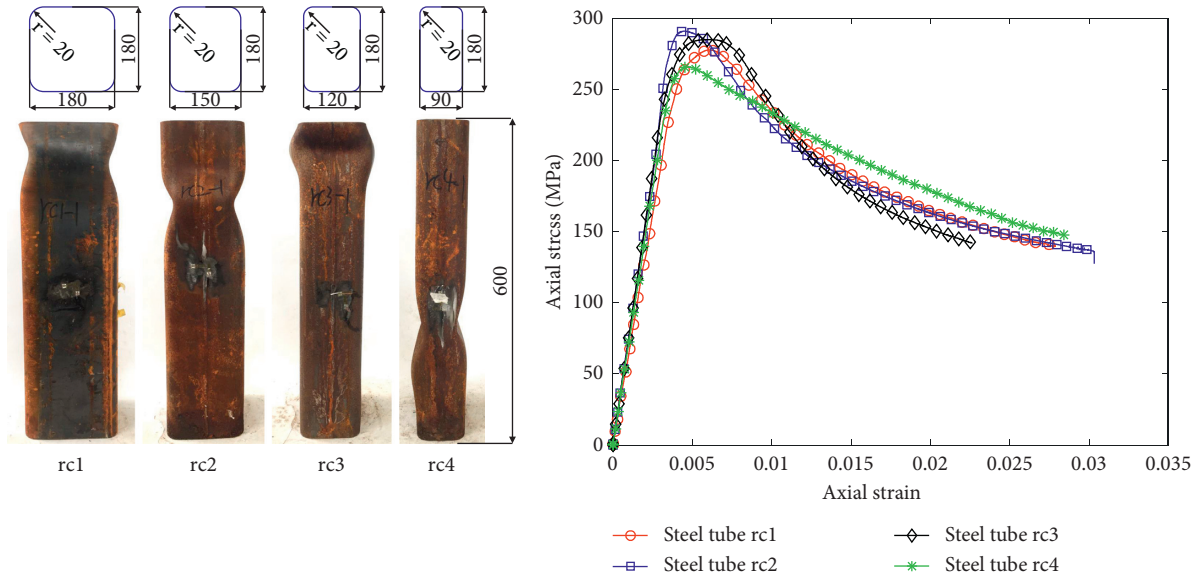

Figure 4: Axial compression test of rectangular hollow steel tubes. (a) Rectangular hollow steel tubes and (b) axial stress-axial strain curves.

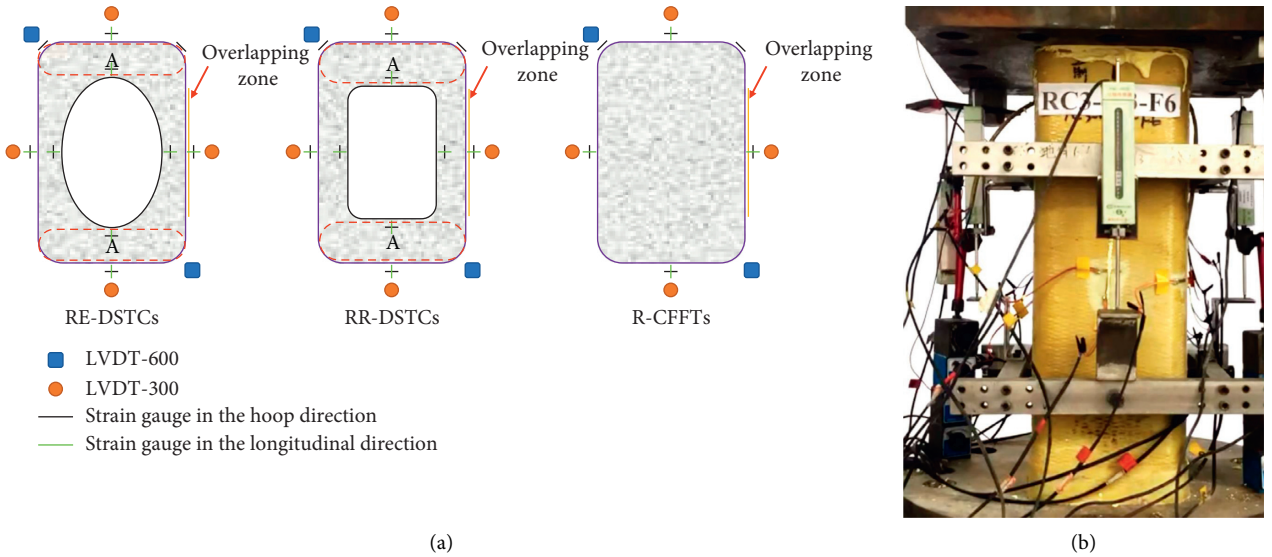

Figure 5: Experimental setup and instrumentation. (a) Planar view of strain gauges and LVDTs and (b) experimental setup.

properties of the FRP tube. The FRP coupon, which contained two layers of fiber sheets, was fabricated using the same wet-layup technique as the FRP tube for rectangular DSTCs. The elastic modulus E_{frp}, the ultimate strength, and the ultimate strain averaged from these FRP flat coupons are 80.1 GPa, 1836.2 MPa, and 2.29%, respectively.

2.2.3. Steel Tube. As shown in Tables 2 and 3, there were four types of elliptical steel tubes and four types of rectangular steel tubes in the present study. All rectangular steel tubes were fabricated using the same batch of raw materials, whereas all elliptical steel tubes were manufactured using another batch of raw materials. All these steel tubes were

manufactured following these four steps: (1) cutting the flat steel plate to designed dimensions; (2) bending the flat steel plate to form half part of a steel tube; (3) welding two identical half parts together by two longitudinal welds; and (4) milling the two ends of each steel tube to achieve flat ends which are perpendicular to its axis.

Tensile tests on steel coupons were conducted following BS 18 [34] for elliptical steel tubes and rectangular steel tubes, respectively. Test results showed the tensile stress-strain curves of these steel coupons had a long yield plateau and then a hardening branch before the final rupture. The average elastic modulus E_s, the average yield stress f_y, and the average ultimate tensile strength f_u are shown in Tables 2 and 3 for elliptical and rectangular steel tubes, respectively. In addition, for each type of these steel tubes, two hollow steel tubes, which had the same height as those used in rectangular DSTCs (i.e., 600 mm), were tested under monotonic axial compression. Four LVDTs were installed to measure the overall axial shortening of each steel tube. The failed steel tubes after axial compression tests and the axial stress-axial strain curves are all shown in Figures 3 and 4, with the axial strain being obtained from LVDTs. All steel tubes suffered severe buckling after the axial compression test.

2.3. Experimental Setup and Instrumentation. Figure 5 shows the experimental setup and instrumentation for all specimens. Six LVDTs were installed to measure the axial deformation of each specimen. Of the six LVDTs, four (i.e., LVDT-300) were used to measure the shortening of the 300 mm midheight region, while the other two (i.e., LVDT-600) were used to measure the total shortening of the specimens. For the outer FRP tube, four hoop strain gauges and four axial strain gauges (gauge length = 20 mm) were installed at the midpoint on each side of the rectangular cross section, while two additional hoop strain gauges were attached at the corner of the rectangular FRP tube. At the midheight of the inner steel tube, four hoop strain gauges and four axial strain gauges with a gauge length of 10 mm were installed and distributed evenly as shown in Figure 5. A large column testing facility with a maximum capacity of 10,000 kN was used to conduct axial compression tests with a displacement control rate of 0.36 mm/min. All the test data, including strains, loads, and displacements, were recorded simultaneously by a data acquiring system.

3. Test Results and Discussion

3.1. General. At the initial stage of the loading test, readings of the four axial strains on the FRP tube were quite uniform, and there was no obvious phenomenon on the FRP tube. When the axial strain readings exceeded around 0.30%, a loud noise emitted from the specimen and a substantial load drop/fluctuation occurred simultaneously, suggesting that severe damage had occurred in the concrete, which was mainly due to the insufficient confinement provided by the rectangular FRP tube. As the loading process progressed, the hoop strain readings of the two strain gauges at the FRP tube corner generally increased faster compared with other hoop strain gauges, indicating the FRP tube provided more effective confinement at the corner of the FRP tube. Noticeable damages were then observed on the outer surface of the FRP tube, which were generally at the corner or close to the corner of the rectangular cross section. At the final stage of the loading test, the progressive snapping noise of fibers was noticed. Finally, the explosive rupture of the FRP tube occurred associated with a big rupture noise.

After the test, the damage of the FRP tube and the inner steel tube was carefully examined (Figure 6). The damage of the FRP tube, which was mainly due to the hoop tension induced by the dilation of the inner concrete, was generally localized at the corner of the rectangular cross section. As expected, the concrete also suffered severe crushing at the location of the FRP rupture. Severe inward deformation and local buckling, which was generally close to the localized rupture of the FRP tube, was observed for both elliptical and rectangular steel tubes.

3.2. Axial Load-Axial Strain Curves. As the axial strain gauges were on the outer surface of the FRP tube or the inner steel tubes, their readings may not closely reflect the strain state of the confined concrete, especially after the development of significant localized damage on the FRP tube. The axial strain obtained from the LVDTs covers the full height of the specimen (i.e., LVDT-600) may not reflect the strain state of the confined concrete, especially at the early stage of the axial compression as there may be initial gaps between the loading plates and the two ends of the specimen. In this paper, the axial strain found from LVDT-300, which reflects the average axial strain of the midheight 300 mm region, is used to represent the axial strain of these specimens.

Axial load-axial strain curves of all specimens are shown in Figure 7 in three groups. As shown in Figure 7(c), the axial load-axial strain curves of R-CFFTs have an initial linear ascending branch and then a severe axial load drop at the axial strain of around 0.30%, followed by an ascending branch until the final failure. For RR-DSTCs (Figure 7(b)), the axial load drop at the axial strain of around 0.30% is much smaller than the corresponding R-CFFTs, whereas corresponding RE-DSTCs have only small axial load fluctuation (Figure 7(a)). The sudden axial load drop/fluctuation was due to the insufficient confinement of rectangular FRP tubes. The existence of the inner steel tube in rectangular DSTCs mitigates the sudden axial load drop as the concrete is confined by both tubes, and the steel tube also contributes directly to the axial load of rectangular DSTCs.

3.3. Key Test Results. For R-CFFTs, the average axial stress of the confined concrete is found as the load resisted by the concrete divided by the cross-sectional area of the concrete. As mentioned before, the FRP tube had fibers oriented only in the hoop direction. Therefore, the direct load contribution of the FRP tube is ignored for all specimens. For rectangular DSTCs, the direct load contribution of the inner steel tube should be considered. The load resisted by the concrete in rectangular DSTCs is assumed to be equal to the load resisted by the specimen subtracted by the load resisted by the inner steel tube at the same axial strain. The load carried

Figure 6: Typical failed specimens after test. (a) RC1-ec1-F6, (b) RC2-ec2-F6, (c) RC3-ec3-F6, (d) RC4-ec4-F6, (e) RC1-rc1-F6, (f) RC2-rc2-F6, (g) RC3-rc3-F6, (h) RC4-rc4-F6, (i) RC1-F6, (j) RC2-F6, (k) RC3-F6, and (l) RC4-F6.

by the inner steel tube was assumed to be the same as the hollow steel tube under axial compression in Figures 3 and 4. The axial loads of the specimen, the concrete, and the steel tube are illustrated for typical rectangular DSTCs in Figure 8.

The method used above may introduce some errors to the axial stress of the confined concrete in rectangular DSTCs, which is believed to be small before the severe buckling of the inner steel tube.

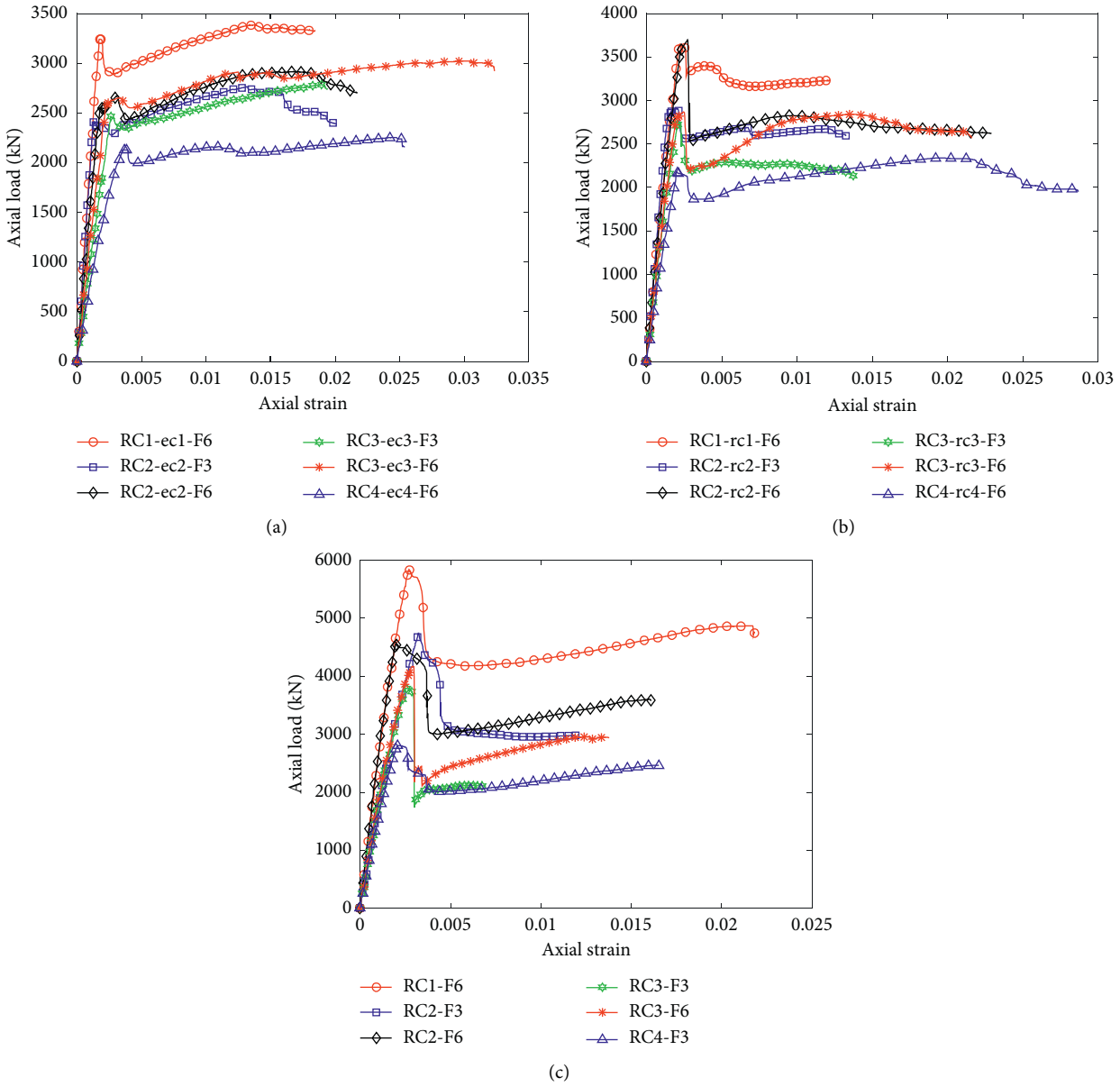

FIGURE 7: Axial load-axial strain curves. (a) RE-DSTCs, (b) RR-DSTCs, and (c) R-FCSCs.

The key test results of all specimens are summarized in Table 4. In this table, P_{max} is the peak axial load of the specimen; f_{cc} is the peak axial stress of the confined concrete; ε_{cu} is the ultimate axial strain of the specimen when the FRP tube ruptured; ε_{hrup} is the rupture strain of FRP tube averaged from the hoop strain gauges outside of the overlapping zone; and f_{cc}/f_{co} and $\varepsilon_{cu}/\varepsilon_{co}$ are the strength enhancement ratio and the strain enhancement ratio of the confined concrete.

3.4. Effect of Cross-Sectional Aspect Ratio. As shown in Figure 9, the axial stress-strain curves of three groups of specimens are compared to evaluate the effect of the cross-sectional aspect ratio. As shown in Figure 9(c), all R-CFFTs exhibit axial stress-strain curves with an ascending branch and a sudden stress drop at the axial strain of around 0.30%, followed by an ascending branch until the final failure. The axial stress at the ultimate axial strain is, however, much lower than the axial stress at the axial strain of around 0.30%. As indicated in Table 4, the average strength enhancement ratio f_{cc}/f_{co} of these four specimens in Figure 9(c) is almost the same (i.e., 1.3), while specimen RC1-F6 had the largest strain enhancement ratio $\varepsilon_{cu}/\varepsilon_{co}$. Although these specimens in Figure 9(c) had different cross-sectional aspect ratios, the axial stress-strain curves of R-CFFTs show a good agreement with each other. As shown in Figure 9(b), similar to R-FCSCs, all RR-DSTCs exhibited a linear ascending branch and followed by a stress drop at the axial strain of around 0.30%. The axial stress is then stabilized for specimens RC1-rc1-F6 and RC2-rc2-F6. In contrast, the axial stress for specimens RC3-rc3-F6 and RC4-rc4-F6 recovered with an

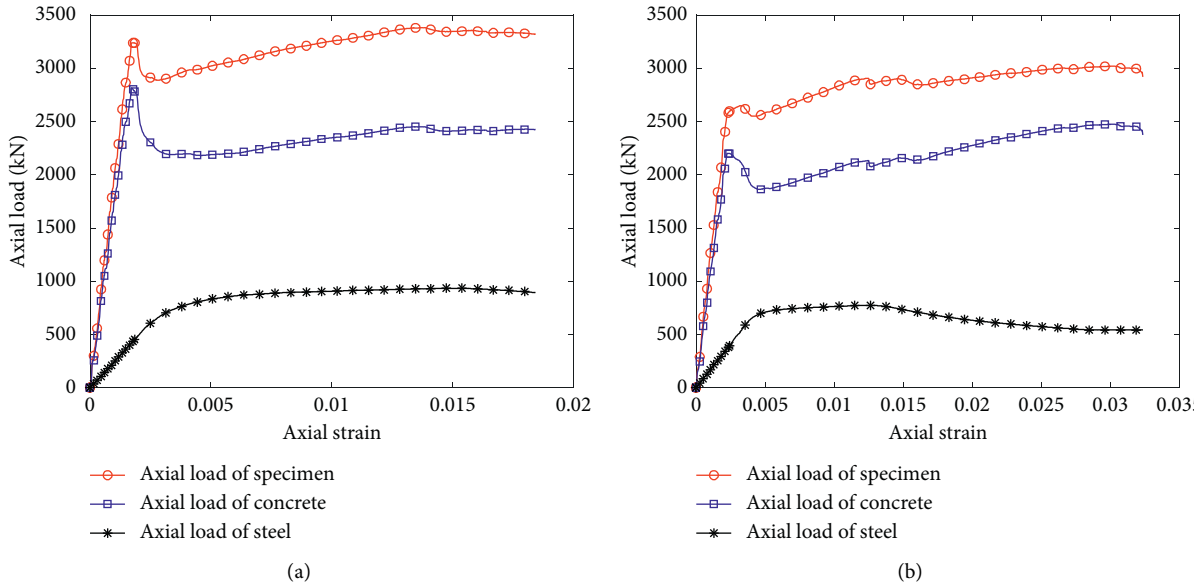

Figure 8: Axial load taken by the concrete and the steel tube. (a) RC1-ec1-F6 and (b) RC3-ec3-F6.

Table 4: Key test results.

Specimen name	P_{max} (kN)	f_{cc} (MPa)	ε_{cu} (%)	ε_{hrup} (%)	f_{cc}/f_{co}	$\varepsilon_{cu}/\varepsilon_{co}$
RC1-ec1-F6	3384	49.9	1.84	0.60	1.0	7.1
RC2-ec2-F3	2763	45.9	2.01	0.54	0.9	7.7
RC2-ec2-F6	2916	46.2	2.17	0.65	0.9	8.4
RC3-ec3-F3	2784	57.0	1.94	0.96	1.1	7.5
RC3-ec3-F6	3023	66.2	3.23	1.32	1.3	12.4
RC4-ec4-F6	2254	61.4	2.54	1.22	1.2	9.8
RC1-rc1-F6	3648	54.5	1.22	0.36	1.1	4.7
RC2-rc2-F3	2907	52.7	1.33	0.27	1.0	5.1
RC2-rc2-F6	3700	64.8	2.29	1.04	1.3	8.8
RC3-rc3-F3	2750	60.0	1.39	1.22	1.2	5.3
RC3-rc3-F6	2868	62.0	2.16	0.95	1.2	8.3
RC4-rc4-F6	2340	66.2	2.87	1.05	1.3	11.0
RC1-F6	5846	65.5	2.18	1.86	1.3	8.4
RC2-F3	4751	64.0	1.19	0.92	1.3	4.6
RC2-F6	4561	61.4	1.61	1.08	1.2	6.2
RC3-F3	3799	64.1	0.70	0.83	1.3	2.7
RC3-F6	4169	70.4	1.38	0.85	1.4	5.3
RC4-F6	2806	63.4	1.65	1.03	1.3	6.4

ascending curve until the final failure. As indicated in Table 4, the average strength enhancement ratio f_{cc}/f_{co} of these four specimens in Figure 9(b) is around 1.2, which are slightly smaller than corresponding R-CFFTs. As shown in Figure 9(a), RE-DSTCs display similar stress drop at the axial strain of around 0.30%. Specimens RC3-ec3-F6 and RC4-ec4-F6 have higher axial stress and larger ultimate axial strain than specimens RC1-ec1-F6 and RC4-ec4-F6. As indicated in Table 4, specimens RC3-ec3-F6 and RC4-ec4-F6 also have higher strength enhancement ratio f_{cc}/f_{co} and strain enhancement ratio $\varepsilon_{cu}/\varepsilon_{co}$ than specimens RC1-ec1-F6 and RC4-ec4-F6. It is evident that a larger aspect ratio will have no negative effect on the confinement effect in rectangular DSTCs. On the contrary, a rectangular DSTC with a larger aspect ratio generally has a larger ultimate axial strain and higher axial stress at the ultimate strain. This observation is inconsistent with the test observation for rectangular FRP-confined concrete columns made in [28, 29] that the confinement effect of the rectangular FRP tube decreases with the increase of the aspect ratio. As shown in Figure 5, with the increase of the aspect ratio, the concrete in the region A is under more effective confinement due to the local confinement effect provided by the steel tube and the FRP tube, leading to higher strength enhancement there.

3.5. Effect of FRP Thickness. As shown in Figure 10, six pairs of rectangular DSTCs, which have the same aspect ratio and the same void ratio but different FRP tube thicknesses, are compared to investigate the effect of FRP tube thickness. For

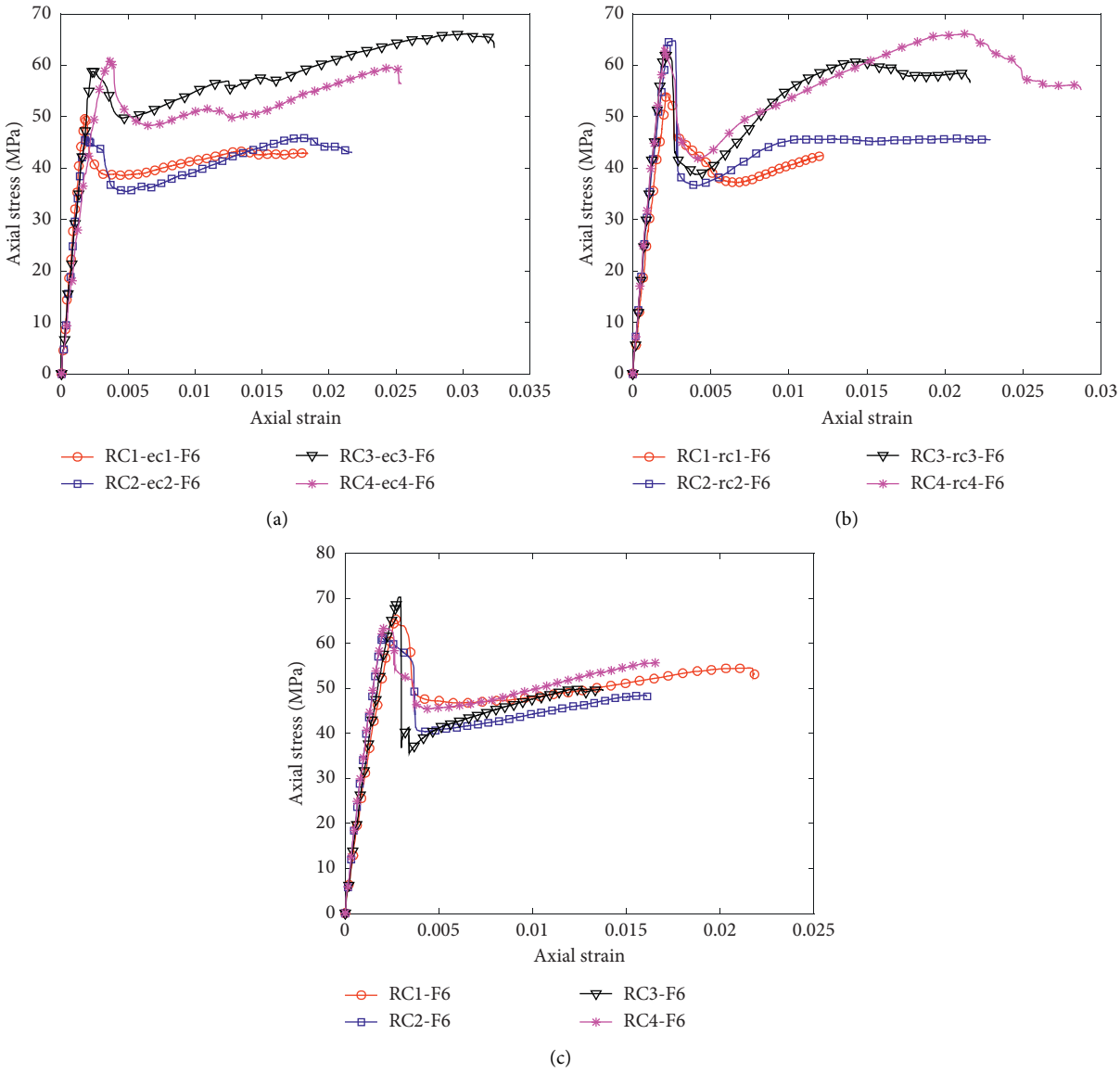

Figure 9: Effect of cross-sectional aspect ratio. (a) RE-DSTCs, (b) RR-DSTCs, and (c) R-FCSCs.

FRP-confined concrete columns, the axial stress-strain behavior of the confined concrete is significantly affected by the confinement stiffness and the hoop rupture strain of the FRP tube [27, 35, 36]. As shown in Table 4, the strength enhancement ratio f_{cc}/f_{co} and the strain enhancement ratio $\varepsilon_{cu}/\varepsilon_{co}$ of rectangular DSTCs with a 6-layer FRP tube are much higher than those of corresponding specimens with a 3-layer FRP tube. As shown in Figure 10, a thicker FRP tube generally leads to a larger stiffness for the second branch of the axial stress-strain curves, a larger strength enhancement ratio, and a larger ductility enhancement ratio.

3.6. Effect of Cross Section of Inner Steel Tube. Six pairs of rectangular DSTCs are compared in Figure 11 to evaluate the effect of the cross sectional shape of the inner steel tube. The axial stress-strain curves of R-CFFTs are also included in Figure 11 for comparison. It is evident that the axial stress-axial strain curves of R-CFFTs have an initial linear ascending branch and then a severe axial stress drop at the axial strain of around 0.30%, followed by an ascending branch until the final failure. This phenomenon is consistent with the observation in [30], which is believed to be associated with the brittle nature of the concrete when the confinement is insufficient. For RE-DSTCs, the axial stress-strain curves have an initial ascending branch and then a fluctuation/drop in the axial stress, followed by a second ascending branch. In contrast, RR-DSTCs experienced a sudden drop in the axial stress starting right at the transition point at their axial stress-strain curves. The sudden drop in the axial stress of RR-DSTCs is smaller than that of corresponding R-CFFTs but much larger than that of corresponding RE-DSTCs. Therefore, the confinement effect of RR-DSTCs is less efficient than that of RE-DSTCs. For RE-DSTCs, their cross section can be regarded as two arcs due to the existence of the elliptical steel tube. The arc effect may

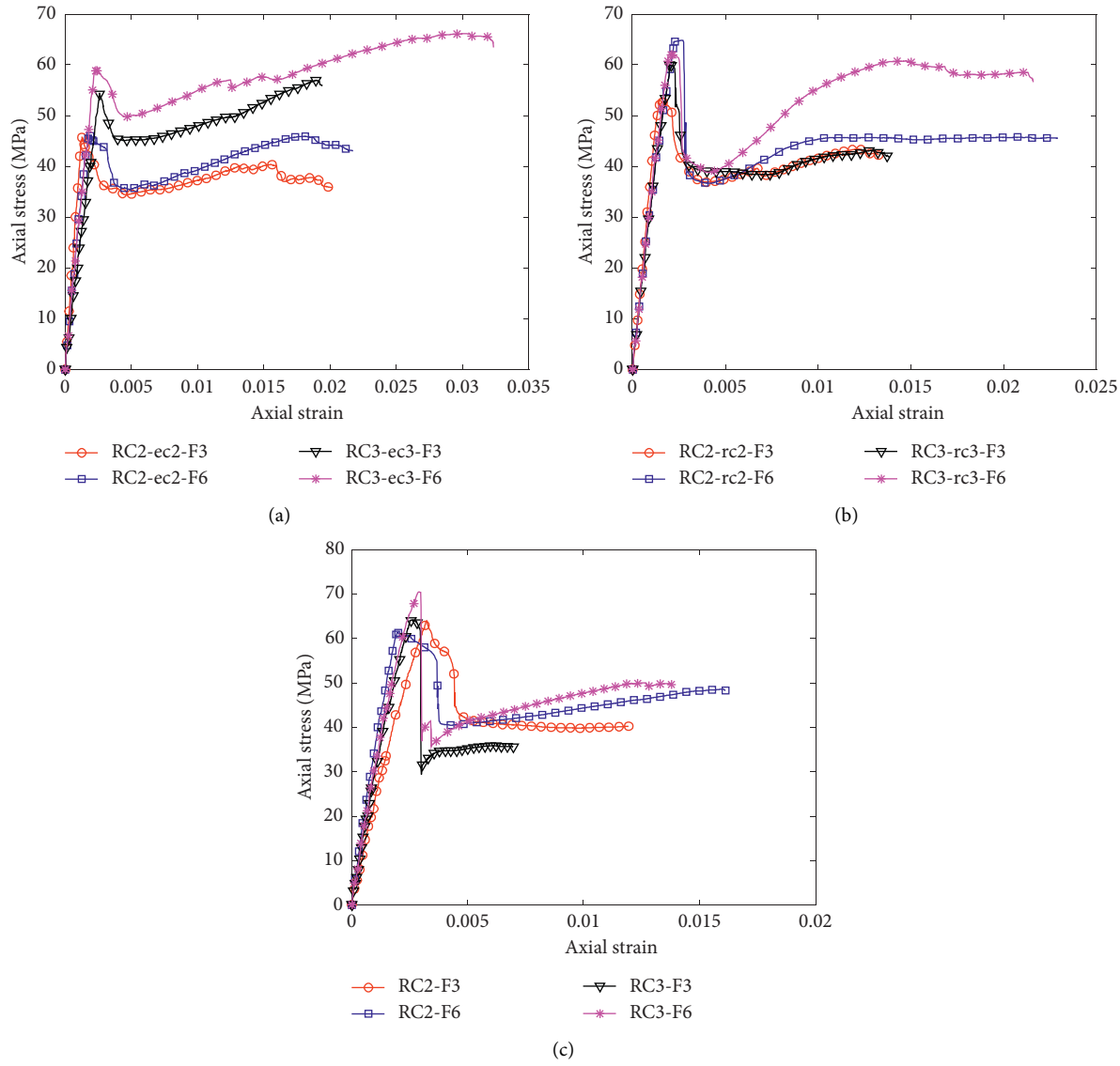

Figure 10: Effect of FRP tube thickness. (a) RR-DSTCs, (b) RE-DSTCs, and (c) R-FCSCs.

exist on the cross section of RE-DSTCs when the concrete layer is under axial compression and under the confinement of the FRP tube, leading to better performance than RR-DSTCs. It is evident that the cross sectional shape of the inner steel tube has a significant effect on the axial stress-strain behavior of the confined concrete in rectangular DSTCs. As illustrated in Figure 11 and Table 4, rectangular DSTCs with an elliptical steel tube generally have better ductility than corresponding specimens with a rectangular steel tube.

4. Comparisons with Stress-Strain Model

Lam and Teng [35] developed a stress-strain model for circular FRP-confined concrete columns, in which a number of important issues including the actual hoop rupture strain, the effect of the hoop stiffness, and the sufficiency of the FRP tube were carefully examined. Based on the model for circular FRP-confined concrete columns, Lam and Teng [27] further developed a stress-strain model for rectangular FRP-confined concrete columns, in which the aspect ratio of the rectangular cross section was considered. In 2009, Teng et al. [36] refined Lam and Teng's [35] model for circular FRP-confined concrete columns, in which more accurate expressions for the ultimate axial strain and the compressive strength were employed. Based on Teng et al.'s [36] model for circular FRP-confined concrete, Yu et al. [10] proposed a simple stress-strain model for the confined concrete in circular DSTCs with a circular inner steel tube. The effect of the inner void in circular DSTCs was considered for the ultimate axial strain of the concrete using the void ratio φ, which was defined as the ratio of the steel tube diameter to the outer diameter of the circular concrete section. In 2013, Yu and Teng [19] conducted an experimental study on hybrid DSTCs with a square outer FRP tube and a circular inner steel tube. Based on the experimental results in Yu and Teng [19], a stress-strain model for concrete in square DSTCs was proposed by combining Lam and Teng's [27]

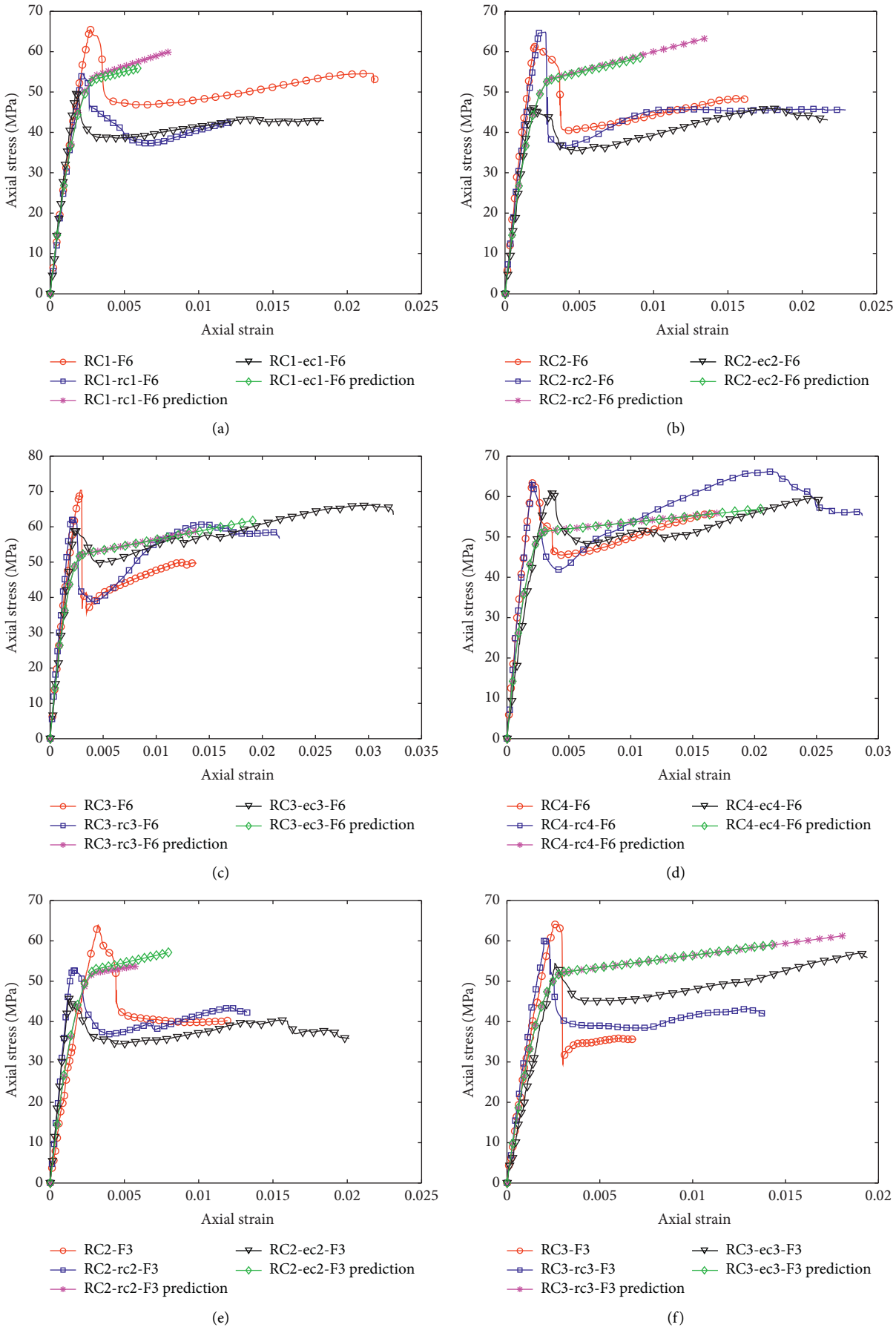

Figure 11: Effect of inner steel tubes.

model for rectangular FRP-confined concrete and Yu et al.'s [10] model for circular DSTCs with a circular inner steel tube. This model also adopted Lam and Teng's [27] equations to consider the effect of the aspect ratio of the rectangular cross section.

Yu and Teng's [19] model consists of a parabolic first portion and a linear second portion for the stress-strain curve of confined concrete in hybrid DSTCs:

$$\sigma_c = E_c\varepsilon_c - \frac{(E_c - E_{2c})^2}{4f_o}\varepsilon_c^2 \cdot 0 \le \varepsilon_c \le \varepsilon_t,$$
$$\sigma_c = f_o + E_{2c}\varepsilon_c \cdot \varepsilon_t \le \varepsilon_c \le \varepsilon_{\mathrm{cu}}, \quad (1)$$

where σ_c and ε_c are the axial stress and the axial strain of confined concrete, respectively; f_o is the intercept of the stress axis by the linear second portion, which is taken to be f'_{co}; E_c is the initial elastic modulus of confined concrete; E_{2c} is the slope of the linear second portion of the stress-strain curve; $\varepsilon_{\mathrm{cu}}$ is the ultimate axial strain of confined concrete; and ε_t is the axial strain at the smooth transition point where the parabolic first portion meets the linear second portion.

The parabolic first portion and the linear second portion are connected with a smooth transition at the transition strain ε_t:

$$\varepsilon_t = \frac{2f_o}{E_c - E_{2c}}. \quad (2)$$

The slope of the linear second portion of the stress-strain curve E_{2c} is given by

$$E_{2c} = \frac{f'_{\mathrm{cc}} - f_o}{\varepsilon_{\mathrm{cu}}}, \quad (3)$$

where f'_{cc} is the compressive strength of confined concrete.

The compressive strength f'_{cc} and the ultimate axial strain $\varepsilon_{\mathrm{cu}}$ of confined concrete are shown in equations (4) and (5). The effect of the aspect ratio for the rectangular cross section is considered for f'_{cc} and $\varepsilon_{\mathrm{cu}}$ using the cross-sectional shape factor for the strength enhancement k_{s1} and the cross-sectional shape factor for the strain enhancement k_{s2}. The void area ratio φ_A (i.e., the ratio of the concrete void area to the area of the gross rectangular concrete section), rather than the void ratio φ (i.e., the ratio of the steel tube diameter to the outer diameter of the circular concrete section), was used in Yu and Teng's [19] model:

$$\frac{f'_{\mathrm{cc}}}{f'_{\mathrm{co}}} = \begin{cases} 1 + 3.5k_{s1}(\rho_K - 0.01)\rho_\varepsilon, & \rho_K \ge 0.01, \\ 1, & \rho_K < 0.01, \end{cases} \quad (4)$$

$$\frac{\varepsilon_{\mathrm{cu}}}{\varepsilon_{\mathrm{co}}} = 1.75 + 6.5k_{s2}\rho_K^{0.8}\rho_\varepsilon^{1.45}\left(1 - \sqrt{\varphi_A}\right)^{-0.22}, \quad (5)$$

$$\varphi = \sqrt{\varphi_A}, \quad (6)$$

$$\rho_K = \frac{E_{\mathrm{frp}}t_{\mathrm{frp}}}{E_{\mathrm{seco}}R_o}, \quad (7)$$

$$\rho_\varepsilon = \frac{\varepsilon_{h,\mathrm{rup}}}{\varepsilon_{\mathrm{co}}}, \quad (8)$$

$$E_{\mathrm{seco}} = \frac{f'_{\mathrm{co}}}{\varepsilon_{\mathrm{co}}}, \quad (9)$$

where f'_{co} and $\varepsilon_{\mathrm{co}}$ are the compressive strength and the axial strain at peak axial stress of unconfined concrete, respectively; φ is the void ratio for circular DSTCs with a circular inner steel tube, which is defined as the ratio of the steel tube diameter to the outer diameter of the circular concrete section; φ_A is the void area ratio for square and rectangular DSTCs, which is defined as the ratio of the concrete void area to the area of the gross concrete section; ρ_K and ρ_ε are the confinement stiffness ratio and the strain ratio, respectively; E_{seco} is the secant modulus of unconfined concrete; E_{frp} is the elastic modulus of FRP in the hoop direction; t_{frp} is the thickness of the FRP tube; and $\varepsilon_{h,\mathrm{rup}}$ is the hoop strain of FRP at the rupture of the tube due to hoop tensile stresses.

The cross-sectional shape factors k_{s1} and k_{s2} for rectangular FRP-confined concrete columns in Lam and Teng's [27] model are given by equations (10) and (11). For hybrid DSTCs with a square cross section, k_{s1} and k_{s2} are the same as used in Yu and Teng's [19] model. In the following predictions, k_{s1} and k_{s2} from Lam and Teng's [27] model are employed to consider the effect of the cross-sectional aspect ratio:

$$k_{s1} = \left(\frac{b}{h}\right)^2\frac{A_e}{A_c}, \quad (10)$$

$$k_{s1} = \left(\frac{h}{b}\right)^2\frac{A_e}{A_c}, \quad (11)$$

$$\frac{A_e}{A_c} = \frac{1 - \left((b/h)(h - 2R_c)^2 + (h/b)(b - 2R_c)^2\right)/3A_g - \rho_{\mathrm{sc}}}{1 - \rho_{\mathrm{sc}}}, \quad (12)$$

$$A_g = bh - (4 - \pi)R_c^2, \quad (13)$$

where b and h are the width (the shorter side) and the breadth (the longer side) of the rectangular cross section, respectively; R_o is the outer radius of the circular section of concrete for circular DSTCs, which is taken as $\sqrt{bh/\pi}$ for rectangular DSTCs in the present study; A_e/A_c is the effective confinement area ratio for rectangular FRP-confined concrete columns; A_g is the gross area of the rectangular column section; and ρ_{sc} is the cross-sectional area ratio of the longitudinal steel reinforcement.

The test results from the present study are compared with Yu and Teng's [19] model in Figures 11 and 12. Due to the existence of the axial stress drop at the axial strain of around 0.30%, Yu and Teng's [19] model could not capture the complicated shape of the axial stress-strain curves of rectangular DSTCs. However, Yu and Teng's [19] model generally provides close predictions for the peak axial stress of the confined concrete in rectangular DSTCs

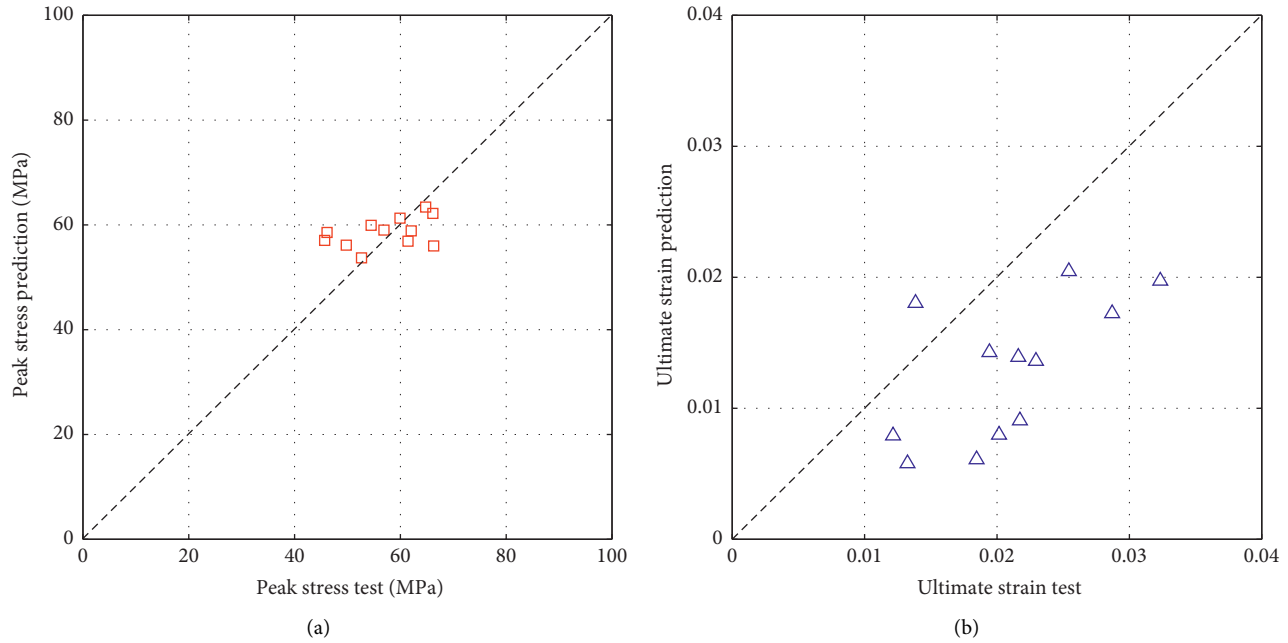

Figure 12: Comparisons with Yu and Teng's [19] model. (a) Peak stress and (b) ultimate strain.

(Figure 12(a)). As shown in Figures 11 and 12(b), Yu and Teng's [19] model yields conservative predictions for the ultimate axial strain of the confined concrete in rectangular DSTCs. Yu and Teng's [19] model, which was originally based on Lam and Teng's [27] model for rectangular FRP-confined concrete and Yu et al.'s [10] model for circular DSTCs with a circular inner steel tube, does not consider the complicated mechanism in such rectangular DSTCs. Further research is needed for the development of a more reliable stress-strain model for the confined concrete in rectangular DSTCs when more test data are available. Such a stress-strain model should take due account of various factors, including the cross-sectional aspect ratio, the void area ratio, the thickness of the steel tube, and the cross-sectional shape of the inner steel tube.

5. Conclusions

This paper presents an experimental study on rectangular DSTCs under axial compression. The test results and discussions allow the following conclusions to be drawn:

(1) A larger aspect ratio will have no negative effect on the confinement effect in rectangular DSTCs. A rectangular DSTC with a larger cross-sectional aspect ratio generally has a larger ultimate axial strain and higher axial stress at the ultimate axial strain.

(2) Rectangular DSTCs with an elliptical steel tube exhibit better performance than corresponding specimens with a rectangular steel tube.

(3) Rectangular DSTCs with a thicker FRP tube generally have a larger stiffness for the second branch of the axial stress-strain curve, a larger strength enhancement ratio, and a ductility enhancement ratio.

(4) Yu and Teng's model generally provides close predictions for the peak axial stress of the confined concrete but yields conservative predictions for the ultimate axial strain of the confined concrete in rectangular DSTCs.

Data Availability

All tests were conducted by the authors. Resuests for data, 12 months after publication of this article, will be considered by the corresponding author.

Conflicts of Interest

The authors declare that they have no conflicts of interest.

Acknowledgments

The authors are grateful for the financial support received from the National Natural Science Foundation of China (grant nos. 51978332 and 51608263) and the Natural Science Foundation of Jiangsu Province (grant no. BK20160998).

References

[1] L. C. Hollaway and J. G. Teng, *Strengthening and Rehabilitation of Civil Infrastructures Using Fibre Reinforced Polymer (FRP) Composites*, Woodhead Publishing, Cambridge, UK, 2008.

[2] J.-J. Xu, Z.-P. Chen, Y. Xiao, C. Demartino, and J.-H. Wang, "Recycled aggregate concrete in FRP-confined columns: a review of experimental results," *Composite Structures*, vol. 174, pp. 277–291, 2017.

[3] Y. Wang, G. Cai, Y. Li, D. Waldmann, A. Si Larbi, and K. D. Tsavdaridis, "Behavior of circular fiber-reinforced polymer-steel-confined concrete columns subjected to

reversed cyclic loads: experimental studies and finite-element analysis," *Journal of Structural Engineering*, vol. 145, no. 9, Article ID 04019085, 2019.

[4] J. G. Teng, "New-material hybrid structures," *China Civil Engineering Journal*, vol. 51, no. 12, pp. 1–11, 2008, in Chinese.

[5] J. G. Teng, T. Yu, Y. L. Wong, and S. L. Dong, "Hybrid FRP-concrete-steel tubular columns: concept and behavior," *Construction and Building Materials*, vol. 21, no. 4, pp. 846–854, 2007.

[6] B. Zhang, J. G. Teng, and T. Yu, "Experimental behavior of hybrid FRP-concrete-steel double-skin tubular columns under combined axial compression and cyclic lateral loading," *Engineering Structures*, vol. 99, pp. 214–231, 2015.

[7] I. A. Omar, M. A. ElGawady, G. Ahmed, A. Sujith, and A. Mohanad, "Seismic performance of innovative hollow-core FRP-concrete-steel bridge columns," *Journal of Bridge Engineering*, vol. 22, no. 2, p. 04016120, 2017.

[8] L.-H. Han, Z. Tao, F.-Y. Liao, and Y. Xu, "Tests on cyclic performance of FRP-concrete-steel double-skin tubular columns," *Thin-Walled Structures*, vol. 48, no. 6, pp. 430–439, 2010.

[9] L. C. Hollaway, "A review of the present and future utilisation of FRP composites in the civil infrastructure with reference to their important in-service properties," *Construction and Building Materials*, vol. 24, no. 12, pp. 2419–2445, 2010.

[10] T. Yu, J. G. Teng, and Y. L. Wong, "Stress-strain behavior of concrete in hybrid FRP-concrete-steel double-skin tubular columns," *Journal of Structural Engineering*, vol. 136, no. 4, pp. 379–389, 2010.

[11] B. Zhang, J.-L. Zhao, T. Huang, N.-Y. Zhang, Y.-J. Zhang, and X.-M. Hu, "Effect of fiber angles on hybrid fiber-reinforced polymer-concrete-steel double-skin tubular columns under monotonic axial compression," *Advances in Structural Engineering*, 2020.

[12] B. Zhang, J. G. Teng, and T. Yu, "Compressive behavior of double-skin tubular columns with high-strength concrete and a filament-wound FRP tube," *Journal of Composites for Construction-ASCE*.

[13] T. Yu, B. Zhang, Y. B. Cao, and J. G. Teng, "Behavior of hybrid FRP-concrete-steel double-skin tubular columns subjected to cyclic axial compression," *Thin-Walled Structures*, vol. 61, pp. 196–203, 2012.

[14] T. Ozbakkaloglu and E. Akin, "Behavior of FRP-confined normal- and high-strength concrete under cyclic axial compression," *Journal of Composites for Construction*, vol. 16, no. 4, pp. 451–463, 2012.

[15] P. Xie, *"Behavior of large-scale hybrid FRP-concrete-steel double-skin tubular columns subjected to concentric and eccentric compression,"* PhD Thesis, The Hong Kong Polytechnic University, Hong Kong, China, 2018.

[16] T. Yu, Y. L. Wong, and J. G. Teng, "Behavior of hybrid FRP-concrete-steel double-skin tubular columns subjected to eccentric compression," *Advances in Structural Engineering*, vol. 13, no. 5, pp. 961–974, 2010.

[17] R. Wang, L.-H. Han, and Z. Tao, "Behavior of FRP-concrete-steel double skin tubular members under lateral impact: experimental study," *Thin-Walled Structures*, vol. 95, pp. 363–373, 2015.

[18] I. A. Omar and M. A. ElGawady, "Performance of hollow-core FRP–concrete–steel bridge columns subjected to vehicle collision," *Engineering Structures*, vol. 123, pp. 517–531, 2016.

[19] T. Yu and J. G. Teng, "Behavior of hybrid FRP-concrete-steel double-skin tubular columns with a square outer tube and a circular inner tube subjected to axial compression," *Journal of Composites for Construction*, vol. 17, no. 2, pp. 271–279, 2012.

[20] T. Ozbakkaloglu, B. A. L. Fanggi, and J. Zheng, "Confinement model for concrete in circular and square FRP-concrete-steel double-skin composite columns," *Materials & Design*, vol. 96, pp. 458–469, 2016.

[21] B. A. L. Fanggi and T. Ozbakkaloglu, "Effect of inner steel tube cross-sectional shape on compressive behavior of square FRP-concrete-steel double-skin tubular columns," *Applied Mechanics and Materials*, vol. 752-753, pp. 578–583, 2014.

[22] B. A. L. Fanggi and T. Ozbakkaloglu, "Influence of inner steel tube diameter on compressive behavior of square FRP-HSC-steel double-skin tubular columns," *Advanced Materials Research*, vol. 1119, pp. 688–693, 2015.

[23] B. Zhang, W. Wei, G. S. Feng, Q. B. Zhang, N. Y. Zhang, and X. M. Hu, "Experimental study of rectangular FRP-concrete-steel double-skin tubular column under axial compression," *Industrial Construction*, vol. 49, no. 12, pp. 195–200, 2019, in Chinese.

[24] X. Li, J. Lu, D.-D. Ding, and W. Wang, "Axial strength of FRP-confined rectangular RC columns with different cross-sectional aspect ratios," *Magazine of Concrete Research*, vol. 69, no. 19, pp. 1011–1026, 2017.

[25] H. Toutanji, M. Han, J. Gilbert, and S. Matthys, "Behavior of large-scale rectangular columns confined with FRP composites," *Journal of Composites for Construction*, vol. 14, no. 1, pp. 62–71, 2009.

[26] T. Ozbakkaloglu and D. J. Oehlers, "Concrete-filled square and rectangular FRP tubes under axial compression," *Journal of Composites for Construction*, vol. 12, no. 4, pp. 469–477, 2008.

[27] L. Lam and J. G. Teng, "Design-oriented stress-strain model for FRP-confined concrete in rectangular columns," *Journal of Reinforced Plastics and Composites*, vol. 22, no. 13, pp. 1149–1186, 2003.

[28] H.-X. Liu, G.-J. Liu, X.-Z. Wang, and X.-Q. Kong, "Effect of cross-sectional aspect ratio and basalt fiber-reinforced polymer-confined number on axial compression behavior of short columns," *Journal of Reinforced Plastics and Composites*, vol. 34, no. 10, pp. 782–794, 2015.

[29] Y.-F. Wu and Y.-Y. Wei, "Effect of cross-sectional aspect ratio on the strength of CFRP-confined rectangular concrete columns," *Engineering Structures*, vol. 32, no. 1, pp. 32–45, 2010.

[30] T. Ozbakkloglu, "Ultra-high-strength concrete-filled FRP tubes: compression tests on square and rectangular columns," *Key Engineering Materials*, vol. 575, pp. 239–244, 2014.

[31] G. Cavill and T. Yu, "Rectangular hybrid FRP-concrete-steel double-skin tubular columns: stub column tests," in *Proceedings of the 23rd Australasian Conference on the Mechanics of Structures and Materials (ACMSM23)*, pp. 521–526, Bryon Bay, Australia, December 2014.

[32] ASTM C39/C39M, *Standard Test Method for Compressive Strength of Cylindrical Concrete Specimens*, American Society for Testing and Materials, Philadelphia, PA, USA, 2008.

[33] ASTM D3039/D3039M, *Standard Test Method for Tensile Properties of Polymer Matrix Composite Materials*, American Society for Testing and Materials, Philadelphia, PA, USA, 2017.

[34] BS 18, *Tensile Testing of Metals (Including Aerospace Materials)*, British Standards Institution, London, UK, 1987.

[35] L. Lam and J. G. Teng, "Design-oriented stress–strain model for FRP-confined concrete," *Construction and Building Materials*, vol. 17, no. 6-7, pp. 471–489, 2003.

[36] J. G. Teng, T. Jiang, L. Lam, and Y. Z. Luo, "Refinement of a design-oriented stress-strain model for FRP-confined concrete," *Journal of Composites for Construction*, vol. 13, no. 4, pp. 269–278, 2009.

Hindawi
Advances in Polymer Technology
Volume 2020, Article ID 9512839, 15 pages
https://doi.org/10.1155/2020/9512839

Research Article

Influence of Polypropylene Fibre (PF) Reinforcement on Mechanical Properties of Clay Soil

Mazahir M. M. Taha[1,2] **Cheng Pei Feng**[1] **and Sara H. S. Ahmed**[3]

[1]*Civil Engineering Department, Northeast Forestry University, P.O. Box 150040, Harbin, China*
[2]*Civil Engineering Department, Faculty of Engineering, Alzaiem Alazhari University, P.O. Box 1432 Khartoum North 13311, Sudan*
[3]*Civil Engineering and Architecture Department, Zhejiang University 866 Yuhangtang Road, Xihu District, Hangzhou 310058, China*

Correspondence should be addressed to Cheng Pei Feng; chengpeifeng@126.com

Received 31 October 2019; Revised 23 December 2019; Accepted 27 February 2020; Published 19 May 2020

Guest Editor: Jinjun Xu

This study investigated the effects of polypropylene fibre (PF) reinforcement on the mechanical behaviour of clay soil. Using clay soil and polypropylene fibres from China's Inner Mongolia and Hebei Provinces, respectively, a series of soil samples with 0%, 1.5%, 2.25%, and 3% PF content by soil weight were subjected to compaction, shear strength, consolidation, California bearing ratio, and microstructure analyses. The study results indicate improved compaction, shear strength, consolidation, and the bearing ratio of the PF-stabilised clay soil. As the PF content increased, its maximum dry density increased and its optimum moisture content decreased; its angle of internal friction increased and its cohesion coefficient decreased; and its void ratio, consolidation coefficient, and hydraulic conductivity all decreased. Comparing the unstabilised (0% PF) and stabilised (3% PF) clay soil, the void ratio, consolidation coefficient, and hydraulic conductivity decreased from 0.96 to 0.93, from 2.52 to 2.34 cm^2/s, and from 1.12 to 1.02 cm/s, respectively. The optimum PF content was determined to be 3% by the weight of the soil, as this quantity resulted in the best improvement in soil properties.

1. Introduction

Highways, bridges, buildings, and hydraulic structures are at high risk for damage if constructed on a swelling soil such as clay. To improve the strength and compactability of clay soil in foundation applications, different stabilisation techniques have been established by targeting various soil parameters, including the shear strength, liquid limit, plasticity index, compaction, and consolidation coefficient. Common stabilisation techniques include the use of chemical additives [1–13], thermal energy [14–18], compaction, and reinforcement with plant-based or synthetic fibres [19–33]. Plant-based fibre reinforcement materials include straw, coir, palm, sisal, and jute and are available at a low cost. The use of synthetic fibre reinforcement materials such as polypropylene, nylon, rubber, or plastic also offers potential waste-reduction benefits. As excessive waste materials pose public safety and logistical challenges regarding disposal [34–36], research into the use of waste materials to stabilise soil is presently a global trend.

Several previous studies have considered the effects of different fibre types on the mechanical properties of soil. Moghal et al. [37] evaluated the effectiveness of Fibre Cast (FC) and Fibre Mesh (FM) in different lengths and dosages on the unconfined compressive strength (UCS) of soil specimens. They observed that the fibre type, length, and dosage all affected the UCS of soil stabilised with lime. Puppala and Musenda [38] investigated the effects of fibre reinforcement on strength and volume changes in expansive soils. Their results show that the fibre reinforcement increased the UCS of the soil and reduced both its volumetric shrinkage and swelling pressures. Yadav and Tiwari [39] found that the use of rubber fibres decreased the compressive and tensile strengths of cement-stabilised clay soil but significantly increased the postpeak strength loss rate and altered the failure mechanism of the cement stabiliser. As the rubber fibre

content increased, the soaked and unsoaked California bearing ratio (CBR) values decreased and increased, respectively. Moghal et al. [40] studied the effect of FC and FM on the CBR of specimens and found that the improvement in CBR increased with the quantity of fibre and fibre lengths. The maximum CBR occurred for a fibre content of 0.6% and fibre length of 12 mm. Phanikumar and Singla [23] investigated the effects of nylon fibres on the swell-consolidation characteristics of a clay soil. They found that the use of nylon fibres improved the soil's secondary consolidation characteristics and that the swell potential and vertical swelling pressure decreased as the length of the fibres increased. Al-Akhras et al. [41] investigated the effect of nylon and palmyra fibre contents of 1%, 2%, 3%, 4, and 5% by soil weight on the swelling properties of clayey soils. The results showed that, for the same quantity of fibre, the palmyra fibres had a greater effect than the nylon fibres in reducing the swelling pressure of the expansive soils. Moghal et al. [42] studied the effects of FC and FM in three dosages each (0.2, 0.4, and 0.6% by soil weight), two fibre lengths each (6 and 12 mm), and with and without lime treatments on the swell-consolidation. The results indicated that FC without lime reduced swelling, while the linear shrinkage decreased with the addition of fibres and lime treatment. Khan and Azam [43] studied the consolidation behaviour of clay slurry, they found that the void ratio significantly decreased following the virgin compression of clay slurry; the soil hydraulic conductivity also decreased because of the low porosity and high torsion. The consolidation and volume change coefficients decreased as the void ratio and hydraulic conductivity decreased but increased as the effective pressure decreased. Most recently, Cui et al. [44] found that the use of carbon fibre and nanosilica significantly improved the soil shear strength based on the internal friction angle and cohesion between the carbon fibres and soil.

To date, few studies have focused specifically on the consolidation coefficient and CBR of polypropylene fibre (PF) stabilised soil. Accordingly, this study investigated the effects of PF stabilisation on the mechanical properties of a clay soil. Using clay soil from China's Inner Mongolia and PF from Hebei Province, a series of laboratory tests were performed to determine the compaction, shear strength, consolidation, and bearing ratio of soil with and without PF stabilisation. The stabilised test specimens were prepared using 0.75%, 1.5%, 2.25%, and 3% PF content by soil weight. The results of this study demonstrate the potential for the use of PF as part of a soil stabilising technique, advancing the state of knowledge regarding the practical stabilization of clay soils.

2. Materials and Methods

2.1. Materials

2.1.1. Clay Soil. The clay soil used in this study was collected in the La Bu Dalin subdistrict of Erguna in China's Inner Mongolia Province. Samples were obtained from 15 cm below ground, placed in a plastic bag to retain moisture, and transported to the Northeast Forestry University laboratory for preliminary analysis. Table 1 summarises the clay soil properties determined according to the American Society for Testing and Materials (ASTM) Standards [45–50]. The particle size distribution of the soil is displayed in Figure 1. The soil was classified as high-plasticity clay (CH) according to the distribution of particle sizes and based on Indian Standard IS: 1498-1970.

Table 1: Index properties of soil.

Property	Value
Specific gravity	2.58
Moisture content (%)	13.35
Liquid limit (%)	67
Plastic limit (%)	36.09
Plasticity index (%)	30.91
Compaction parameters	
Optimum moisture content (%)	27.38
Maximum dry density (g/cm^3)	1.52
Shear strength parameters	
C (kN/cm^2)	175
Φ (°)	2.83

2.1.2. Polypropylene Fibre. Fibres are one of the most widely used synthetic materials for reinforcing soil because of their nontoxicity, corrosion resistance, and high tensile strength. The PF used in this study was produced in China's Hebei Province. The PF was 12 mm in length [51, 52] with a mean diameter of 0.034 mm. Table 2 summarises the additional properties of the PF.

2.2. Test Specimen Preparation. To prepare the clay soil for testing, the sample was first dried in an oven at 50°C for 24 h then mixed manually with 0%, 0.75%, 1.5%, 2.25%, and 3% PF by dry weight of soil and distilled water for at least 10 min to create a series of test mixtures. These mixtures were then placed in plastic bags, where they were continuously shaken for at least 5 min to remove all air. Finally, after squeezing any remaining air out of each bag by hand, the plastic bags were sealed and stored in desiccators for 24 h.

Immediately prior to testing, the materials were remixed in the plastic bags by shaking and squeezing the bags. The resultant mixtures contained no clumps larger than 5 mm in diameter. Sufficient numbers of unstabilised (0% PF) and stabilised (0.75%, 1.5%, 2.25%, and 3% PF by dry weight of the soil) test specimens were prepared from these mixtures to allow for a minimum of three measurements per test; these measurements were then averaged to produce the final test results.

2.3. Experimental Methods

2.3.1. Photoelectric Liquid-Plastic Limits Test. The liquid-plastic limit test was conducted using the GYS-2 photoelectric liquid-plastic tester from the Nanjing Ningxi Soil Instrument Co., Ltd, in Nanjing, China. The liquid-plastic limits were measured by the cone depth of the soil with the cone mass of 100 g and cone angle of 30°. A cone penetrator was used to determine the liquid limit (WL), plastic limit (WP),

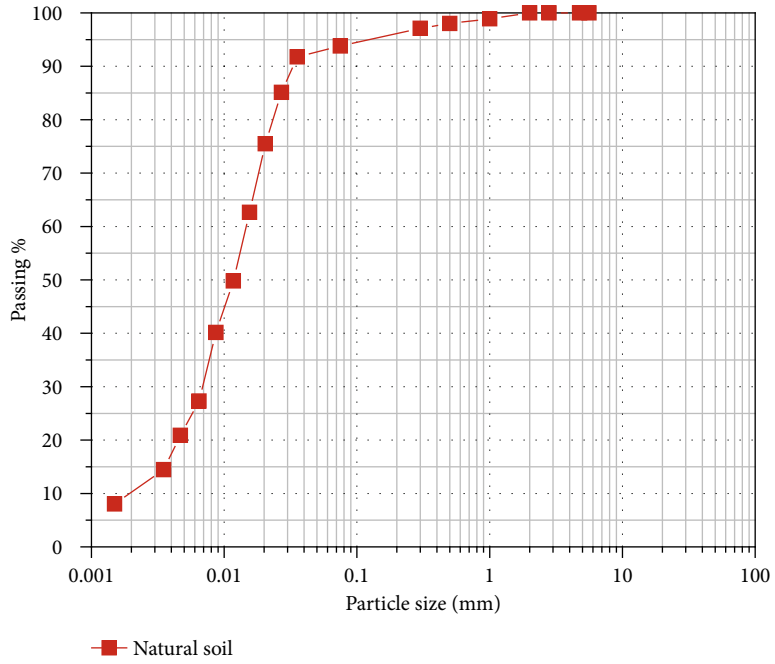

Figure 1: Particle size distribution of the natural soil.

Table 2: Properties of polypropylene fibre.

Property	Value
Density	0.91 g/cm^3
Cut length	12 mm
Diameter	0.034 mm
Colour	White
Humidity	<0.1%
Acid resistance	Very good
Alkali resistance	Very good

and plasticity index (*PI*) of the soil with and without PF. Figure 2 presents a schematic diagram of photoelectric liquid-plastic limit testing apparatus used in this study. The principle of the photoelectric test is based on the GB/T 50123-1999 standard soil test method and JTG E40-2007 method of soil testing for highway engineering methods [53, 54]. The moisture content (*wc*) was measured corresponding to each penetration depth of the cone (≤5 mm, 9–11 mm, and 20 ± 0.2 mm) to draw Lines AB, AC, and AD. The *WL* was determined from the test result as the moisture content at which the *hp* equal to 20 ± 0.2 mm using this *WL* in Eq. (1) to determine the penetration depth *hp*. The *PL* was then determined from Figure 3, based on the penetration depth obtained from Eq. (1) for each of the three straight lines AB, AC, and AD of the soil specimen. Consequently, the *PI* was calculated by using Eq. (2).

$$hp = W_L/(0.524\,W_L - 7.606) \quad (1)$$

where *hp* is the cone penetration depth and *WL* is the liquid limit.

$$P_I = W_L - P_L \quad (2)$$

where *PI* is the plasticity index, *WL* is the liquid limit and *PL* is the plastic limit.

2.3.2. Proctor Compaction Test. Proctor compaction tests were conducted on the unstabilised and stabilised test specimens according to ASTM Standard D698-00a (2006) [49] to determine their maximum dry density (MDD, g/cm^3) and optimum moisture content (OMC, %) as indicators of their compaction potential. The compaction properties of the unstabilised soil and the stabilised soils with varying PF contents were subsequently compared.

2.3.3. Triaxial Compression Test. Triaxial compression tests were performed to measure the shear strength of the clay soil specimens based on their angle of internal friction (Φ, °) and cohesion coefficient (*c*, kg/cm^2). Unstabilised and stabilised specimens in their MDD and OMC states were placed in moulds measuring 80 mm in length with a diameter of 39.1 mm. Triaxial compression tests were subsequently performed using the fully automatic TSZ-1 triaxial test apparatus (Nanjing Ningxi Soil Instrument Co., Ltd., Nanjing, China). During testing, the rate of axial strain was set at 0.800 mm/min, the axial force at 10 kN, and the confining pressures at 100, 200, and 300 kPa.

2.3.4. Consolidation Test. Consolidation tests were performed to measure the consolidation of the clay soil specimens based on the void ratio (*e*), consolidation coefficient (*cv*, cm^2/s), and hydraulic conductivity (*k*, cm/s). The unstabilised and stabilised specimens, again in their MDD and OMC states, were placed in ring moulds measuring 20 mm thick with a diameter of 61.8 mm. The consolidation tests were

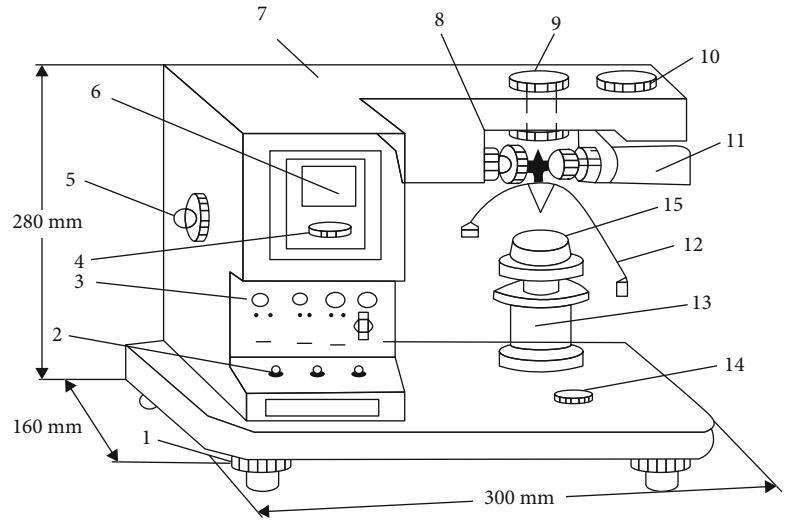

Figure 2: Schematic diagram of photoelectric liquid/plastic limit testing machine: (1) water adjusting screw; (2) control switch; (3) indicator light; (4) zero line adjusting screw; (5) reflector adjusting screw; (6) screen; (7) housing; (8) objective adjustment screw; (9) battery devices; (10) light source adjusting screw; (11) light source; (12) cone instrument; (13) lift table; (14) horizontal bubbles; (15) soil cup.

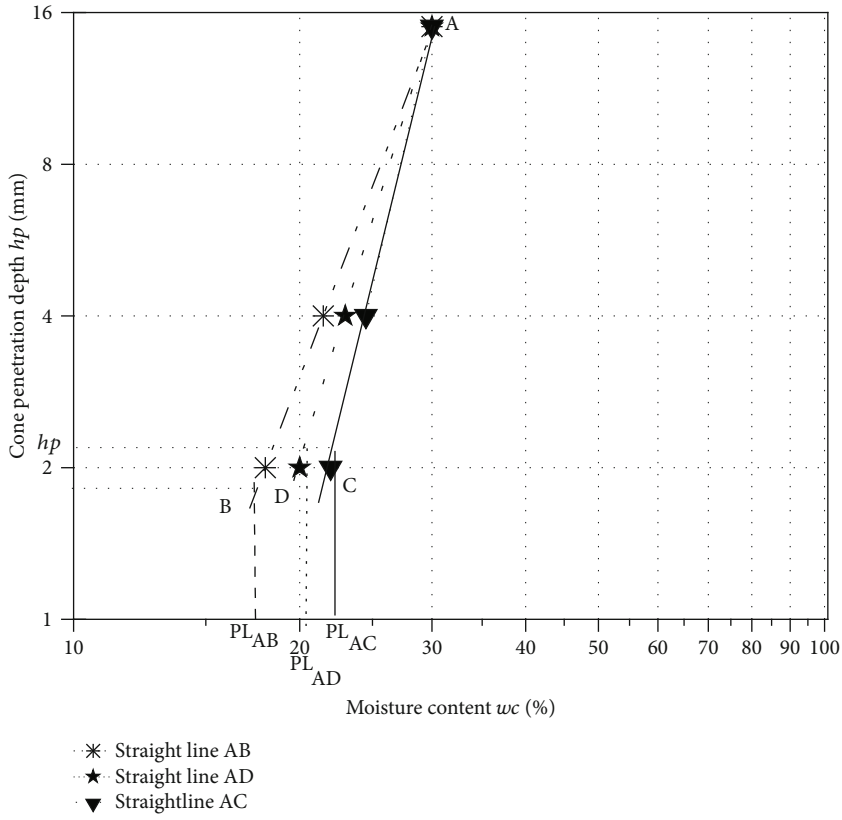

Figure 3: Relationship between the cone penetration depth (hp) and moisture content (wc).

subsequently performed using the fully automatic GZQ-1 pneumatic consolidometer testing machine with a capacity of 4.5 kN (Nanjing Ningxi Soil Instrument Co., Ltd., Nanjing, China). Comprised of a pneumatic controller, multiple channels, a communication converter, and a data system, this device was used to determine the compression properties of the soil under different loads and pressures (12.5, 25, 50, 100, 200, 300, 400, and 800 kPa). The errors in test force and displacement were found to be within ±1% of the indicated values.

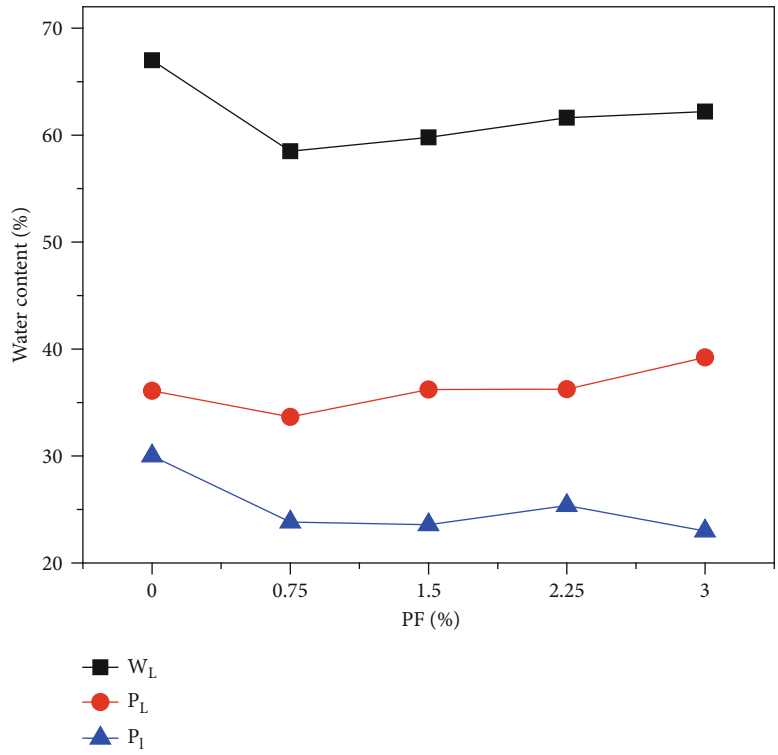

Figure 4: Effect of PF on the Atterberg limits of the soils.

2.3.5. California Bearing Ratio Test. To determine the CBR (%) of the clay soil, we performed CBR tests in accordance with JTG-E40-2007 [54]. The soil mixture was filled in the cylindrical mould of 150 mm diameter and 180 mm height in three equal layers and each layer was compacted with 98 blows per layer with a loading rate of 1.25 mm per minute. The soil samples for unstabilised and stabilised soil were prepared as per prescribed standard procedures and guidelines. The CBR test was performed on the soaked samples, and the CBR is the ratio of force per unit area required to penetrate into a soil mass with a circular plunger of 50 mm diameter at the rate of 1.25 mm/min. The CBR tests on unstabilised and stabilised soil for soaked conditions were carried out as per the guidelines prescribed in JTG-E40-2007. The specimens for the tests were prepared at the MDD and OMC of the mixtures. For soaked conditions, the specimens were soaked in water for 96 h prior to testing [39]. The CBR value of unstabilised and stabilised soil was obtained by dividing the loads and the corresponding forces to achieve 2.5 and 5 mm penetration to the standard loads of 1370 and 2055 kg, respectively. The associated CBR values (%) were subsequently determined.

2.3.6. Microstructure Analysis. As a final task in this study, scanning electron microscopy (SEM) and energy dispersive X-ray (EDX) analyses were performed to compare the microstructures of the unstabilised and stabilised test specimens. These methods are widely used to identify and characterise microstructures, particle sizes, and chemical compositions in a broad range of current research practices.

3. Results and Discussion

3.1. Photoelectric Liquid - Plastic Limit. As indicators of photoelectric liquid-plastic limit, Figure 4 shows the *WL*, *PL*, and *PI* of the unstabilised and stabilised test specimens. As the PF content increased, its *WL* and *PL* decreased and then increased while the *PI* decreased. The observed decrease in the *WL* and *PL* when PF is first introduced in the soil could be attributed to the effect of the resulting interlocking and friction between the PF and soil particles. The *WL* of the untreated soil was 67%, which decreased 4.8% to 62.20% at 3% PF. Similarly, the *PI* of the unstabilised soil was 30.01%, which then decreased 7.03% to 22.98%. The observed increase in the *WL* of the stabilised soil can be attributed to the replacement of soil grains by PF. The PF-stabilised soil maintains more material continuity than the unstabilised soil, and the PF does not absorb moisture. The observed increase in *WL* with PF content is likely also due to the fact that the type of mixture, the relative amount of clay mineral, and the consistency limits of the mixture changed. It is clear that an addition of PF was sufficient to enhance the workability of the soil by reducing the *PI*. Mishra and Gupta [55] also confirmed that the *PI* decreased when the (PET) fibre in combination with the fly ash increased.

3.2. Soil Compaction. To investigate the compaction potential of the soils, the MDD and OMC of the unstabilised and stabilised soils were determined with the results depicted in Figure 5. Increasing the PF content caused a corresponding increase in the MDD and decrease in the OMC. Comparing the unstabilised (0% PF) and stabilised (3% PF) clay soils,

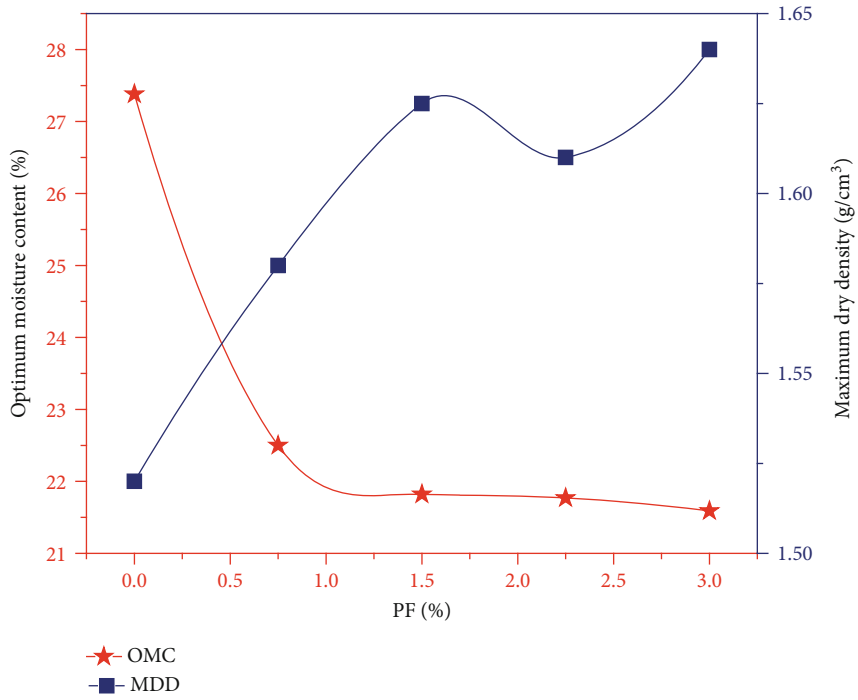

Figure 5: Maximum dry density (MDD) and optimum moisture content (OMC) for unstabilised and PF-stabilised soils.

the MDD increased 7.9% from 1.52 g/cm^3 to 1.64 g/cm^3, whereas the OMC decreased 5.8% from 27.4% to 21.6%. As PF has a lower OMC than the clay soil particles, increasing the PF content reduces the overall OMC of the combined system. Notably, the observed increase in MDD may be due to a decrease in the interstitial voids in the PF-stabilised soil. The small decrease in MDD for a PF content of 2.25% may be due to the presence of overlapping PF in the matrix, which creates pockets of low density. This may also due to the replacement of a certain quantity of compacted soil by an equivalent volume of PF, resulting in a loss of compaction efficiency due to the PF overlap. A previous report by Tran et al. [29] demonstrated that the length and content of soil matrix fibres have a significant effect on the MDD and OMC. Similar to the current study, an increase in fibre content was observed to lead to an increase in MDD and a decrease in OMC. These findings are consistent with results from previous studies by Yadav and Tiwari [39].

3.3. Triaxial Compressive Test. The triaxial compressive test results for the unstabilised and PF-stabilised soils were analysed to determine the angle of internal friction (Φ) and cohesion coefficient (c) shear strength parameters, with the results shown in Figure 6. Clearly, the PF improved the angle of internal friction and cohesion of the stabilised soil. The optimal PF content was 3%, at which these samples exhibited the maximum angle of internal friction and lowest cohesion coefficient. As the PF stabilisation enhanced the interlocking between soil particles, the angle of internal friction of PF stabilised soil increases. A reasonable explanation for the observed temporary decrease in the angle of internal friction is that the PF present in the matrix stuck together to the form lumps that created pockets of low density in the matrix, or because large pores otherwise formed in the fibre–soil matrix. These findings are consistent with previously reported results [12, 44, 51, 56].

3.4. Consolidation. An important concept was proposed by Zeng et al. [57], in which compressibility, shear resistance, and hydraulic conductivity are considered to be interdependent and representative of the same physical phenomenon. Accordingly, in this study, a consolidation test utilizing a modified oedometer provided data to analyses variations in compressibility and hydraulic conductivity while increasing the stress applied during compression. Previous studies on clay compressibility were used as guides to evaluate the clay void ratio. To study the consolidation potential, the void ratio (e) was obtained as a function of effective pressure (P, using a logarithmic scale) for the unstabilised and stabilised soils; the results are depicted in Figure 7. The stabilised soil specimens had consistently lower void ratios than the unstabilised soil specimen: the void ratio markedly decreased from 0.96 to 0.86 (0% PF) and from 0.93 to 0.73 (3% PF). This decrease can be attributed to low porosity and interlocking and friction between the PF and soil. Phanikumar and Singla [23], previously demonstrated that unreinforced expansive clay soils from Amalapuram, AP, India, attained the highest equilibrium void ratio and that the fibre-reinforced expansive clays attained lower equilibrium void ratios upon saturation by inundation. Fibre-reinforcement of the expansive clay specimens induces an interlocking effect and a friction effect, resulting in a further decrease in the equilibrium void ratio. The same phenomenon was reported by Zeng et al. [57] where the $e - logP$ compression curves of undisturbed soils generally lie above the remoulded specimen curves.

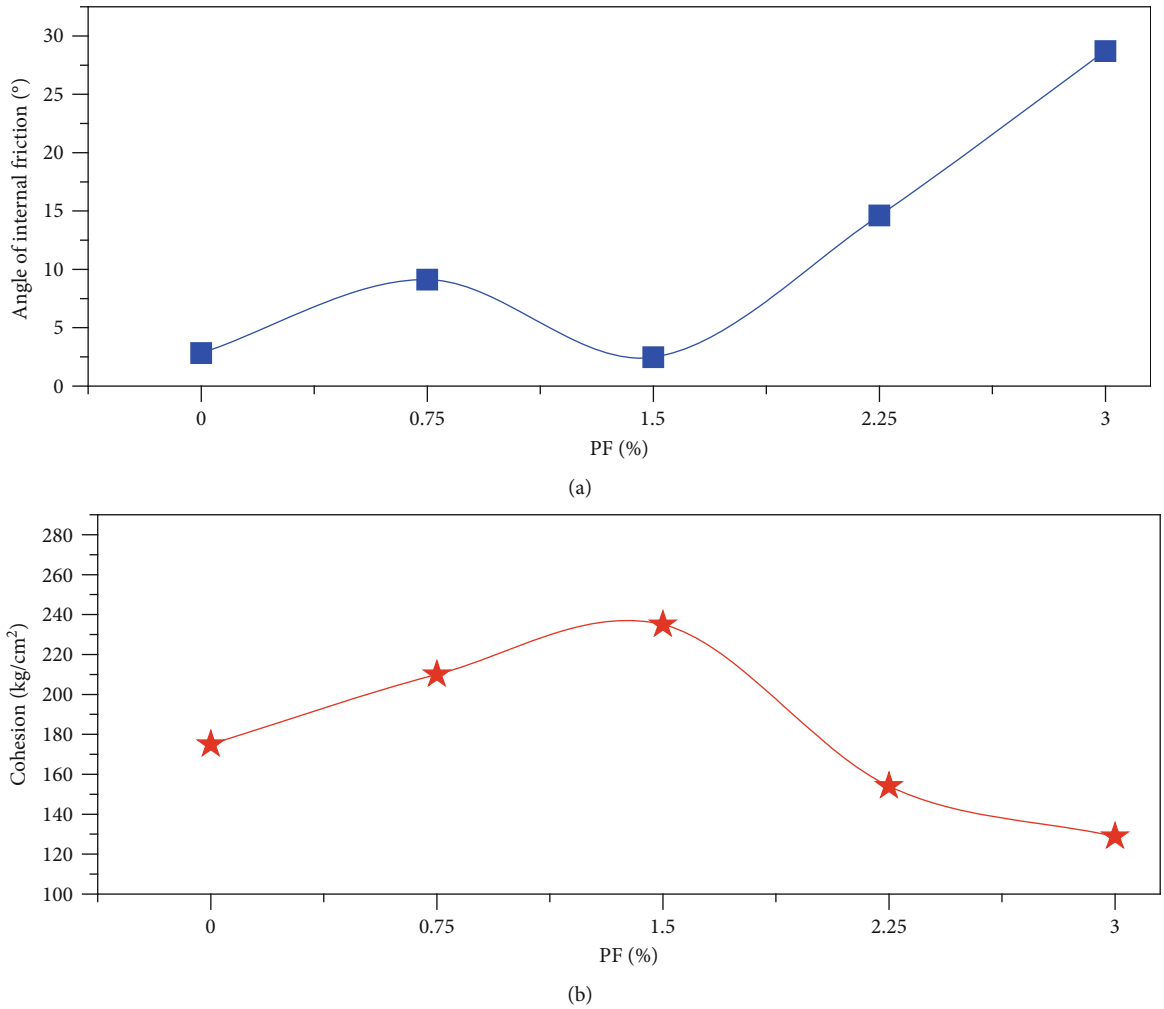

Figure 6: Relationship between PF content and shear strength parameters (a) angle of internal friction and (b) cohesion.

Based on the void ratio values in Figure 7, the rate of consolidation using the consolidation coefficient was determined. Figure 8 shows the consolidation coefficient (Cv) as a function of effective pressure (P, using a logarithmic scale) for the unstabilised and stabilised soil specimens. As the PF content increased, the Cv decreased. Over the range of effective pressures studied, the Cv values ranged from 2.52 to 1.71 cm^2/s for the unstabilised (0% PF) clay soil and from 2.34 to 1.40 cm^2/s for the stabilised (3% PF) clay soil. This decrease in Cv can be attributed to the initial clay soil conditions (e.g., water content or void ratio), the formation of a torsional flow path in the clay soil, or the clay soil inherent properties (e.g., specific gravity, grain size distribution, or mineral composition). Khan and Azam [43] also confirmed that the Cv behaviour of clay slurries decreased with an increase in effective pressure but increased with increasing e values.

Similar to the $e - \log P$ compression curves, the $k - e$ curves of the clays, shown in Figure 9, indicate that the vertical hydraulic conductivity (k) of the unstabilised soil specimens was higher than that of stabilised soil specimens for the same (e) value. The hydraulic conductivity was measured throughout the test up to the applied pressure reached 800 kPa. The hydraulic conductivity was observed to increase with the increasing void ratio and decrease with increasing PF content, in a manner consistent with the previously observed trends of the void ratio and consolidation coefficient. Within the range of void ratios studied, the hydraulic conductivity decreased from its maximum values for a PF content of 0% (1.12 to 0.83 cm/s) to its minimum values for a PF content of 3% (1.02 to 0.53 cm/s). As noted previously, this reduction in hydraulic conductivity can be attributed to the interlock between soil particles and the PF surface. These findings are consistent with results from some previous studies [57, 58]. However, the FM fibre type and a fibre content of 0.6% were found to increase the hydraulic conductivity compared with the FC fibre type and 0.2% fibre content [59]. Divya et al. [60] studied the hydraulic conductivity of soil with different fibre types, dosages, and lengths, finding that shorter fibres and lower fibre contents decreased the hydraulic conductivity of the soil.

3.5. California Bearing Ratio. The CBR testing was performed on 4-day soaked samples and the results for the unstabilised and PF-stabilised soils are plotted in Figure 10. The results indicate that the addition of PF increases the

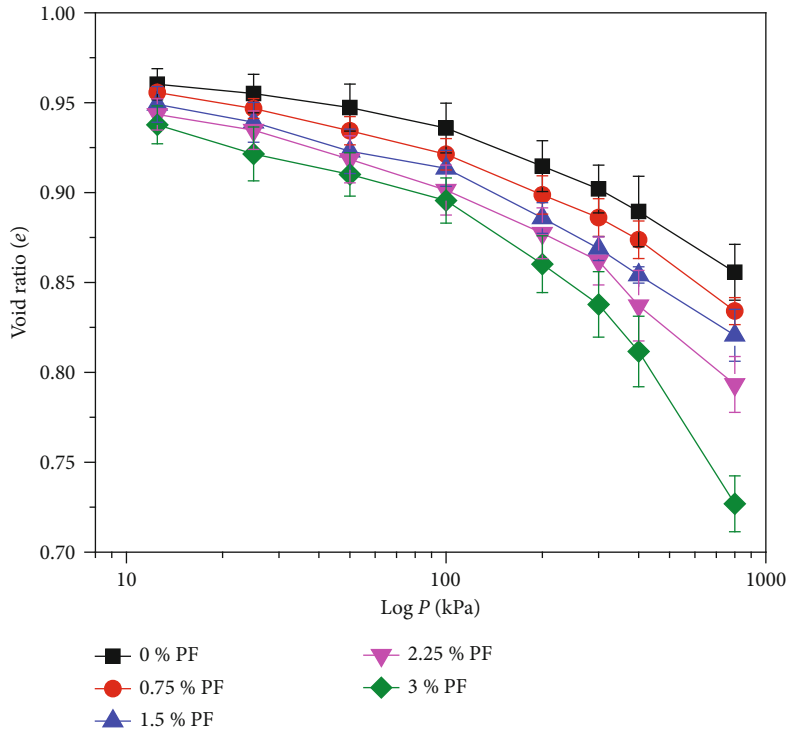

Figure 7: Void ratio (e) and log P values for unstabilised and PF-stabilised soils.

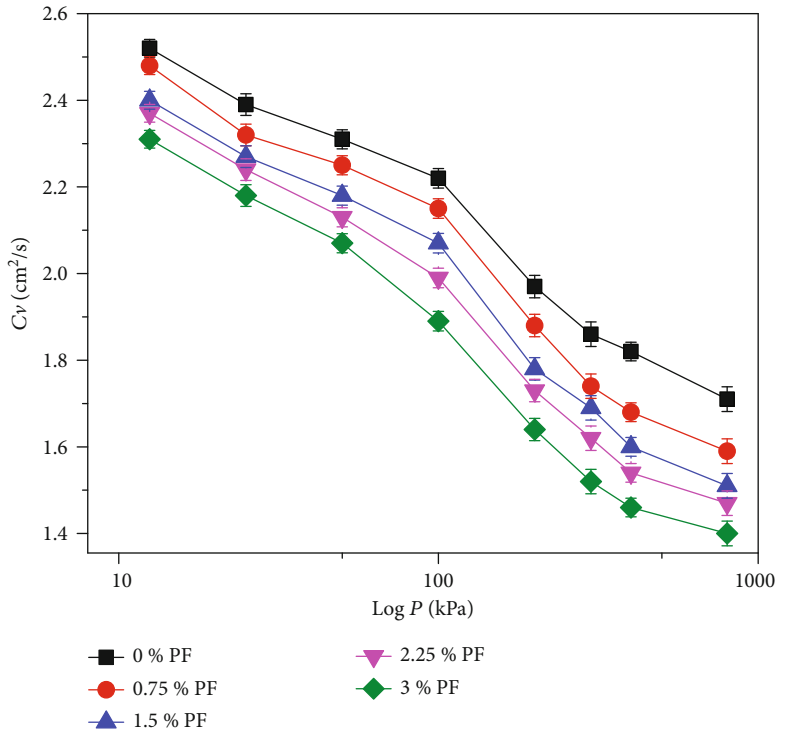

Figure 8: Coefficient of consolidation (Cv) for unstabilised and PF-stabilised soils.

CBR, which is indicative of an improvement in soil strength. The highest CBR was observed for PF contents of 3% by weight of soil. This is due to the fact that a higher PF content increases the interfaces between the fibres and the particles of the soil, so that greater friction is mobilised in the form of cohesion, assisted by the rough micro surface texture of the PF. This finding is similar to other recent results in which the addition of fibres was

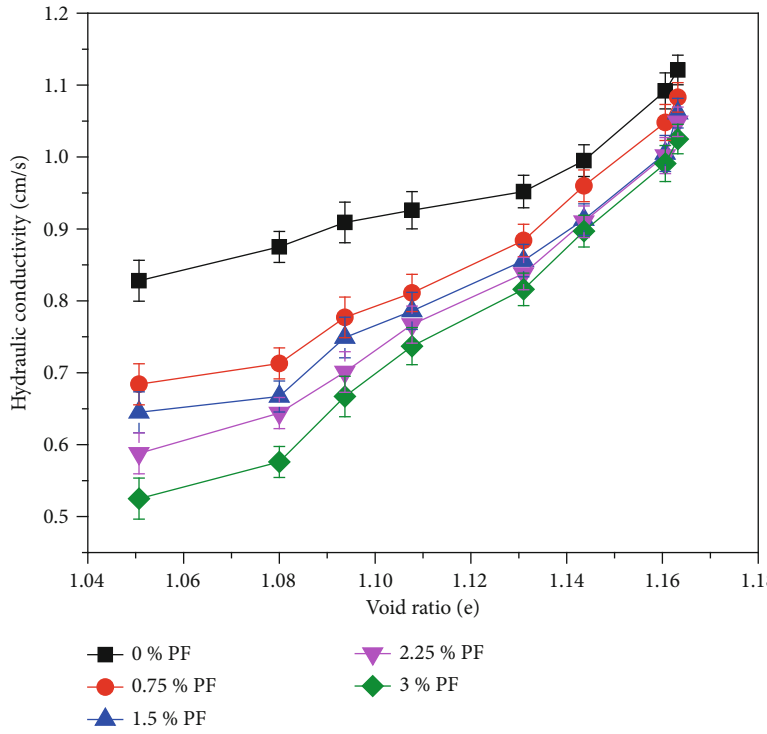

Figure 9: Hydraulic conductivity and void ratio relationship.

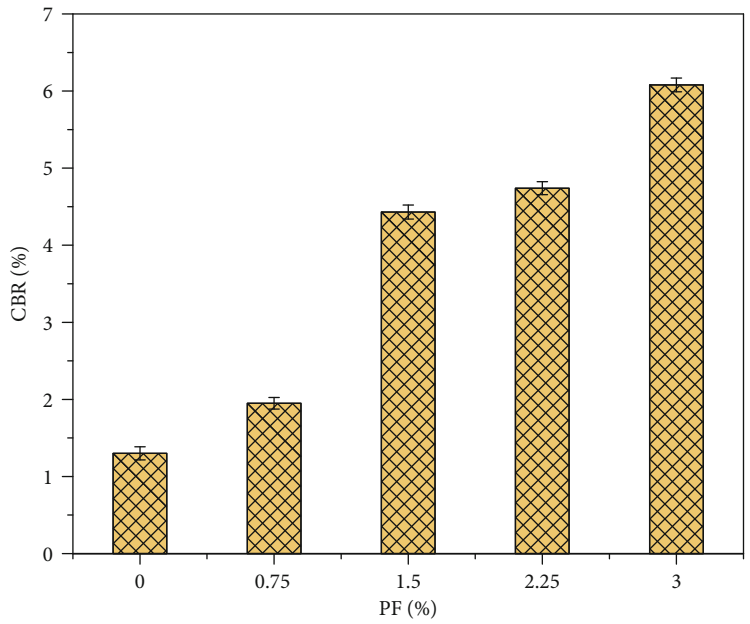

Figure 10: Effect of PF content on CBR value.

observed to increase the CBR in a variety of clays [9, 39, 40]. Moghal et al. [40] used two different types of synthetic fibres (FC and FM) in different quantities and lengths to determine the effects on the CBR. They determined that the CBR value increased with higher fibre contents and longer fibre lengths, and that this effect was most notable when lime was used as a stabiliser. Notably, IRC: 37-2011 states the thickness of pavements under a given traffic loading condition can be decreased as the CBR value increases. Consequently, the incorporation of fibre-reinforcement in soils could ultimately result in substantial cost savings when constructing roads on poor soils due to the potential reduction in the total required thickness of the road surface under selected traffic loads [55].

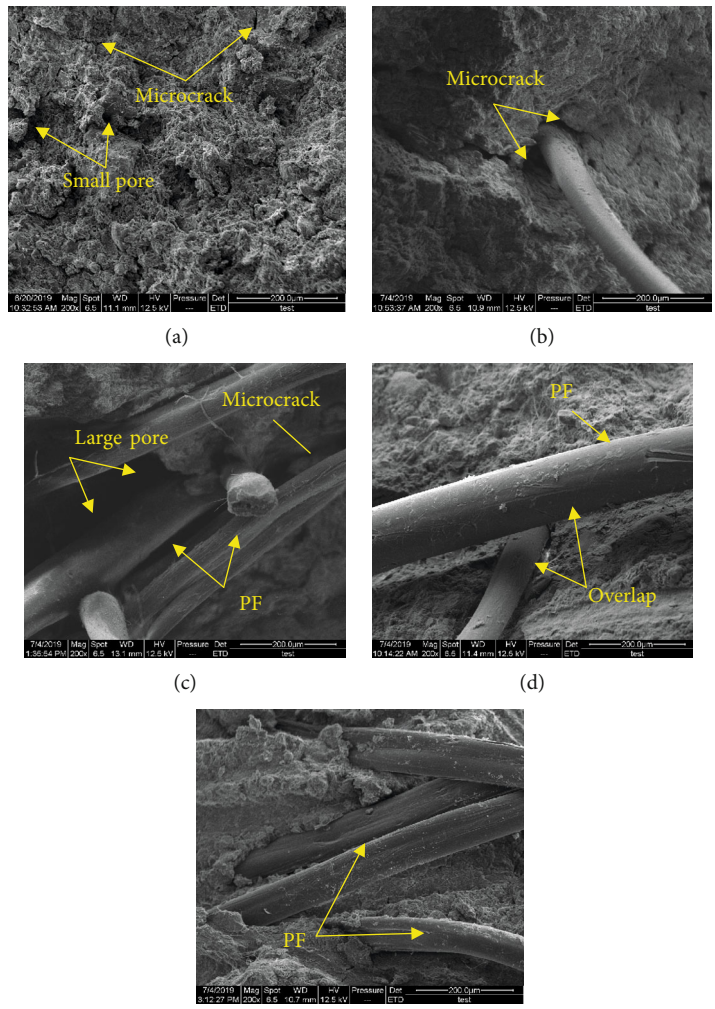

Figure 11: SEM images of (a) untreated soil, (b) soil with 0.75% PF, (c) soil with 1.5% PF, (d) soil with 2.25% PF, and (e) soil with 3% PF.

3.6. Microstructure Analysis. The microstructures of the unstabilised and stabilised test specimens were compared using the results of the SEM and EDX analyses shown in Figures 11 and 12, respectively. The SEM images show distinct microstructural differences between the unstabilised (Figure 11(a)) and stabilised (Figures 11(b)–11(e)) clay soils. The bond between the soil and PF, which is responsible for the observed improvements in the strength and stability of the soil, can be seen in the microstructural phase of the specimens with different PF contents in Figures 11(b), 11(d), and 11(e). Note that a gap can be observed at the interface between the soil and PF specimen in Figure 11(c): this large pore and other microcracks in the soil and on the PF surface may be responsible for the low matrix density reported in section 3.3. This supports the idea that the observed decrease in the angle of internal friction and cohesion was due to the weak interfacial interaction between PF and soil, causing the PF in the matrix to stick together and form lumps that caused pockets of low density in the matrix. Similarly, the effects of this weak interfacial interaction between the soil and PF and overlapping of PF can be seen in Figure 11(d), and may be responsible for the observations in section 3.2.

The EDX analysis results (Figure 12) show a few distinct differences between the chemical compositions of the unstabilised and stabilised clay soils. The PF itself contained varying amounts of O, C, Na, Mg, Al, Si, K, Ca, and Fe. The 1.5% PF-stabilised test specimen in Figure 12(c) accordingly shows higher contents of Ca, Al, and O but a lower content of C than in the unstabilised specimens; this variation is likely due to replacement of soil particles by PF. The increase in Ca results in a more brittle soil system behaviour. This may be responsible for the observed low matrix density in section 3.3, as brittle soil would make the PF present in the matrix more likely to stick together and form lumps, causing pockets of low density.

4. Conclusions

In this study, the effects of PF content on the geotechnical properties of a clay soil were investigated using a series of

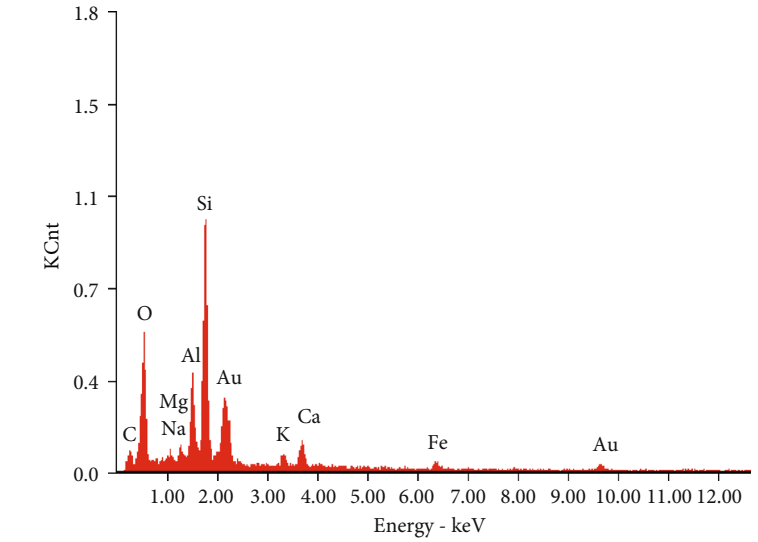

(a)

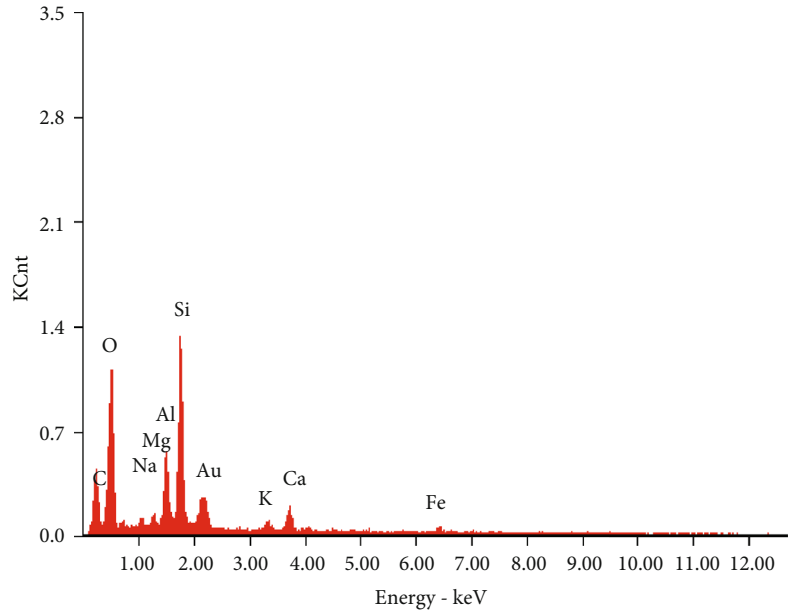

(b)

Figure 12: Continued.

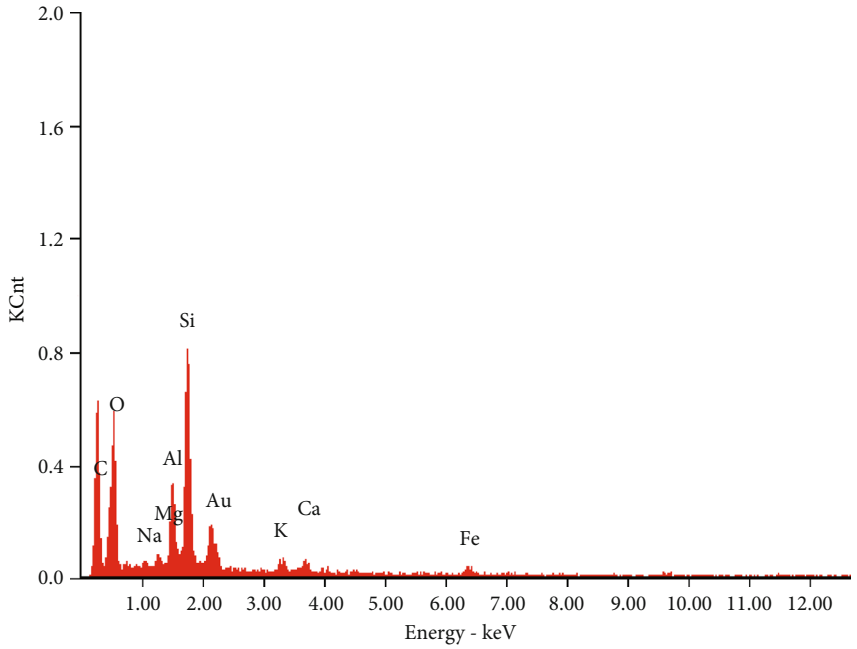

(c)

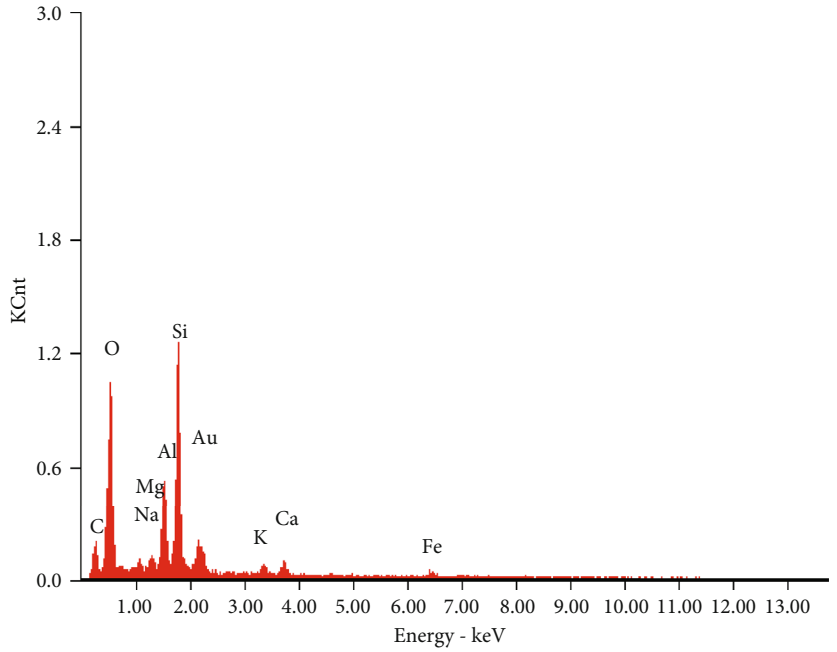

(d)

Figure 12: Continued.

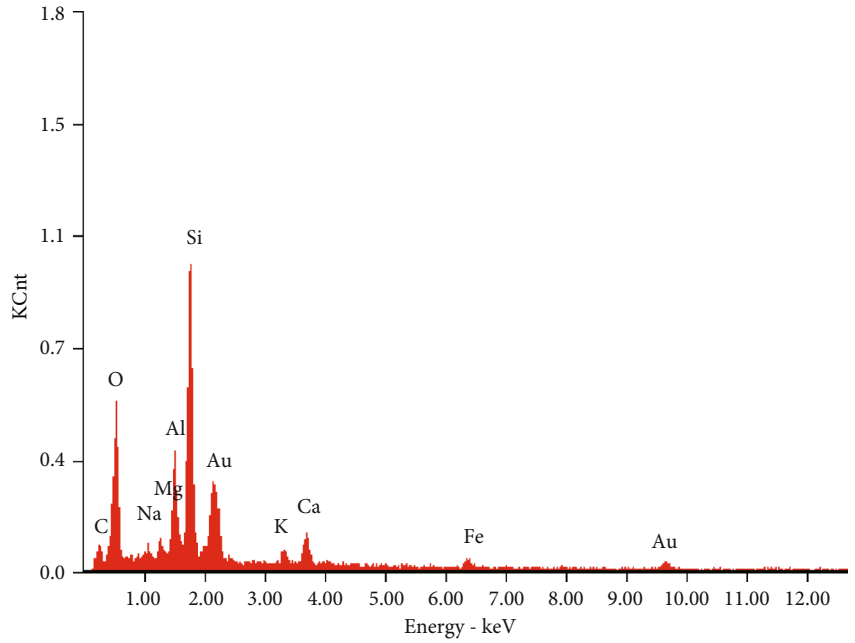

Figure 12: EDX spectra of (a) untreated soil, (b) soil with 0.75% PF, (c) soil with 1.5% PF, (d) soil with 2.25% PF, and (e) soil with 3% PF.

laboratory tests to determine the compaction, shear strength, consolidation, bearing resistance, and microstructure of soil specimens stabilised with 0%, 0.75%, 1.5%, 2.25%, and 3% PF. The key findings from this study are as follows:

(i) As the PF content increased, the PI decreased. The decreased in PI improved the stability and workability of the soil

(ii) As the PF content of the clay soil increased, its MDD increased and its OMC decreased, indicating improved compaction

(iii) As the PF content of the clay soil increased, its angle of internal friction (Φ) increased and its cohesion coefficient (c) decreased, indicating improved shear strength. The maximum angle of internal friction and minimum cohesion coefficient were obtained with a 3% PF content

(iv) As the PF content of the clay soil increased, its void ratio, consolidation coefficient, and hydraulic conductivity all decreased, indicating improved consolidation

(v) As the PF content of the clay soil increased, its CBR increased

(vi) Finally, distinct microstructural differences observed between the unstabilised and stabilised clay soils suggest that the addition of PF alters the soil microstructure by creating bonds between the soil and PF to improve its overall stability

The findings of this study demonstrate the potential for the use of PF as part of a soil stabilising technique. This is expected to contribute to the development of effective, codified methods to improve the safety and stability of such soils and thus the engineering structures built atop them.

Data Availability

The data used to support the findings of this study are available from the corresponding author upon request.

Conflicts of Interest

No conflict of interest was reported by the authors.

Acknowledgments

We gratefully acknowledge the financial support for this research from the Civil Engineering Department of Northeast Forestry University, Harbin, PR. China.

References

[1] A. Sezer, G. İnan, H. R. Yılmaz, and K. Ramyar, "Utilization of a very high lime fly ash for improvement of Izmir clay," *Building and Environment*, vol. 41, no. 2, pp. 150–155, 2006.

[2] M. Al-Mukhtar, S. Khattab, and J.-F. Alcover, "Microstructure and geotechnical properties of lime-treated expansive clayey soil," *Engineering Geology*, vol. 139-140, pp. 17–27, 2012.

[3] M. A. Lav and A. H. Lav, "Effects of stabilization on resilient characteristics of fly ash as pavement material," *Construction and Building Materials*, vol. 54, pp. 10–16, 2014.

[4] E. Garzón, M. Cano, B. C. O'Kelly, and P. J. Sánchez-Soto, "Phyllite clay–cement composites having improved engineering properties and material applications," *Applied Clay Science*, vol. 114, pp. 229–233, 2015.

[5] Y. Yilmaz, "Compaction and strength characteristics of fly ash and fiber amended clayey soil," *Engineering Geology*, vol. 188, pp. 168–177, 2015.

[6] A. Al-Swaidani, I. Hammoud, and A. Meziab, "Effect of adding natural pozzolana on geotechnical properties of lime- stabilized clayey soil," *Journal of Rock Mechanics and Geotechnical Engineering*, vol. 8, no. 5, pp. 714–725, 2016.

[7] E. Garzón, M. Cano, B. C. O`Kelly, and P. J. Sánchez-Soto, "Effect of lime on stabilization of phyllite clays," *Applied Clay Science*, vol. 123, pp. 329–334, 2016.

[8] S. T. Gilazghi, J. Huang, S. Rezaeimalek, and S. Bin-Shafique, "Stabilizing sulfate-rich high plasticity clay with moisture activated polymerization," *Engineering Geology*, vol. 211, pp. 171–178, 2016.

[9] J. S. Yadav and S. K. Tiwari, "A study on the potential utilization of crumb rubber in cement treated soft clay," *Journal of Building Engineering*, vol. 9, pp. 177–191, 2017.

[10] H. Ali and M. Mohamed, "The effects of lime content and environmental temperature on the mechanical and hydraulic properties of extremely high plastic clays," *Applied Clay Science*, vol. 161, pp. 203–210, 2018.

[11] J. P. Temga, A. B. Madi, S. B. Djakba et al., "Lime – and sand – stabilization of clayey materials from the Logone valley (Lake Chad basin) for their utilisation as building materials," *Journal of Building Engineering*, vol. 19, pp. 472–479, 2018.

[12] L. Wei, S. X. Chai, H. Y. Zhang, and Q. Shi, "Mechanical properties of soil reinforced with both lime and four kinds of fiber," *Construction and Building Materials*, vol. 172, pp. 300–308, 2018.

[13] S. Islam, N. M. R. Hoque, M. A. Haque, P. N. Mishra, M. M. H. Mamun, and S. Dey, "Strength development in fine-grained paddy field soil by lime addition," *Journal of Building Engineering*, vol. 26, article 100857, 2019.

[14] H. Güllü and A. Khudir, "Effect of freeze–thaw cycles on unconfined compressive strength of fine- grained soil treated with jute fiber, steel fiber and lime," *Cold Regions Science and Technology*, vol. 106-107, pp. 55–65, 2014.

[15] A. Boz and A. Sezer, "Influence of fiber type and content on freeze-thaw resistance of fiber reinforced lime stabilized clay," *Cold Regions Science and Technology*, vol. 151, pp. 359–366, 2018.

[16] M. Ding, F. Zhang, X. Ling, and B. Lin, "Effects of freeze-thaw cycles on mechanical properties of polypropylene fiber and cement stabilized clay," *Cold Regions Science and Technology*, vol. 154, pp. 155–165, 2018.

[17] E. Kravchenko, J. Liu, W. Niu, and S. Zhang, "Performance of clay soil reinforced with fibers subjected to freeze-thaw cycles," *Cold Regions Science and Technology*, vol. 153, pp. 18–24, 2018.

[18] Y. L. Xiong, G. B. Liu, R. Y. Zheng, and X. H. Bao, "Study on dynamic undrained mechanical behavior of saturated soft clay considering temperature effect," *Soil Dynamics and Earthquake Engineering*, vol. 115, pp. 673–684, 2018.

[19] Z. Sun and Q. Xu, "Microscopic, physical and mechanical analysis of polypropylene fiber reinforced concrete," *Materials Science and Engineering: A*, vol. 527, no. 1-2, pp. 198–204, 2009.

[20] S. N. Monteiro, V. Calado, R. J. S. Rodriguez, and F. M. Margem, "Thermogravimetric behavior of natural fibers reinforced polymer composites—an overview," *Materials Science and Engineering: A*, vol. 557, pp. 17–28, 2012.

[21] R. Noorzad and P. F. Amini, "Liquefaction resistance of Babolsar sand reinforced with randomly distributed fibers under cyclic loading," *Soil Dynamics and Earthquake Engineering*, vol. 66, pp. 281–292, 2014.

[22] A. A. S. Correia, P. J. Venda Oliveira, and D. G. Custódio, "Effect of polypropylene fibres on the compressive and tensile strength of a soft soil, artificially stabilised with binders," *Geotextiles and Geomembranes*, vol. 43, no. 2, pp. 97–106, 2015.

[23] B. R. Phanikumar and R. Singla, "Swell-consolidation characteristics of fibre-reinforced expansive soils," *Soils and Foundations*, vol. 56, no. 1, pp. 138–143, 2016.

[24] J. S. Yadav and S. K. Tiwari, "Behaviour of cement stabilized treated coir fibre-reinforced clay-pond ash mixtures," *Journal of Building Engineering*, vol. 8, pp. 131–140, 2016.

[25] S. Bordoloi, R. Hussain, A. Garg, S. Sreedeep, and W. H. Zhou, "Infiltration characteristics of natural fiber reinforced soil," *Transportation Geotechnics*, vol. 12, pp. 37–44, 2017.

[26] S. Orasutthikul, D. Unno, and H. Yokota, "Effectiveness of recycled nylon fiber from waste fishing net with respect to fiber reinforced mortar," *Construction and Building Materials*, vol. 146, pp. 594–602, 2017.

[27] A. A. Diab, S. S. Najjar, S. Sadek, H. Taha, H. Jaffal, and M. Alahmad, "Effect of compaction method on the undrained strength of fiber-reinforced clay," *Soils and Foundations*, vol. 58, no. 2, pp. 462–480, 2018.

[28] P. F. Amini and R. Noorzad, "Energy-based evaluation of liquefaction of fiber-reinforced sand using cyclic triaxial testing," *Soil Dynamics and Earthquake Engineering*, vol. 104, pp. 45–53, 2018.

[29] K. Q. Tran, T. Satomi, and H. Takahashi, "Effect of waste cornsilk fiber reinforcement on mechanical properties of soft soils," *Transportation Geotechnics*, vol. 16, pp. 76–84, 2018.

[30] P. J. V. Oliveira, A. A. S. Correia, and J. C. A. Cajada, "Effect of the type of soil on the cyclic behaviour of chemically stabilised soils unreinforced and reinforced with polypropylene fibres," *Soil Dynamics and Earthquake Engineering*, vol. 115, pp. 336–343, 2018.

[31] M. Bekhiti, H. Trouzine, and M. Rabehi, "Influence of waste tire rubber fibers on swelling behavior, unconfined compressive strength and ductility of cement stabilized bentonite clay soil," *Construction and Building Materials*, vol. 208, pp. 304–313, 2019.

[32] N. Esmaeilpour Shirvani, A. Taghavi Ghalesari, M. K. Tabari, and A. J. Choobbasti, "Improvement of the engineering behavior of sand-clay mixtures using kenaf fiber reinforcement," *Transportation Geotechnics*, vol. 19, pp. 1–8, 2019.

[33] K. Q. Tran, T. Satomi, and H. Takahashi, "Tensile behaviors of natural fiber and cement reinforced soil subjected to direct tensile test," *Journal of Building Engineering*, vol. 24, article 100748, 2019.

[34] A. Ateş, "Mechanical properties of sandy soils reinforced with cement and randomly distributed glass fibers (GRC)," *Composites Part B: Engineering*, vol. 96, pp. 295–304, 2016.

[35] A. Kumar and D. Gupta, "Behavior of cement-stabilized fiber-reinforced pond ash, rice husk ash–soil mixtures," *Geotextiles and Geomembranes*, vol. 44, no. 3, pp. 466–474, 2016.

[36] P. Jamsawang, H. Poorahong, N. Yoobanpot, S. Songpiriyakij, and P. Jongpradist, "Improvement of soft clay with cement and bagasse ash waste," *Construction and Building Materials*, vol. 154, pp. 61–71, 2017.

[37] A. A. B. Moghal, B. C. S. Chittoori, B. M. Basha, and M. A. al-Shamrani, "Target reliability approach to study the effect of fiber reinforcement on UCS behavior of lime treated semiarid soil," *Journal of Materials in Civil Engineering*, vol. 29, no. 6, article 04017014, 2017.

[38] A. J. Puppala and C. Musenda, "Effects of fiber reinforcement on strength and volume change in expansive soils," *Transportation Research Record*, vol. 1736, no. 1, pp. 134–140, 2000.

[39] J. S. Yadav and S. K. Tiwari, "Effect of waste rubber fibres on the geotechnical properties of clay stabilized with cement," *Applied Clay Science*, vol. 149, pp. 97–110, 2017.

[40] A. A. B. Moghal, B. C. S. Chittoori, and B. M. Basha, "Effect of fibre reinforcement on CBR behaviour of lime-blended expansive soils: reliability approach," *Road Materials and Pavement Design*, vol. 19, no. 3, pp. 690–709, 2018.

[41] N. M. Al-Akhras, M. F. Attom, K. M. Al-Akhras, and A. I. H. Malkawi, "Influence of fibers on swelling properties of clayey soil," *Geosynthetics International*, vol. 15, no. 4, pp. 304–309, 2008.

[42] A. A. B. Moghal, B. C. S. Chittoori, B. M. Basha, and A. M. Al-Mahbashi, "Effect of polypropylene fibre reinforcement on the consolidation, swell and shrinkage behaviour of lime-blended expansive soil," *International Journal of Geotechnical Engineering*, vol. 12, no. 5, pp. 462–471, 2017.

[43] F. S. Khan and S. Azam, "Determination of consolidation behaviour of clay slurries," *International Journal of Mining Science and Technology*, vol. 26, no. 2, pp. 277–283, 2016.

[44] H. Cui, Z. Jin, X. Bao, W. Tang, and B. Dong, "Effect of carbon fiber and nanosilica on shear properties of silty soil and the mechanisms," *Construction and Building Materials*, vol. 189, pp. 286–295, 2018.

[45] *ASTM D 854-02: Standard test method for specific gravity of soil solids by water pycnometer*, American Society for Testing and Materials, West Conshohocken, PA, 2006.

[46] *ASTM D 422-63: Standard test method for particle-size analysis of soils*, American Society for Testing and Materials, West Conshohocken, PA, 2006.

[47] *ASTM D 4318-00: Standard test methods for liquid limit, plastic limit, and plasticity index of soils*, American Society for Testing and Materials, West Conshohocken, PA, 2006.

[48] ASTM, *D2487-00: Standard Practice for Classification of Soils for Engineering Purposes (Unified Soil Classification System)*, American Society for Testing and Materials, West Conshohocken, PA, 2006.

[49] *ASTM D 698-00a: Standard test methods for laboratory compaction characteristics of soil using standard effort (12, 400 ft-lbf/ft^3 (600 kN-m/m^3))*, American Society for Testing and Materials, West Conshohocken, PA, 2006.

[50] *ASTM D 2850-03a: Standard test method for unconsolidated–undrained triaxial compression test on cohesive soils*, American Society for Testing and Materials, West Conshohocken, PA, 2006.

[51] C. Tang, B. Shi, W. Gao, F. Chen, and Y. Cai, "Strength and mechanical behavior of short polypropylene fiber reinforced and cement stabilized clayey soil," *Geotextiles and Geomembranes*, vol. 25, no. 3, pp. 194–202, 2007.

[52] J. S. Yadav, S. K. Tiwari, and P. Shekhwat, "Strength behaviour of clayey soil mixed with pond ash, cement and randomly distributed fibres," *Transportation Infrastructure Geotechnology*, vol. 5, no. 3, pp. 191–209, 2018.

[53] *GB/T 50123-1999 Standard for Soil Test Method*, Standardization Administration of China, Beijing, 1999.

[54] *JTG E40-2007 Test Methods of Soils for Highway Engineering*, Ministry of Transportation, Beijing, China, 2007.

[55] B. Mishra and M. K. Gupta, "Use of randomly oriented polyethylene terephthalate (PET) fiber in combination with fly ash in subgrade of flexible pavement," *Construction and Building Materials*, vol. 190, pp. 95–107, 2018.

[56] F. Changizi and A. Haddad, "Strength properties of soft clay treated with mixture of nano-SiO_2 and recycled polyester fiber," *Journal of Rock Mechanics and Geotechnical Engineering*, vol. 7, no. 4, pp. 367–378, 2015.

[57] L. L. Zeng, Z. S. Hong, Y. Q. Cai, and J. Han, "Change of hydraulic conductivity during compression of undisturbed and remolded clays," *Applied Clay Science*, vol. 51, no. 1-2, pp. 86–93, 2011.

[58] K. S. Heineck, R. G. Lemos, J. A. A. Flores, and N. C. Consoli, "Influence of particle morphology on the hydraulic behavior of coal ash and sand," *Geotechnical and Geological Engineering*, vol. 28, no. 4, pp. 325–335, 2010.

[59] A. A. B. Moghal, B. M. Basha, B. Chittoori, and M. A. Al-Shamrani, *Effect of fiber reinforcement on the hydraulic conductivity behavior of lime-treated expansive soil—reliability-based optimization perspective*, vol. 263, ASCE Geotech Special Publication, 2016.

[60] P. V. Divya, B. V. S. Viswanadham, and J. P. Gourc, "Hydraulic conductivity behaviour of soil blended with geofiber inclusions," *Geotextiles and Geomembranes*, vol. 46, no. 2, pp. 121–130, 2018.

Hindawi
Advances in Polymer Technology
Volume 2020, Article ID 8638076, 18 pages
https://doi.org/10.1155/2020/8638076

Research Article

Circumferential Expansion Property of Composite Wrapping System for Main Cable Protection of Suspension Bridge

Pengfei Cao,[1] Hai Fang,[1] Weiqing Liu,[1] Yong Zhuang,[2] Yuan Fang,[1] and Chenglin Li[1]

[1]*College of Civil Engineering, Nanjing Tech University, Nanjing 211816, China*
[2]*China Railway Major Bridge Reconnaissance & Design Institute Co. Ltd., Wuhan 430050, China*

Correspondence should be addressed to Hai Fang; fanghainjut@163.com

Received 6 October 2019; Accepted 2 April 2020; Published 5 May 2020

Guest Editor: Guangming Chen

A composite wrapping system for main cable protection of suspension bridges was designed by using prepreg fiber-reinforced composites and nitrile rubber. The circumferential expansion performance of the system was tested, and the curves of circumferential bearing capacity and radial displacement of the components were obtained. Failure modes of each group of components were compared and analyzed. The results show that most of the components are vertically fractured at the lap transition. The increase of the number of prepreg layers contributed the most to the circumferential bearing capacity of components, with a growth rate of 65.31%~109.01%. The increase of rubber belt layers had the most significant effect on the radial displacement of the components, with a growth rate of 7.06%~23.5%. In the initial stage of the test, the strain of each part of the component was smaller due to the compaction by the loading device, and the strain value of the component was generally linearly increased during the loading process, during which the strain of the overlap was the smallest. The calculated cross-sectional temperature deformation of the main cable is in good agreement with the experimental data. The application of the rubber belt increases the deformation of the main cable; therefore, the protection system for the main cable could have more deformation redundancy and delay the arrival of the ultimate strain of the outer prepreg wrap.

1. Introduction

With the rapid development of technology and the continuous improvement of material properties, modern suspension bridge [1], with its superior engineering structure [2], has become the preferred bridge type for the construction of long-distance bridges in the world. The main cable, sling, cable tower, floor system, and anchorage are five main structures of suspension bridges. According to different stiffness, suspension bridges are divided into two types [3], flexible suspension bridges and rigid suspension bridges. Flexible suspension bridge is a kind of low-load bridge with bridge decks directly laid on the suspended cable, which is mostly used for short-span bridges. Rigid suspension bridge is to lay the deck on the rigid beam; the rigid beam is suspended on the suspension cable through the suspension rod. Most modern suspension bridges are rigid suspension bridge, and Figure 1 is a general arrangement diagram of the second bridge of Yueyang Dongting Lake.

Among all structural components of a suspension bridge, main cables are the main supporting component of the entire bridge, and the service life of the main cable is accompanied by the full life cycle of the bridge. Corrosion of main cables on suspension bridge [4] is a nonnegligible problem on a worldwide basis. The corroded main cables are shown in Figure 2.

There have been some researches on the main cable protection system. The so-called Roebling system, created by John A Reobling [5] in the United States in the 1840s, is most widely used in traditional main cable protection systems. As shown in Figure 3, the sealing material is filled in the main cable wire and the putty is applied to the surface, then a wire of approximately 4 mm in diameter is wound along the main cable on the putty layer. Finally, the laminated coating [6] is homogeneously applied on the surface of the wound wire. The main purpose of this system is to seal the outer surface of the main cable to prevent and isolate the corrosion of the water, salt, and other corrosive

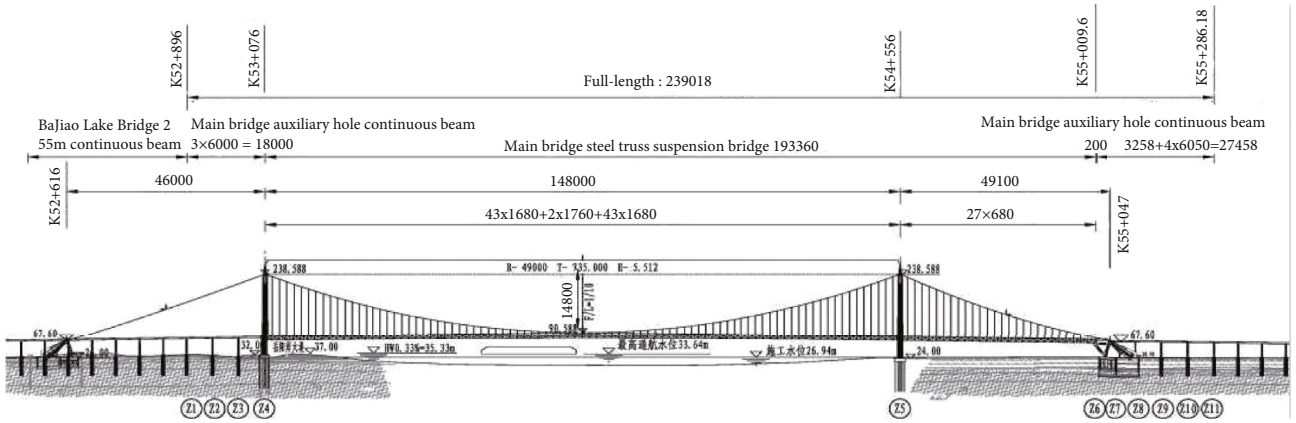

Figure 1: The general arrangement diagram of the second bridge of Yueyang Dongting Lake.

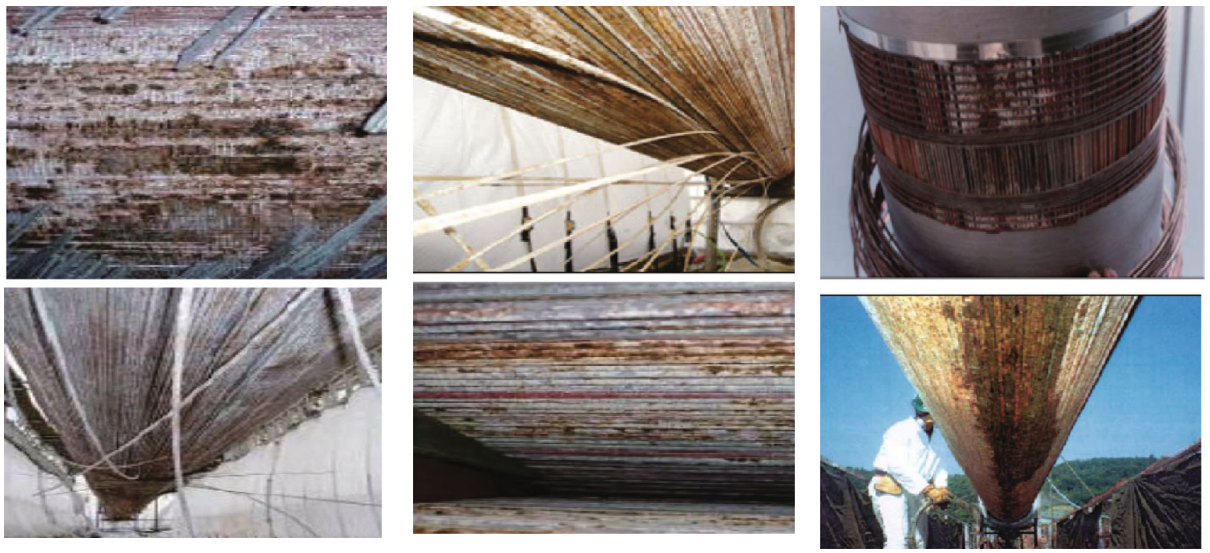

(a) (b) (c)

Figure 2: Corrosion of main cables on suspension bridge: (a) the Golden Gate Bridge, (b) Forth Road Bridge, and (c) Japan Dashima Bridge.

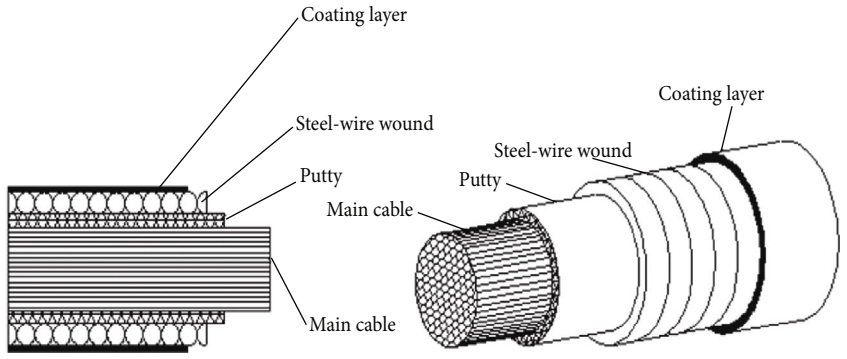

Figure 3: Schematic diagram of the Roebling system.

substances. However, the installation process of the system takes a long time from erection to completion; the aging and cracking phenomena will gradually appear in the coating layer. With the vibration of the suspension bridge, the length and the cross section of the main cable will be axially deformed at the same time. External coating is less elastic and easy to experience cracking, which leads to introduction of humid air.

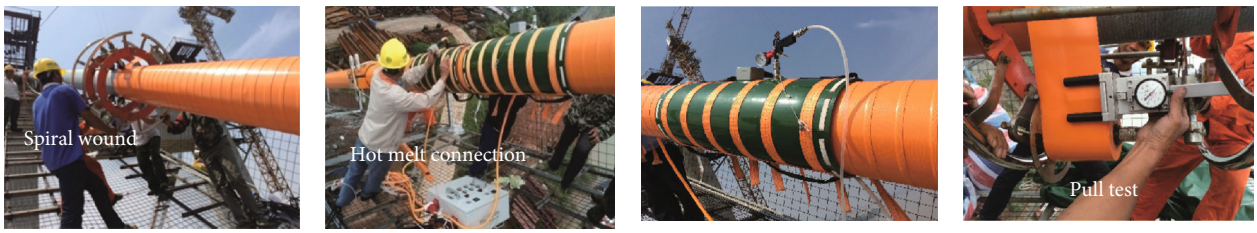

(a) (b) (c) (d)

Figure 4: The construction process of winding and heating pressure vulcanization.

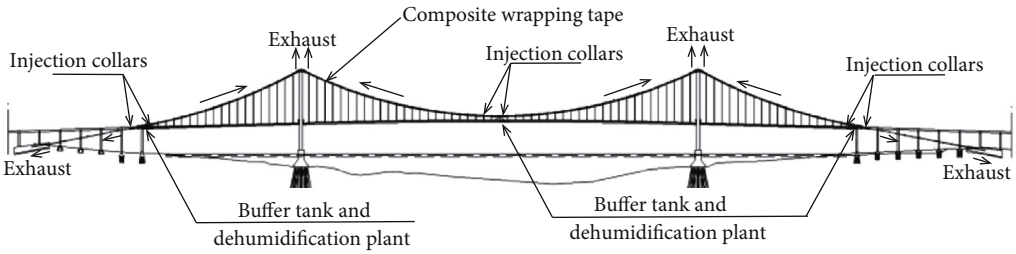

Figure 5: Principle of dehumidification and protection of the main cable.

Another protection system called synthetic sheath [7] was developed in the United States in the 1960s and 1970s to replace the Roebling system. The first layer of the protection system is wrapped with nylon belt on the main cable, then coated with binder on the nylon belt, finally wrapped with glass fiber polychloroprene rubber wrapping tape, polyester film, and polypropylene resin wrapping tape. Compared with the Roebling system, the construction process of the system is reduced. However, due to the instability of the early composite material performance, the technology is not mature enough. The effect of this protective system is not ideal, and it has not been widely used. In recent years, the fiber-reinforced composite wrapping tape structure was invented. It consists of unvulcanized chlorosulfonated polyethylene, fiber grid layout, and chlorosulfonated polyethylene. The matrix material of wrapping tape is chlorosulfonated polyethylene and the reinforcing material is fiber grid layout. This anticorrosion protection system of fiber-reinforced wrapping tape was first applied to Fengxi Bridge in Zhuzhou City, Hunan Province in China. Compared with the American Brown Wrap Belt, the elongation and tear strength have increased by 54% and 62%, respectively. Fiber-reinforced composite wrapping tape has excellent properties such as ageing resistance, easy maintenance, and replacement and gives full play to the remarkable advantages of lightweight, high strength, and corrosion resistance of fiber-reinforced composite materials. However, as shown in Figure 4, the biggest disadvantage of this system is that the installation process is cumbersome and complex.

Many examples have illustrated that the above two traditional protection systems for main cables cannot prevent corrosion basically, as such, a new system of corrosion management is necessary. A dehumidification system [8] was developed by Japan at the end of the 20th century. As shown in Figure 5, the main method of the system is to continuously fill the main cable with relatively dry air (humidity 40%-50%) and destroy the corrosion condition of the main cable so as to prevent the corrosion of the main cable steel wire. The cable dehumidification system was first applied to the Akashi Kaikyo Bridge [9], and it was understood that it had been performing adequately. Since then a small number of suspension bridges had been retrofitted with this system, and the majority of new bridges had been constructed with dehumidification installed as standard practice. The key to the dehumidification system was that the surface of the main cable could not be cracked; otherwise, it would seriously affect the dehumidification effect. On the other hand, the protection system needed to continuously provide dry air for the main cable throughout its life cycle, so the cost of the whole system was high.

There have been some researches on the influence of temperature field on the main cable. Taking Xihoumen Bridge as an example, it was found that under the effects of environmental factor, the cross-sectional temperature field of the main cable was obviously inhomogeneous. The temperature inside and outside the main cable had obvious phase difference, and the temperature amplitude was very different. For the suspension bridge with large-diameter main cable, even if the ambient temperature at night was relatively stable, there was a large difference between sectional weighted average temperature and superficial arithmetic mean temperature. The axial stress and average stress decrease with the increase of temperature, while the vertical moment increases with the increase of temperature. Under the effects of nonuniform temperature, the transverse moment of the main cable was produced, and the direction of the transverse moment pointed to the side with high temperature. So the main cable was deformed and damaged.

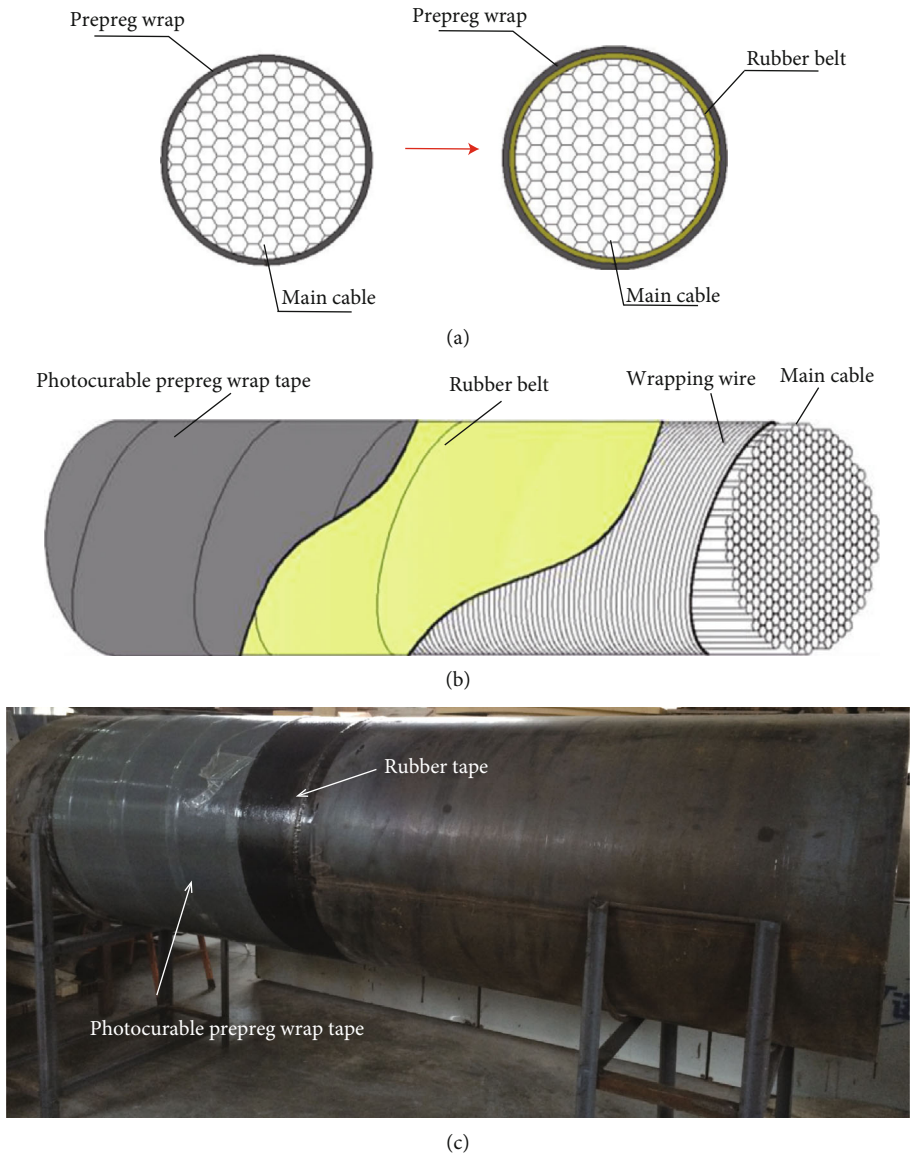

Figure 6: Schematic diagram of two samples: (a) section diagram of specimens, (b) structure diagram, and (c) actual diagram.

In view of the excellent protective performance and high corrosion resistance of FRP (Fiber-Reinforced Polymer) [10], sealing performance, and characteristics of reducing stress concentration of rubber material, this paper introduces the design and preparation process of the main cable protection system for the new suspension bridge using these two materials. This protection system needs to consider the influence of circumferential expansion of the main cable to protection system due to the external environment. This paper refers to the mechanical properties of FRP pipe under vertical compression of FRP-confined concrete members and uses this as a clue to study the mechanical properties of the main cable protection system under the action of internal circumferential expansion force, so as to guide the design of the new composite main cable protection system. Specimens were grouped, and circumferential expansion tests of specimens were carried out to study the different failure modes of specimens in each group. The circumferential bearing capacity-radial displacement curves and circumferential strain-radial displacement curves of components were obtained. The influences of the number of prepreg layers and rubber belt layers on the performance of the specimen were analyzed.

2. Experiment

2.1. Specimen Preparation. The sample materials were made of photocurable prepreg wrap tape and nitrile rubber belt. Specimens were divided into two types, as shown in Figure 6; one was a hoop specimen only made of photocurable prepreg wrap tape, and the other was a composite wrap tape made of photocurable prepreg wrap tape and nitrile rubber belt.

The first kind of specimens was divided into three groups; the first group was wrapped with 1-layer photocurable prepreg tape, the second group was wrapped with 2-layer

Table 1: Details of specimen.

Specimen	Layer of light-cured prepreg	Layer of elastic	Outer diameter (mm)	Inner diameter (mm)	Height (mm)	Number	FRP required (m^2)	Elastic layer required (m^2)
G-1-X	1	—	304	300	150	3	0.177	—
G-2-X	2	—	308	300	150	3	0.318	—
G-3-X	3	—	312	300	150	3	0.459	—
G-1-R-X	1	1	308	300	150	3	0.177	0.141
G-2-R-X	2	1	312	300	150	3	0.318	0.141
G-3-R-X	3	1	316	300	150	3	0.459	0.141
G-1-2R-1	1	2	312	300	150	1	0.177	0.282
G-2-2R-1	2	2	316	300	150	1	0.318	0.282
G-3-2R-1	3	2	318	300	150	1	0.459	0.282

G-1: a layer of photocurable prepreg FRP; R: a layer of elastic layer; 2R: two layers of elastic layer; X: the label of each component in a set of specimens.

photocurable prepreg tape, and the third group was wrapped with 3-layer photocurable prepreg tape.

The second kind of specimens was divided into four groups; the difference between the first three groups in the second kind and the first kind of specimens was that a 1-layer nitrile rubber tape was wrapped inside of the first kind of specimens. The fourth group of the second kind of specimens was internally wrapped with 2-layer nitrile rubber belt, and the outer layer was wrapped with 1-layer, 2-layer, and 3-layer photocurable prepreg tape, respectively.

The specifications of specimen are shown in Table 1. The overlap width of the prepreg tape was 235.5 mm. Both two kinds of specimen should be wound on the expansion device, and the prepreg tap needed to be hardened by ultraviolet illumination radiation for more than 40 minutes. Vaseline was applied to the surface of the expansion device before the specimens were made, then covered with a film to reduce the friction between specimens and the expansion device. Both two kinds of specimens were wound directly on the outer layer of the expansion device without angle. The inner nitrile rubber belt and the outer prepreg tape in the second kind of specimens had staggered lap joints. The nitrile rubber had two sides; one side was smooth and the other side was rough. In this paper, the rough surface of the nitrile rubber belt was used to bond with the prepreg wrap. After the surface was completely hardened, the strain gauges were attached to the corresponding position as shown in Figure 7.

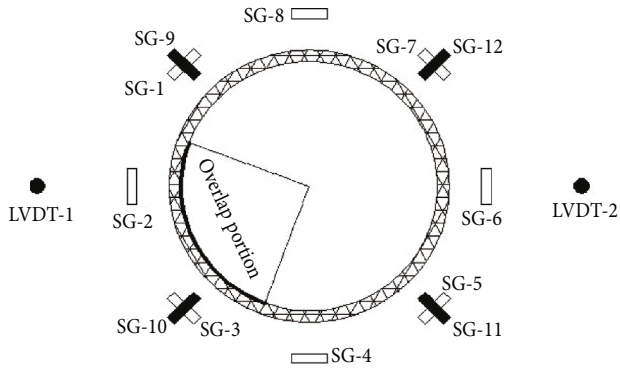

Figure 7: The position of strain gauge and displacement meter.

2.2. Specimen Manufacturing. The specimens were manufactured using the following sequences (Figure 8): (a) the 18 pieces of the middle part of the expansion device were spliced into a cylinder, and both ends were fixed with galvanized iron wire; (b) the steel cover was buckled to two ends of the middle part of the device and fixed with screws and nuts; (c) the device assembled in the first two steps was placed between two benches or cement piers, on which upper angle steel fixed screw was placed; (d) applying Vaseline to the outer surface of the middle device homogeneously, flipping the fixed device manually, and wrapping the tape, rollers were used to remove the bubbles in the specimen to keep the surface smooth and flat, the inner rubber layer of the second specimen could be fixed simply with tape; (e) specimens were placed under a sufficient light source for UV curing, and it was necessary to constantly flip the device so that all parts of the specimen could receive the same amount of ultraviolet radiation and cure homogeneously; (f) after specimens were fully cured (single layer for 15 minutes and double layers for more than 30 minutes under sufficient illumination, multilayer curing was required); marking it in the corresponding position, polishing it smoothly, wiping it clean, and sticking strain gauges; (g) after the strain gauges were stuck to the glue, two steel caps and screws were removed, the device was placed in the middle of the two steel plugs that had been fixed on the universal testing machine, and the contact region between steel plugs and middle part of the device should be smeared with Vaseline for lubrication.

2.3. Auxiliary Device for Expansion

2.3.1. Design of Auxiliary Device for Expansion. There have been some researches on the mechanical properties of FRP-jacketed concrete under vertical compression, mainly on the failure mode and bearing capacity of FRP-jacketed concrete; types of specimens are mainly divided into circular [11–15], rectangular [16–18], square [19], elliptical [20], and other cross-sectional [21] FRP-jacketed concrete columns. Samaan et al. [13] performed axial compression tests on three GFRP-jacketed concrete. Through the analysis of the stress-strain curve, it can be found that the load was

Figure 8: The manufacturing process of the specimen: (a) installing component, (b) wire fixing, (c) lubricating surface, (d) wrapping rubber band, (e) winding prepreg sheet, (f) dislocation overlap, (g) UV curing, (h) applying strain gauge, (i) lubricating surface, and (j) completion.

supported by the concrete in the first half of curve; in the second half of curve, after the concrete was crushed, the load was mainly supported by GFRP tube. This paper will refer to the above research methods to study the mechanical properties of the main cable protection system under the internal circumferential expansion force and design an auxiliary device for expansion [22, 23].

The constitutive relation of confined concrete under compression is fitted according to the experimental data; the constitutive relation of confined concrete under compression is fitted.

During the test, two kinds of specimens were covered outside the middle part, and upper and lower steel disks were inserted into the ends of the auxiliary expansion device. Specimens and the auxiliary expansion device were put into the universal testing machine as a whole. Pressing the plugs at both ends up and down at a certain rate, finally the tapes would crack. The specific dimensions of the auxiliary expansion device are shown in Figure 9.

2.3.2. Force Analysis of Auxiliary Device for Expansion. As shown in Figure 10, the conversion formula of circumferential bearing capacity and the radial displacement can be obtained by calculating longitudinal and transverse force systems of the auxiliary expansion device.

The equation of equilibrium equations of longitudinal force system is

$$F_1 \cos\theta + F_2 \sin\theta = \frac{P}{2\pi R}. \quad (1)$$

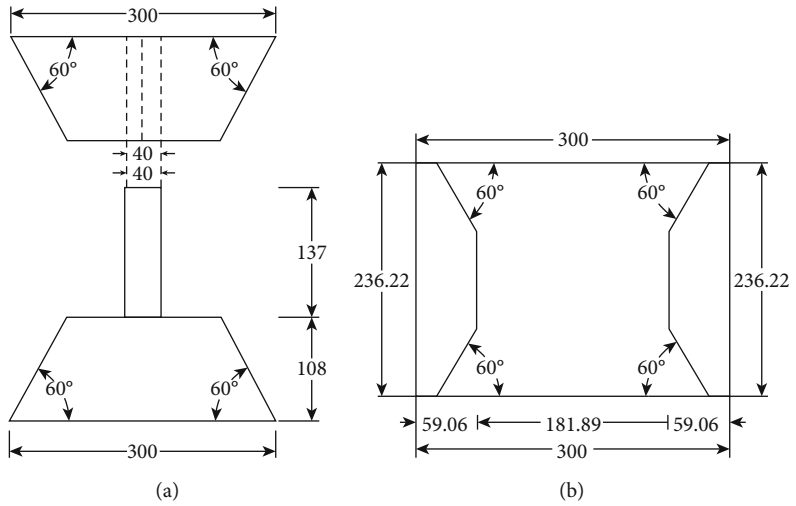

Figure 9: Specific size of the auxiliary expansion device: (a) front view and (b) top view.

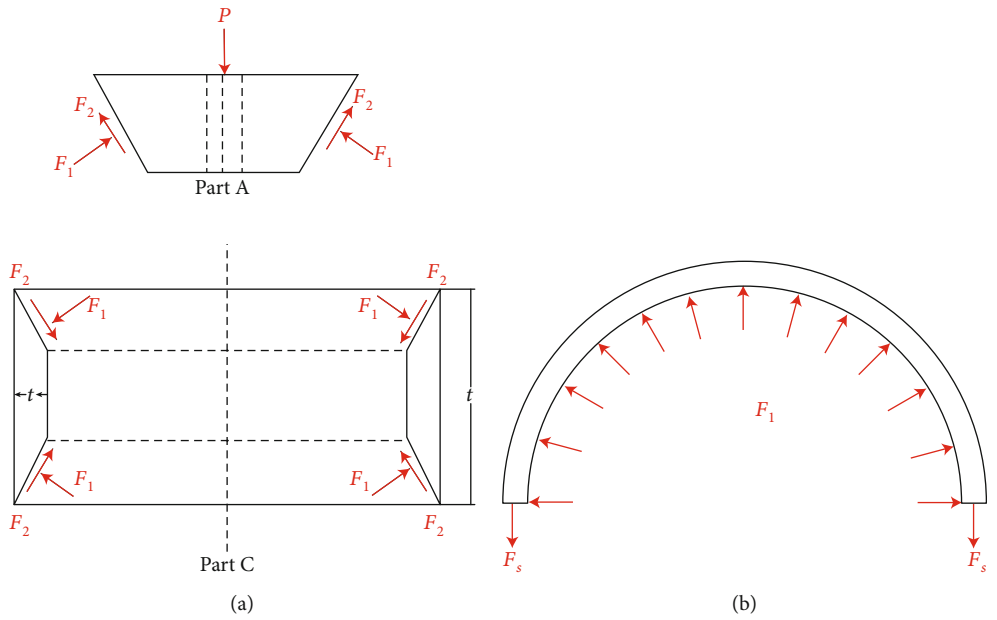

Figure 10: Force analysis of expansion test auxiliary device: (a) force analysis of front view and (b) force analysis of top view.

Supposing the frictional coefficient between A and C is k, $F_2 = F_1 k$,

$$F_1 = \frac{P}{2\pi R(k \sin\theta + \cos\theta)}, \tag{2}$$

$$F_2 = \frac{Pk}{2\pi R(k \sin\theta + \cos\theta)}. \tag{3}$$

In the horizontal direction:

$$F^* = 2(F_1 \sin\theta - F_2 \cos\theta), \tag{4}$$

$$F_s = RF^*. \tag{5}$$

It can be obtained from the specific size of the auxiliary expansion device, $\theta = 60^\circ$, $R = 150$ mm. The frictional coefficient $k = 0.3$ [24] is set here due to the sufficient lubrication between part A and part C and between part C and the specimen. The conversion relationship between the circumferential bearing capacity F and the vertical load P can be obtained by substituting the size of the auxiliary expansion device into equation (4).

$$F = 2\pi R \cdot F^* = 1.885P. \tag{6}$$

The conversion formula of vertical displacement to radial displacement:

$$D_h = \frac{D_v}{\tan\theta}. \tag{7}$$

Substituting the value to equation (7),

$$D_h = 0.577 D_v. \tag{8}$$

According to the solution of the polar coordinate plane of the component under axisymmetric stress, the problem of considering displacement of ring or cylinder under uniform pressure is similar to that under internal pressure of the main cable protection system studied in this paper. Therefore, referring to the above theory, the formula of radial displacement of the main cable protection system can be derived under axisymmetric load.

$$u_\rho = \frac{a^2 q_a (1+\mu)}{E\left(b^2 - a^2\right)} \left[\rho(1-2\mu) - \frac{b^2}{\rho}\right]. \tag{9}$$

The radial displacement value of the main cable protection system can be obtained by substituting the parameters such as inner diameter a, outer diameter b, elastic modulus E, and the Poisson ratio of the specimen into equation (9).

2.4. Experimental Scheme. The test was carried out by using the universal testing machine in Nanjing Tech University, the auxiliary expansion device was used to convert the vertical load of the universal testing machine into a uniform circumferential expansion force, and then, the antiexpansion performance of the composite protection system was tested. The universal testing machine was used with a loading rate of 0.5 mm/min, the accuracy of the universal testing machine could reach up to 0.5 grade, and the loading force could reach up to 600 kN. There were 12 strain gauges on each specimen, 8 in transverse direction and 4 in vertical direction, uniformly arranged along the circumference of the ring of the protection system. In order to compensate for the displacement errors measured by the universal testing machine, two LVDT with a range of 10 cm were installed on the front, back, and two sides of the testing machine to measure the vertical displacement of the testing machine.

The photocurable sheets were cured by a high-power UV curing lamp, and the strain data of the specimen were collected by Static Strain Gauge DN-3816. The experimental phenomena, force, and displacement values should be recorded, so as to analyze the experimental phenomena according to the force-displacement curve. The schematic diagram of the test loading device is shown in Figure 11.

2.5. Experimental Process. In group G-1-X, all three components were wrapped with a layer of photocurable prepreg fiber-reinforced composite tape around the expansion auxiliary device. The loading rate of component G-1-1 was 2 mm/min. The component was destroyed quickly due to the excessive loading rate, and the whole loading process lasted only 85 s. The loading rate of component G-1-2 was adjusted to 0.5 mm/min (the rest of the specimens were all at this rate). In group G-2-X, all three components were wrapped with two layers of photocurable prepreg fiber-reinforced composite tape. The outer two layers of prepreg wrapping tape of the first component were cured simultaneously by continuous wrapping. After curing for 30 minutes, it was found that the thickness of the lap joint was too thick which could not be fully cured. Therefore, the latter two specimens were fabricated by layered wrapping and incremental curing, and each layer was cured for 15 minutes. The following components all adopted this process. In group G-3-X, all three components were wrapped with 3 layers of photocurable prepreg fiber-reinforced composite tape. Specimens were manufactured by layered wrapping and incremental curing, and each layer was cured for 15 minutes. The lap joints of each layer did not coincide with each other. In group G-1-R-X, all three components were wrapped with a layer of nitrile rubber belt and a layer of photocurable prepreg fiber-reinforced composite wrapping tape. In group G-2-R-X, all three components were wrapped with a layer of nitrile rubber belt and 2 layers of photocurable prepreg fiber-reinforced composite wrapping tape. In group G-3-R-X, all three components were wrapped with a layer of nitrile rubber belt and 3 layers of light-cured prepreg fiber-reinforced composite wrapping tape. In group G-X-2R-1, all three components were wrapped with two layers of nitrile rubber belt and then wrapped with one, two, and three layers of light-cured prepreg fiber-reinforced composite wrapping tape, respectively. The time history, maximum circumferential bearing capacity, and radial displacement can be seen in Table 2.

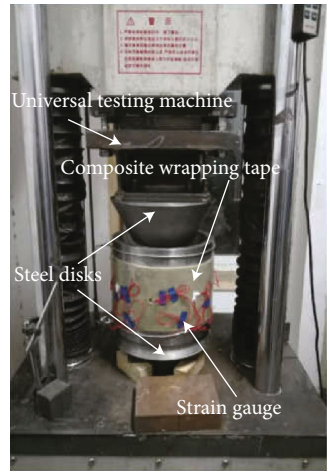

Figure 11: Testing loading device.

3. Experiment Result Analysis

3.1. Failure Modes. Failure modes of the test group without rubber belt are shown in Figure 12. As shown in Figure 12(a), the crack of specimen G-1-X is at the lap joint of prepreg wrapping tape; this specimen broke instantaneously and cracks were vertical. A large number of fibrils were pulled out around it, and no obvious damage was found in other parts. As shown in Figure 12(b), the crack of specimen G-2-X is at the lap joint of the outer prepreg wrapping tape; the specimen broke instantaneously, the broken sound was loud, and the cracks were vertical; a large number of fibrils were pulled out around it. Sounds of fiber breakage were produced during this loading process. As shown in

Table 2: Results of circumferential expansion test.

Specimen	Loading rate (mm (min)-1)	Time history (s)	Maximum circumferential bearing capacity (kN)	Radial displacement (mm)
G-1-X				
G-1-1	2	85	74.18	3.24
G-1-2	0.5	700	57.14	2.47
G-1-3	0.5	912	83.57	3.53
G-2-X				
G-2-1	0.5	750	109.13	2.42
G-2-2	0.5	798	120.46	2.87
G-2-3	0.5	1156	189.54	3.78
G-3-X				
G-3-1	0.5	1414	340.52	5.22
G-3-2	0.5	773	135.41	2.84
G-3-3	0.5	960	216.92	3.33
G-1-R-X				
G-1-R-1	0.5	1392	100.51	4.67
G-1-R-2	0.5	876	75.14	3.22
G-1-R-3	0.5	742	57.34	2.53
G-2-R-X				
G-2-R-1	0.5	926	138.82	3.44
G-2-R-2	0.5	679	140.94	3.43
G-2-R-3	0.5	1148	178.59	4.33
G-3-R-X				
G-3-R-1	0.5	1257	298.94	4.60
G-3-R-2	0.5	1216	278.76	4.35
G-3-R-3	0.5	1200	272.59	4.22
G-X-2R-1				
G-1-2R-1	0.5	791	85.75	3.82
G-2-2R-1	0.5	1127	178.85	4.15
G-3-2R-1	0.5	1333	304.76	4.70

Figure 12(c), the location of cracks in the three layers was not the same, at least one layer destroyed at the lap joint. This specimen broke instantaneously, the sound was loud, and the cracks were vertical; a large number of fibrils were pulled out. Sounds of fiber breakage always occurred during this loading process.

Failure modes of 1-layer rubber belt test group are shown in Figure 13. As shown in Figure 13(a), the crack of specimen G-1-R-X is at the lap joint of the outer prepreg wrapping tape, the specimen broke instantaneously, and cracks were vertical; a small amount of fibrils were pulled out. White vertical cracks appeared during this process and the rubber belt inside was in good condition. As shown in Figure 13(b), the crack of specimen G-2-R-X is at the lap joint of the outer or inner prepreg wrapping tape; the specimen broke instantaneously, the broken sound was loud, and the cracks were vertical. Sounds of fiber breakage and many white vertical cracks were produced during this loading process. The rubber belt was in good condition and bonded well to the prepreg wrapping tape when it was damaged. As shown in Figure 13(c), the cracks of three layers of the two components were all connected, and at least one layer of cracks was in the lap transition position. The specimen broke instantaneously, the broken noise was huge, and the cracks were vertical. Sounds of fiber breakage and white vertical cracks always occurred during this loading process. The rubber belt was in good condition and bonded well to the prepreg wrapping tape when it was damaged.

Failure modes of 2-layer rubber belt test group are shown in Figure 14. As shown in Figure 14(a), the crack of specimen G-1-2R-1 is at the nonlap joint; the specimen broke instantaneously and produced zigzag cracks. White vertical cracks occurred during this loading process. The rubber belt was in good condition. As shown in Figure 14(b), the crack of specimen G-2-2R-1 is at the lap joint of the outer prepreg wrapping tape; the specimen broke instantaneously, broken sound was loud, and outer cracks were vertical. Sounds of fiber breakage and many white vertical cracks were produced during this loading process. The rubber belt was in good condition and bonded well to the prepreg wrapping tape when it was damaged. As shown in Figure 14(c), the cracks of the three layers did not coincide with each other. All of them were not at the lap joint. The specimen broke instantaneously and produced zigzag cracks. Broken noise was huge. Sounds

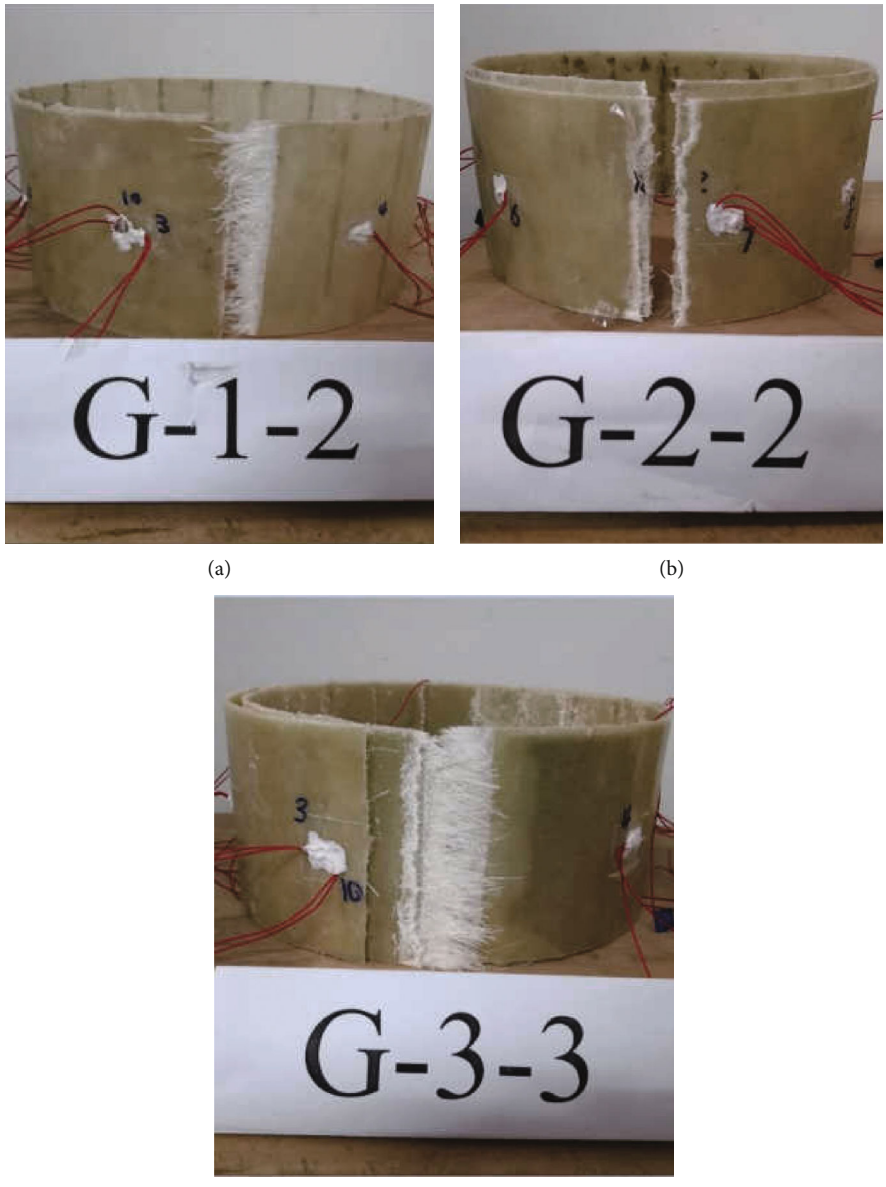

(a) (b)

(c)

Figure 12: Failure modes of the test group without rubber belt.

of fiber breakage and white vertical cracks always occurred during this loading process. The rubber belt was in good condition and bonded well to the prepreg wrapping tape when it was damaged.

3.2. Load-Displacement Curves. Comparisons of circumferential bearing capacity-radial displacement curves of specimens with or without rubber belt are shown in Figure 15. The results of circumferential expansion of the test group without rubber belt are shown in Table 3.

According to the comparable results of the circumferential expansion test between specimens with 2-layer rubber belt and 1-layer rubber belt in Table 4, it can be obtained that when 1-layer prepreg wrap is wrapped around, the circumferential bearing capacity of specimen with 2-layer rubber belt increased by 10.19% and the radial displacement increased by 10.09% compared to the specimen with 1-layer rubber belt; when 2-layer prepreg wrap is wrapped around, the circumferential bearing capacity of specimen with 2-layer rubber belt increased by 3.8% and the radial displacement increased by 11.26% compared to the specimen with 1-layer rubber belt; when 3-layer prepreg wrap is wrapped around the periphery, the circumferential bearing capacity of specimen with 2-layer rubber belt increased by 12.15% and the radial displacement increased by 7.06% compared to the specimen with 1-layer rubber belt. It can be seen that the radial displacement of specimens increases with the increase of rubber belt layers, but the increase rate decreases gradually.

The contribution of the change of layers of the prepreg wrap and rubber belt to the circumferential bearing capacity and the radial displacement of the specimens can be obtained

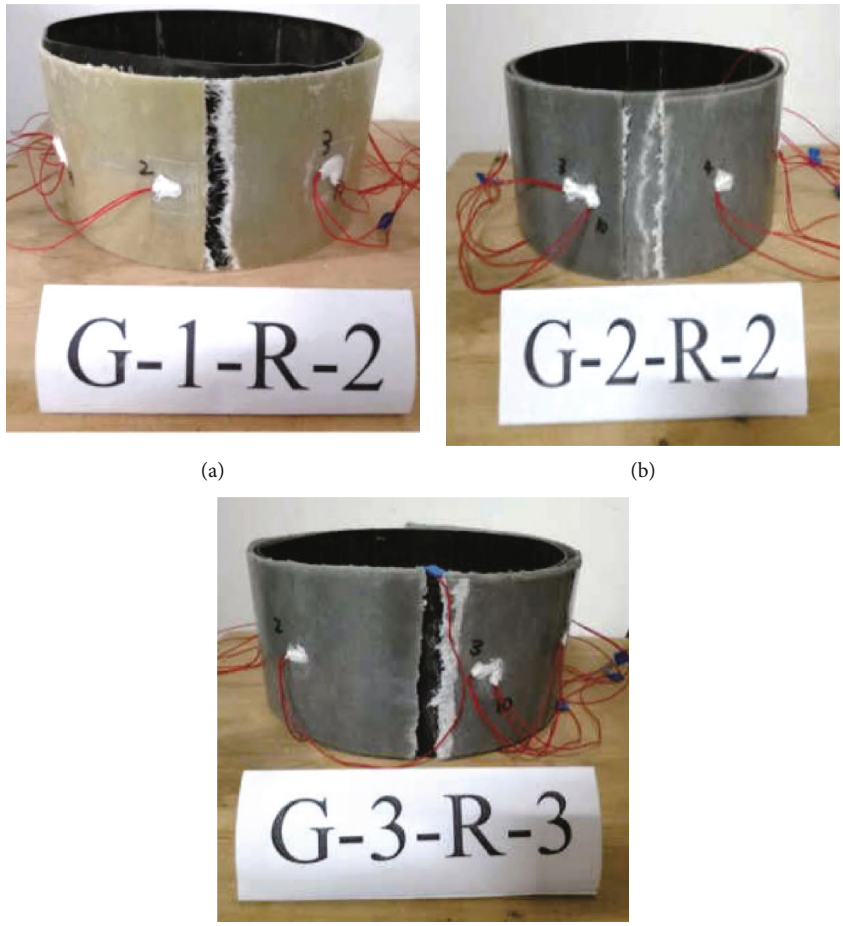

(a) (b)

(c)

Figure 13: Failure modes of 1-layer rubber belt test group.

from Table 5; the change of the number of prepreg layers contributes more to the circumferential bearing capacity than the change of rubber belt layers. When the number of rubber belt layer is the same, the variation of the number of prepreg layers from 1 to 2 on the circumferential bearing capacity is greater than the contribution of the prepreg layers from 2 to 3. The increase of the rubber belt layers also increases the circumferential bearing capacity of the specimen, but there is no obvious regulation to follow. When the number of prepreg layer is the same, the variation of the number of prepreg layers from 2 to 3 on the radial displacement is greater than the contribution of prepreg layers from 1 to 2. However, this trend has gradually declined with the increase of rubber belt. When the number of prepreg layer is the same, the variation of number of rubber belt layers from 0 to 1 is greater than the contribution of the rubber belt layers from 1 to 2, and this trend is most significant when the number of prepreg layer is 2.

3.3. Circumferential Strain-Radial Displacement Curve. This section only selects the circumferential strain-radial displacement curve of representative specimens of each group. The failure modes are analyzed with the change of rubber belt layers under the same number of prepreg layer.

It can be seen from the circumferential strain-radial displacement curve of specimens with 1-layer prepreg wrap from Figure 16 that the closer to the crack position, the greater the strain value is. The strain value of the lap joint of the specimen is the smallest among the all strain gauges. There is also a phenomenon in which the strain of nondestructive position suddenly increases during the loading process. It is suggested that this is mainly caused by instant stretching of the internal fiber fold or the fracture of the internal fiber fabric. The radial displacement of the component is 2.44 mm without rubber belt, 2.58 mm for 1-layer rubber belt, and 2.72 mm for 2-layer rubber belt when the failure strain of the component reaches 95%. As the number of rubber belt layers increases, the radial displacement of components becomes larger when they are damaged.

It can be seen from the circumferential strain-radial displacement curve of specimens with 2-layer prepreg wrap from Figure 17 that the strain values of components are small at the initial stage of loading, which is caused by the compaction of components of the loading device. When the layers of external prepreg wrap increases to 2, the radial displacement becomes larger as the number of rubber belt increases. The radial displacement of the component is 2.31 mm without rubber belt, 3.28 mm for 1-layer rubber belt, and 3.95 mm

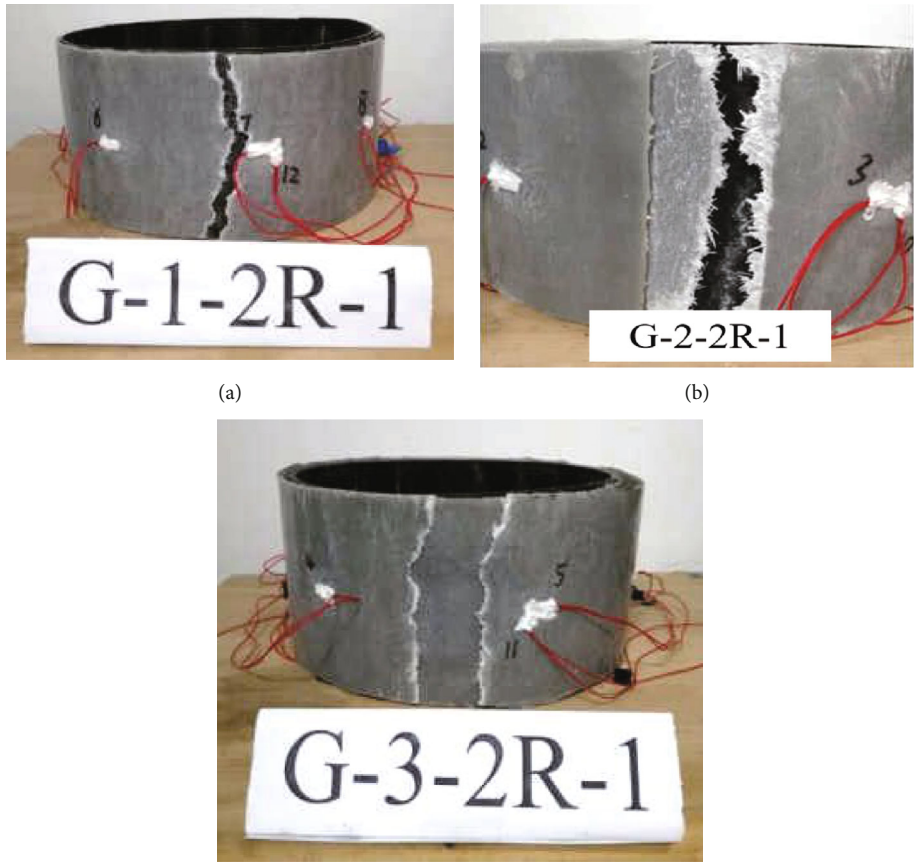

(a) (b)

(c)

Figure 14: Failure modes of 2-layer rubber belt test group.

for 2-layer rubber belt when the failure strain of 2-layer prepreg wrap reaches 95%. The strain value of the specimen close to the failure position is the largest, and the value of the overlap portion is smaller.

It can be seen from the circumferential strain-radial displacement curve of specimens with 3-layer prepreg wrap from Figure 18 that the strain values of components are small at the initial stage of loading, which is caused by the compaction of components of the loading device. The value at most locations during the loading process increases substantially linearly. Similar to the former two groups, the increase in the number of rubber belt layer significantly affects the radial displacement of the specimen when they are broken. As the number of rubber belt layer increases, the radial displacement of the component is 3.18 mm without rubber belt, 4.04 mm for 1-layer rubber belt, and 4.51 mm for 2-layer rubber tape when the failure strain of the component reaches 95%. Similar to the previous two groups, the strain value of the specimen close to the failure position is the largest, and the strain value of the overlap portion is smaller.

4. Expansion Force of the Main Cable

In this paper, the main research direction of the main cable protection system of new suspension bridge is to resist the expansion performance of the main cable affected by temperature. Therefore, this section begins with the expansion of the main cable, focusing on the expansion of the main cable in plane. The temperature stress of the main cable can be obtained according to the following:

$$\varepsilon_t = \Delta t \cdot \alpha = \frac{\sigma_t}{E}. \tag{10}$$

Δt is the maximum temperature difference of the environment, α is the linear expansion coefficient of the main cable, E is the elastic modulus of steel wire for the main cable, σ_t is the temperature stress of the main cable, and ε_t is the temperature strain of the main cable.

The temperature stress of the main cable can be calculated as follows:

$$\sigma_t = \Delta t \cdot \alpha \cdot E. \tag{11}$$

Aiming at the expansion of the main cables in plane affected by temperature, the expansive force along the circumferential direction of the main cable mainly focused on the ring of the protective system of unit thickness, so the value of A and expansion force of the main cable protection

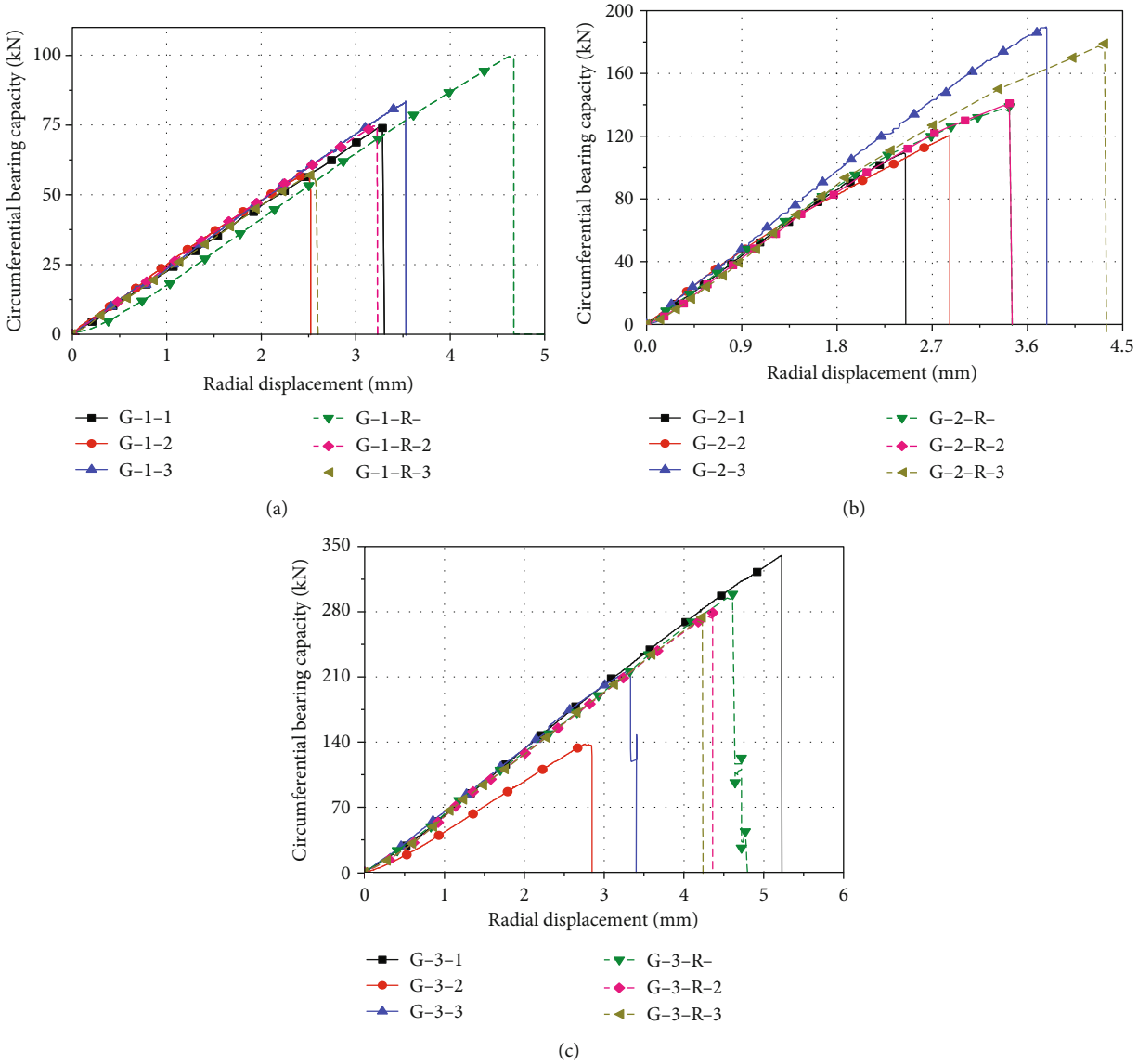

Figure 15: Comparison of circumferential bearing capacity-radial displacement curves of specimens with or without rubber belt: (a) 1-layer prepreg component, (b) 2-layer prepreg component, and (c) 3-layer prepreg component.

Table 3: Results of circumferential expansion test of the test group without rubber belt.

Group	Specimen	Circumferential bearing capacity (kN)	Average (kN)	Radial displacement (mm)	Average (mm)
G-1-X	G-1-1	74.18	71.63	3.24	3.08
	G-1-2	57.14		2.47	
	G-1-3	83.57		3.53	
G-2-X	G-2-1	109.13	139.71	2.42	3.02
	G-2-2	120.46		2.87	
	G-2-3	189.54		3.78	
G-3-X	G-3-1	340.52	230.95	5.22	3.80
	G-3-2	135.41		2.84	
	G-3-3	216.92		3.33	

Table 4: Results of circumferential expansion test of rubber belt test group.

Group	Specimen	Circumferential bearing capacity (kN)	Average (kN)	Radial displacement (mm)	Average (mm)
G-1-R-X	G-1-R-1	100.51	77.66	4.67	3.47
	G-1-R-2	75.14		3.22	
	G-1-R-3	57.34		2.53	
G-1-2R-1	G-1-2R-1	—	85.57	—	3.82
G-2-R-X	G-2-R-1	138.82	152.78	3.44	3.73
	G-2-R-2	140.94		3.43	
	G-2-R-3	178.59		4.33	
G-2-2R-1	G-2-2R-1	—	178.85	—	4.15
G-3-R-X	G-3-R-1	298.94	283.43	4.60	4.39
	G-3-R-2	278.76		4.35	
	G-3-R-3	272.59		4.22	
G-3-2R-1	G-3-2R-1	—	304.76	—	4.70

Table 5: The influence of the number of the prepreg wrap and rubber belt layers on the circumferential bearing capacity and radial displacement of the specimen.

	Number of rubber layer	Number of prepreg layer ($1 \rightarrow 2$)	Number of prepreg layer ($2 \rightarrow 3$)	Number of prepreg layer	Number of rubber belt layer ($0 \rightarrow 1$)	Number of rubber belt layer ($1 \rightarrow 2$)
Growth rate of radial displacement	0	-1.95%	25.83%	1	12.66%	10.09%
	1	7.49%	17.69%	2	23.51%	11.26%
	2	8.64%	13.25%	3	15.53%	7.06%
Growth rate of circumferential bearing capacity	0	95.04%	65.31%	1	8.42%	10.19%
	1	96.73%	85.52%	2	9.36%	17.64%
	2	109.01%	70.4%	3	22.72%	7.53%

system affected by temperature F_r can be calculated by the following:

$$\begin{aligned} A &= \pi D, \\ F_r &= \sigma_t \cdot A. \end{aligned} \tag{12}$$

Therefore, the linear expansive force of the main cable cross section is $(\pi D \cdot \Delta t \cdot \alpha \cdot E)$ kN.

According to the force balance on the compressive performance of CFRP sheath confined concrete [25], the relationship between confined sheath stress and circumferential stress can be obtained, which can be used to calculate the confined stress circumferential tensile stress of FRP sheath confined to the main cable. The diagram of restrained and circumferential stress of FRP sheath is shown in Figure 19.

$$f_r = -\frac{2t_j}{D} f_{j\theta}. \tag{13}$$

f_r is the constrained stress, $f_{j\theta}$ is the circumferential stress, t_j is the thickness of FRP sheath, and D is the diameter of the main cable.

When the temperature difference reaches Δt, the stress produced by the main cable under temperature load $\sigma_t = f_r = \Delta t \cdot \alpha \cdot E$. So the circumferential stress can be obtained from the following:

$$f_{j\theta} = \left| -\frac{f_r \cdot D}{2t_j} \right|. \tag{14}$$

When the tensile strength of the prepreg sheet measured by the material characteristic test is less than the circumferential stress $f_{j\theta}$, the use of prepreg wrapping tape alone cannot meet the requirements of the protection system. The energy of main cable deformation is absorbed by the deformation of rubber belt, so as to reduce the force on the FRP wrapping tape.

The linear expansion coefficient of the main cable is used to calculate the cross-sectional deformation of the main cable:

$$\varepsilon_R = \frac{R_t - R_0}{R_0} = \alpha \cdot \Delta t. \tag{15}$$

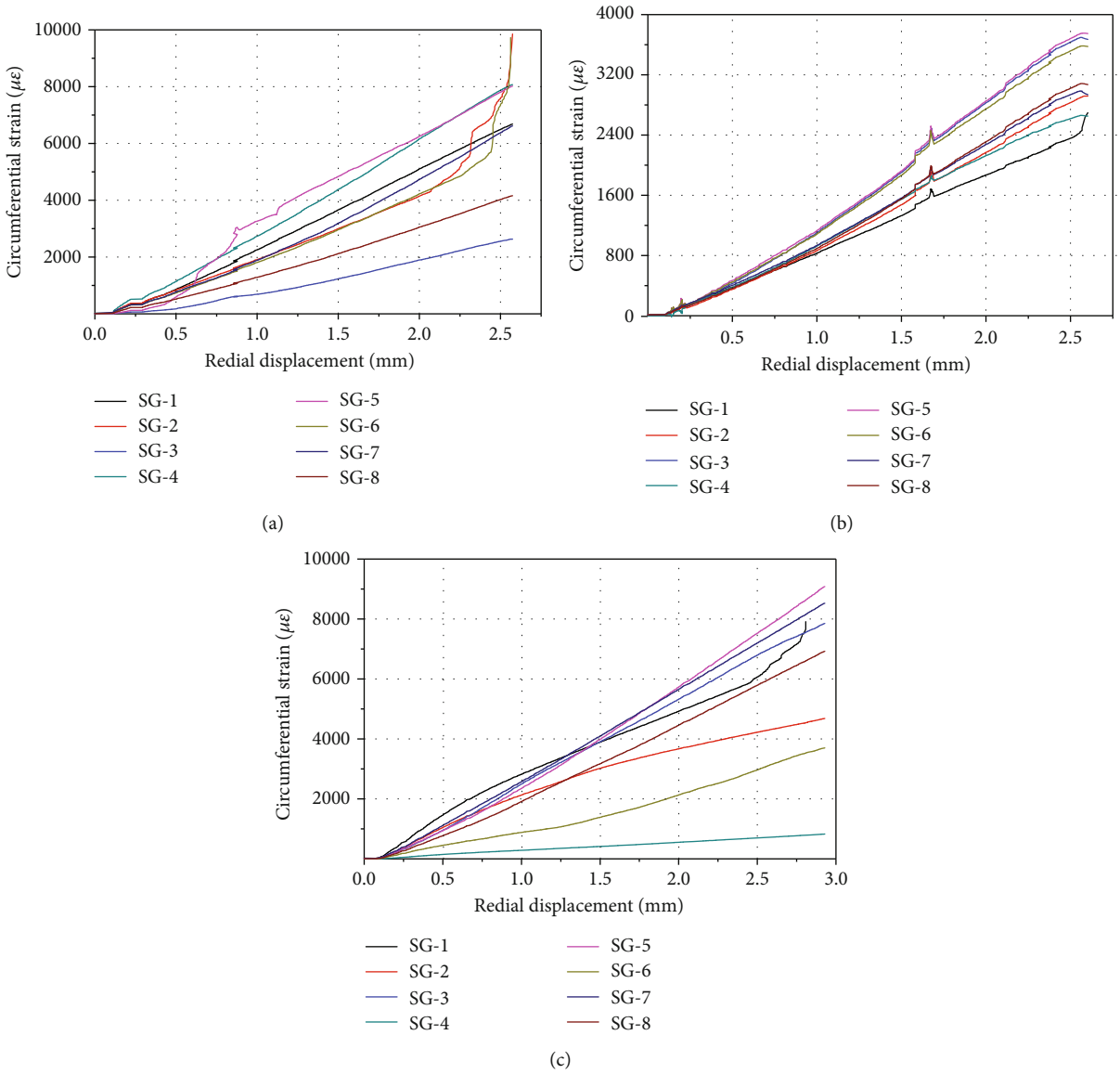

Figure 16: The circumferential strain-radial displacement curve of the test group with 1-layer prepreg wrap: (a) G-1-2 curve, (b) G-1-R-3 curve, and (c) G-1-2R-1 curve.

ε_R is the radius strain of the main cable cross section, R_t is the radius of the main cable after expansion, and R_0 is the radius of the main cable before expansion.

Querying the related parameters, the linear expansion coefficient of the main cable is $1.2 \times 10^{-5}/^{\circ}\mathrm{C}$, and the maximum temperature difference is 60°C.

$$\Delta R = \alpha \cdot \Delta t \cdot R_0. \tag{16}$$

The radius difference of the main cable before and after expansion is 0.108 mm. In addition to temperature deformation, the main cable will also be deformed by the sloshing and vibration of the main cable; the use of rubber belt can play a role in shock absorption. According to the expansion test of the main cable, the radial displacement of 1, 2, and 3 layers of prepreg wrap protection system increases by 0.39 mm, 0.71 mm, and 0.59 mm, respectively, when the rubber belt layer increases from 0 to 1. It can be seen that when the outer prepreg layer is 2, the radial displacement increment of the inner rubber belt is the largest, and the increment is also greater than the main cable deformation 0.108 mm, which can meet the deformation requirements of the main cable.

5. Conclusions

In this paper, the circumferential expansion test of the composite wrap system for main cable protection of new suspension bridge is studied. The failure modes of the protective system of different prepreg wraps and with or without rubber belts are compared. Based on theoretical analysis, the theoretical values of the circumferential bearing capacity and radial displacement of specimen under the action of

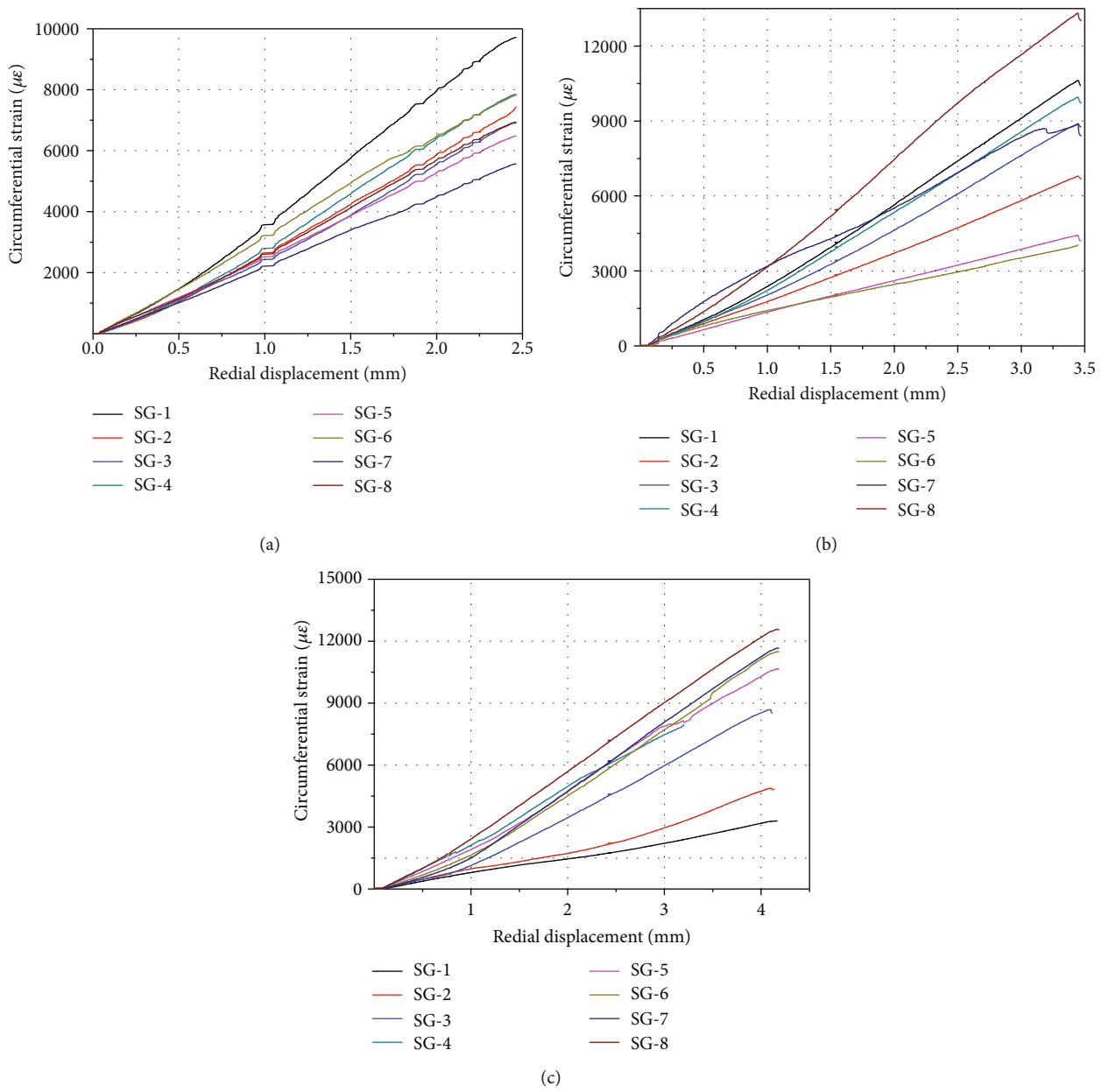

Figure 17: The circumferential strain-radial displacement curve of the test group with 2-layer prepreg wrap: (a) G-2-1 curve, (b) G-2-R-1 curve, and (c) G-2-2R-1 curve.

circumferential expansion force are derived. The corresponding major conclusions are summarized as follows:

(1) An experiment scheme for circumferential expansion of the main cable protection system is designed. The failure modes of components with different prepreg wrap layers and rubber belt layers were compared and analyzed. The radial displacement of the component is the most obviously affected by the increase of rubber belt layers. When the rubber belt layer is added, the deformation of the main cable is increased and the component has more deformation redundancy, which delays the ultimate strain of the outer prepreg wrap. The entire system can be better deformed following the deformation of the main cable

(2) The change of the number of prepreg wrap layers contributes more to the circumferential capacity. When the number of rubber belt layers is the same, with the increase of prepreg layers, the growth rate of circumferential bearing capacity decreases gradually; conversely, the growth rate of radial displacement increases gradually. When the number of prepreg layers is 2 and the number of rubber belt layers is 1, the growth rates of radial displacement and circumferential bearing capacity are maximal

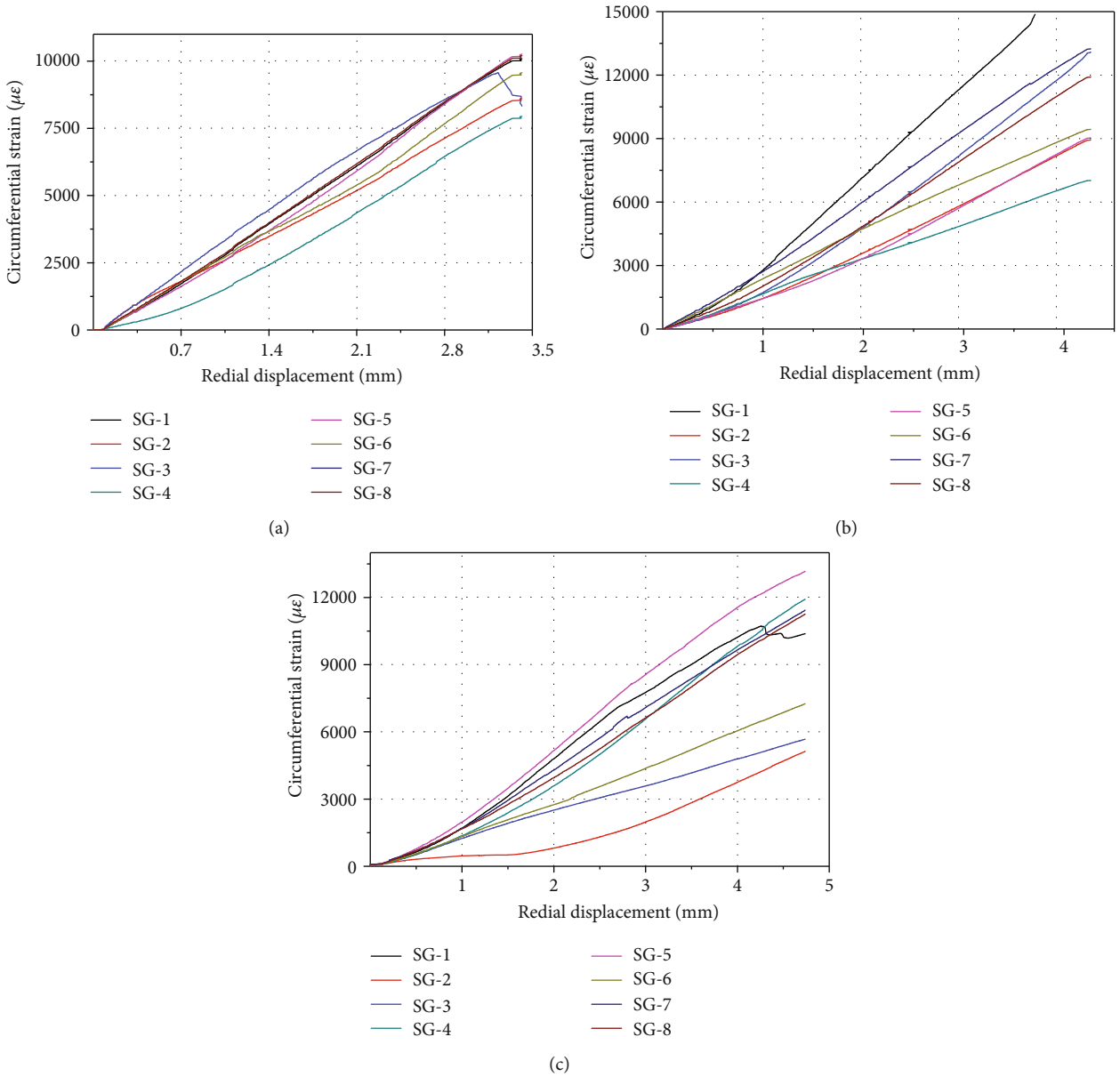

Figure 18: The circumferential strain-radial displacement curve of the test group with 3-layer prepreg wrap: (a) G-3-3 curve, (b) G-3-R-3 curve, and (c) G-3-2R-1 curve.

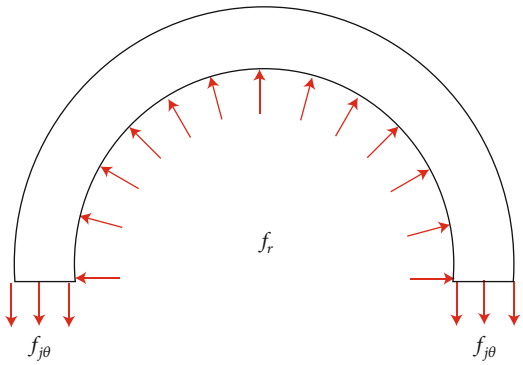

Figure 19: Restrained stress and circumferential stress of FRP sheath.

(3) At the initial stage of loading, the strain values of components are small; the value at most locations during the loading process increases substantially linearly. The strain value of the specimen close to the failure position is the largest, and the value of the overlap portion is smaller

(4) When the tensile strength of the prepreg sheet measured by the material characteristic test is less than the circumferential stress $f_{j\theta}$, the use of prepreg wrapping tape alone cannot meet the requirements of the protection system. When the rubber belt is introduced, the component has more redundant deformation, which delays the arrival of limit strain of the outer prepreg wrapping tape, and makes the

whole system better follow the deformation of the main cable

Data Availability

The data used to support the findings of this study are available from the corresponding author upon request.

Conflicts of Interest

The authors declare that they have no conflicts of interest.

Acknowledgments

The research described here was supported by the National Natural Science Foundation of China (Grant No. 51778285), the Natural Science Foundation for Distinguished Young Scholars of Jiangsu Province (Grant No. BK20190034), the National Key Research and Development Program of China (2019YFD1101205), and the Funds for Youth Creative Research Groups of Nanjing Tech University.

References

[1] H. Q. Zhao, X. J. He, M. Zhao, and J. W. Zhao, "On the development and innovation of modern suspension bridge in China," *Applied Mechanics and Materials*, vol. 587-589, pp. 1435–1438, 2014.

[2] M. R. T. Arruda and J. P. M. Serafim, "Parametric test for the preliminary design of suspension bridges," *International Journal of Advanced Structural Engineering*, vol. 9, no. 2, article 156, pp. 165–176, 2017.

[3] A. Juozapaitis, S. Idnurm, G. Kaklauskas, J. Idnurm, and V. Gribniak, "Non-linear analysis of suspension bridges with flexible and rigid cables," *Journal of Civil Engineering and Management*, vol. 16, no. 1, pp. 149–154, 2010.

[4] T. L. M. Morgado and A. Sousa e Brito, "A failure analysis study of a prestressed steel cable of a suspension bridge," *Case Studies in Construction Materials*, vol. 3, pp. 40–47, 2015.

[5] J. A. Roebling, *Columbia Electronic Encyclopedia*, Columbia University Press, New York, 6th edition, 2019.

[6] T. Tarui, S. Konno, and T. Takahashi, "High strength galvanized wire for bridge cables," *Materials Science Forum*, vol. 426-432, pp. 829–834, 2003.

[7] T. Kitada, "Considerations on recent trends in, and future prospects of, steel bridge construction in Japan," *Journal of Constructional Steel Research*, vol. 62, no. 11, pp. 1192–1198, 2006.

[8] M. L. Bloomstine, O. Sørensen, and J. V. Thomsen, "Main cable corrosion protection by dehumidification," *IABSE Symposium Report*, vol. 91, no. 2, pp. 1–8, 2006.

[9] H. Petroski, "Akashi Kaikyo Bridge," *American Scientist*, vol. 97, no. 3, pp. 192–196, 2009.

[10] H. Fang, Y. Bai, W. Liu, Y. Qi, and J. Wang, "Connections and structural applications of fibre reinforced polymer composites for civil infrastructure in aggressive environments," *Composites Part B: Engineering*, vol. 164, pp. 129–143, 2019.

[11] A. Nanni and N. M. Bradford, "FRP jacketed concrete under uniaxial compression," *Construction and Building Materials*, vol. 9, no. 2, pp. 115–124, 1995.

[12] A. Mirmiran and M. Shahawy, "Behavior of concrete columns confined by fiber composites," *Journal of Structural Engineering*, vol. 123, no. 5, pp. 583–590, 1997.

[13] M. Samaan, A. Mirmiran, and M. Shahawy, "Model of concrete confined by fiber composites," *Journal of Structural Engineering*, vol. 124, no. 9, pp. 1025–1031, 1998.

[14] G. Lin, T. Yu, and J. G. Teng, "Design-oriented stress–strain model for concrete under combined FRP-steel confinement," *Journal of Composites for Construction*, vol. 20, no. 4, article 04015084, 2016.

[15] H. M. Elsanadedy, Y. A. Al-Salloum, S. H. Alsayed, and R. A. Iqbal, "Experimental and numerical investigation of size effects in FRP-wrapped concrete columns," *Construction and Building Materials*, vol. 29, pp. 56–72, 2012.

[16] P. Rochette and P. Labossière, "Axial testing of rectangular column models confined with composites," *Journal of Composites for Construction*, vol. 4, no. 3, pp. 129–136, 2000.

[17] H. Toutanji, M. Han, J. Gilbert, and S. Matthys, "Behavior of large-scale rectangular columns confined with FRP composites," *Journal of Composites for Construction*, vol. 14, no. 1, pp. 62–71, 2010.

[18] P. Sadeghian, A. R. Rahai, and M. R. Ehsani, "Experimental study of rectangular RC columns strengthened with CFRP composites under eccentric loading," *Journal of Composites for Construction*, vol. 14, no. 4, pp. 443–450, 2010.

[19] M. A. G. Silva, "Behavior of square and circular columns strengthened with aramidic or carbon fibers," *Construction and Building Materials*, vol. 25, no. 8, pp. 3222–3228, 2011.

[20] J. G. Teng and L. Lam, "Compressive behavior of carbon fiber reinforced polymer-confined concrete in elliptical columns," *Journal of Structural Engineering*, vol. 128, no. 12, pp. 1535–1543, 2002.

[21] P. Feng, S. Cheng, Y. Bai, and L. Ye, "Mechanical behavior of concrete-filled square steel tube with FRP-confined concrete core subjected to axial compression," *Composite Structures*, vol. 123, pp. 312–324, 2015.

[22] T. Yu, B. Zhang, and J. G. Teng, "Unified cyclic stress–strain model for normal and high strength concrete confined with FRP," *Engineering Structures*, vol. 102, pp. 189–201, 2015.

[23] Y. M. Hu, T. Yu, and J. G. Teng, "FRP-confined circular concrete-filled thin steel tubes under axial compression," *Journal of Composites for Construction*, vol. 15, no. 5, pp. 850–860, 2011.

[24] K. Shimizu, T. Noguchi, H. Seitoh, and E. Muranaka, "FEM analysis of the dependency on impact angle during erosive wear," *Wear*, vol. 233-235, pp. 157–159, 1999.

[25] Y. Xiao and H. Wu, "Compressive behavior of concrete confined by carbon fiber composite jackets," *Journal of Materials in Civil Engineering*, vol. 12, no. 2, pp. 139–146, 2002.

Hindawi
Advances in Polymer Technology
Volume 2020, Article ID 7358930, 11 pages
https://doi.org/10.1155/2020/7358930

Research Article

Elasticity Solutions for Sandwich Arches considering Permeation Effect of Adhesive

Ruili Huo, Yichen Liu, Peng Wu, Hai Fang, Weiqing Liu, and Ding Zhou

College of Civil Engineering, Nanjing Tech University, Nanjing 211816, China

Correspondence should be addressed to Weiqing Liu; wqliu@njtech.edu.cn and Ding Zhou; dingzhou57@yahoo.com

Received 21 October 2019; Accepted 7 March 2020; Published 28 March 2020

Guest Editor: Guangming Chen

In this work, analytical solution of simply supported sandwich arches considering permeation effect of adhesives is presented. The permeation layer is described by the functionally graded material, exponentially graded in the radial direction. The stresses and deformations of each layer are based on the two-dimensional (2D) elasticity theory in the polar coordinate. The governing equations of the arch are solved by the layer-wise method, which turns the differential equations with variable coefficients into constant coefficients. The solution can be obtained efficiently by means of the recursive matrix method, especially for the arch with many layers. The present solution agrees well with the finite element solution with a fine mesh, while the finite element method is time consuming in mesh division and calculation. The one-dimensional (1D) solution based on the Euler–Bernoulli theory is close to the present one; however, the error increases as the arch becomes thick. The effect of permeation layer thickness on the stresses is studied. It is indicated that the stress distributions tend to be smooth along the radial direction as the permeation layer thickness increases.

1. Introduction

Owing to various advantages such as corrosion resistance, antifatigue, and high specific strength and stiffness, composite structures are increasingly used in different branches of engineering. In addition, their mechanical behavior can be optimized by ingeniously choosing the material type and composite pattern. A typical application is the sandwich structures [1–5], usually composed of two stiff face layers and a relatively soft core layer, bonded together by the adhesive. It is known that the interfacial damage exists widely in sandwich structures due to the discontinuity of material property at the interface. In practice, the adhesive will permeate into adjacent macrovoid materials such as glass fiber, balsa wood, and aluminum honeycomb, which leads to a refined sandwich model, as shown in Figure 1. The permeation layer is the mixture of the face (or core) layer and the adhesive. This makes the material property smoothly vary along the radial direction, like of functionally graded material (FGM). Such a problem deserves to be deeply investigated. For sandwich plates considering permeation effect, analytical solution has been proposed by Huo et al. [6]. In addition to sandwich plates, sandwich arches have also received a lot of attention due to their advantage of artistic appearance and excellent load-carrying capacity. The present study aims at extending their work to investigate the sandwich arch with permeation effect.

A review of the literature indicates that many analytical models have been proposed for the mechanical behaviors of sandwich structures. Galuppi and Royer-Carfagni [7] studied the bending behavior of the sandwich arch formed by two elastic facial layers and a thin polymeric interlayer. In their report, the deformation of the arch was based on the Euler–Bernoulli assumption, which was suitable for thin arches with moderate curvature. The stress distribution in a sandwich plate with the FG face was studied by Raissi et al. [8] by the use of the layer-wise method based on the first-order shear deformation theory. The vibration of sandwich microplates with nanocomposite face layers under magnetic and electric fields was studied by Mohammadimehr et al. [9]

by virtue of the sinusoidal shear deformation theory. Livani et al. [10] investigated the supersonic flutter of doubly curved sandwich panels with variable thickness subjected to thermal load. In their study, the governing equations were based on a new higher-order shear deformation theory, in which the vertical and in-plane displacement components were assumed as quadratic and cubic functions, respectively. Bouchafa et al. [11] presented a new refined hyperbolic shear deformation theory with only four unknown functions to analyze the thermoelastic bending of FG sandwich plates. Bending, vibration, and buckling analysis of FG sandwich plates were analyzed by Nguyen et al. [12] according to the refined higher-order shear deformation theory. By using a higher-order sandwich theory, Rahmani et al. [13] tackled the free vibration of the composite sandwich shell with a flexible core.

In addition to the aforementioned analytical models, some numerical methods are efficient for the analysis of sandwich structures. By means of the differential quadrature finite element method, Liu et al. [14] investigated bending of the sandwich shell consisting of two homogenous face sheets and a FG core. Natarajan and Manickam [15] presented a QUAD-8 shear flexible element method based on higher-order shear deformation theory to study the bending and free flexural vibration of FG sandwich plates. Dynamic behavior of corrugated-core sandwich plates was analyzed by Peng et al. [16] via a mesh-free Galerkin method, in which the domain of the plate was discretized by scattered nodes, and no elements were required. By virtue of the isogeometric method, Thai et al. [17] studied the free vibration and buckling analysis of sandwich plates. This method has the advantage to exactly represent domains and achieve approximation with arbitrarily high smoothness. Mantari et al. [18] developed a layer-wise finite element formulation-based trigonometric layer-wise shear deformation theory for the bending of thick sandwich plates.

The analytical solution based on the elasticity theory is important because it can be used as a benchmark to assess other simplified solutions [19]. Based on the elasticity theory, Pagano [20] proposed an analytical solution for the bending of simply supported composite and sandwich plates. The elasticity solution of the cylindrical sandwich shell subjected to radial and axial loads was presented by Kardomateas [21]. Zenkour [22] studied the bending problem of cross-ply laminated plates by the use of the elasticity equations linked with the state space method. Kashtalyan and Menshykova [23] developed elasticity solution for sandwich plates with a FG core.

However, in the above investigations, the permeation effect of the adhesive between layers is neglected. In this paper, 2D elasticity solution is presented for a refined sandwich arch model considering the permeation effect of the adhesive. In the present work, the permeation layer is described as FGM, exponentially graded along the radial direction. The general solution of stresses and deformations with unknown coefficients is obtained by means of the layer-wise method. The coefficients are determined via the recursive matrix method, which is efficient for arches with many layers. The solution obtained is compared with the finite element solution and 1D solution based on the Euler–Bernoulli theory, respectively.

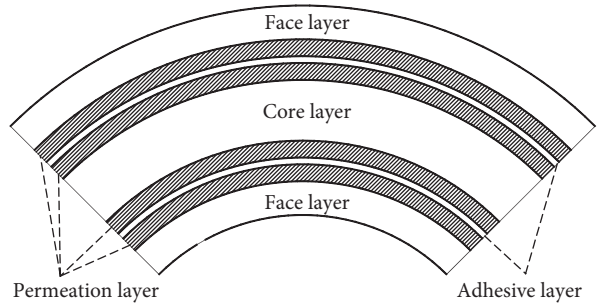

Figure 1: Permeation effect in the sandwich arch.

2. Analytical Model

2.1. Basic Equations. Without loss of generality, we consider a sandwich arch with internal radius R_1, external radius R_2, thickness H, and angle β, composed of p FG layers with each thickness h_i, as shown in Figure 2. The adjacent layers are perfectly bonded, i.e., the deformations are continuous along the radial direction. A polar coordinate system $r-\theta$ is established. The arch is simply supported at two edges and is subjected to radial load $q(\theta)$ acting on the external surface. The permeation layer is the material consisting in the mixture of face (or core) layer material and the adhesive material. Here, we assume its elastic modulus to be exponentially graded along the radial direction, i.e., $E_i(r) = E_0^i e^{k_i r}$, in which E_0^i represents the elastic modulus at the internal surface of the i-th layer and k_i denotes the gradient index. Poisson's ratio μ_i is constant in each layer. The homogeneous layers, i.e., face, core, and adhesive layers, can be included in the model by letting $k_i = 0$ only.

According to the 2D elasticity theory in the polar coordinate [24], the constitutive relations are given by

$$\begin{aligned}
\sigma_r^i &= \frac{E_i(r)}{1-\mu_i^2}\left(\varepsilon_r^i + \mu_i \varepsilon_\theta^i\right),\\
\sigma_\theta^i &= \frac{E_i(r)}{1-\mu_i^2}\left(\mu_i \varepsilon_r^i + \varepsilon_\theta^i\right),\\
\tau_{r\theta}^i &= \frac{E_i(r)}{2\left(1+\mu_i\right)}\gamma_{r\theta}^i,\\
&\qquad\qquad i = 1, 2, \ldots, p,
\end{aligned} \tag{1}$$

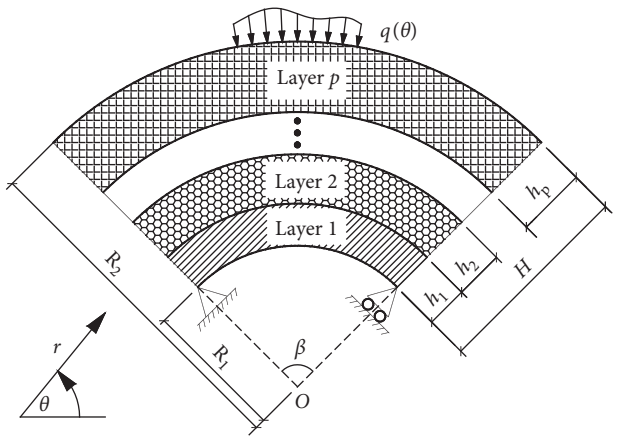

Figure 2: Simply supported sandwich FGM arch.

in which σ_θ^i and σ_r^i are the circumferential and radial normal stresses, respectively; $\tau_{r\theta}^i$ is the shear stress; ε_θ^i and ε_r^i are the circumferential and radial normal strains, respectively; and $\gamma_{r\theta}^i$ is the shear strain. The geometrical equations are

$$\begin{aligned}
\varepsilon_r^i &= \frac{\partial u_r^i}{\partial r},\\
\varepsilon_\theta^i &= \frac{u_r^i}{r} + \frac{1}{r}\frac{\partial u_\theta^i}{\partial \theta},\\
\gamma_{r\theta}^i &= \frac{1}{r}\frac{\partial u_r^i}{\partial \theta} + \frac{\partial u_\theta^i}{\partial r} - \frac{u_\theta^i}{r},\\
&\qquad i = 1, 2, \ldots, p,
\end{aligned} \tag{2}$$

in which u_θ^i and u_r^i are the deformation components in the circumferential and radial directions, respectively. The equilibrium equations are given by

$$\begin{aligned}
\frac{\partial \sigma_r^i}{\partial r} + \frac{1}{r}\frac{\partial \tau_{r\theta}^i}{\partial \theta} + \frac{\sigma_r^i - \sigma_\theta^i}{r} &= 0,\\
\frac{1}{r}\frac{\partial \sigma_\theta^i}{\partial \theta} + \frac{\partial \tau_{r\theta}^i}{\partial r} + \frac{2\tau_{r\theta}^i}{r} &= 0,\\
&\qquad i = 1, 2, \ldots, p.
\end{aligned} \tag{3}$$

The simply supported boundary conditions of the arch are

$$\sigma_\theta^i = u_r^i = 0, \quad \text{at } \theta = 0, \beta, i = 1, 2, \ldots, p. \tag{4}$$

The load condition on the external and internal surfaces of the arch can be expressed by

$$\begin{aligned}
\sigma_r^p &= -q(\theta),\\
\tau_{r\theta}^p &= 0,\\
&\qquad \text{at } r = R_2,\\
\sigma_r^1 &= 0,\\
\tau_{r\theta}^1 &= 0,\\
&\qquad \text{at r} = R_1.
\end{aligned} \tag{5}$$

2.2. General Solution for a Sublayer. By combining equations (1)–(3), two partial differential equations with respect to u_θ^i and u_r^i are derived:

$$\begin{aligned}
&\frac{\partial^2 u_r^i}{\partial r^2} + \frac{1}{r}\frac{\partial u_r^i}{\partial r} - \frac{u_r^i}{r^2} + \frac{1+\mu_i}{2}\frac{1}{r}\frac{\partial^2 u_\theta^i}{\partial r\,\partial \theta} - \frac{3-\mu_i}{2}\frac{1}{r^2}\frac{\partial u_\theta^i}{\partial \theta}\\
&\quad + \frac{1-\mu_i}{2r^2}\frac{\partial^2 u_r^i}{\partial \theta^2} + k_i\frac{\partial u_r^i}{\partial r} + k_i\mu_i\frac{u_r^i}{r} + k_i\mu_i\frac{1}{r}\frac{\partial u_\theta^i}{\partial \theta} = 0,\\
&\frac{\partial^2 u_\theta^i}{\partial r^2} + \frac{1}{r}\frac{\partial u_\theta^i}{\partial r} - \frac{u_\theta^i}{r^2} + \frac{1+\mu_i}{1-\mu_i}\frac{1}{r}\frac{\partial^2 u_r^i}{\partial r\,\partial \theta} + \frac{3-\mu_i}{1-\mu_i}\frac{1}{r^2}\frac{\partial u_r^i}{\partial \theta}\\
&\quad + \frac{2}{1-\mu_i}\frac{1}{r^2}\frac{\partial^2 u_\theta^i}{\partial \theta^2} + k_i\frac{1}{r}\frac{\partial u_r^i}{\partial \theta} + k_i\frac{\partial u_\theta^i}{\partial r} - k_i\frac{u_\theta^i}{r} = 0,\\
&\qquad i = 1, 2, \ldots, p.
\end{aligned} \tag{6}$$

Here, the above equations are solved by the layer-wise method [25]. According to this method, each arch layer is divided into λ sublayers each with very small thickness so that the variable r in equation (6) can be taken as a constant. The radius, the middle plane of the j-th ($j = 1,2, \ldots, p\lambda$) sublayer, is denoted by $\widehat{r}_j$. The distances from the arch center O to the internal and external surfaces of the j-th sublayer are, respectively, represented by d_j^0 and d_j^1. Then, we expand the deformation components of the j-th sublayer into Fourier series:

$$\begin{aligned}
u_r^j(r,\theta) &= \sum_{m=1}^{\infty} R_m^j r)\sin(\alpha_m\theta),\\
u_\theta^j(r,\theta) &= \sum_{m=1}^{\infty} \Theta_m^j(r)\cos(\alpha_m\theta),\\
&\qquad j = 1, 2, \ldots, p\lambda,
\end{aligned} \tag{7}$$

where $\alpha_m = (m\pi/\beta)$. Substituting equation (7) into equation (6), we obtain two ordinary differential equations:

$$\begin{aligned}
&\frac{d^2 R_m^j(r)}{dr^2} + \frac{1}{\widehat{r}_j}\frac{dR_m^j(r)}{dr} - \left[1 + \frac{(1-\mu_i)(\alpha_m)^2}{2}\right]\frac{R_m^j(r)}{(\widehat{r}_j)^2}\\
&\quad - \frac{(1+\mu_i)\alpha_m}{2}\frac{1}{\widehat{r}_j}\frac{d\Theta_m^j(r)}{dr} + \frac{(3-\mu_i)\alpha_m}{2}\frac{\Theta_m^j(r)}{(\widehat{r}_j)^2}\\
&\quad + k_i\frac{dR_m^j(r)}{dr} + k_i\mu_i\frac{R_m^j(r)}{\widehat{r}_j} - k_i\alpha_m\mu_i\frac{\Theta_m^j(r)}{\widehat{r}_j} = 0,\\
&\frac{d^2\Theta_m^j(r)}{dr^2} + \frac{1}{\widehat{r}_j}\frac{d\Theta_m^j(r)}{dr} - \left[1 + \frac{2(\alpha_m)^2}{1-\mu_i}\right]\frac{\Theta_m^j(r)}{(\widehat{r}_j)^2}\\
&\quad + \frac{(1+\mu_i)\alpha_m}{1-\mu_i}\frac{1}{\widehat{r}_j}\frac{dR_m^j(r)}{dr} + \frac{(3-\mu_i)\alpha_m}{1-\mu_i}\frac{R_m^j(r)}{(\widehat{r}_j)^2}\\
&\quad + k_i\alpha_m\frac{R_m^j(r)}{\widehat{r}_j} + k_i\frac{d\Theta_m^j(r)}{dr} - k_i\frac{\Theta_m^j(r)}{\widehat{r}_j} = 0,\\
&\qquad m = 1, 2, 3, \ldots, j = 1, 2, \ldots, p\lambda, i = \left[\frac{j}{\lambda}\right] + 1,
\end{aligned} \tag{8}$$

where $[j/\lambda]$ means the integer part of j/λ. The solution of equation (8) is

$$R_m^j(r) = \sum_{n=1}^{4} a_{mn}^j e^{s_{mn}^j r},$$
$$\Theta_m^j(r) = \sum_{n=1}^{4} \xi_{mn}^j a_{mn}^j e^{s_{mn}^j r}, \quad (9)$$
$$m = 1, 2, 3 \ldots, j = 1, 2, \ldots, p\lambda,$$

in which a_{mn}^j are unknown coefficients, and s_{mn}^j are the four roots of the following quartic equation:

$$\left[(\widehat{r}_j)^2 (s_{mn}^j)^2 + \widehat{r}_j (k_i \widehat{r}_j + 1) s_{mn}^j - k_i \widehat{r}_j - 1 + \frac{2(\alpha_m)^2}{1-\mu_i}\right]$$
$$\cdot \left[(\widehat{r}_j)^2 (s_{mn}^j)^2 + \widehat{r}_j (k_i \widehat{r}_j + 1) s_{mn}^j + k_i \mu_i \widehat{r}_j - 1 + \frac{(1-\mu_i)(\alpha_m)^2}{2}\right]$$
$$+ \left[\frac{(1+\mu_i)\alpha_m}{1-\mu_i} \widehat{r}_j s_{mn}^j + k_i \alpha_m \widehat{r}_j + \frac{(3-\mu_i)\alpha_m}{1-\mu_i}\right] \quad (10)$$
$$\times \left[\frac{(1+\mu_i)\alpha_m}{2} \widehat{r}_j s_{mn}^j + k_i \alpha_m \mu_i \widehat{r}_j - \frac{(3-\mu_i)\alpha_m}{2}\right] = 0,$$
$$m = 1, 2, 3 \ldots, n = 1, 2, 3, 4, j = 1, 2, \ldots, p\lambda, i = \left[\frac{j}{\lambda}\right] + 1,$$

and ξ_{mn}^j can be expressed by s_{mn}^j as follows:

$$\xi_{mn}^j = \frac{(\widehat{r}_j)^2 (s_{mn}^j)^2 + k_i (\widehat{r}_j)^2 s_{mn}^j + k_i \mu_i \widehat{r}_j + s_{mn}^j \widehat{r}_j + ((1-\mu_i)(\alpha_m)^2/2) - 1}{((1+\mu_i)\alpha_m/2) r s_{mn}^j + k_i \alpha_m \mu_i \widehat{r}_j - ((3-\mu_i)\alpha_m/2)}, \quad (11)$$
$$m = 1, 2, 3 \ldots, n = 1, 2, 3, 4, j = 1, 2, \ldots, p\lambda, i = \left[\frac{j}{\lambda}\right] + 1.$$

Substituting equation (9) into equation (7), the general solutions of the deformation components with unknown coefficients are obtained:

$$u_r^j(r, \theta) = \sum_{m=1}^{\infty} \sum_{n=1}^{4} a_{mn}^j e^{s_{mn}^j r} \sin(\alpha_m \theta),$$
$$u_\theta^j(r, \theta) = \sum_{m=1}^{\infty} \sum_{n=1}^{4} \xi_{mn}^j a_{mn}^j e^{s_{mn}^j r} \cos(\alpha_m \theta), \quad (12)$$
$$j = 1, 2, \ldots, p\lambda.$$

Substitution of equation (12) into equations (1) and (2) gives the general solutions of the stress components

$$\sigma_r^i(r, \theta) = \frac{E_i(r)}{1-\mu_i^2} \sum_{m=1}^{\infty} \sum_{n=1}^{4} \left(s_{mn}^j + \frac{\mu_i}{r} - \frac{\alpha_m \mu_i \xi_{mn}^j}{r}\right) a_{mn}^j e^{s_{mn}^j r} \sin(\alpha_m \theta),$$
$$\sigma_\theta^i(r, \theta) = \frac{E_i(r)}{1-\mu_i^2} \sum_{m=1}^{\infty} \sum_{n=1}^{4} \left(\mu_i s_{mn}^j + \frac{1}{r} - \frac{\alpha_m \xi_{mn}^j}{r}\right) a_{mn}^j e^{s_{mn}^j r} \sin(\alpha_m \theta),$$
$$\tau_{r\theta}^i = \frac{E_i(r)}{2(1+\mu_i)} \sum_{m=1}^{\infty} \sum_{n=1}^{4} \left(\frac{\alpha_m}{r} + \xi_{mn}^j s_{mn}^j - \frac{\xi_{mn}^j}{r}\right) a_{mn}^j e^{s_{mn}^j r} \cos(\alpha_m \theta),$$
$$j = 1, 2, \ldots, p\lambda, i = \left[\frac{j}{\lambda}\right] + 1. \quad (13)$$

2.3. Recursive Matrix Method. The out-of-plane variables, i.e., u_θ^j, u_r^j, σ_r^j, and $\tau_{r\theta}^j$, of each sublayer can be rearranged into the vector form

$$\begin{bmatrix} u_\theta^j(r,\theta) \\ u_r^j(r,\theta) \\ \sigma_r^j(r,\theta) \\ \tau_{r\theta}^j(r,\theta) \end{bmatrix} = \sum_{m=1}^{\infty} \begin{bmatrix} \Theta_m^j(r)\cos(\alpha_m\theta) \\ R_m^j(r)\sin(\alpha_m\theta) \\ Y_m^j(r)\sin(\alpha_m\theta) \\ Z_m^j(r)\cos(\alpha_m\theta) \end{bmatrix}, \quad j = 1, 2, \ldots, p\lambda. \tag{14}$$

By substituting equations (12) and (13) into equation (14), $\Theta_m^j(r)$, $R_m^j(r)$, $Y_m^j(r)$, and $Z_m^j(r)$ can be further rearranged into the matrix form as follows:

$$\boldsymbol{\Psi}_m^j(r) = \boldsymbol{\Omega}_m^j(r)\Gamma_m^j(t), \quad m = 1, 2, 3 \ldots, j = 1, 2, \ldots, p\lambda, i = \left[\frac{j}{\lambda}\right] + 1, \tag{15}$$

in which

$$\boldsymbol{\Psi}_m^j(r) = \begin{bmatrix} \Theta_m^j(r) & R_m^j(r) & Y_m^j(r) & Z_m^j(r) \end{bmatrix}^T,$$

$$\Gamma_m^j = \begin{bmatrix} a_{m1}^j & a_{m2}^j & a_{m3}^j & a_{m4}^j \end{bmatrix}^T,$$

$$\boldsymbol{\Omega}_m^j(r) = \begin{bmatrix} \xi_{m1}^j a_{m1}^j e^{s_{m1}^j r} & \xi_{m2}^j a_{m2}^j e^{s_{m2}^j r} & \xi_{m3}^j a_{m3}^j e^{s_{m3}^j r} & \xi_{m4}^j a_{m4}^j e^{s_{m4}^j r} \\ a_{m1}^j e^{s_{m1}^j r} & a_{m2}^j e^{s_{m2}^j r} & a_{m3}^j e^{s_{m3}^j r} & a_{m4}^j e^{s_{m4}^j r} \\ \frac{E_i(r)}{1-\mu_i^2}\left(s_{m1}^j + \frac{\mu_i - \mu_i\alpha_m\xi_{m1}^j}{r}\right)a_{m1}^j e^{s_{m1}^j r} & \frac{E_i(r)}{1-\mu_i^2}\left(s_{m1}^j + \frac{\mu_i - \mu_i\alpha_m\xi_{m1}^j}{r}\right)a_{m2}^j e^{s_{m2}^j r} & \frac{E_i(r)}{1-\mu_i^2}\left(s_m^j + \frac{\mu_i - \mu_i\alpha_m\xi_m^j}{r}\right)a_{m3}^j e^{s_{m3}^j r} & \frac{E_i(r)}{1-\mu_i^2}\left(s_m^j + \frac{\mu_i - \mu_i\alpha_m\xi_m^j}{r}\right)a_{m4}^j e^{s_{m4}^j r} \\ \frac{E_i(r)}{2(1+\mu_i)}\left(\frac{\alpha_m - \xi_{m1}^j}{r} + \xi_{m1}^j s_{m1}^j\right)a_{m1}^j e^{s_{m1}^j r} & \frac{E_i(r)}{2(1+\mu_i)}\left(\frac{\alpha_m - \xi_{m2}^j}{r} + \xi_{m2}^j s_{m2}^j\right)a_{m2}^j e^{s_{m2}^j r} & \frac{E_i(r)}{2(1+\mu_i)}\left(\frac{\alpha_m - \xi_{m3}^j}{r} + \xi_{m3}^j s_{m3}^j\right)a_{m3}^j e^{s_{m3}^j r} & \frac{E_i(r)}{2(1+\mu_i)}\left(\frac{\alpha_m - \xi_{m4}^j}{r} + \xi_{m4}^j s_{m4}^j\right)a_{m4}^j e^{s_{m4}^j r} \end{bmatrix}. \tag{16}$$

By replacing r in the above equation with d_j^0 and d_j^1, respectively, one has

$$\begin{aligned} \boldsymbol{\Psi}_m^j(d_j^0) &= \boldsymbol{\Omega}_m^j(d_j^0)\Gamma_m^j, \\ \boldsymbol{\Psi}_m^j(d_j^1) &= \boldsymbol{\Omega}_m^j(d_j^1)\Gamma_m^j, \\ m &= 1, 2, 3 \ldots, j = 1, 2, \ldots, p\lambda, \end{aligned} \tag{17}$$

By eliminating Γ_m^j in the two equations of equation (17), we obtain

$$\boldsymbol{\Psi}_m^j(d_j^1) = \boldsymbol{\Omega}_m^j(d_j^1)\boldsymbol{\Omega}_m^j(d_j^0)^{-1}\boldsymbol{\Psi}_m^j(d_j^0), \quad m = 1, 2, 3 \ldots, j = 1, 2, \ldots, p\lambda. \tag{18}$$

The out-of-plane variables are continuous between the adjacent sublayers, i.e.,

$$\boldsymbol{\Psi}_m^j(d_j^1) = \boldsymbol{\Psi}_m^j(d_{j+1}^0), \quad m = 1, 2, 3 \ldots, j = 1, 2, \ldots, p\lambda. \tag{19}$$

By combining equation (18) with equation (19), the relation between the internal and external surfaces of the arch is obtained:

$$\begin{aligned} \boldsymbol{\Psi}_m^p(d_p^1) &= \left[\prod_{j=p\lambda}^{1} \boldsymbol{\Omega}_m^j(d_j^1)\boldsymbol{\Omega}_m^j(d_1^0)^{-1}\right]\boldsymbol{\Psi}_m^1(d_1^0), \\ m &= 1, 2, 3 \ldots, j = 1, 2, \ldots, p\lambda. \end{aligned} \tag{20}$$

We define

$$\begin{bmatrix} S_m^{11}(t) & S_m^{12}(t) \\ S_m^{21}(t) & S_m^{22}(t) \end{bmatrix} = \left[\prod_{j=p\lambda}^{1} \boldsymbol{\Omega}_m^j(d_j^1)\boldsymbol{\Omega}_m^j(d_j^0)^{-1}\right], \quad m = 1, 2, 3 \ldots, \tag{21}$$

in which $S_m^{11}(t)$, $S_m^{12}(t)$, $S_m^{21}(t)$, and $S_m^{22}(t)$ are the 2×2 submatrixes. Equation (20) can be written as

$$\begin{bmatrix} \Theta_m^p(d_p^1) \\ R_m^p(d_p^1) \\ Y_m^p(d_p^1) \\ Z_m^p(d_p^1) \end{bmatrix} = \begin{bmatrix} S_m^{11}(t) & S_m^{12}(t) \\ S_m^{21}(t) & S_m^{22}(t) \end{bmatrix} \begin{bmatrix} \Theta_m^1(d_1^0) \\ R_m^1(d_1^0) \\ Y_m^1(d_1^0) \\ Z_m^1(d_1^0) \end{bmatrix}, \quad m = 1, 2, 3 \ldots. \tag{22}$$

Then, equation (22) is further decomposed into two matrix equations as follows:

$$\begin{aligned} \begin{bmatrix} \Theta_m^p(d_1^0) \\ R_m^p(d_1^0) \end{bmatrix} &= S_m^{11}(t)\begin{bmatrix} \Theta_m^1(d_1^0) \\ R_m^1(d_1^0) \end{bmatrix} + S_m^{12}(t)\begin{bmatrix} Y_m^1(d_1^0) \\ Z_m^1(d_1^0) \end{bmatrix}, \\ \begin{bmatrix} Y_m^p(d_p^1) \\ Z_m^p(d_p^1) \end{bmatrix} &= S_m^{21}(t)\begin{bmatrix} \Theta_m^1(d_1^0) \\ R_m^1(d_1^0) \end{bmatrix} + S_m^{22}(t)\begin{bmatrix} Y_m^1(d_1^0) \\ Z_m^1(d_1^0) \end{bmatrix}, \\ m &= 1, 2, 3, \ldots \end{aligned} \tag{23}$$

The load function $q(\theta)$ in equation (5) can be expanded into Fourier series

$$q(\theta) = \sum_{m=1}^{\infty} q_m \sin(\alpha_m \theta),$$
$$q_m = \frac{2}{\beta} \int_0^{\beta} q(\theta) \sin(\alpha_m \theta) \mathrm{d}\theta. \quad (24)$$

Substituting the load condition into equation (23), one has

$$\begin{bmatrix} \Theta_m^1(d_1^0) \\ R_m^1(d_1^0) \end{bmatrix} = S_m^{21}(t)^{-1} \begin{bmatrix} -q_m \\ 0 \end{bmatrix}, \quad m = 1, 2, 3, \ldots. \quad (25)$$

By reusing equations (18) and (19), $\mathbf{\Psi}_m^j(d_j^1)$ is obtained:

$$\mathbf{\Psi}_m^j(d_j^1) = \left[\prod_{k=j}^{1} \mathbf{\Omega}_m^k(d_k^1) \mathbf{\Omega}_m^k(d_k^0)^{-1} \right] \mathbf{\Psi}_m^1(d_1^0), \quad j = 1, 2, \ldots, p\lambda, m = 1, 2, 3, \ldots. \quad (26)$$

Finally, the coefficients are determined:

$$\Gamma_m^j = \mathbf{\Omega}_m^j(d_j^1)^{-1} \mathbf{\Psi}_m^j(d_j^1), \quad j = 1, 2, \ldots, p\lambda, m = 1, 2, 3, \ldots. \quad (27)$$

Substituting the coefficients back into equations (12) and (13), the solution of stress and deformation components is obtained.

It can be observed that, as the layer number increases, only the computation effort in equation (23) slightly increases. Therefore, the present method is highly efficient for arches with many layers. Moreover, other boundary conditions can also be applied in the present model. For example, the clamped condition can be equivalent to the simply supported one acted by the unknown horizontal reaction, which can be further determined by the zero displacement condition at the clamped end [26].

3. Example and Discussion

In the following examples, the infinite series in the solution are truncated into the finite term, i.e., $m = 1,2, \ldots, N$.

3.1. Convergence Study. Consider a simply supported sandwich arch with $R_1 = 1000$ mm, $R_2 = 1240$ mm, and $\beta = \pi/4$. The face, core, and adhesive layers are made of carbon fiber, polyurethane foam, and epoxy, respectively. The thickness, elastic modulus, and Poisson's ratio of each arch layer are listed in Table 1.

Since the governing equations of equation (6) are solved by the layer-wise method, the effect of the divided number on the solution accuracy should be analyzed first. We assume the arch is subjected to radial load $q(\theta) = \sin(\pi/\beta)$ N/mm. For sinusoidal load, one series term is sufficient, i.e., $N = 1$. Table 2 gives the present solution of stresses and deformations in the face layer and permeation layer with different divided number λ, respectively. It can be found that the solution tends to be convergent with the increase of λ. Moreover, the solution in the face layer converges faster than that in the permeation layer. The solution is accurate with at least three significant figures when $\lambda = 10$. Therefore, the divided number is taken as $\lambda = 10$ for the following calculations.

Table 1: The thickness and material property for each layer in the sandwich arch with nine layers.

i	Layer type	h_i(mm)	E_i(MPa)	μ_i
1	Face	18	120000	0.3
2	Permeation	20	$E_1 e^{[(r-18)\ln(E_3/E_1)]/h_2}$	0.3
3	Adhesive	2	11000	0.3
4	Permeation	20	$E_3 e^{[(r-40)\ln(E_5/E_3)]/h_4}$	0.3
5	Core	120	70	0.3
6	Permeation	20	$E_5 e^{[(r-180)\ln(E_7/E_5)]/h_6}$	0.3
7	Adhesive	2	11000	0.3
8	Permeation	20	$E_7 e^{[(r-222)\ln(E_9/E_7)]/h_8}$	0.3
9	Face	18	120000	0.3

Table 2: The present solution of stresses and deformations in the face layer ($i = 1$) and permeation layer ($i = 2$) with different sublayer divided number λ, respectively.

r (mm)	λ	σ_θ^i (MPa) $\theta = \pi/8$	σ_r^i (MPa) $\theta = \pi/8$	$\tau_{r\theta}^i$ (MPa) $\theta = 0$	u_θ^i (mm) $\theta = 0$	u_r^i (mm) $\theta = \pi/8$
1018 ($i = 1$)	2	−24.52	0.8247	−4.114	−1.271	−5.295
	4	−25.24	0.8295	−4.141	−1.287	−5.366
	6	−25.40	0.8303	−4.145	−1.290	−5.379
	8	−25.44	0.8306	−4.147	−1.291	−5.384
	10	−25.47	0.8307	−4.147	−1.292	−5.386
1038 ($i = 2$)	2	−33.75	−0.02910	−1.485	−0.8844	−5.290
	4	−25.42	−0.01452	−1.541	−0.8952	−5.360
	6	−23.07	−0.01168	−1.553	−0.8973	−5.373
	8	−21.98	−0.01068	−1.557	−0.8980	−5.376
	10	−21.90	−0.01061	−1.558	−0.8984	−5.378

Then, the convergence property associated with the series terms for the solution is studied. The arch is acted by uniform load $q(\theta) = 1$ N/mm. The present solution of stresses and deformations with different series number N is given in Table 3. It can be found that the present solution is rapidly convergent and has high convergence precision with four significant digits when $N = 9$. Thus, the number of series terms is fixed at $N = 9$ unless stated.

3.2. Comparison Study. We still consider the simply supported sandwich arch in Section 3.1; however, the acting load is $q(\theta) = 1$ N/mm and β is the variable. The present solution is compared with the finite element (FE) solution obtained by ANSYS. In the FE modeling, the PLANE-182 element is used to simulate all the layers. Due to the symmetry of the arch, only half part of the arch is modeled, as shown in Figure 3. The FE mesh is created by dividing the arch length into 50 elements, while the thicknesses of face, adhesive, core, and permeation layers is divided into 4, 1, 20, and 10 elements, respectively. Figure 4 shows the comparison of stresses and deformations between the present solution and FE solution with different arch angle β. It can be found that the FE solution is in good agreement with the present one; however, the FE solution with the fine mesh is time

Table 3: The convergence property of the present solution in the face layer ($i = 1$) and permeation layer ($i = 2$) with different series number N, respectively.

r (mm)	N	σ_θ^i(MPa) $\theta = \pi/8$	σ_r^i(MPa) $\theta = \pi/8$	$\tau_{r\theta}^i$(MPa) $\theta = 0$	u_θ^i(mm) $\theta = 0$	u_r^i(mm) $\theta = \pi/8$
1018 ($i = 1$)	1	−32.43	1.058	−5.280	−1.645	−6.858
	3	−32.13	1.068	−5.424	−1.645	−6.851
	5	−32.13	1.068	−5.427	−1.645	−6.851
	7	−32.13	1.068	−5.428	−1.645	−6.851
	9	−32.13	1.068	−5.428	−1.645	−6.851
1038 ($i = 2$)	1	−27.17	−0.01300	−1.984	−1.144	−6.850
	3	−26.92	0.02640	−2.037	−1.143	−6.843
	5	−26.93	0.02445	−2.039	−1.143	−6.844
	7	−26.93	0.02459	−2.039	−1.143	−6.844
	9	−26.93	0.02459	−2.039	−1.143	−6.844

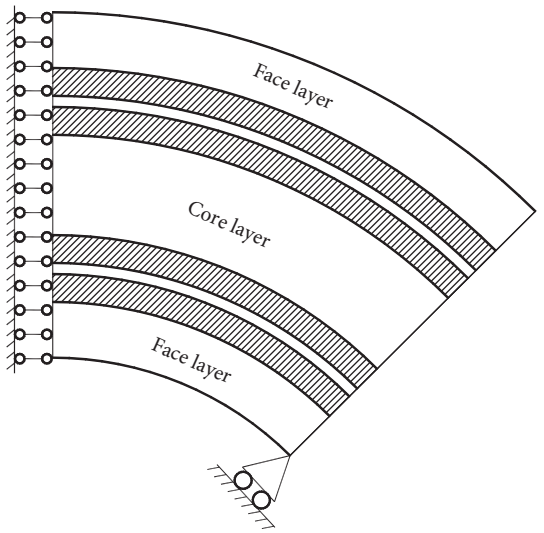

Figure 3: Schematic of the half part in the FE modeling.

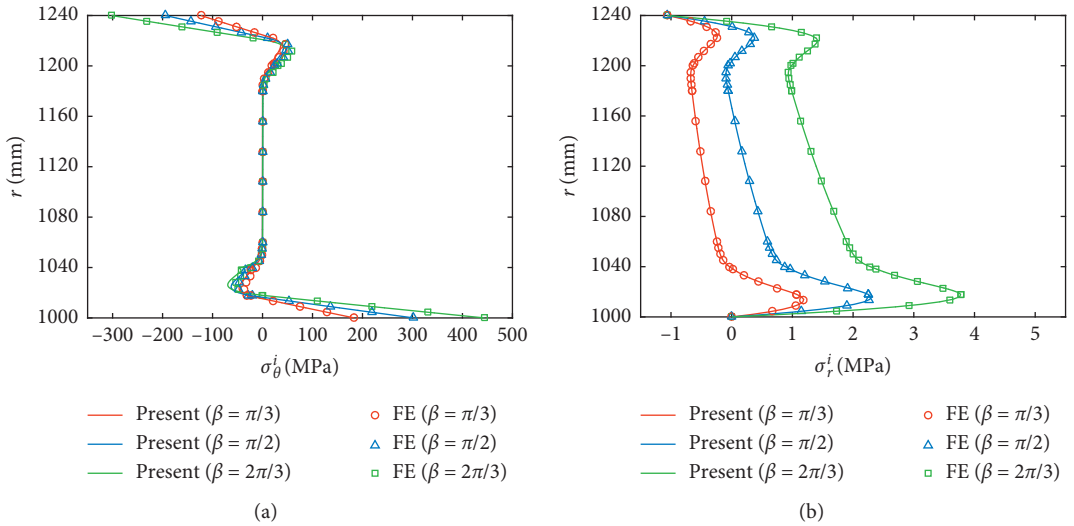

Figure 4: Continued.

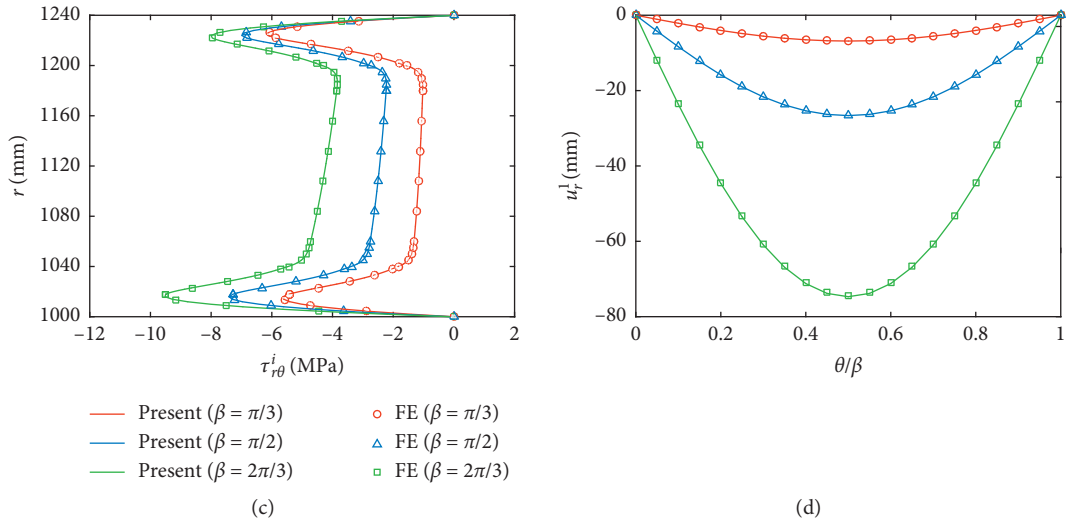

FIGURE 4: The comparison of stresses and deformations between the present solution and FE solution with different arch angles. (a) σ^i_θ at $\theta = \beta/2$. (b) σ^i_r at $\theta = \beta/2$. (c) $\tau^i_{r\theta}$ at $\theta = 0$. (d) u^1_r at $r = R_1$.

TABLE 4: Comparisons of FE results with the present results for different length-to-thickness ratios a/H when $t = 104$ (s), respectively.

h_1 (mm)	Solutions	Present	FE	1D	R_{FE} (%)	R_{1D} (%)
25	σ_m (MPa)	204.8	204.7	204.3	0.0805	0.199
	τ_m (MPa)	−0.7713	−0.7698	−0.7645	0.198	0.691
	u_{rm} (mm)	−15.58	−15.55	−15.44	0.163	0.710
40	σ_m (MPa)	87.21	86.72	86.30	0.563	0.487
	τ_m (MPa)	−0.3445	−0.3441	−0.3413	0.105	0.799
	u_{rm} (mm)	−4.268	−4.246	−4.134	0.516	2.64
50	σ_m (MPa)	57.73	57.28	55.97	0.778	2.28
	τ_m (MPa)	−0.2404	−0.2400	−0.2381	0.165	0.820
	u_{rm} (mm)	−2.326	−2.304	−2.108	0.956	8.53
75	σ_m (MPa)	26.40	26.06	23.44	1.27	10.1
	τ_m (MPa)	−0.1326	−0.1321	−0.1309	0.408	0.878
	u_{rm} (mm)	−0.7969	−0.7856	−0.6401	1.41	18.5

Note: R_{FE} means |(FE-Present)/Present|; R_{1D} means |(1D-Present)/Present|.

TABLE 5: The thickness and material properties for each layer in the sandwich arch with seven layers.

i	Layer type	h_i(mm)	E_i(MPa)	μ_i
1	Face	16	40000	0.3
2	Adhesive	4	9000	0.3
3	Permeation	h_3	$E_2 e^{[(z-20)\ln(E_4/E_2)]/h_3}$	0.3
4	Core	$60 - 2h_3$	70	0.3
5	Permeation	h_3	$E_4 e^{[(z-80+h_3)\ln(E_6/E_4)]/h_5}$	0.3
6	Adhesive	4	9000	0.3
7	Face	16	40000	0.3

consuming, especially in mesh division and calculation. Besides, the stresses and deformations, in absolute values, increase with the increase of β.

By letting $k_i = 0$ in the basic equations, the present solution can be used to predict stresses and deformations for the fully homogeneous layered arch. Consider a sandwich arch composed two face layers sandwiching a relatively soft thin interlayer, which was studied by Galuppi and Royer-Carfagni [7] based on the 1D Euler–Bernoulli theory. The geometric and material parameters are fixed at $q(\theta) = 0.5\,\text{N/mm}^2$, $E_1 = E_3 = 70000\,\text{MPa}$, $E_2 = 2.6\,\text{MPa}$, $\mu_1 = \mu_2 = \mu_3 = 0.3$, $R_1 = 1000\,\text{mm}$, $\beta = \pi/4$, $h_1 = h_3$, and $h_2 = 2\,\text{mm}$. We define three variables: $\sigma_m = \sigma^1_\theta$ at $\theta = 0.5\beta$, $r = R_1$; $\tau_m = \tau^1_{r\theta}$ at $\theta = 0$, $r = R_1 + h_1$; and $u_{rm} = u^1_r$ at $\theta = 0.5\beta$, $r = R_1$. The comparison of σ_m, τ_m, and u_{rm} between the present, FE, and 1D solutions with different layer

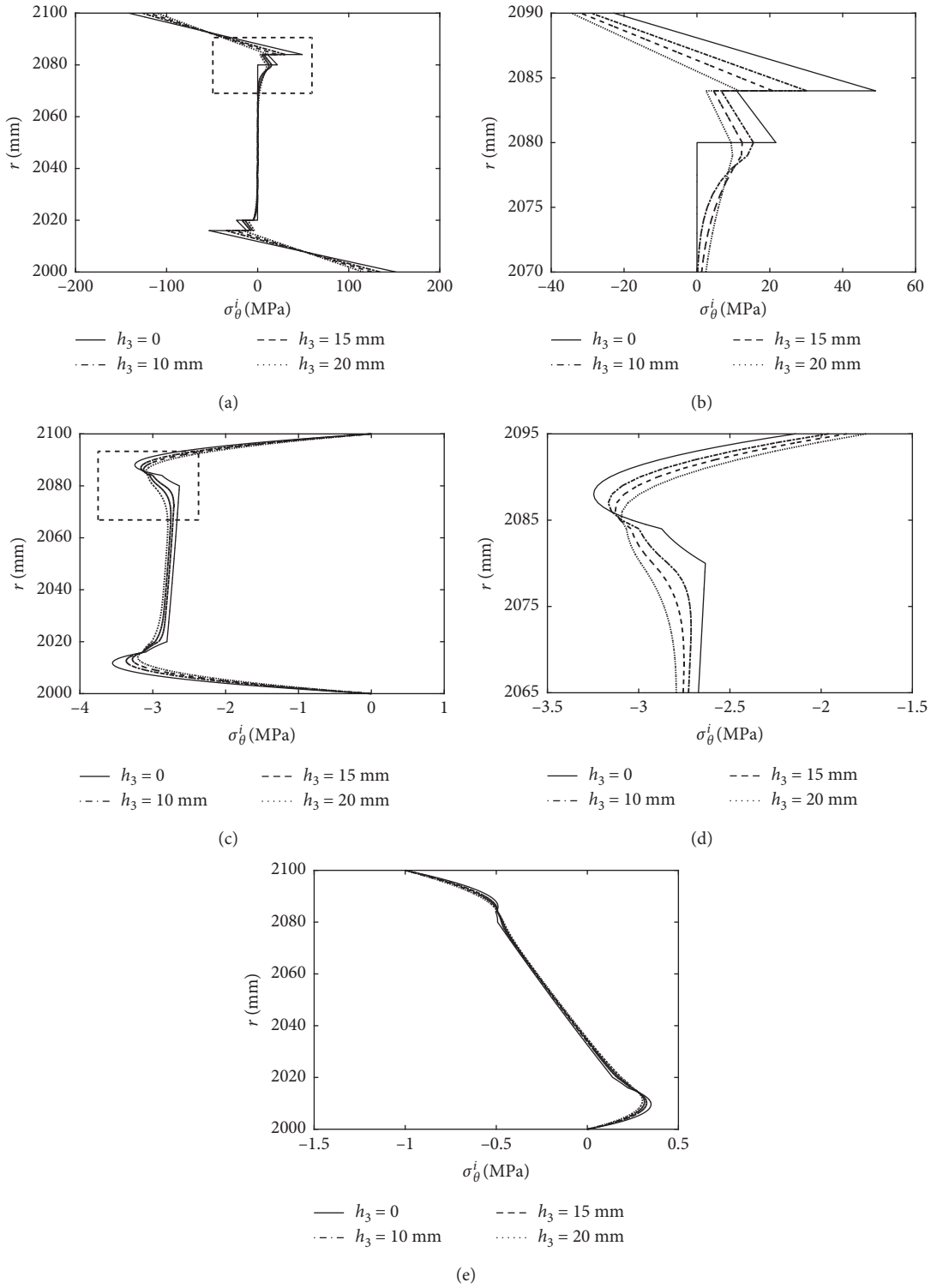

Figure 5: Stress distribution along the radial direction with different permeation thicknesses $h_3 = 0$, 10, 15, and 20 mm, respectively. (a) σ_θ^i at $\theta = \beta/2$. (b) Enlarged view of σ_θ^i. (c) $\tau_{r\theta}^i$ at $\theta = 0$. (d) Enlarged view of $\tau_{r\theta}^i$. (e) σ_r^i at $\theta = 0$.

thicknesses is shown in Table 4. It can be found that the FE solution agrees well with the present solution for all cases. The 1D solution is close to the present one for the thin arch, while the error of 1D solution increases when the arch becomes thick. The errors of σ_m and u_{rm} in 1D solution reach 10.1% and 18.5%, respectively.

3.3. Parametric Study. Consider a simply supported sandwich arch with five layers with $R_1 = 2000$ mm, $R_2 = 2100$ mm, and $\beta = \pi/8$ acted by distributed load $q(\theta) = \sin(\pi/\beta)$ N/mm. Here, only the permeation effect between the adhesive and core layers is considered. The thickness and the material property of each layer are given in Table 5. The distributions of

σ_θ^i, $\tau_{r\theta}^i$, and σ_r^i along the radial direction with different permeation thicknesses $h_3 = 0$, 10, 15, and 20 mm are shown in Figure 5, in which $h_3 = 0$ means the special case of the sandwich arch without the permeation layer. It can be found that (i) the absolute value of σ_θ^i at the internal and external surfaces in the face layers decreases with the increase of h_3; (ii) the absolute peak value of $\tau_{r\theta}^i$ in the face layers decreases with the increase of h_3, while that in the core layer increases with the increase of h_3; (iii) the distributions of σ_θ^i and $\tau_{r\theta}^i$ tend to be smooth with the increase of h_3; and (iv) the distribution of σ_r^i is less affected by h_3.

4. Conclusions

Based on the elasticity theory in the polar coordinate, a refined model of the simply supported sandwich arch considering the permeation effect of the adhesive is presented. By means of the recursive matrix method, the solution can be efficiently obtained for the arch with many layers. Conclusions are summarized as follows:

(1) The present solution is rapidly convergent with the increase of series term and sublayer number.

(2) The finite element solution with the fine mesh is in agreement with the present solution, while the finite element method is time consuming in mesh division and calculation.

(3) The 1D solution, based on the Euler–Bernoulli theory, is close to the present solution for thin arches; however, the error increases with the increase of arch thickness.

(4) The permeation thickness has considerable effect on the stress and deformation distributions. The distributions of circumferential normal stress and the shear stress tend to be smooth in the radial direction as the permeation thickness increases.

Data Availability

The data used to support the findings of this study are available from the corresponding author upon request.

Conflicts of Interest

The authors declare that they have no conflicts of interest.

Acknowledgments

This work was financially supported by the National Natural Science Foundation of China (Grant nos. 51608264, 51978336, and 51778285) and the Natural Science Foundation for distinguished Young Scholars of Jiangsu Province (Grant no. BK20190034).

References

[1] J. B. Yan, J. R. Liew, M. H. Zhang, and K. M. A. Sohel, "Experimental and analytical study on ultimate strength behavior of steel-concrete-steel sandwich composite beam structures," *Materials and Structures*, vol. 48, no. 5, pp. 1523–1544, 2015.

[2] S. Pappadà, R. Rametta, A. Passaro, L. Lanzilotto, and A. Maffezzoli, "Processing, mechanical properties, and interfacial bonding of a thermoplastic core-foam/composite-skin sandwich panel," *Advances in Polymer Technology*, vol. 29, no. 3, pp. 137–145, 2010.

[3] C.-S. Chen, F.-H. Liu, and W.-R. Chen, "Dynamic characteristics of functionally graded material sandwich plates in thermal environments," *Mechanics of Advanced Materials and Structures*, vol. 24, no. 2, pp. 157–167, 2016.

[4] S. Cheng, P. Qiao, F. Chen, W. Fan, and Z. Zhu, "Free vibration analysis of fiber-reinforced polymer honeycomb sandwich beams with a refined sandwich beam theory," *Journal of Sandwich Structures & Materials*, vol. 18, no. 2, pp. 242–260, 2016.

[5] V. Tahouneh, "Vibration and mode shape analysis of sandwich panel with MWCNTs FG-reinforcement core," *Steel and Composite Structures*, vol. 25, no. 3, pp. 347–360, 2017.

[6] R. Huo, W. Liu, P. Wu, and D. Zhou, "Analytical solutions for sandwich plates considering permeation effect by 3-D elasticity theory, steel," *Steel and Composite Structures*, vol. 25, no. 2, pp. 127–139, 2017.

[7] L. Galuppi and G. Royer-Carfagni, "Analytical approach à la Newmark for curved laminated glass," *Composites Part B: Engineering*, vol. 76, pp. 65–78, 2015.

[8] H. Raissi, M. Shishehsaz, and S. Moradi, "Stress distribution in a five-layer sandwich plate with FG face sheets using layerwise method," *Mechanics of Advanced Materials and Structures*, vol. 26, no. 14, pp. 1234–1244, 2019.

[9] M. Mohammadimehr, H. B. Zarei, A. Parakandeh, and A. G. Arani, "Vibration analysis of double-bonded sandwich microplates with nanocomposite facesheets reinforced by symmetric and un-symmetric distributions of nanotubes under multi physical fields," *Structural Engineering and Mechanics*, vol. 64, no. 3, pp. 361–379, 2017.

[10] M. Livani, K. MalekzadehFard, and S. Shokrollahi, "Higher order flutter analysis of doubly curved sandwich panels with variable thickness under aerothermoelastic loading," *Structural Engineering and Mechanics*, vol. 60, no. 1, pp. 1–19, 2016.

[11] A. Bouchafa, M. B. Bouiadjra, M. S. A. Houari, and A. Tounsi, "Thermal stresses and deflections of functionally graded sandwich plates using a new refined hyperbolic shear deformation theory," *Steel and Composite Structures*, vol. 18, no. 6, pp. 1493–1515, 2015.

[12] K. T. Nguyen, T. H. Thai, and T. P. Vo, "A refined higher-order shear deformation theory for bending, vibration and buckling analysis of functionally graded sandwich plates," *Steel and Composite Structures*, vol. 18, no. 1, pp. 91–120, 2015.

[13] O. Rahmani, S. M. R. Khalili, and K. Malekzadeh, "Free vibration response of composite sandwich cylindrical shell with flexible core," *Composite Structures*, vol. 92, no. 5, pp. 1269–1281, 2010.

[14] B. Liu, A. J. M. Ferreira, Y. F. Xing, and A. M. A. Neves, "Analysis of functionally graded sandwich and laminated shells using a layerwise theory and a differential quadrature finite element method," *Composite Structures*, vol. 136, pp. 546–553, 2016.

[15] S. Natarajan and G. Manickam, "Bending and vibration of functionally graded material sandwich plates using an accurate theory," *Finite Elements in Analysis and Design*, vol. 57, pp. 32–42, 2012.

[16] L.-X. Peng, S.-T. Yan, G.-K. Mo, and X. Zhang, "Free vibration analysis of corrugated-core sandwich plates using a meshfree Galerkin method based on the first-order shear

deformation theory," *International Journal of Mechanical Sciences*, vol. 78, pp. 8–18, 2014.

[17] C. H. Thai, A. J. M. Ferreira, S. P. A. Bordas, T. Rabczuk, and H. Nguyen-Xuan, "Isogeometric analysis of laminated composite and sandwich plates using a new inverse trigonometric shear deformation theory," *European Journal of Mechanics—A/Solids*, vol. 43, pp. 89–108, 2014.

[18] J. L. Mantari, A. S. Oktem, and C. Guedes Soares, "A new trigonometric layerwise shear deformation theory for the finite element analysis of laminated composite and sandwich plates," *Computers & Structures*, vol. 94-95, pp. 45–53, 2012.

[19] W. Q. Chen and K. Y. Lee, "Three-dimensional exact analysis of angle-ply laminates in cylindrical bending with interfacial damage via state-space method," *Composite Structures*, vol. 64, no. 3-4, pp. 275–283, 2004.

[20] N. J. Pagano, "Exact solutions for composite laminates in cylindrical bending," *Journal of Composite Materials*, vol. 3, no. 3, pp. 398–411, 1969.

[21] G. A. Kardomateas, "Elasticity solutions for sandwich orthotropic cylindrical shells under external/internal pressure or axial force," *AIAA Journal*, vol. 39, no. 4, pp. 713–719, 2001.

[22] A. M. Zenkour, "Three-dimensional elasticity solution for uniformly loaded cross-ply laminates and sandwich plates," *Journal of Sandwich Structures & Materials*, vol. 9, no. 3, pp. 213–238, 2007.

[23] M. Kashtalyan and M. Menshykova, "Three-dimensional elasticity solution for sandwich panels with a functionally graded core," *Composite Structures*, vol. 87, no. 1, pp. 36–43, 2009.

[24] S. P. Timoshenko and J. C. Goodier, *Theory of Elasticity*, McGraw-Hill, New York, NY, USA, 1970.

[25] W. Q. Chen, Y. F. Wang, J. B. Cai, and G. R. Ye, "Three-dimensional analysis of cross-ply laminated cylindrical panels with weak interfaces," *International Journal of Solids and Structures*, vol. 41, no. 9-10, pp. 2429–2446, 2004.

[26] Y.-p. Xu, D. Zhou, and Y. K. Cheung, "Elasticity solution of clamped-simply supported beams with variable thickness," *Applied Mathematics and Mechanics*, vol. 29, no. 3, pp. 279–290, 2008.

Hindawi
Advances in Polymer Technology
Volume 2020, Article ID 1973626, 15 pages
https://doi.org/10.1155/2020/1973626

Research Article

A Research on Modification Method for NSM FRP-Concrete Bonded Joints Strength Models

Jing Li,[1] Liwen Zhang ,[1] Yanggui Deng,[2] and Junping Zhang[1]

[1]*Department of Civil Engineering, Guangzhou University, Guangzhou, China*
[2]*Zhongdu Engineering Design Co., Ltd., Guangzhou, China*

Correspondence should be addressed to Liwen Zhang; lwzhang@gzhu.edu.cn

Received 7 November 2019; Accepted 17 January 2020; Published 12 March 2020

Guest Editor: Tianyu Xie

A modification method was proposed for near-surface mounted (NSM) fiber-reinforced polymer (FRP)-concrete bonded joints strength prediction models considering model uncertainty. A database consisting of 246 test records was involved. Three bonded joints strength prediction models for NSM FRP reinforcement system were selected for modification. All the three selected models have model uncertainty factors associated with input design parameters. Spearman correlation analysis was used to prove the systematic correlation of the model uncertainty factors. For each model, a regression function f was established to eliminate the systematic nonrandom part of the model uncertainty factor. Then, the model uncertainty factors could be described by random variables obeying logarithmic normal distribution. A reliability analysis using the JC method was carried out to validate the practical significance and value of model modification. This study improves the predictability of FRP NSM reinforcement systems and provides valuable references for model calibration in practical engineering.

1. Introduction

As one of the most effective techniques for the strengthening of aged concrete structures [1, 2], near-surface mounted (NSM) reinforcement involves inserting a reinforcing material into the concrete cover of the structural member which needs to be reinforced. In the past decade, researchers have been working on various studies of the NSM FRP reinforcement techniques, promoting its widespread application [3, 4]. For FRP NSM reinforcement systems, the utilization of FRP's mechanical properties and reinforcement effects depends mainly upon their bonded joints strength [5–7].

Some prediction models have been proposed for NSM FRP-concrete bonded joints strength [2, 8–11]. Model uncertainty inevitably exists due to limited experimental data, incomplete research parameters, and idealized calculation methods, resulting in a certain error between the predicted value and the experimental value. From the perspective of engineering application, the calculated strength less than the measured value is regarded to be conservative, while the opposite is unsafe [12]. At present, the study on how to calibrate existing NSM FRP-concrete bonded joints strength models is still insufficient, unsystematic, and superficial, requiring relative further research [13–16]. Thus, our study is aimed at proposing a calibrating method for commonly used NSM FRP-concrete bonded joints strength models with the consideration of model uncertainty.

A model uncertainty factor was defined and adopted to quantitatively describe the model uncertainty [17]. The key is that this model uncertainty factor must be "random" and should have no dependence on the input design parameters [18]. For some NSM FRP-concrete bonded joints strength prediction models, the model uncertainty factor has a dependency on the design parameters, which does not match the definition. Hence, a regression analysis is needed to eliminate the systematic part from the model uncertainty factor, and the randomness of regression residual needs to be verified.

In this paper, a total of 246 effective NSM FRP pullout test data were gathered. Three NSM FRP-concrete bonded

joints strength models presented by Seracino et al. [19–21], which were confirmed to have model uncertainties, were incorporated for model calibration. The systematic effect on the model uncertainty factor was eliminated by carrying out a multiple regression analysis. The residual part was checked for randomness, and three modified models were obtained. This research can improve the prediction precision of NSM FRP reinforcement systems and provide valuable references for model calibration in practical engineering.

2. Bonded Joints Strength Models

A number of prediction models have been applied to calculate the NSM FRP-concrete bonded joints strength. Three commonly used NSM FRP-concrete bond stress models with model uncertainty were incorporated in this paper. They were proposed by Seracino et al. [16], Ali et al. [20], and Zhang et al. [21] as listed in Table 1 and were abbreviated as SR Model, AM Model, and Zhang Model hereinafter. In this paper, the bonded joints strength was defined as the maximum load in a pullout test [22]. Hence, for the three selected bonded joints stress models, peak loads (bonded joints strength) were calculated according to the bonded joints strength model presented by Seracino et al. [19], as shown in the fifth row in Table 1. In this table, $\tau_{\max}$ is the peak bond stress, f_c is the concrete compression strength, b_p is the width of groove, t_p is the height of FRP, γ is the height-to-width ratio of groove, φ_f is the length-to-width ratio of failure surface, P_{IC} is the peak bond load, $\delta_{\max}$ is the maximum bond slip, L_{per} is the perimeter of failure surface, and $(EA)_P$ is the stiffness of FRP.

3. Experimental Data

Research shows that the bonded joints strength of a FRP NSM reinforcement system is concerned with a variety of factors, e.g., physical dimension and material property [23]. However, it is impractical to take all relevant factors into account [24]. In this paper, five significant influence parameters were selected as the key factors: (1) concrete compression strength f_c, (2) FRP modulus of elasticity E_f, (3) FRP height t_p, (4) FRP thickness t_f, and (5) groove width t_g [25].

A database covering all the five selected key factors and the related bonded joints strength was collected for analysis [26, 27]. Five typical failure modes, occurring on three intermediate materials (FRP, adhesive, and concrete) as well as two interfaces (adhesive-concrete and adhesive-FRP), were incorporated into this paper. According to the critical region where failure may occur, they were, respectively, failures in the interface of concrete and adhesive, in the interface of adhesive and FRP, within the adhesive, in a single material (concrete crushing or FRP rupture), and in the surface of concrete (cracks propagate through the concrete). Of particular note is that this study only took pullout tests into account instead of bending tests here [28]. Because the bonded joints strength of a FRP NSM reinforcement system is normally evaluated by a pullout test.

Table 1: Selected bonded joints strength models.

Reference	Model
Ali et al. [20]	$\tau_{\max} = 0.54\sqrt{f_c}\, b_p^{0.4} t_p^{0.3}$
Zhang et al. [21]	$\tau_{\max} = 1.15\gamma^{0.138} f_c^{0.613}$
Seracino et al. [16]	$\tau_{\max} = (0.802 + 0.078\varphi_f^{0.526}) f_c^{0.6}$
Seracino et al. [19]	$P_{\mathrm{IC}} = \sqrt{\tau_{\max}\delta_{\max}}\sqrt{L_{\mathrm{per}}(EA)_P}$

A total of 246 test data were collected and divided into five sets in terms of their failure modes (as shown in Tables 2–6). As for the fiber type, 5 different fiber were involved, such as carbon FRP (CFRP), aramid FRP (AFRP), glass FRP (GFRP), basalt FRP (BFRP), and graphite FRP.

4. Model Uncertainty Factor

Model uncertainty inevitably exists due to varying degrees of idealization involved in calculation methods. The error between the predicted strength and the experimental value was described by a model uncertainty factor, which can be defined by the following formula [38, 39]:

$$P_u^m = \varepsilon \times P_u^c. \tag{1}$$

P_u^m herein is the actual measuring bonded joints strength, P_u^c is the calculated prediction value, and ε is the model uncertainty factor which can quantitatively evaluate the impact of model uncertainty on the structure. A model uncertainty factor greater than 1 means that the measured value is larger than the calculated strength, and vice versa. Theoretically, the best value of ε is 1.0; therefore, the value getting closer to 1.0 suggests a more accurate model. The coefficient of variance (CV) of ε indicates the dispersion degree of prediction models. The smaller the CV of ε is, the higher the accuracy of the model is.

Practically, ε greater than 1 is regarded to be conservative, while the opposite is unsafe. On the basis of the collected pullout test data, the P_u^c under different failure modes could be calculated. Then, the model uncertainty factor ε could be obtained according to equation (1).

Figures 1–5 plot the contrast between the calculated value P_u^c (vertical axis) and the experimental value P_u^m (horizontal axis) for the three models under five failure modes. If the data points are tightly distributed near the 45-degree line, the model is considered to be accurate. Conversely, the model has a great dispersion. As shown in Figures 1–5, for the three models under the five failure modes, their data points are not distributed near the 45-degree line, indicating that these three models are very discrete.

Tables 7–11 display the statistics of calculated ε under five failure modes, including their mean value, the standard deviation (SD), and the coefficient of variation (CV). The tables below have shown the CV of ε ranging from 0.4 (the AM Model and Zhang Model under adhesive failure mode) to 0.61 (the three models under adhesive-concrete interface failure mode). However, the CV of a model uncertainty factor ranging from 0.2 to 0.3 is usually considered to be reasonable [40].

Table 2: Database under the adhesive-concrete interface failure mode.

Reference	Tests number	Material	f_c (MPa)	E_f (GPa)	t_p (mm)	t_f (mm)	t_g (mm)
[13]	16	CFRP/GFRP	22	37.17–174.17	8–11.3	8–11.3	10–24
[24]	6	CFRP	34.5	124	12	12	20–25
[29]	13	BFRP/GFRP/CFRP	19	46–182	6–15	1.4–10	5–15
[30]	28	BFRP/GFRP/CFRP	19	42–182	6–15	2.5–10	8–20
[31]	11	BFRP/GFRP/CFRP	19.6–49.3	51–177	6–15	1.4–8	5–15
[32]	15	CFRP	34	124–210	12	12	20
Total	89	BFRP/GFRP/CFRP	19–49.3	37.17–210	6–15	1.4–12	5–25

Table 3: Database under the adhesive-FRP interface failure mode.

Reference	Number of tests	FRP material	f_c (MPa)	E_f (GPa)	t_p (mm)	t_f (mm)	t_g (mm)
[33]	3	CFRP	36.199	37.17–174.17	11	11	14
[24]	2	CFRP	34.5	124	12	12	25
[29]	7	GFRP/CFRP	19	46–182	8	8	14–15
[30]	4	GFRP/CFRP	19	51–159	8–10	8–10	14–15
[34]	6	BFRP/GFRP/CFRP	36.2	40.8–155	6–10	6–10	5–15
[35]	6	CFRP	34.86	124–165	8–20	1.4–8	6–20
[31]	1	CFRP	19.6	155	8	8	14
[36]	2	CFRP	28.5	149–155	9.5	9.5	14.25–19
Total	31	BFRP/GFRP/CFRP	19–36.2	37.17–182	6–20	1.4–12	5–25

Table 4: Database under the adhesive failure mode.

Reference	Number of tests	FRP material	f_c (MPa)	E_f (GPa)	t_p (mm)	t_f (mm)	t_g (mm)
[13]	2	CFRP	22	37.17	11	11	14–18
[31]	9	BFRP/GFRP/CFRP	19.6–49.3	46–182	6–15	2.5–8	8–14
[36]	16	GFRP/CFRP	28.5	41–155	7.5–16	4.5–10	8–20
[37]	13	GFRP/CFRP	41	42–139	9.5–12.7	9.5–12.7	14.25–25.4
[6]	2	CFRP	34–65.7	146	12	12	20
[16]	3	GFRP	33.4–49.2	161.8–162.3	14.9–20.37	1.26–1.28	3.26–3.27
Total	45	BFRP/GFRP/CFRP	19–65.7	37.17–182	6–20.37	1.26–12.7	3.26–25.4

Table 5: Database under the concrete crush or FRP rupture failure mode.

Reference	Number of tests	FRP material	f_c (MPa)	E_f (GPa)	t_p (mm)	t_f (mm)	t_g (mm)
[33]	4	CFRP	34.47–36.199	227.54	11	11	14
[16]	10	GFRP	33.4–53	161.8–162.3	10.1–20.47	1.24–1.28	3.24–3.28
[29]	4	BFRP/CFRP	19	46–177	6–10	1.4–6	10
[30]	4	BFRP/CFRP	19	46–177	6–10	1.4–6	5–10
[37]	8	CFRP/GFRP	41	43.5–128	9.5–12.7	9.5–12.7	14.25–25.4
[6]	4	CFRP	34–65.7	146	12	12	30
[31]	4	CFRP/GFRP/BFRP	29.7	48–180	8–10	8–10	13–15
Total	38	CFRP/GFRP/BFRP	19–65.7	43.5–227.54	6–20.47	1.24–12.7	3.24–30

Table 6: Database under the concrete surface failure mode.

Reference	Number of tests	FRP material	f_c (MPa)	E_f (GPa)	t_p (mm)	t_f (mm)	t_g (mm)
[16]	12	CFRP	38.8	140–170	10	3.6–6	20
[19]	9	GFRP	30–64.8	144.6–162.3	9.95–20.23	1.2–2.97	3.26–3.27
Total	33	CFRP/GFRP	30–64.8	140–170	9.95–20.23	1.2–6	3.26–20

Therefore, for the models with quite high CV, such as the three models under the adhesive-concrete interface failure mode with a CV of 0.61 as listed in Table 7, a further investigation into the systematic reason which causes a large prediction deviation was required [41]. That is to say, the model uncertainty factor ε directly calculated

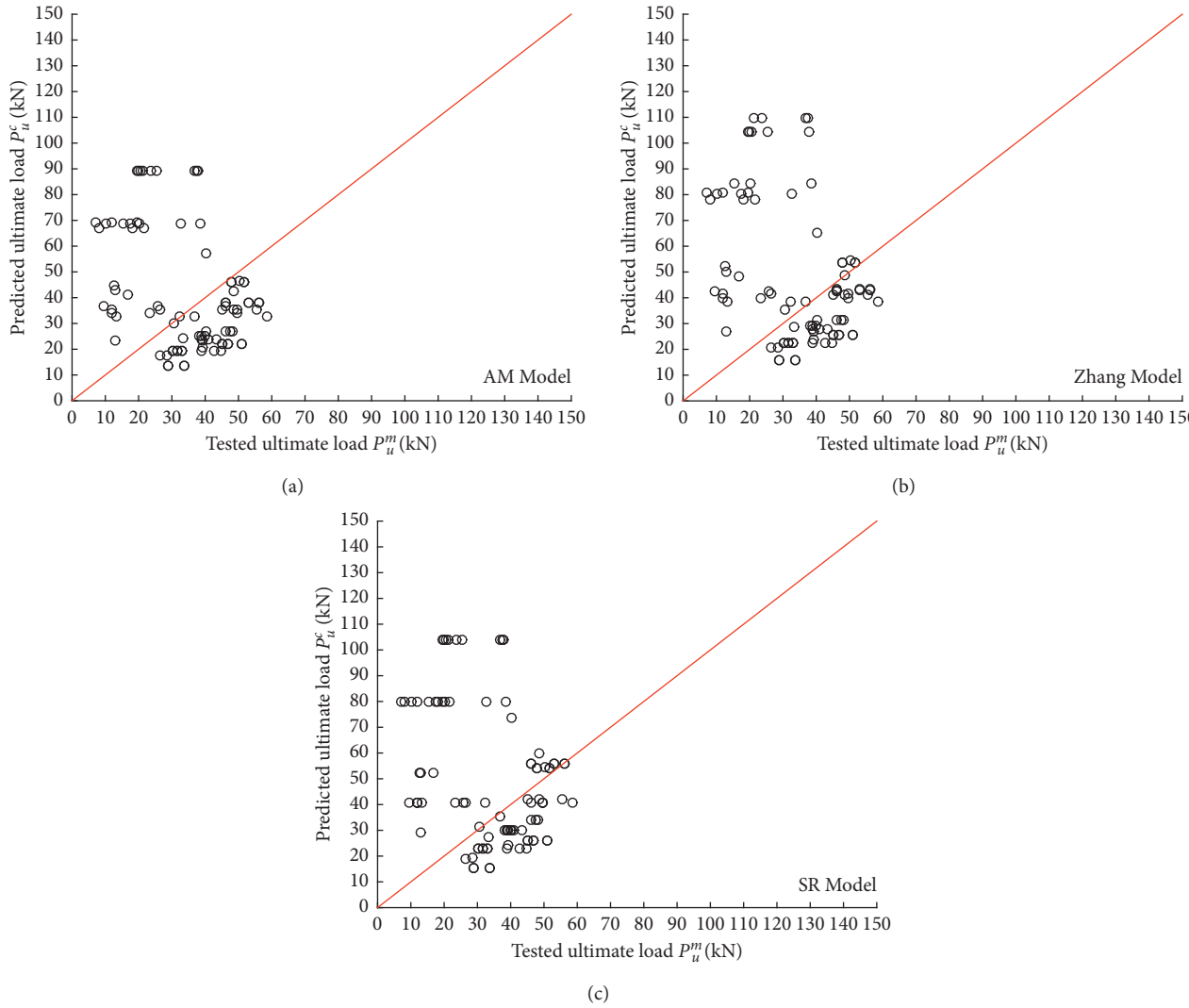

FIGURE 1: Comparison between the calculated value and the experimental value for the three models under the adhesive-concrete interface failure mode: (a) AM Model, (b) Zhang Model, and (c) SR Model.

by equation (1) was necessary to be checked for randomness.

Take the AM Model as an example, a scatter plot of the model uncertainty factor (written as ε_{AM}) against the concrete compression strength f_c is shown in Figure 6, where an obvious nonlinear relationship existed, indicating that the model uncertainty factor ε calculated by equation (1) was not a random variable but with an obvious dependence upon the design parameters, i.e., the concrete compression strength f_c in this case.

In order to clarify whether the model uncertainty factor is systematically dependent on the design parameters, a correlation analysis is needed.

In this paper, the distribution of the model uncertainty factor is featured by uncertainty. Hence, the Spearman correlation coefficient method, which has no specific requirements on the distribution characteristics of the data, was adopted to perform a correlation analysis for the model uncertainty factor and the five input parameters.

When the significance level (p value) is larger than 0.05, the Spearman correlation coefficient method is a nonparametric test with a null hypothesis of zero-rank correlation. In a Spearman correlation analysis, a customary significance value is larger than 0.05, and the absolute value of r close to 1.0 means high dependence. The Spearman correlation analysis showed that there was a negative correlation between ε_{AM} and the design parameters, with a high level of r-value ranging from −0.450 to −0.728 and a low level of p value ranging from 0.001 to 0.013 (see the second and fourth columns in Table 12). It statistically demonstrated that the model uncertainty factor ε_{AM} was systematically dependent on the five input parameters.

Similarly, Spearman correlation analysis was performed for Zhang Model and SR Model, respectively. The results indicated that the uncertainty factors of all the three models were statistically dependent upon the design parameters. Therefore, a further analysis for the dependency was necessary.

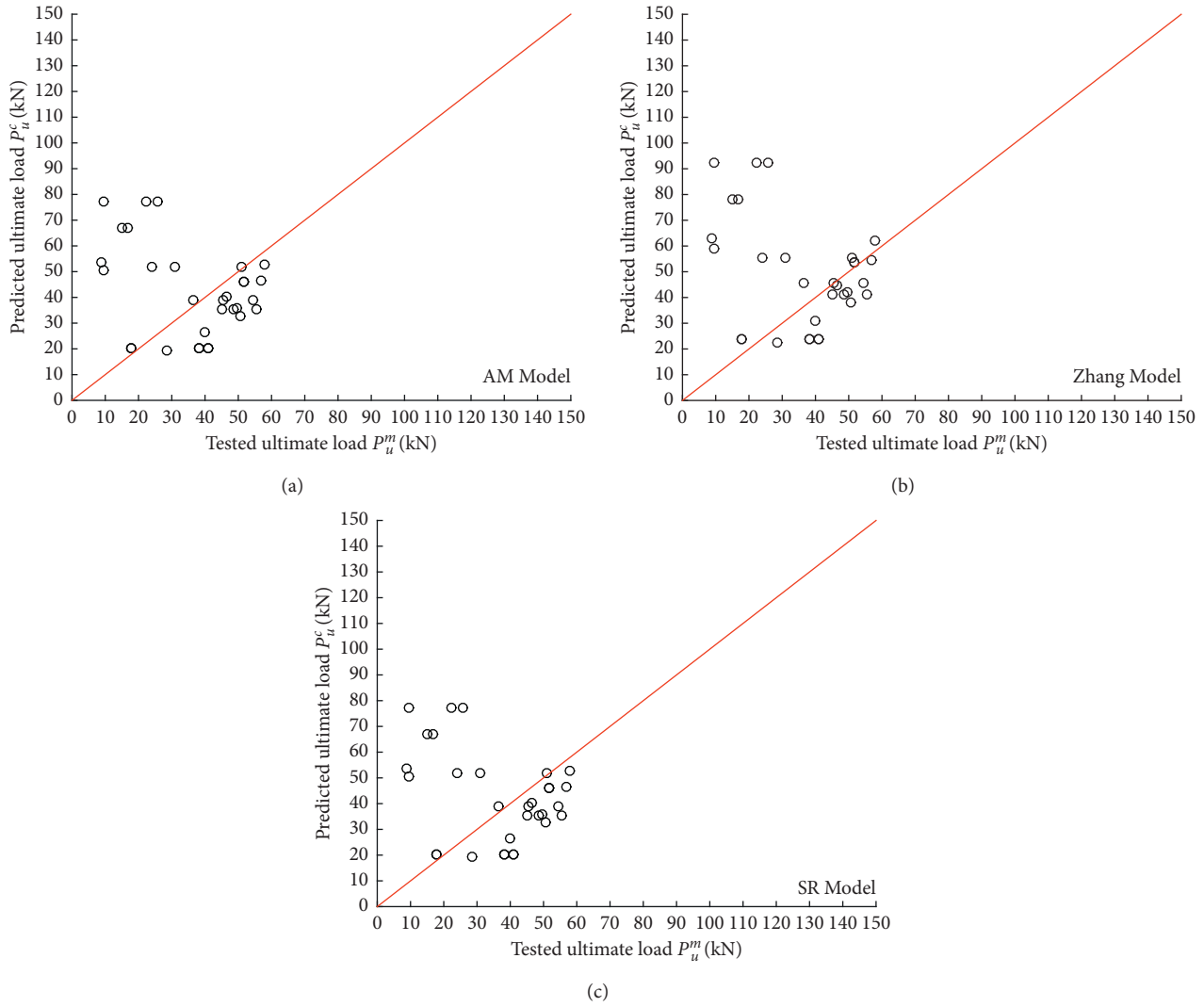

Figure 2: Comparison between the calculated value and the experimental value for the three models under the adhesive-FRP interface failure mode: (a) AM Model, (b) Zhang Model, and (c) SR Model.

By definition, since the model uncertainty factor must be a random variable with no dependency on the design parameters, a multiple regression analysis should be performed to eliminate the correlation between the model uncertainty factor and the design parameters, which is resulted from the systematic correlation part.

The residual random factor (represented by ε^*) could be obtained by eliminating the systematic dependence (expressed by a multiple regression function f). That is, the model uncertainty factor ε can be regarded as a composition of a systematic correlation part f and a residual random factor ε^*:

$$\varepsilon = f \times \varepsilon^*. \tag{2}$$

Substituting equation (2) into equation (1), equation (1) then turns into

$$P_u^m = \varepsilon^* \times f \times P_u^c. \tag{3}$$

Since the CV of the three selected models was high, the model uncertainty factor was then characterized by reducing the CV. Subsequently, a proper regression function f was built and the residual random factor ε^* was characterized. Thus, ε^* was defined as the updated model uncertainty factor.

5. Model Modification

Regression analysis can explain the relationship between the model uncertainty factor and the design parameters by a regression equation which was established by collecting data points from test results. Then, the randomness of the model uncertainty factor and the precision of the regression equation were checked by the rest data points. In this study, all the three selected models under the five failure modes were calibrated, but only the AM Model under the adhesive-concrete interface failure mode was discussed in detail. In total, 89 data points have been collected for AM Model under adhesive-concrete interface failure mode (as shown in Table 2). 59 data points were used to establish the regression equation, and the rest 30 data points were used to check for randomness.

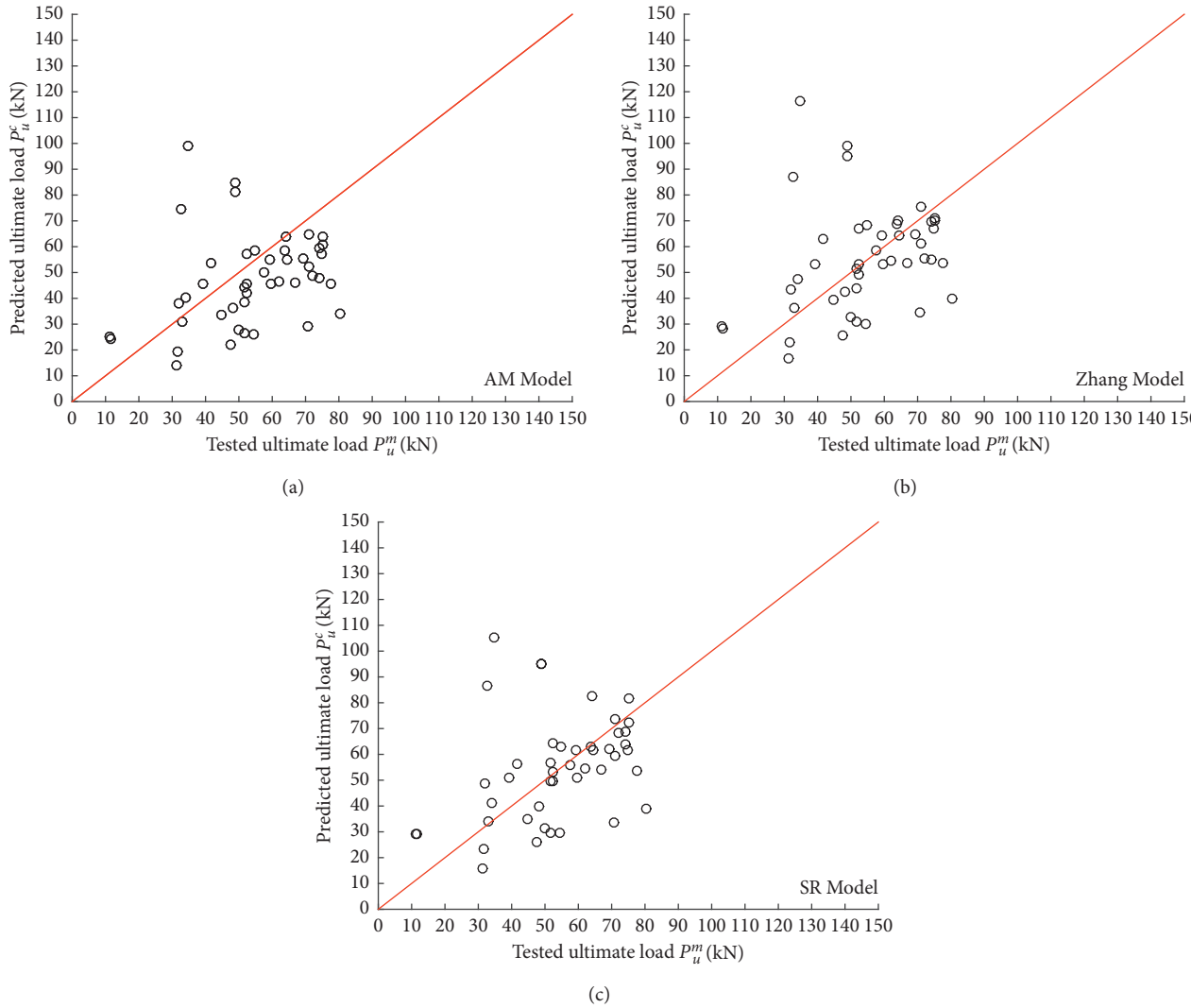

Figure 3: Comparison between the calculated value and the experimental value for the three models under the adhesive failure mode: (a) AM Model, (b) Zhang Model, and (c) SR Model.

The multiple regression analysis included two steps. In step one, the form of a correlation function (i.e., core function) was determined. The relationship between the model uncertainty factor and the design parameters can be expressed by the core function. The concerned functional relation equation was fitted by a MATLAB program written according to the damped LM algorithm [42, 43], and the calculated model uncertainty factors ε were plotted against the specific parameters by scatter plots in Figure 7.

The fitting function graphs show that the relation between the model uncertainty factor ε and each of the five design parameters was obviously nonlinear. The nonlinear trends with respect to the concrete compression strength f_c and the FRP height t_p were quite significant as shown in Figures 7(a) and 7(c). It can be noticed that the variation of ε with f_c and t_p can be more accurately fitted by a power function and an exponential function, respectively. For consistency reason, the exponential function and the power function were also adopted to fit the variation of ε with the other three input parameters. Then, the core functions for the five input parameters can be gained as follows:

$$\varepsilon \propto f_c^{b_1}, \tag{4a}$$

$$\varepsilon \propto E_f^{b_2}, \tag{4b}$$

$$\varepsilon \propto e^{b_3 t_p}, \tag{4c}$$

$$\varepsilon \propto e^{b_4 t_f}, \tag{4d}$$

$$\varepsilon \propto e^{b_5 t_g}, \tag{4e}$$

where b_i is the regression coefficient. It must be noted that the regression coefficient b_i for each of the five core functions was still undetermined in the first step of regression. This is because the influence effect arising from the other four input parameters was represented by each b_i in the five equations above.

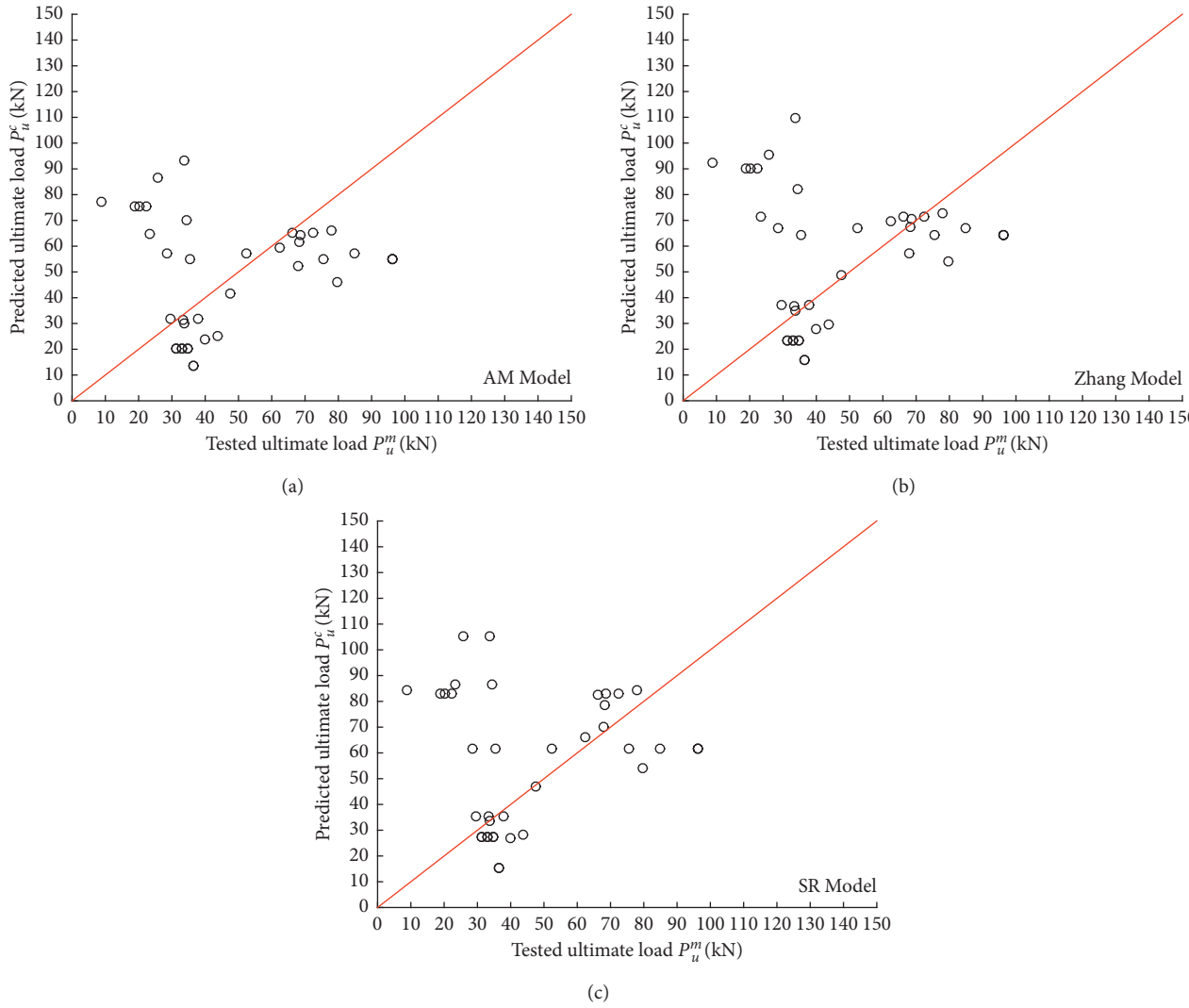

FIGURE 4: Comparison between the calculated value and the experimental value for the three models under concrete crush or FRP rupture failure mode: (a) AM Model, (b) Zhang Model, and (c) SR Model.

In the second step of regression, five core functions were combined together to constitute a multiplicative model f. Therefore, a regression function f was generated to multiplicatively describe the systematic dependence of the uncertainty factor on the five design parameters as follows:

$$f = e^{b_0} * e^{b_1 \ln f_c} * e^{b_2 \ln E_f} * e^{b_3 t_p} * e^{b_4 t_f} * e^{b_5 t_g}, \quad (5)$$

where b_i herein is the coefficient of the regression equation f. The model uncertainty factor can be given as follows:

$$\varepsilon = f * \varepsilon^* = e^{b_0} * e^{b_1 \ln f_c} * e^{b_2 \ln E_f} * e^{b_3 t_p} * e^{b_4 t_f} * e^{b_5 t_g} * \varepsilon^*. \quad (6)$$

ε^* herein is the residual random factor, obtained by removing the correlation function f from the model uncertainty factor ε. The regression function can be transformed from a product form into a summation form through a logarithmic transformation on the two sides of equation (5). So the multiple nonlinear regression analysis can be mathematically reduced to a multiple linear regression analysis.

The least square method was used to determine the five regression coefficients b_i. In our paper, a multiple linear regression analysis was carried out using SPSS to determine all the coefficients b_i as listed in Table 13. It can be seen from the table that each of the three models has a high determination of coefficient R^2 (0.854 for the AM Model, 0.858 for the Zhang Model, and 0.840 for the SR Model).

According to the regression principles, the residual ε^* is a random variable with no dependence on the design parameters. However, it is necessary to check the residual ε^* for randomness by using a new set of test data. Hence, the remaining 30 data points were adopted here for the randomness verification.

With the AM Model as example, the results of Spearman correlation analysis are shown in Table 12, including the correlation coefficient r and the significance p value before and after the modification. The dependency of the model

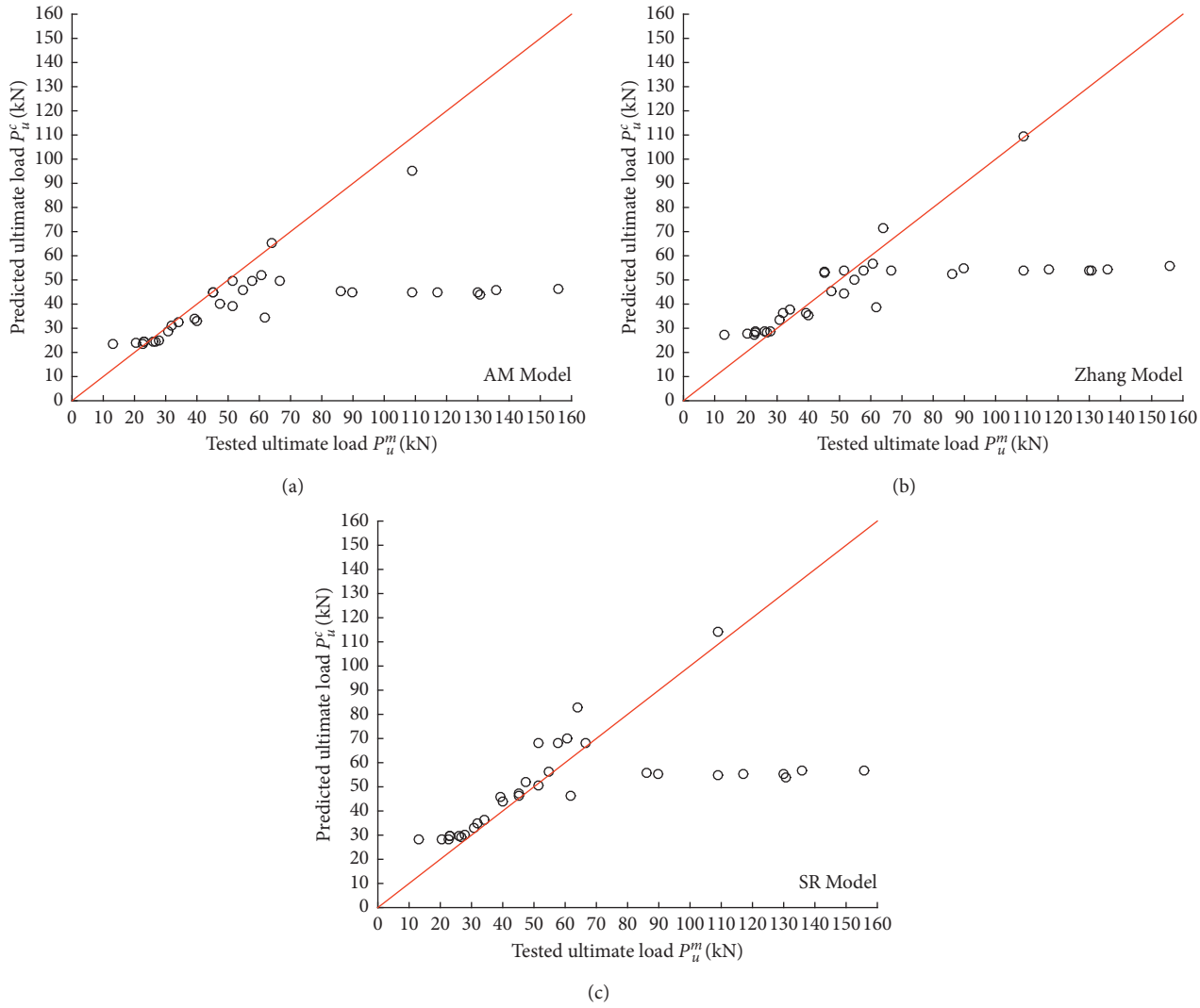

Figure 5: Comparison between the calculated value and the experimental value for the three models under concrete surface failure mode: (a) AM Model, (b) Zhang Model, and (c) SR Model.

Table 7: The statistics of calculated ε under adhesive-concrete interface failure mode.

Model	Mean	SD	CV
AM Model	1.17	0.7	0.61
Zhang Model	0.99	0.61	0.61
SR Model	0.96	0.59	0.61

Table 8: The statistics of calculated ε under adhesive-FRP interface failure mode.

Model	Mean	SD	CV
AM Model	1.05	0.58	0.55
Zhang Model	0.90	0.49	0.55
SR Model	1.05	0.58	0.55

uncertainty factor on the five input parameters was statistically proved to be sharply reduced. Thus, the residual factor ε^* can be regarded as a random part of ε.

Figure 8 plots the histogram of the residual part ε^* for each of the three modified models. As seen from the figure, for the three modified models, the mean value of ε^* was about 1.06, which was obviously closer to 1.00 in contrast to the original mean value of ε. Moreover, a mean value a little greater than 1.00 is regarded to be conservative and acceptable. Besides, for all the three models, the CV values of ε^* were markedly decreased to an acceptable 0.3, fully demonstrating that the systematic correlation has been effectively eliminated by regression. Now, those three models' uncertainty factors have been adequately characterized.

The determined systematic correlation function f can be used for model modification, as shown below:

$$P_u^{c'} = f * P_u^c. \tag{7a}$$

$P_u^{c'}$ herein is the predicted bonded joints strength after modification. The residual factor ε^*, a random variable, can

Table 9: The statistics of calculated ε under adhesive failure mode.

Model	Mean	SD	CV
AM Model	1.25	0.5	0.4
Zhang Model	1.08	0.43	0.4
SR Model	1.08	0.44	0.41

Table 10: The statistics of calculated ε under concrete crush or FRP rupture failure mode.

Model	Mean	SD	CV
AM Model	1.47	0.74	0.5
Zhang Model	1.26	0.6	0.48
SR Model	1.19	0.6	0.50

Table 11: The statistics of calculated ε under concrete surface failure mode.

Model	Mean	SD	CV
AM Model	1.17	0.62	0.53
Zhang Model	1.01	0.54	0.53
SR Model	0.98	0.54	0.55

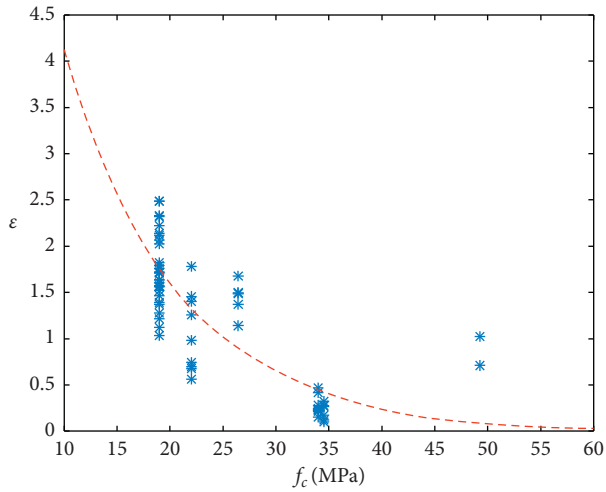

Figure 6: The model uncertainty factor ε against concrete compression strength f_c (AM Model).

then be regarded as the new model uncertainty factor for modified prediction models:

$$P_u^m = \varepsilon^* * P_u^{c'}. \tag{7b}$$

For all the three models, the comparison between the modified calculated value $P_u^{c'}$ and the measured value P_u^m was replotted (Figures 9(a)–9(c)). It is observed that all the modified data points are distributed near the 45-degree line after eliminating the systematic correlation.

In contrast with the original data (Figures 1(a)–1(c)), the difference between the calculated strength and the test value has been reduced significantly.

Table 12: Check for the randomness of the model uncertainty factor (AM Model).

Design parameter	Correlation coefficient r		Significance p value	
	Before ε	After ε^*	Before ε	After ε^*
f_c	−0.728	0.090	0.001	0.634
E_f	−0.553	0.158	0.001	0.405
t_p	−0.450	0.318	0.013	0.087
t_f	−0.636	0.380	0.001	0.038
t_g	−0.528	0.31	0.003	0.096

6. Reliability Analysis

According to the formula put forward by the ACI code [44, 45], for the FRP NSM reinforcement system, the limit state function for a bonded joints strength design can be given as follows:

$$G = R - D - L. \tag{8}$$

G herein is the limit state function, R is the bearing capacity, D is the dead load, and L is the live load. In a NSM FRP reinforced concrete structure, another factor, for example, the steel reinforcement, has also contributed much to the bearing capacity. However, as this part of resistance is hard to determine [30–32], only the FRP-concrete bonded joints resistance was therefore considered as the resistance in this paper [33], but not the contribution of steel reinforcement. Hence, for the NSM FRP reinforced concrete structure design, the capacity R is equivalent to the experimental value P_u:

$$R_d = P_u. \tag{9a}$$

The load combination can typically be presented as follows [46]:

$$S_d = 1.2D_n + 1.6L_n. \tag{9b}$$

S_d herein is the design load, and D_n and L_n are the nominal dead load and live load, respectively. From the perspective of design, the nominal load is associated with the resistance. As a result, the nominal load can be represented by the resistance [36, 47]:

$$S_d = \varphi \times P_u^c, \tag{9c}$$

where φ herein is the reduction factor for getting an appropriate reliability index [48, 49]. With no model uncertainty factor, the value of reduction factor will vary from 0.2 to 0.8 in different models [40]. However, by calibrating the model uncertainties, we could acquire a uniform value of reduction factor [34–37]. In this paper, for achieving an appropriate reliability index β (about 3.00), the value of the reduction factor φ was set uniformly as 0.6. Considering that the NSM FRP reinforcement system may be applied in different loading conditions, the live-to-dead load ratio $\eta = L_n/D_n$ was set as 0.50, 0.75, 1.00, 1.25, and 1.50, respectively.

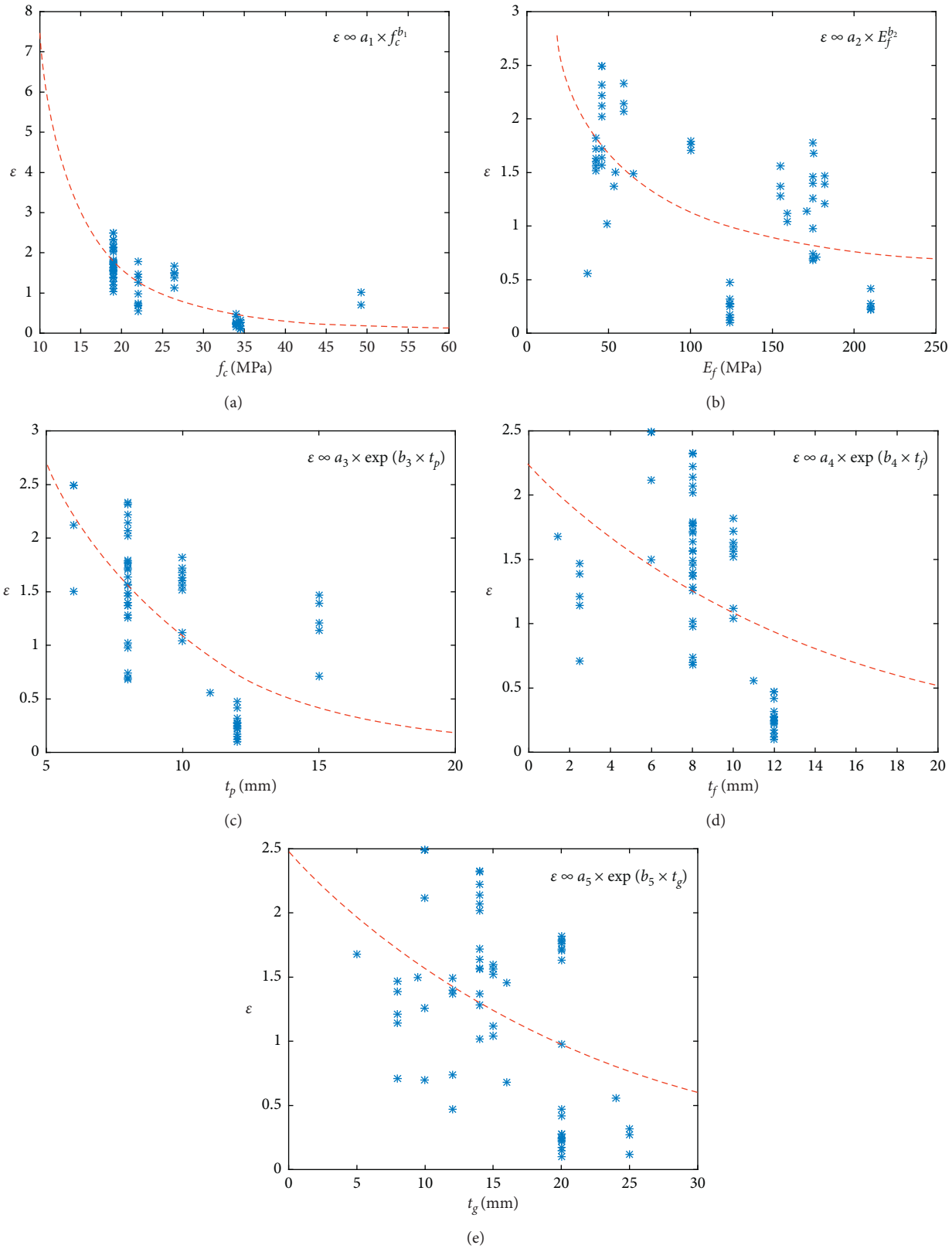

Figure 7: Fitting function graph: (a) concrete compression strength, (b) FRP modulus of elasticity, (c) FRP height, (d) FRP thickness, and (e) groove width.

Table 13: Coefficients in the regression function f for the three models.

Coefficients	AM Model	Zhang Model	SR Model
b_0	7.494	7.389	7.686
b_1	−1.245	−1.256	−1.036
b_2	−0.327	−0.331	−0.364
b_3	−0.090	−0.087	−0.114
b_4	−0.150	−0.154	−0.140
b_5	0.003	0.003	−0.005
R^2	0.854	0.858	0.840

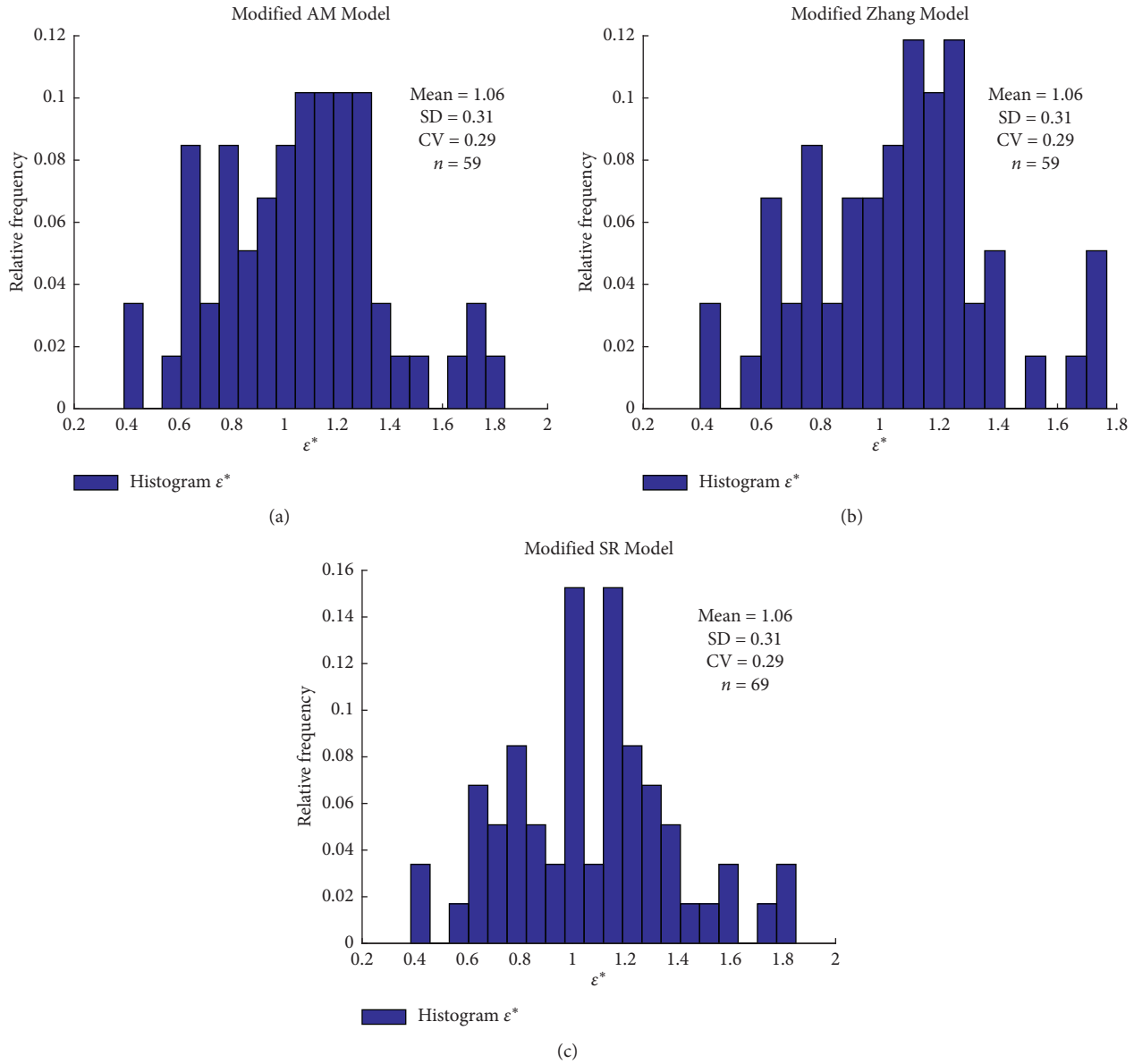

Figure 8: Histogram of ε^* for each modified model: (a) AM Model, (b) Zhang Model, and (c) SR Model.

Obviously, the five design parameters (i.e., f_c, E_f, t_p, t_f, and t_g) were the main influence factors in the reliability analysis. In Table 14, two groups of commonly used nominal parameters (A and B) were included for reliability analysis [50]. These two groups of parameters were from the literature review and were frequently used in the NSM FRP-concrete bonded joints reliability analysis. A set of groove width t_g was selected from the references and experiments (i.e., 21.3,

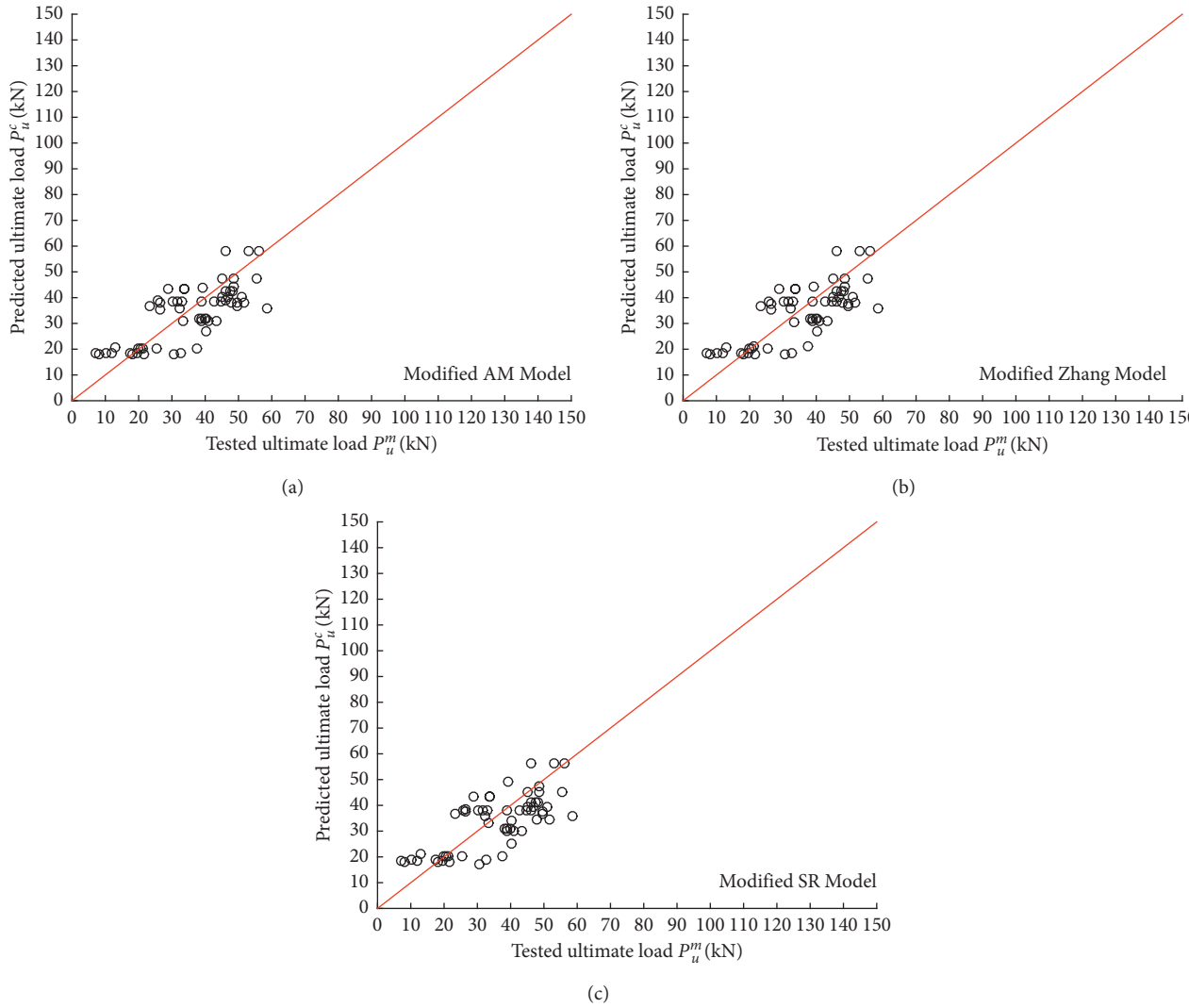

Figure 9: Comparison between the calculated value and the experimental value for the three modified models under adhesive-concrete interface failure mode: (a) AM Model, (b) Zhang Model, and (c) SR Model.

Table 14: Two groups of nominal parameters for the reliability analysis.

Design parameter	Nominal value A	Nominal value B	Reference
f_c (MPa)	27.56	41.3	[35, 36]
E_f (GPa)	52	165	[37]
t_p (mm)	4	8	[35]
t_f (mm)	8	12	[50], measured date
t_g (mm)	19	9	Measured date
D (kN)	Equation (9)	Equation (9)	Galambos et al. [51]
L (kN)	Equation (9)	Equation (9)	Galambos et al. [51]

22.33, 21.87, 23.19, 20.53, 21.57, 19.53, 20.30, 19.77, 19.67, 19.80, and 22.97). The nominal t_g was set to 19 based on the 95% probability of these values. Each of the other four design parameters (i.e., f_c, E_f, t_p, and t_f) was selected from one of the two groups (A and B). Thus, a sample space was generated by the five design parameters, with a sample size of $1 \times 2 \times 2 \times 2 \times 2 = 16$. Taking each of the five η (i.e., 0.50, 0.75, 1.00, 1.25, and 1.50) into account, we had $16 \times 5 = 80$ cases of reliability analysis. For every case, JC method was applied for the calculation of the reliability index β [51–53].

Table 15 lists out three groups of reliability index β calculated in 16 design cases. In group 1, model uncertainty factor was not taken into account. In group 2, model uncertainty factor was considered, but its systematic

Table 15: Reliability index of 16 cases for AM Model.

Case no.	Group 1: without considering the model uncertainty factor	Group 2: with the unmodified model uncertainty factor considered	Group 3: with the modified model uncertainty factor considered
1	2.58	1.53	3.15
2	3.56	1.62	3.05
3	4.82	2.36	2.98
4	3.43	2.47	3.12
5	0.78	1.64	3.48
6	1.39	1.35	3.23
7	3.47	2.94	3.78
8	1.09	3.08	3.09
9	6.62	1.51	2.95
10	4.22	1.73	2.91
11	2.45	1.61	3.96
12	4.58	1.93	4.03
13	5.12	1.54	3.26
14	3.27	1.26	3.01
15	4.40	3.13	2.87
16	5.03	2.98	2.95
Average	3.55	2.04	3.27
CV of β	0.44	0.32	0.11

dependence being not eliminated (abbreviated as unmodified model). In group 3, the model uncertainty factor was considered, as well as its systematic dependence being eliminated (abbreviated as modified model).

Take the AM model as an example, with the live-to-dead load ratio η at 1.00, the calculated reliability index β in 16 design cases is listed in Table 15 [6, 38]. In group 1 (no model uncertainty factor), the calculated reliability index β had an average value of 3.5, which was the highest among the three groups. In group 2 (unmodified model) and group 3 (modified model), the average calculated reliability index β decreased to 2.04 and 3.27, respectively. In group 3 (modified model), the CV of β has a lowest value of 0.11, which was clearly less than the other two groups (0.32 and 0.44).

Generally, when the uncertainty is significantly underestimated, the reliability of design considering no model uncertainty factor is very unsafe [29, 43]. Our result also indicated that very different reliability did exist in the same design case, which is due to the systematic correlation of ε. While practically, the same input parameters leading to quite different output reliability levels are unreasonable [42]. In summary, by eliminating the systematic correlation of ε, all the problems above can get effective solutions.

7. Conclusions

Some prediction models have been proposed for NSM FRP-concrete bonded joints strength. Model uncertainty inevitably does exit due to limited experimental data, incomplete research parameters, and idealized calculation method. A method of model calibration for these prediction models is presented in this study. The main conclusions were summarized as follows:

(1) A total of 246 pullout test data were collected to calibrate three selected prediction models. The model uncertainty factor was defined to quantitatively evaluate the uncertainties in a model. By using the Spearman correlation analysis, the model uncertainty factor calculated by a prediction model was checked for randomness and was proved to have a strong dependency on the design parameters.

(2) A multiple regression analysis was applied and a regression equation was established to reduce the value of CV for the model uncertainty factor. The systematical dependence of the model uncertainty factor on design parameters was then eliminated, and the residual factor after regression was checked for randomness. After modification, the model uncertainty factors of the three selected models have become reasonable random variables which followed the logarithmic normal distribution.

(3) For different NSM FRP bonded joints strength models, the model uncertainties can be brought to the same level after model modification. The model uncertainty factor after modification was appreciated for its merit by performing a reliability analysis using the JC method, and the calibration significantly increased the accuracy of the prediction models.

This study has widened and deepened the knowledge of the NSM FRP interfacial bonded joints strength prediction models and is desirable for guidelines to standardize the calibration of model uncertainties.

Data Availability

Data in this article used to support this study are currently under embargo while the research findings are commercialized. Requests for data will be considered 6 months after the publication of this article by the corresponding author.

Conflicts of Interest

The authors declare that they have no conflicts of interest regarding this work.

Acknowledgments

This work was supported by the National Natural Science Foundation of China (Project no. 51608137).

References

[1] T. Hassan and S. Rizkalla, "Investigation of bond in concrete structures strengthened with near surface mounted carbon fiber reinforced polymer strips," *Journal of Composites for Construction*, vol. 7, no. 3, pp. 248–257, 2003.

[2] R. El-Hacha and S. H. Rizkalla, "Near-surface-mounted fiber-reinforced polymer reinforcements for flexural strengthening of concrete structures," *ACI Structural Journal*, vol. 101, no. 5, pp. 717–726, 2004.

[3] V. Turco, N. Galati, L. De Lorenzis et al., "Bond between near surface mounted FRP rods and masonry in structural strengthening," in *Proceedings of the Advancing with Composites*, pp. 7–9, Plast, Russia, 2003.

[4] L. De Lorenzis and J. G. Teng, "Near-surface mounted FRP reinforcement: an emerging technique for strengthening structures," *Composites Part B: Engineering*, vol. 38, no. 2, pp. 119–143, 2007.

[5] D. Van Gemert, "Force transfer in epoxy bonded steel/concrete joints," *International Journal of Adhesion and Adhesives*, vol. 1, no. 2, pp. 67–72, 1980.

[6] F. Al-Mahmoud, A. Castel, R. François, and C. Tourneur, "Anchorage and tension-stiffening effect between near-surface-mounted CFRP rods and concrete," *Cement and Concrete Composites*, vol. 33, no. 2, pp. 346–352, 2011.

[7] H. Yoshizawa, "Analysis of debonding fracture properties of CFS strengthened RC member subject to tension: non-metallic (FRP) reinforcement for concrete structures," in *Proceedingsof the 3rd International Symposium*, pp. 287–294, The JapanConcrete Institute, Brno, Czech Republic, January 1997.

[8] S. S. Zhang, "Bond strength model for near-surface mounted (NSM) FRP bonded joints: effect of concrete edge distance," *Composite Structures*, vol. 201, pp. 664–675, 2018.

[9] J.-J. Zeng, W.-Y. Gao, Z.-J. Duan, Y.-L. Bai, Y.-C. Guo, and L.-J. Ouyang, "Axial compressive behavior of polyethylene terephthalate/carbon FRP-confined seawater sea-sand concrete in circular columns," *Construction and Building Materials*, vol. 234, p. 117383, 2020.

[10] Z. Yang, A. Liu, J. Yang, J. Fu, and B. Yang, "Dynamic buckling of functionally graded graphene nanoplatelets reinforced composite shallow arches under a step central point load," *Journal of Sound and Vibration*, vol. 465, p. 115019, 2020.

[11] Y.-F. Wu and C. Jiang, "Quantification of bond-slip relationship for externally bonded FRP-to-concrete joints," *Journal of Composites for Construction*, vol. 17, no. 5, pp. 673–686, 2013.

[12] K. Nakaba, T. Kanakubo, T. Furuta et al., "Bond behavior between fiber-reinforced polymer laminates and concrete," *ACI Structural Journal*, vol. 98, no. 3, pp. 359–367, 2001.

[13] L. De Lorenzis, A. Rizzo, and A. La Tegola, "A modified pull-out test for bond of near-surface mounted FRP rods in concrete," *Composites Part B: Engineering*, vol. 33, no. 8, pp. 589–603, 2002.

[14] T. Hassan and S. Rizkalla, "Bond mechanism of NSM FRP bars for flexural strengthening of concrete structures," *ACI Structural Journal*, vol. 101, no. 6, pp. 830–839, 2004.

[15] D. J. Oehlers, M. Haskett, C. Wu, and R. Seracino, "Embedding NSM FRP plates for improved IC debonding resistance," *Journal of Composites for Construction*, vol. 12, no. 6, pp. 635–642, 2008.

[16] R. Seracino, N. M. Jones, M. S. Ali, M. W. Page, and D. J. Oehlers, "Bond strength of near-surface mounted FRP strip-to-concrete joints," *Journal of Composites for Construction*, vol. 11, no. 4, pp. 401–409, 2007.

[17] X. Z. Lu, J. G. Teng, L. P. Ye, and J. J. Jiang, "Bond-slip models for FRP sheets/plates bonded to concrete," *Engineering Structures*, vol. 27, no. 6, pp. 920–937, 2005.

[18] Y.-F. Wu, X.-S. Xu, J.-B. Sun, and C. Jiang, "Analytical solution for the bond strength of externally bonded reinforcement," *Composite Structures*, vol. 94, no. 11, pp. 3232–3239, 2012.

[19] R. Seracino, M. R. Raizal Saifulnaz, and D. J. Oehlers, "Generic debonding resistance of EB and NSM plate-to-concrete joints," *Journal of Composites for Construction*, vol. 11, no. 1, pp. 62–70, 2007.

[20] M. S. M. Ali, D. J. Oehlers, M. C. Griffith, and R. Seracino, "Interfacial stress transfer of near surface-mounted FRP-to-concrete joints," *Engineering Structures*, vol. 30, no. 7, pp. 1861–1868, 2008.

[21] S. S. Zhang, J. G. Teng, and T. Yu, "Bond-slip model for CFRP strips near-surface mounted to concrete," *Engineering Structures*, vol. 56, pp. 945–953, 2013.

[22] J. F. Chen and J. G. Teng, "Anchorage strength models for FRP and steel plates bonded to concrete," *Journal of Structural Engineering*, vol. 127, no. 7, pp. 784–791, 2001.

[23] N. T. K. Al-Saadi and R. Al-Mahaidi, "Modelling of NSM CFRP strips embedded in concrete using lap shear tests with epoxy adhesive," *Composite Structures*, vol. 153, pp. 662–672, 2016.

[24] D. Novidis, S. J. Pantazopoulou, and E. Tentolouris, "Experimental study of bond of NSM-FRP reinforcement," *Construction and Building Materials*, vol. 21, no. 8, pp. 1760–1770, 2007.

[25] J. G. Teng, J. F. Chen, S. T. Smith et al., *FRP: Strengthened RC Structures*, Wiley, UK, 2002, ISBN: 978-0-471-48706-7.

[26] J. Yao, J. G. Teng, and J. F. Chen, "Experimental study on FRP-to-concrete bonded joints," *Composites Part B: Engineering*, vol. 36, no. 2, pp. 99–113, 2005.

[27] Z. Wu, H. Yuan, and H. Niu, "Stress transfer and fracture propagation in different kinds of adhesive joints," *Journal of Engineering Mechanics*, vol. 128, no. 5, pp. 562–573, 2002.

[28] J. P. Lin and Y. F. Wu, "Numerical analysis of interfacial bond behavior of externally bonded FRP-to-concrete joints," *Journal of Composites for Construction*, vol. 20, no. 5, Article ID 04016028, 2016.

[29] A. Bilotta, F. Ceroni, M. Di Ludovico, E. Nigro, M. Pecce, and G. Manfredi, "Bond efficiency of EBR and NSM FRP systems for strengthening concrete members," *Journal of Composites for Construction*, vol. 15, no. 5, pp. 757–772, 2011.

[30] A. Bilotta, F. Ceroni, E. Nigro, and M. Pecce, "Strain assessment for the design of NSM FRP systems for the strengthening of RC members," *Construction and Building Materials*, vol. 69, pp. 143–158, 2014.

[31] A. Bilotta, F. Ceroni, J. A. O. Barros et al., "Bond of NSM FRP-strengthened concrete: round robin test initiative," *Journal of Composites for Construction*, vol. 20, no. 1, Article ID 04015026, 2016.

[32] D. G. Novidis and S. J. Pantazopoulou, "Bond tests of short NSM-FRP and steel bar anchorages," *Journal of Composites for Construction*, vol. 12, no. 3, pp. 323–333, 2008.

[33] X. Yan, B. Miller, A. Nanni et al., "Characterization of CFRP rods used as near surface mounted reinforcement," in

Proceedings of the 8th International Conference on Structural Faults and Repair, pp. 1–12, London, UK, 1999.

[34] A. Palmieri, S. Matthys, and L. Taerwe, "Double bond shear tests on NSM FRP strengthened members," in *Proceedings of the 6th international conference on FRP composites in civil engineering (CICE-2012)*, pp. 1–8, Rome, Italy, June 2012.

[35] R. Capozucca, "Analysis of bond-slip effects in RC beams strengthened with NSM CFRP rods," *Composite Structures*, vol. 102, pp. 110–123, 2013.

[36] D. Lee, L. Cheng, and J. Yan-Gee Hui, "Bond characteristics of various NSM FRP reinforcements in concrete," *Journal of Composites for Construction*, vol. 17, no. 1, pp. 117–129, 2013.

[37] S. M. Soliman, E. El-Salakawy, and B. Benmokrane, "Bond performance of near-surface-mounted FRP bars," *Journal of Composites for Construction*, vol. 15, no. 1, pp. 103–111, 2010.

[38] K.-K. Phoon and F. H. Kulhawy, "Characterisation of model uncertainties for laterally loaded rigid drilled shafts," *Géotechnique*, vol. 55, no. 1, pp. 45–54, 2005.

[39] C. Chen, X. Li, D. Zhao et al., "Mechanism of surface preparation on FRP-Concrete bond performance: a quantitative study," *Composites Part B: Engineering*, vol. 163, pp. 193–206, 2019.

[40] J. Shi, Z. Wu, X. Wang, and M. Noori, "Reliability analysis of intermediate crack-induced debonding failure in FRP-strengthened concrete members," *Structure and Infrastructure Engineering*, vol. 11, no. 12, pp. 1651–1671, 2015.

[41] D. M. Zhang, K. K. Phoon, H. W. Huang, and Q. F. Hu, "Characterization of model uncertainty for cantilever deflections in undrained clay," *Journal of Geotechnical and Geoenvironmental Engineering*, vol. 141, no. 1, Article ID 04014088, 2014.

[42] G. T. Kung, C. H. Juang, E. C. Hsiao, and Y. M. Hashash, "Simplified model for wall deflection and ground-surface settlement caused by braced excavation in clays," *Journal of Geotechnical and Geoenvironmental Engineering*, vol. 133, no. 6, pp. 731–747, 2007.

[43] C. Tang, K. K. Phoon, L. Zhang et al., "Model uncertainty for predicting the bearing capacity of sand overlying clay," *International Journal of Geomechanics*, vol. 17, no. 7, Article ID 04017015, 2017.

[44] N. Wang, B. R. Ellingwood, and A.-H. Zureick, "Reliability-based evaluation of flexural members strengthened with externally bonded fiber-reinforced polymer composites," *Journal of Structural Engineering*, vol. 136, no. 9, pp. 1151–1160, 2010.

[45] C. Chen, X. Li, X. Wang et al., "Effect of transverse groove on bond behavior of FRP-concrete interface: experimental study, image analysis and design," *Composites Part B: Engineering*, vol. 161, pp. 205–219, 2019.

[46] C. Chen, L. Sui, F. Xing, D. Li, Y. Zhou, and P. Li, "Predicting bond behavior of HB FRP strengthened concrete structures subjected to different confining effects," *Composite Structures*, vol. 187, pp. 212–225, 2018.

[47] Z. Yang, Y. Huang, A. Liu, J. Fu, and D. Wu, "Nonlinear in-plane buckling of fixed shallow functionally graded graphene reinforced composite arches subjected to mechanical and thermal loading," *Applied Mathematical Modelling*, vol. 70, pp. 315–327, 2019.

[48] I. A. Sharaky, L. Torres, M. Baena, and C. Miàs, "An experimental study of different factors affecting the bond of NSM FRP bars in concrete," *Composite Structures*, vol. 99, pp. 350–365, 2013.

[49] L. Torres, I. A. Sharaky, C. Barris, and M. Baena, "Experimental study of the influence of adhesive properties and bond length on the bond behaviour of NSM FRP bars in concrete," *Journal of Civil Engineering and Management*, vol. 22, no. 6, pp. 808–817, 2016.

[50] R. A. Atadero and V. M. Karbhari, "Calibration of resistance factors for reliability based design of externally-bonded FRP composites," *Composites Part B: Engineering*, vol. 39, no. 4, pp. 665–679, 2008.

[51] T. V. Galambos, B. Ellingwood, J. G. MacGregor et al., "Probability based load criteria: assessment of current design practice," *Journal of the Structural Division*, vol. 108, no. 5, pp. 959–977, 1982.

[52] A. M. Okeil, A. Belarbi, and D. A. Kuchma, "Reliability assessment of FRP-strengthened concrete bridge girders in shear," *Journal of Composites for Construction*, vol. 17, no. 1, pp. 91–100, 2012.

[53] A. S. Nowak and M. M. Szerszen, "Calibration of design code for buildings (ACI 318): Part 1-Statistical models for resistance," *ACI Structural Journal*, vol. 100, no. 3, pp. 377–382, 2003.

Hindawi
Advances in Polymer Technology
Volume 2020, Article ID 6346471, 11 pages
https://doi.org/10.1155/2020/6346471

Research Article

An Investigation on Mechanical Behavior of Tooth-Plate-Glass-Fiber Hybrid Sandwich Beams

Honglei Xie,[1] **Li Wan**,[1,2] **Bo Wang**,[3] **Haiping Pei**,[1] **Weiqing Liu**,[1,2] **Kong Yue**,[1,2] **and Lu Wang**[1,2]

[1]*College of Civil Engineering, Nanjing Tech University, Nanjing, China*
[2]*Advanced Engineering Composites Research Center, Nanjing Tech University, Nanjing, China*
[3]*Nanjing Metro Construction Co., Ltd., Nanjing, China*

Correspondence should be addressed to Li Wan; wanli@njtech.edu.cn

Received 16 October 2019; Accepted 14 January 2020; Published 12 February 2020

Guest Editor: Tianyu Xie

Tooth-plate-glass-fiber hybrid sandwich (TFS) is a type of sandwich composites fabricated by vacuum-assisted resin infusion process, in which glass fiber facesheets reinforced by metal plate are connected to foam core through tooth nails. Bending properties and interlaminar properties of TFS beams with various foam densities were investigated by flexural tests and DCB (double cantilever beam) tests. The test results showed that by increasing the foam core density from 35 kg/m^3 to 150 kg/m^3, the peak strength of TFS beams significantly increased by 168% to 258% compared with similar sandwich beams with fibrous composite facesheets. With the change of foam density and span length, the main failure modes are core shear and facesheet indentation beneath the loading roller. The interlaminar strain energy release rates of TFS specimens also increased by increasing the density of the foam. In addition, an analytical model was used to predict the ultimate bending strength of TFS beams, which were in good accordance with the experimental results.

1. Introduction

A composite sandwich structure consists of facesheets and core and has been widely used in structural engineering, marine, and transportation industry [1]. The fiber-reinforced plastics (FRP) or metallic layers are usually used as skin materials. Metal sheets are heavy but have better resistance against impact load. Compared with metal facesheet, with the characteristics of high strength-to-weight ratio and stiffness-to-weight ratio, fiber facesheets have, respectively, lower resistance of local impact. In order to combine the advantages of both structures, fiber metal laminates (FMLs) were created, which built up from interlacing layers of thin metals and fiber-reinforced composite [2]. FMLs have superior specific static properties and excellent damage resistance, including high impact resistance and flame resistance [3–5].

In the past two decades, many researchers have studied the mechanical properties of FMLs under various mechanical loads. Kashani et al. [6] investigated the scaling effects of fiber metal laminates by tensile and three-point bending tests. FMLs were made of aluminum 1050 and unidirectional glass-epoxy. The test results showed that scaling has no effect on general tensile behaviors of FMLs. The failure modes of FMLs were fiber breakage, delamination between composite layers, debonding between metal and composite layers, and aluminum fracture in tensile tests. They also found that fiber metal laminates obey scaling law under three-point bending load and the main failure mode was debonding between metal and composite layers.

Steeves and Fleck [7] investigated collapse mechanisms of sandwich beams with composite faces and a foam core under three-point bending load. The results showed that main failure modes are facesheet microbuckling, plastic shear of the core, and facesheet indentation beneath the middle loading roller. The failure mode depends primarily on the geometry of the sandwich beam and the density of foam core.

Kabir et al. [8] investigated the response of sandwich panels with aluminium facesheets under three-point bending load. They indicated that the failure modes were influenced by the strength of facesheets, foam core thickness, and span length. They found that sandwich panels with very thin aluminium facesheets were generally dominated by indentation failure mode. Face yielding occurred when low-strength facesheets were used, and core yielding occurred when strong facesheets were used. They also pointed out that a significant increase of the facesheets strength only marginally increases panels' resistance to bending. Meanwhile, theoretical models were proposed to predict the failure loads of each failure mode.

Dariushi and Sadighi [9] studied the bending properties of sandwich beams with fiber metal laminates facesheets and compared them with similar sandwich beams with fibrous composite faces. The results showed that FML faces have better resistance against transverse local loads and minimize stress concentration and local deformations of skin and core under the loading tip. In addition, sandwich beams with FML faces have larger elastic region and absorb more energy. Furthermore, they proposed a geometrical nonlinear theory to predict force-deflection behavior.

Reyes [10] investigated the flexural properties of FML reinforced sandwich panel with aluminum foam core. The test results showed that the use of fiber metal laminates as the skin material can improve the impact behavior, damage resistance, and damage tolerance of sandwich structures. Meanwhile, energy absorption characteristics of the sandwich components were studied, and the proposed energy balance model was in good accordance with the experiment results. Ortiz de Mendibil et al. [11] studied the impact behavior of glass fiber-reinforced epoxy/aluminum fiber metal laminate. Fiber metal laminates were manufactured by liquid molding. The test results revealed that the holes located out of the impact zone have no effect in the damage mechanisms. The failure mode of the FMLs was metal dominated. The first delamination appeared between metal and composite layers at 20 J, the first crack in the aluminum layers appeared at 40 J, and afterwards fiber breakage started at 42 J. Reyes Villanueva and Cantwell [12] studied the high velocity impact response of a range of novel aluminum foam sandwich structures with FML skins. The test results revealed that sandwich structures with FML faces have an excellent energy absorption characteristic when subjected to dynamic load. Further studies of the mechanical behavior of glass fiber-reinforced polypropylene FMLs had been conducted by Reyes and Cantwell [13]. They pointed out that the interfacial fracture toughness of FMLs initially increases with the crosshead displacement rate up to 100 mm/min before reducing again at higher displacement rates. Meanwhile, single cantilever beam tests and low-velocity impact tests were conducted. The test results showed that these materials offer excellent resistance to dynamic load and the incident energy was absorbed through plastic deformation in the aluminum layers and localized microcracking within the composite plies. Srinivasagupta et al. [14] pointed out that the interfacial bonding performance had a great influence on the reliability of sandwich materials with foam core. During the compression, tension, and bending tests, the failure was initiated through the interface. In this paper, the effects of processing conditions and material properties on the interfacial strength of sandwich structures were studied. The test results revealed that the debonding fracture toughness of foam core sandwich composites increased with the increase of the temperature. The compliance derivative method was proposed to evaluate the mode I fracture toughness or the critical fracture energy rate [15]. Vadakke and Carlsson [16] studied the interfacial bonding behavior between the facesheets and the foam core. They concluded that the density of foam core has a great influence on the interfacial bonding strength. Meanwhile, the interfacial bonding strength increased with the increase in the density of foam core.

In this paper, a new type of foam sandwich structure (tooth-plate-glass-fiber hybrid foam sandwich beam, TFS) was proposed. Tooth plate was connected with foam core through tooth nails, which is different from FML facesheets, in which the metal plate and the glass fiber-reinforced composite were bonded together. Three-point bending test and DCB (double cantilever beam) test were carried out to obtain the load-displacement curves, failure modes, bending properties, and interlaminar behavior of the sandwich structures. Meanwhile, an analysis model was proposed to predict the peak load of the TFS.

2. Experimental Program

2.1. Specimens. Specimens were fabricated using a vacuum-assisted resin infusion process at Composite Structure Lab of Nanjing Tech University. The materials used in the specimens were polyurethane foam with various density (35 kg/m^3, 80 kg/m^3, and 150 kg/m^3), Q235 steel, galvanized metal tooth nail made by punching machine, E-type glass fiber fabric without alkali with density of 800 g/m^2, and the HS-2100-type two formic acid unsaturated polyester resin. The thickness of tooth plate is 0.7 mm, with tooth length of 8 mm, width of 3 mm, each pair of teeth along the longitudinal spacing of 25 mm, horizontal spacing of 12 mm, and cross equidistant arrangement. At first, the surface of metal plate was modified with organic solvent (such as acetone) to remove the surface grease. The steel tooth plates were pressed into polyurethane foam, and then the upper and lower surfaces of tooth plate were covered with two layers of glass fiber fabric and the fiber orientation angel is 0/90° to the panel horizontal axis. Finally, the vacuum-assisted resin infusion process was used to fabricate the specimens, in which all the raw materials were immersed by the resin. The real component is shown in Figure 1. The similar sandwich beams with fiber facesheet thickness of 1.5 mm and 2.1 mm were fabricated to compare with the TFS specimens.

2.2. Material Properties. Tension tests of steel facesheets and GFRP facesheets were conducted according to ASTM D 3039 [17] to characterize the mechanical properties of the materials. The strength and stiffness of the steel sheets and GFRP sheets obtained from these experiments were detailed in Table 1. The tensile strength and elastic modulus of tooth plate were equivalent strength and elastic modulus,

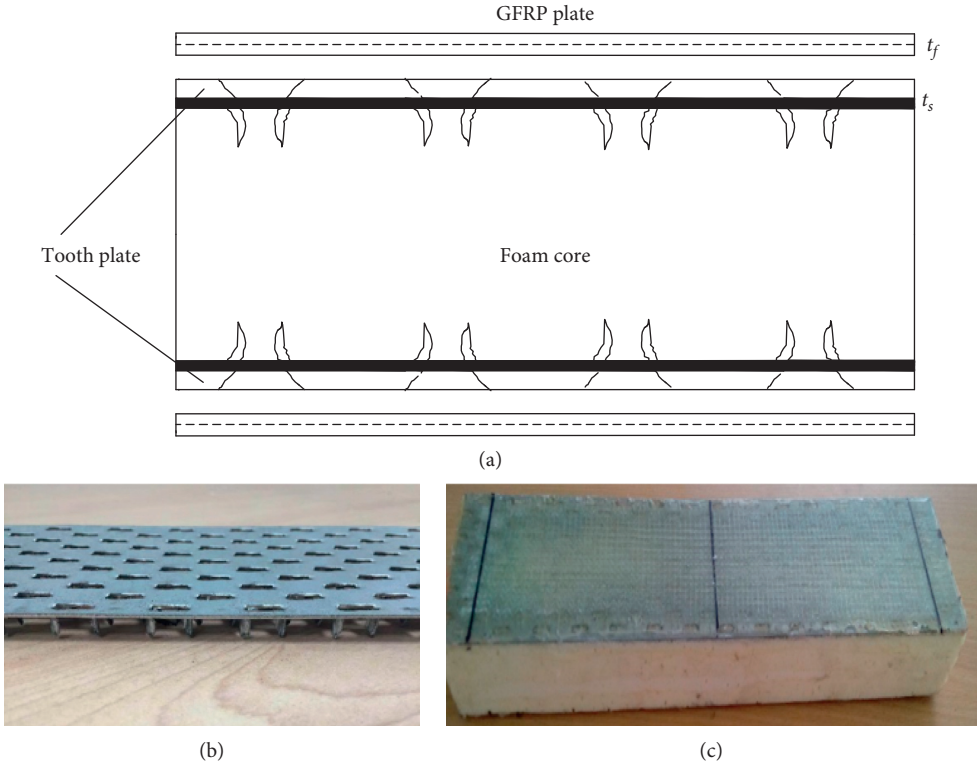

Figure 1: (a) Schematic illustration of TFS specimen; (b) photo of tooth plate; (c) photo of TFS specimen.

Table 1: Mechanical properties of GFRP and tooth plate.

Type	Tensile strength (MPa)	Elastic modulus (GPa)
2 layers of GFRP	150.73	8.53
3 layers of GFRP	178.90	9.32
Tooth plate	111.02 (equivalent)	50.02 (equivalent)

Table 2: Mechanical properties of foam core.

Density (kg/m^3)	35	80	150
Compressive strength (MPa)	0.10	0.35	0.92
Shear strength (MPa)	0.10	0.28	0.43
Compressive modulus (GPa)	6.76	18.56	48.51
Shear modulus (GPa)	2.84	8.06	18.56

for there were regularly arranged holes on the tooth plate. In order to obtain the compressive strength and Young's modulus of the foam specimens, polyurethane (PU) foam specimens with dimension of $50 \times 50 \times 50\,\text{mm}^3$ were prepared and tested according to ASTM D 1621 [18]. Foam samples were tested under displacement control mode with loading rate of 0.5 mm/min. The mechanical behavior of PU foam was given in Table 2. To achieve more accurate numerical results, three samples of each dimension had been tested and the mean values of the data had been calculated as the final results.

2.3. Three-Point Bending Tests. In order to evaluate the flexural behavior of TFS beams, three-point bending tests were conducted according to ASTM C 393-62 [19]. For each span, there were three specimens. In Figure 2, all specimens had the same width ($b = 75$ mm) and core height ($h = 40$ mm). Specimens NS3D1, NS3D2, and NS3D3 were the ordinary sandwich beams with GFRP facesheets. The other specimens were strengthened by tooth plate with various density (ρ) and span (s). The details of specimens were shown in Table 3. *T* in specimen name is the symbol of the sandwich beams with tooth plate facesheets. Beam spans of 300 mm, 400 mm, and 500 mm, respectively, were presented as S3, S4, and S5 and foam density of 35 kg/m^3, 80 kg/m^3, and 150 kg/m^3 was presented as D1, D2, and D3. All the specimens were loaded under displacement control mode with loading rate of 2.0 mm/min and load-displacement data were recorded by a universal test machine with the capacity of 200 kN.

2.4. Double Cantilever Beam Tests. In order to study the interfacial fracture behavior of TFS beams, double cantilever beam test was performed in accordance with ASTM 5528-01 [20]. In this study, the specimens with different core density (35 kg/m^3, 80 kg/m^3, and 150 kg/m^3) were fabricated using a vacuum-assisted resin infusion process. In Figure 3, an initial interface crack had been made between the upper facesheet and the foam core. The lengths of specimen and initial crack were 254 mm and 50 mm, and the thicknesses of foam core and facesheet and were 40 mm and 2.2 mm. Metallic hinges were glued on both sides of the facesheets. The loading cell and a steel block bonded on the upper

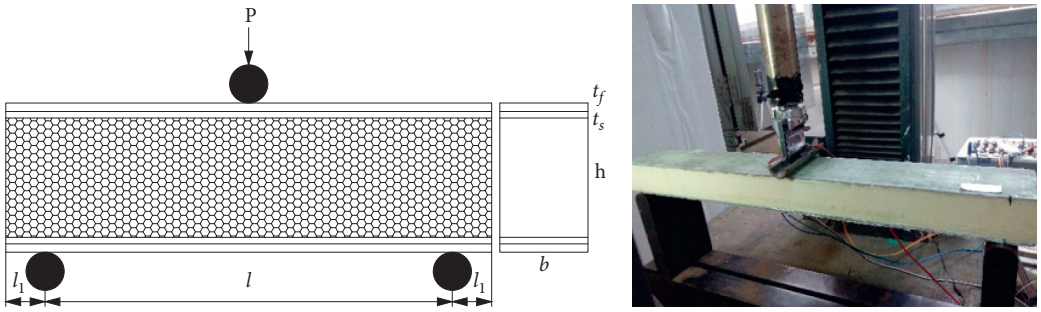

(a) (b)

Figure 2: (a) Three-point bending test configuration according to ASTM C 393-62; (b) test specimen under loading.

Table 3: Specimen parameters of ordinary sandwich beams and hybrid sandwich beams.

Specimen	H (mm)	L (mm)	l (mm)	t_f	t_s	ρ (kg/m^3)
NS3D1	44.2	340	300	2.1	—	35
NS3D2	44.2	340	300	2.1	—	80
NS3D3	44.2	340	300	2.1	—	150
TS3D1	44.4	340	300	1.5	0.8	35
TS3D2	44.4	340	300	1.5	0.8	80
TS3D3	44.4	340	300	1.5	0.8	150
TS4D1	44.4	440	400	1.5	0.8	35
TS4D2	44.4	440	400	1.5	0.8	80
TS4D3	44.4	440	400	1.5	0.8	150
TS5D1	44.4	540	500	1.5	0.8	35
TS5D2	44.4	540	500	1.5	0.8	80
TS5D3	44.4	540	500	1.5	0.8	150

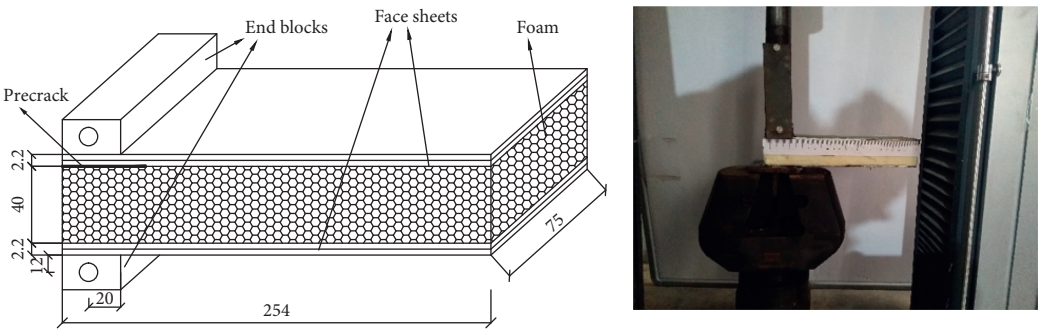

(a) (b)

Figure 3: (a) Test setup of DCB tests (unit: mm); (b) DCB specimen.

facesheet were connected by a stainless bar. In order to monitor the length of the crack propagation, the specimen edges were coated with a thin layer of water-soluble correction fluid from the side of the initial crack. The specimens were tested under displacement control mode with loading rate of 2.0 mm/min. During the tests, the load-displacement data were recorded by the computer whereas the crack lengths were recorded by a high-resolution digital camera. In addition, it should be mentioned in this context that there were not any separation between the FRP and tooth plate in all the tests.

3. Results and Discussions

3.1. Flexural Characteristic of Sandwich Structures. The test results of all specimens under three-point bending loading conditions, including the peak strength (P_u) and absorbed energy (E_a), were summarized in Table 4. The load-displacement data recorded during the tests were plotted in Figure 4. Figure 4(a) showed the effects of tooth plate on P_u of sandwich beams. Comparing with NS3D1 ($P_u = 234$ N), NS3D2 ($P_u = 490$ N), and NS3D3 ($P_u = 916$ N), the peak load of specimens TS3D1, TS3D2, and TS3D3 increased by 168%,

Table 4: Absorbed energy and peak load of specimens.

Specimen	E_a (J)	P_u (N)
NS3D1	1.15	234
NS3D2	1.29	490
NS3D3	1.14	916
TS3D1	19.72	627
TS3D2	23.28	1524
TS3D3	32.42	3280
TS4D1	13.80	605
TS4D2	21.20	1421
TS4D3	25.04	2784
TS5D1	12.25	576
TS5D2	17.86	1362
TS5D3	21.95	2218

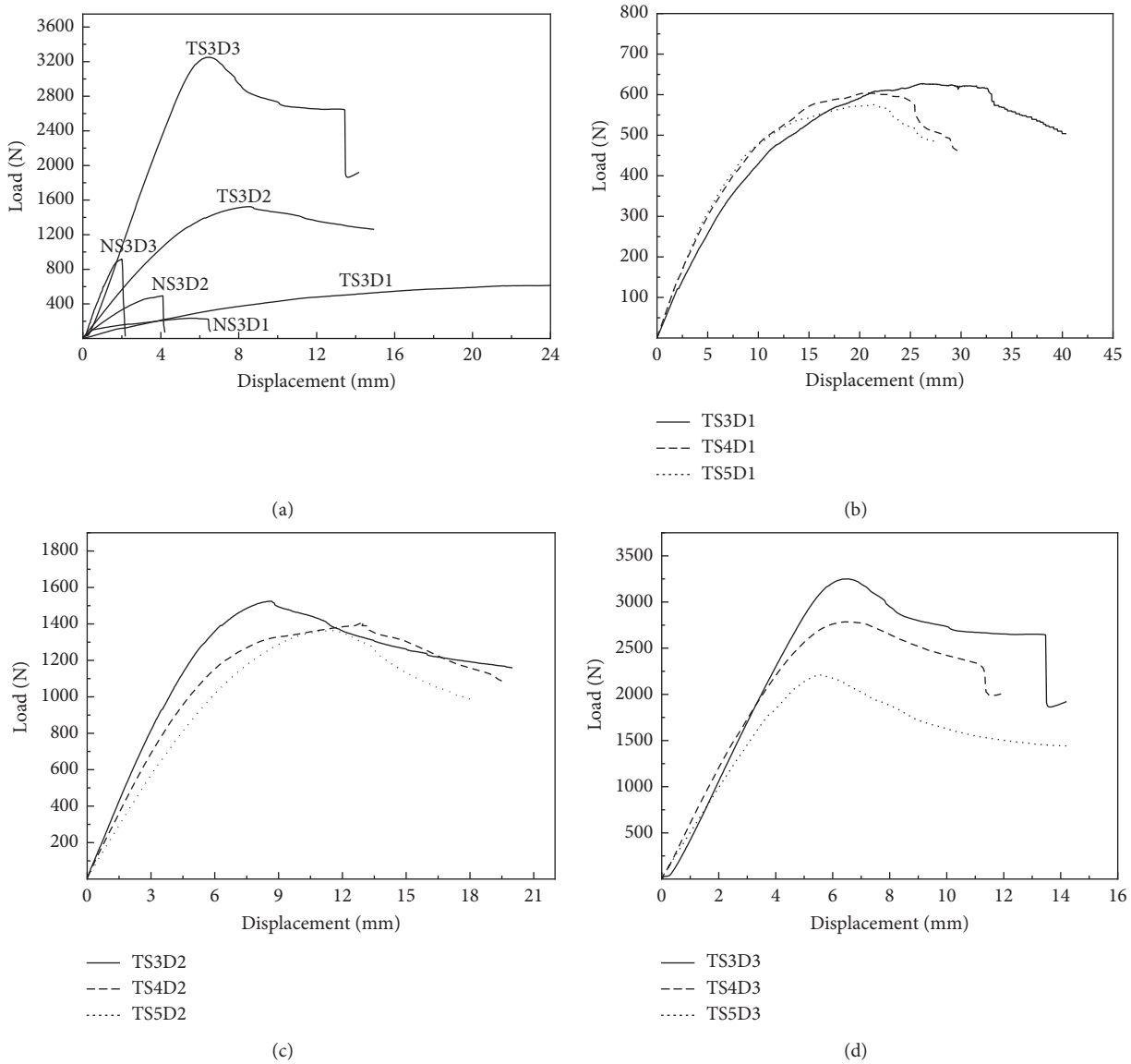

Figure 4: The load-displacement curves of specimens: (a) the normal sandwich beams and TFS beams with 300 span length, (b) the TFS beams with different span length and 35 kg/m^3 foam core, (c) the TFS beams with different span length and 80 kg/m^3 foam core, and (d) the TFS beams with different span length and 150 kg/m^3 foam core.

211%, and 258%, respectively. It is due to the fact that the tooth plate could significantly increase the stiffness of facesheets. Hence, the use of tooth plate can increase the peak strength of sandwich beams significantly. Figure 4(a) also showed the effects of foam density on P_u of TFS beams. For the specimens with 300 mm span, P_u of TS3D2 and TS3D3 were 1524 N and 3280 N, which were 143% and 423% larger than P_u of specimen TS3D1, respectively. That is mainly due to the fact that the foam with higher density has a higher strength. Higher density of foam can provide a good resistance to the applied load. Additionally, since the metal tooth had been embedded into the core foam, the debonding failure could scarcely be witnessed, in which the core foam with higher density enhanced the laminar property between the tooth surface and the core foam.

The effects of foam density on the energy absorption of TFS beams were illustrated in Figure 5. For the specimens with 300 mm span, E_a of specimens TS3D2 and TS3D3 were 23.28 J and 32.40 J, which were 18.1% and 64.3% larger than those of specimen TS3D1. For the specimens with 400 mm span, E_a of specimens TS4D2 and TS4D3 were 21.2 J and 25.04 J, which were 53.6% and 81.7% larger than those of specimen TS4D1. For the specimens with 500 mm span, E_a of specimens TS5D2 and TS5D3 were 17.86 J and 21.95 J, which were 45.8% and 79.1% larger than those of Specimen TS3D1. Therefore, the energy absorption capacity of TFS beams could be improved by increasing the foam density.

According to the load-displacement curves, all specimens exhibited an initial linear-elastic response with a subsequent nonlinear part near to the peak load. The foam density increase resulted in the increase of both equivalent flexural stiffness and the slope of the linear-elastic region. The force level after peak load showed some differences between TFS and sandwich beams with fiber composite faces. For TFS specimens, the load-displacement curves exhibited a smooth force drop after the maximum force value. However, an abrupt load drop was observed in the normal sandwich beams after the peak value, which was associated with foam failed by bulking of cell walls and edges. Hence, it can be concluded that TFS beams have a good integrity after plateau region and good resistance against transverse loads. Two main failure modes were observed during the bending tests: core shear and the facesheet indentation. For TFS specimens with foam density of 35 kg/m^3 and 80 kg/m^3, the main failure mode was facesheet indentation beneath the loading roller, which is shown in Figure 6(a). For TFS specimens with span of 400 mm and 500 mm and foam density of 150 kg/m^3, the failure mode was core shear. Shearing of the foam core occurred between upper loading indenter and lower support. The direction of shear crack was about 45° angel to the horizontal, which is shown in Figure 6(b). For TFS specimens with 300 mm span length, the failure mode was facesheet indentation.

3.2. Failure Mechanical of Double Cantilever Tests. As shown in Figure 7, the failure in the DCB specimen was mainly through the interface. The typical load-displacement curves

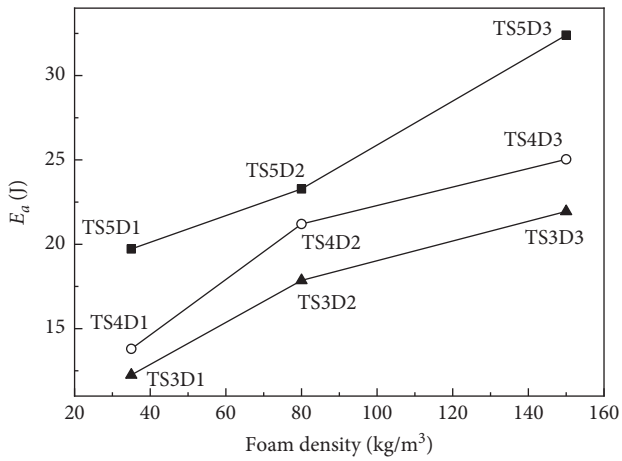

Figure 5: The effects of foam density on energy absorption of TFS beams.

obtained from the tests were shown in Figure 8. It could be found that the initial loading curves exhibited a linear-elastic response and the crack propagation was stable. After the peak load, the curves showed a saw-tooth and the growth of the crack propagation turned unstable.

The energy release rate was calculated by the experimental compliance calibration method. The compliance (C) is the ratio of load and displacement during the test, which can be determined using the following equation:

$$C = \frac{\delta}{P}, \tag{1}$$

where P is the load and δ is the load point displacement.

The relationship of specimen compliance versus crack length could be expressed as [21]

$$C = C_0 a^m, \tag{2}$$

where a is the crack length and C_0 and m are experiment determined constants measured from a linear fit to double logarithmic plot of C versus a. The value of m is the slope of compliance data.

The strain energy release rate of mode I interfacial fracture can be calculated by the Irwin-Kies equation [22]:

$$G_I = \frac{P^2}{2b}\frac{dC}{da}, \tag{3}$$

leading to

$$G_I = \frac{P^2}{2b}\left(mC_0 a^{m-1}\right), \tag{4}$$

in which b is the width of the specimen.

A typical double logarithmic plot of TFS specimen compliance versus the crack length is shown in Figure 9. From the figure, the slopes were found to be 2.174, 2.012, and 2.869 with foam density of 35 kg/m^3, 80 kg/m^3, and 150 kg/m^3. To bring constant m into equation (4) can obtain the experimental strain release rate of this system. Figure 10 showed a typical plot of strain energy rate versus crack length for DCB specimens loaded at 1 mm/min. It was found that the peak value of strain energy release rate increased

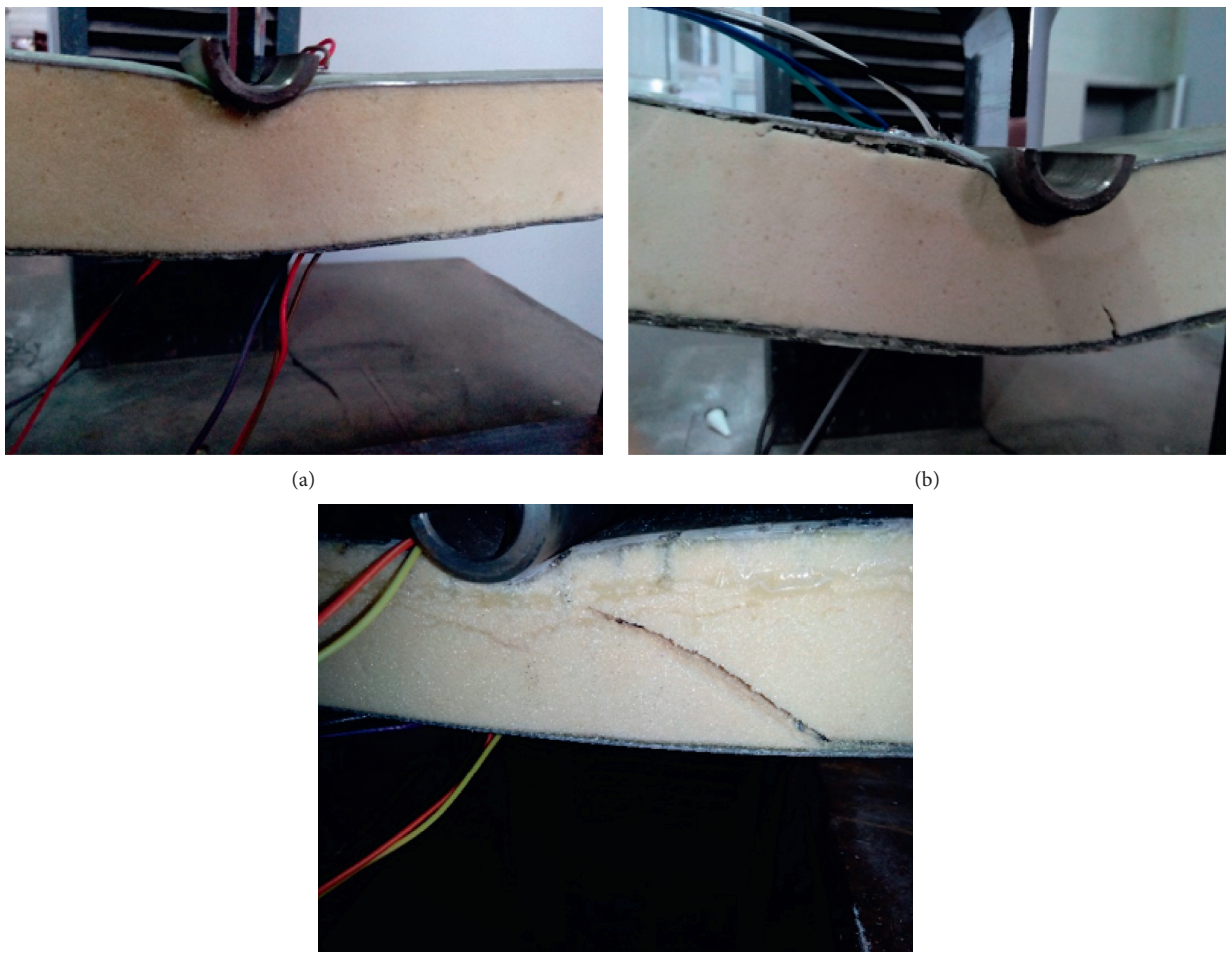

(a) (b)

(c)

Figure 6: The failure modes of TFS beams: (a) core indentation failure of hybrid sandwich beams with foam core density of 35 kg/m^3, (b) core indentation failure of hybrid sandwich beams with foam core density of 80 kg/m^3, and (c) core shear failure of hybrid sandwich beams with foam core density of 150 kg/m^3 under the span of 300 mm and 400 mm.

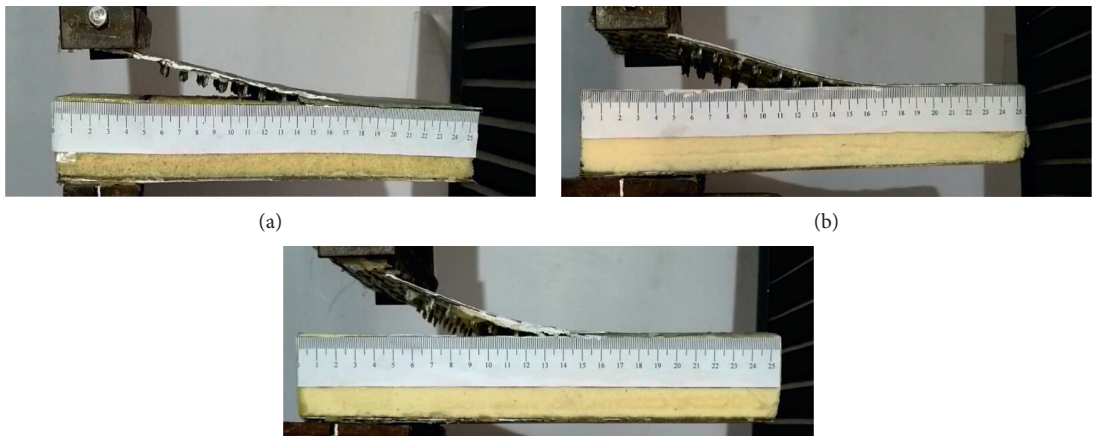

(a) (b)

(c)

Figure 7: Failure mode of DCB specimen: (a) DCB specimen of 35 kg/m^3 foam core, (b) DCB specimen of 80 kg/m^3 foam core, and (c) DCB specimen of 150 kg/m^3 foam core.

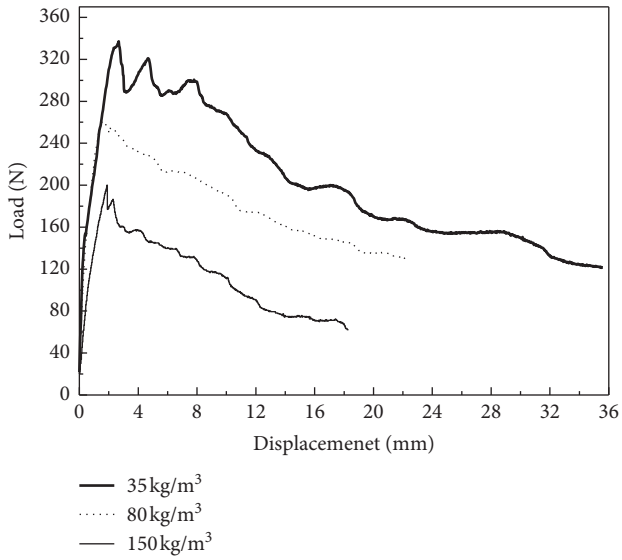

Figure 8: Load-displacement curves of DCB specimens.

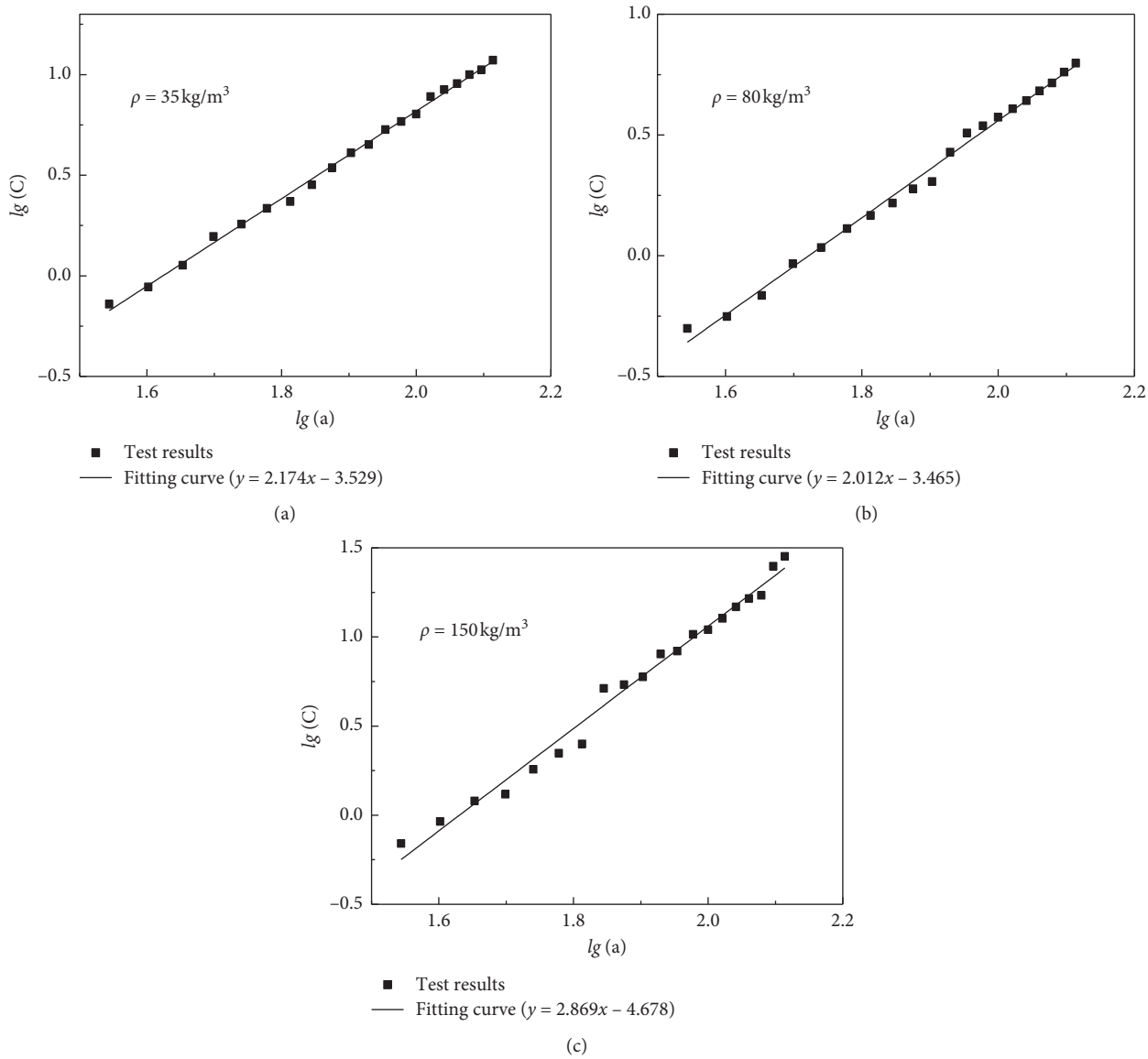

Figure 9: The values of m determined under different foam core density.

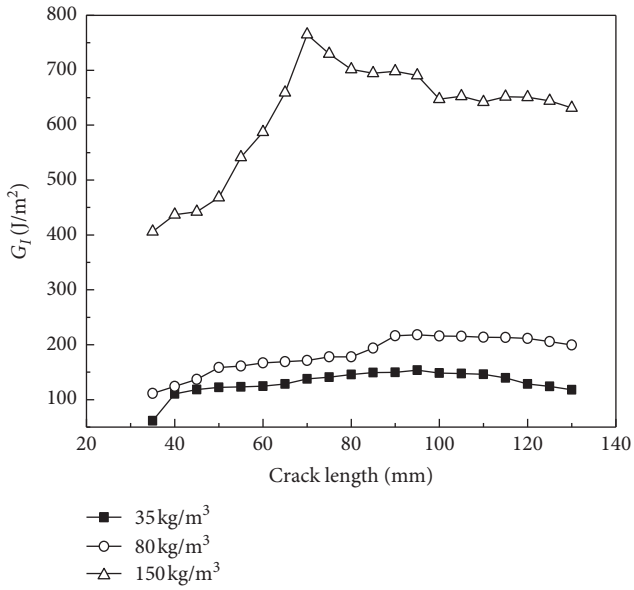

Figure 10: Strain energy release rate of specimens under different foam core density.

with the increase of foam density. Compared with the specimens of foam density 35 kgm^3, the peak value of strain energy release rate increased by 100% and 600%, respectively. It was concluded that the density of foam core had a great effect on the value of strain energy release rate in Figure 10.

4. Analysis Model

An analytical model was used to predict the peak loading of TFS beam under three-point bending test, including the failure modes of foam core shear and facesheet indentation (seen in Figure 11).

4.1. Core Shear. The shear failure occurs when the transverse shear stress exceeds the core shear strength. The collapse mechanics could be defined in equation (5). It had been assumed that the facesheets on the right side of the sandwich panel rotates through an angle θ whereas the left side rotates through $-\theta$. Thus, the foam core shears by an angle 2θ. It had been assumed that the bottom facesheet is subjected to tensile fracture when the foam core shear failure.

The external work done by applied load can be calculated by the following equation:

$$W_e = \frac{Pl\theta}{2}. \tag{5}$$

Internal work absorbed by the foam core and facesheet can be calculated by the following equation [23]:

$$W_i = 4M_f'\theta + bt_c\tau_c(2l_1 + l)\theta, \tag{6}$$

in which τ_c is the core shear strength, b is the width of TFS beams, and M_f' is the initial bending moment of brittle fracture of hybrid facesheet, which can be calculated by the following equation:

$$M_f' = \frac{bt_f^2}{6}\sigma_{fy} + \frac{bt_s^2}{6}\sigma_{sy}, \tag{7}$$

in which t_f and t_s are the thickness of facesheet and tooth plate, respectively, and σ_{fy} and σ_{sy} are the tensile strength of GFRP skin and tooth plate. Equating the external work done by applied force P to the internal work, the peak load due to core shear failure of composite sandwich beam could be obtained by the following equation:

$$P_{cr} = 2bt_c\tau_c\frac{2l_1 + l}{l} + \frac{4b\left(t_f^2\sigma_{fy} + t_s^2\sigma_{sy}\right)}{3l}. \tag{8}$$

4.2. Indentation. In three-point bending, the bending moment induced by the applied transverse load P is $M = Pl/4$, the compressive axial force of upper facesheet is $F = M/(c + t_f)$ and the lower facesheet experiences a tensile force of equal magnitude. The indentation failure occurs if the foam core is compressed by mid-roller with an indentation zone of 2λ in a rigid-ideally plastic manner. The transverse load from sandwich face to foam core is $q = \sigma_c\ b$, where σ_c is the crushing strength of a rigid-ideally plastic core and b is the width of the TFS beam, as shown in Figure 11. The indentation failure had been analyzed by Steeves and Fleck [7] based on a plastically deforming foundation model. The indentation failure load could be calculated by the following equation:

$$P = b\left(t_s + t_f\right)\left(\frac{\pi^2\sigma_c^2E_f'\left(t_s + t_f + c\right)}{3l}\right)^{1/3}, \tag{9}$$

where c is the thickness of foam core and E_f' is the equivalent elastic modulus of hybrid facesheet, which can be calculated by the following equation:

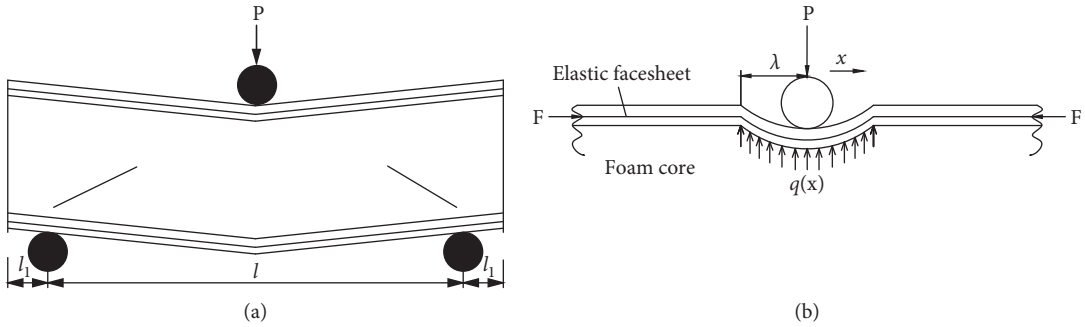

Figure 11: Failure types of TFS sandwich structures: (a) core shear failure and (b) indentation.

Table 5: Comparison of experimental and analytical results.

Specimen	Ultimate load (kN)		Difference	Failure mode
	Test result	Analytical result		
TS3D1	0.627	0.767	22.3%	Indentation
TS4D1	0.605	0.697	15.2%	Indentation
TS5D1	0.576	0.647	12.3%	Indentation
TS3D2	1.524	1.769	16.1%	Indentation
TS4D2	1.412	1.607	13.8%	Indentation
TS5D2	1.362	1.492	9.5%	Indentation
TS3D3	3.280	3.055	−6.9%	Core shear
TS4D3	2.784	2.936	5.5	Core shear
TS5D3	2.218	2.738	23.4%	Indentation

$$E_f' = \frac{E_f t_f + E_s t_s}{t_f + t_s}, \tag{10}$$

where E_f and E_s are the elastic modulus of GFRP and tooth plate, respectively.

The predicted peak load of TFS beams under three-point bending load condition is presented in Table 5. By comparing the analytical and experimental results, it was found that the largest variation between predicted and experimental results in peak load was 23.4%. Mostly, the peak load of TFS can be well predicted by the analytical model. For the failure mode of indentation, the differences were greater than the mode of core shear, probably due to the special structure of the facesheets. Equation (9) could not consider the holes in the tooth plates, which were surrounded by the resins and fibers in the facesheet.

5. Conclusion

In this study, three-point bending tests and double cantilever tests had been conducted on a new family of sandwich beams with fiber-metal hybrid facesheets. Both foam core density and span length parameters were selected to investigate the flexural behavior of sandwich structures. From the tests, the following conclusions can be obtained through the above research:

(1) For common composite sandwich structure, there were many kinds of failure modes, like indentation, core shear, facesheet debonding, and kinking, under bending load. Because of the insertion of the tooth plate, just indentation mode and core shear mode happened, while some initial interfacial failures were avoided, which indicates that the tooth in the steel plate could effectively enhance the interlaminar behavior.

(2) With the increasing of foam density, the foam shear strength and compressive strength improved. Tooth plate in the specimens had minor influence on the shear behavior, while it could improve the local indentation of the facesheet for its higher stiffness compared to FRP. The core material could support the facesheets more effectively, and it suppressed the local compression at the loading point, which was the major factor that ultimate bending capacity increased.

(3) The interlaminar behavior had been further researched in DCB test. In the test, there was no damage on the tooth plate, while foam cracked into the internal part of the core, unlike the nearby interfacial damage in common FRP sandwich beam. The foam was obviously weaker than the steel tooth plate, so the damage happened in the foam. There was still potential improvement by increasing the core material properties.

Data Availability

The data used to support the findings of this study are available from the corresponding author upon request.

Conflicts of Interest

The authors declare that they have no conflicts of interest.

Acknowledgments

This research was supported by the Key Program of National Natural Science Foundation of China (Grant no. 51238003) and Key University Science Research Project of Jiangsu Province (Grant no. 15KJA560001).

References

[1] L. C. Hollaway, "A review of the present and future utilisation of FRP composites in the civil infrastructure with reference to

their important in-service properties," *Construction and Building Materials*, vol. 24, no. 12, pp. 2419–2445, 2010.

[2] L. B. Vogelesang and A. Vlot, "Development of fibre metal laminates for advanced aerospace structures," *Journal of Materials Processing Technology*, vol. 103, no. 1, pp. 1–5, 2000.

[3] H. G. Vlot and J. E. Perez Ipiña, "Short-beam shear fatigue behavior of fiber metal laminate (Glare)," *International Journal of Fatigue*, vol. 95, pp. 236–242, 2017.

[4] R. Alderliesten and J. Homan, "Fatigue and damage tolerance issues of Glare in aircraft structures," *International Journal of Fatigue*, vol. 28, no. 10, pp. 1116–1123, 2006.

[5] E. K. Baumert, W. S. Johnson, R. J. Cano, B. J. Jensen, and E. S. Weiser, "Fatigue damage development in new fibre metal laminates made by the VARTM process," *Fatigue & Fracture of Engineering Materials & Structures*, vol. 34, no. 4, pp. 240–249, 2011.

[6] M. H. Kashani, M. Sadighi, M. Mohammadkhah, and H. S. Alavijeh, "Investigation of scaling effects on fiber metal laminates under tensile and flexural loading," *Proceedings of the Institution of Mechanical Engineers, Part L: Journal of Materials: Design and Applications*, vol. 229, no. 3, pp. 189–201, 2015.

[7] C. A. Steeves and N. A. Fleck, "Collapse mechanisms of sandwich beams with composite faces and a foam core, loaded in three-point bending—part I: analytical models and minimum weight design," *International Journal of Mechanical Sciences*, vol. 46, no. 4, pp. 561–583, 2004.

[8] K. Kabir, T. Vodenitcharova, and M. Hoffman, "Response of aluminium foam-cored sandwich panels to bending load," *Composites Part B: Engineering*, vol. 64, pp. 24–32, 2014.

[9] S. Dariushi and M. Sadighi, "A study on flexural properties of sandwich structures with fiber/metal laminate face sheets," *Applied Composite Materials*, vol. 20, no. 5, pp. 839–855, 2013.

[10] G. Reyes, "Mechanical behavior of thermoplastic FML-reinforced sandwich panels using an aluminum foam core: experiments and modeling," *Journal of Sandwich Structures & Materials*, vol. 12, no. 1, pp. 81–96, 2010.

[11] I. Ortiz de Mendibil, M. Sarrionandia, M. Mateos, J. Aurrekoetxea, and L. Aretxabaleta, "Impact behaviour of glass fibre-reinforced epoxy/aluminium fibre metal laminate manufactured by Vacuum Assisted Resin transfer moulding," *Composite Structures*, vol. 140, pp. 118–124, 2016.

[12] G. Reyes Villanueva and W. J. Cantwell, "The high velocity impact response of composite and FML-reinforced sandwich structures," *Composites Science and Technology*, vol. 64, no. 1, pp. 35–54, 2004.

[13] J. G. Carrillo and W. J. Cantwell, "Mechanical properties of a novel fiber-metal laminate based on a polypropylene composite," *Mechanics of Materials*, vol. 41, no. 7, pp. 828–838, 2009.

[14] D. Srinivasagupta, B. Joseph, P. Majumdar, and H. Mahfuz, "Effect of processing conditions and material properties on the debond fracture toughness of foam-core sandwich composites: process model development," *Composites Part A: Applied Science and Manufacturing*, vol. 34, no. 11, pp. 1085–1095, 2003.

[15] F. Avilés and L. A. Carlsson, "Analysis of the sandwich DCB specimen for debond characterization," *Engineering Fracture Mechanics*, vol. 75, no. 2, pp. 153–168, 2008.

[16] V. Vadakke and L. A. Carlsson, "Experimental investigation of compression failure of sandwich specimens with face/core debond," *Composites Part B: Engineering*, vol. 35, no. 6–8, pp. 583–590, 2004.

[17] ASTM D3039-08, *Standard Test Method for Tensile Properties of Polymer Matrix Composite Materials*, ASTM, West Conshohocken, PA, USA, 2008.

[18] ASTM D695-10, *Standard Test Method for Compressive Properties of Rigid Plastics*, ASTM, West Conshohocken, PA, USA, 2015.

[19] ASTM C393-62, *Standard Test Method for Flexural Properties of Sandwich Constructions*, ASTM, West Conshohocken, PA, USA, 2000.

[20] ASTM D. 5528-01, *Standard Test Method for Mode I Interlaminar Fracture Toughness of Unidirectional Fiber-Reinforced Polymer Matrix Composites*, ASTM, West Conshohocken, PA, USA, 2001.

[21] T. S. Gates, X. Su, F. Abdi, G. M. Odegard, and H. M. Herring, "Facesheet delamination of composite sandwich materials at cryogenic temperatures," *Composites Science and Technology*, vol. 66, no. 14, pp. 2423–2435, 2006.

[22] G. R. Irwin and J. A. Kies, "Critical energy rate analysis of fracture strength," *Welding Journal Research Supplement*, vol. 33, pp. 193–198, 1954.

[23] K. Mohan, Y. T. Hon, S. Idapalapati, and H. P. Seow, "Failure of sandwich beams consisting of alumina face sheet and aluminum foam core in bending," *Materials Science and Engineering: A*, vol. 409, no. 1-2, pp. 292–301, 2005.

Hindawi
Advances in Polymer Technology
Volume 2020, Article ID 2097369, 13 pages
https://doi.org/10.1155/2020/2097369

Research Article

Bond Performance of Carbon Fiber-Reinforced Polymer Bar with Dual Functions of Reinforcement and Cathodic Protection for Reinforced Concrete Structures

Yingwu Zhou, Lili Sui, Feng Xing, Xiaoxu Huang, Yaowei Zheng, and Debo Zhao

Guangdong Provincial Key Laboratory of Durability for Marine Civil Engineering, Shenzhen University, Shenzhen 518060, China

Correspondence should be addressed to Debo Zhao; debozhao@163.com

Received 7 November 2019; Accepted 18 December 2019; Published 25 January 2020

Guest Editor: Tianyu Xie

The dual function of a carbon fiber-reinforced polymer (CFRP) bar working as reinforcement and impressed current cathodic protection (ICCP) anode for reinforced concrete structures has been proposed and researched in this paper. The ICCP tests with different current densities and polarization durations were first conducted for the concrete with high chloride content. After the ICCP application, pull out tests were then performed to investigate the bond behaviors of CFRP bars. Experimental results have shown the effectiveness of the new-type ICCP system with the CFRP bar as the anode on corrosion protection. The ICCP system provided electrons to the steel bar continuously and brought the potential of the steel bar down to the immunity region. Under the anodic polarization with a large current density of 100 mA/m^2, the CFRP bar-concrete interface presented acidification and the chemical adhesion on the interface was decreased significantly. However, for cases in the experiment, the ICCP application had an insignificant influence on the ultimate bond strength.

1. Introduction

The durability of reinforced concrete (RC) structures (Figure 1(a)) can be significantly deteriorated due to the impact of rebar corrosion [1–3]. In order to overcome the corrosion issue, research has been carried out in recent decades to incorporate corrosion-resistant materials, such as fiber-reinforced polymer (FRP), into concrete structures [4, 5]. Replacing traditional steel bars with FRP bars can effectively inhibit corrosion and improve the durability of concrete structures [6, 7]. However, due to the low elastic modulus and brittle behavior of some FRP materials, problems exist in FRP-reinforced concrete (FRPRC) structures (Figure 1(b)), such as the high deformability, the lack of ductility, and large crack widths [8–11]. Thus, the design of FRPRC components is generally dominated by the serviceability limit state requirements, such as the crack width and deformation limits. Moreover, the bond performance between FRP bars and matrix become crucial because it influences the crack width and spacing of FRPRC components significantly [12, 13]. The performances of concrete structures can be improved significantly by utilizing a combination of FRP and steel reinforcements [14–18]. In a hybrid FRP-steel reinforced concrete (hybrid FRPRC) beam (Figure 1(c)), the corrosion-resistant FRP bars are usually placed at the lower layer of the tensile zone, while the corrodible steel bars are placed at the upper layer of the tensile zone far from the environmental aggressive agents, mainly chloride ion. By optimizing the design, the hybrid reinforced concrete structures can be featured with large rigidity, high ductility and ultimate bearing capacity, and good corrosion resistance and durability.

Besides, the steel corrosion in RC structures can be inhibited with electrochemical technologies. The impressed current cathodic protection (ICCP) technique, as illustrated in Figure 2, is widely accepted as an effective approach to prevent corrosion of steel reinforcements [19, 20]. By applying a current to a steel bar with an external power supply, the steel bar becomes a cathode and its potential is adjusted down to suppress the migration of electrons generated by the

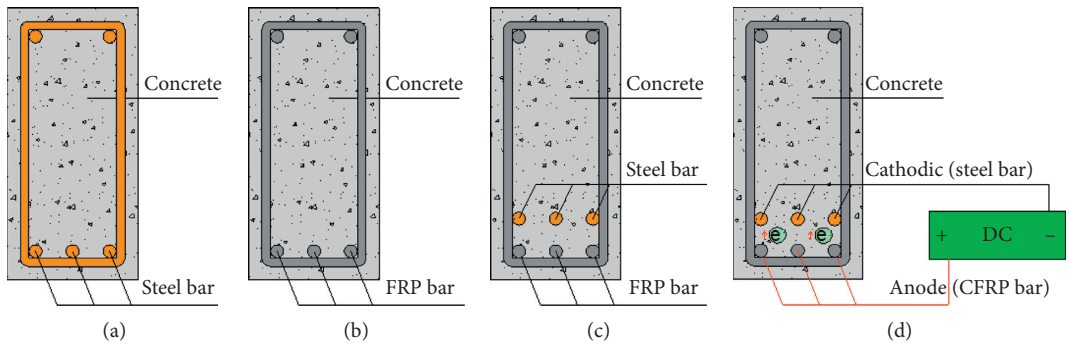

Figure 1: Illustrations of (a) RC structure; (b) FRPRC structure; (c) hybrid FRPRC structure; (d) hybrid FRPRC structure with ICCP-CB technique.

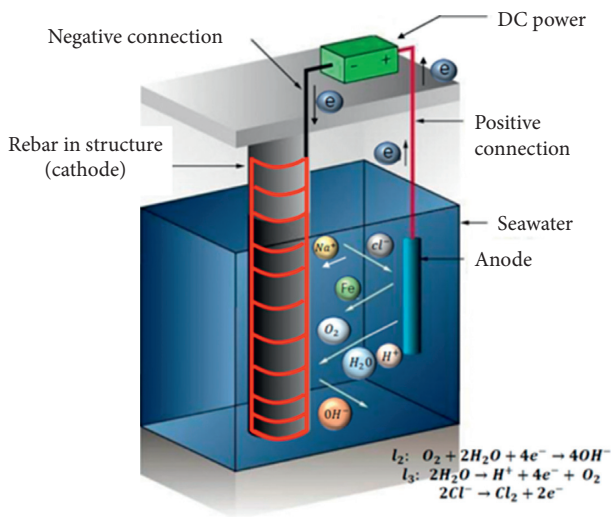

Figure 2: Schematic diagram of the ICCP technique.

corrosion. The failure of the ICCP system is mainly due to the deterioration of the anode material or bond interface between the anode and concrete [21, 22]. Therefore, intensive research has focused on the development of anode with better performance characteristics, such as lower bond deficiency and acidification. Recent research shows that CFRP is a promising anode material because of its good conductivity and electrochemical stability. Lee-Orantes et al. [23] conducted an experimental investigation on a reinforced concrete cathodic protection system with CFRP anodes, and no apparent degradation of carbon composites and conductive resins was observed. The ICCP tests of RC beams conducted by Gadve et al. [24] demonstrated that using FRP wraparounds as an anode effectively retarded the corrosion of steel, and the loss of bond between steel and concrete can be avoided by selecting the appropriate protection current density. Moreover, considering its excellent mechanical properties, FRP can be applied to RC structures with dual functions of corrosion protection and structural strengthening, and in this case, the bond degradation between FRP and concrete during the ICCP process plays a crucial role in structural performances. Lambert et al. [25] used CFRP fabric for both flexural strengthening of precorroded reinforced concrete beams and a dual functional capacity as an ICCP anode. The flexural testing after a period of ICCP operation showed that FRP debonding induced a 13.5% decrease in the ultimate strength of RC beams incorporating dual function CFRP anodes, compared with corresponding beams with CFRP strengthening only. Van Nguyen et al. [26] investigated the dual function of a CFRP rod working as the near-surface mounted (NSM) strengthening and ICCP anode, and in this system, the bonding between the CFRP rod anode and concrete interface was improved by using a combination of geopolymer and epoxy resin. Experimental results showed that the high current density did not affect the bonding of the CFRP rod significantly.

The ICCP technique can be applied to the hybrid FRPRC structures by using CFRP bars (CB) embedded in the structures as the anode. The resulting structure (Figure 1(d)) is expected to have excellent mechanical performances as well as corrosion resistance, which is especially suitable for chloride-rich environments such as coastal and offshore areas. To evaluate the feasibility of the ICCP-CB technique, the electrochemical properties and bond performances of CFRP bar anode were investigated using a simulated ICCP system in this paper. In the simulated ICCP system, current density and duration were varied to determine appropriate protection parameters. After that, pull out tests were performed on specimens to study the short-term bond behaviors of the CFRP bar-concrete interface in the anode region after high-current cathodic protection.

2. Experimental Program

2.1. Material Properties. CFRP bars and steel bars used in the experiment both have a diameter of 12 mm, and the mechanical properties are shown in Table 1. The ribbed CFRP bar is depictured in Figure 3. In order to exert a better conductivity, CFRP bars were polished to remove the surface resin before the electrochemical test. In order to simulate the chloride-rich environment, sea-sand (Cl^- content: 0.05%) and seawater (Cl^- content: 2.00×10^4 mg/L) were used to mix the concrete. The natural sea-sand and seawater were obtained from the offshore area of Fuyong wharf, Shenzhen, China. The detailed chemical compositions of natural

Table 1: Mechanical properties of CFRP bars and steel bars.

Bar type	Diameter (mm)	Initial stiffness (GPa)	Yield strain (%)	Yield strength (MPa)	Ultimate strain (%)	Ultimate stress (MPa)
CFRP	12	125	—	—	—	788
Steel	12	201.37	0.23	433.21	0.48	582.52

Figure 3: Shape of the CFRP bar.

seawater are listed in Table 2. Ordinary Portland cement (P.O 42.5 R) was used for the cement, and gravels with a diameter between 12 mm~20 mm were used for the coarse aggregate. The mix proportion of concrete in weight was 1 : 0.49 : 1.58 : 2.81 (cement : water : sand : gravel). The compressive strengths of concrete at 28 days and before pull out tests were 42.4 MPa and 54.2 MPa, respectively, which were determined with cubic specimens with a side length of 100 mm.

2.2. Specimen Design. A total of 15 specimens were prepared for the ICCP test and pull out test, which were divided into five groups according to different experimental variables, and each group had three identical specimens. The shape of the specimen is illustrated in Figure 4. The specimens was designed according to the Chinese standard GB 50152-92 [27], and the specimens dimensions were adjusted a little to fit the existing molds in the laboratory. The concrete matrix of each specimen was a cubic with a length of 100 mm. A CFRP bar with a length of 450 mm was laid through the centerline of the specimen. The CFRP bar was extended from the specimen left surface for 300 mm to facilitate applying load and installing extensometers in the pull out test. Meanwhile, a 50 mm CFRP bar was extended beyond the right surface of the cylinder for the connection of anode in the ICCP test and the installation of extensometers in the pull out test. In the 100 mm midsection, the bonding area was designed as 48 mm and the left 52 mm section was set to be nonbonding areas, where Teflon tape was used to separate the concrete from the CFRP bar. The nonbonding area was designed primarily to avoid local failure of the ends resulting from stress concentration. A steel bar with 98 mm length was arranged right above the CFRP bar, with a center to center distance of 25 mm. The steel bar was embedded in the concrete with a length of 48 mm, and the extended 50 mm section was for the connection of cathode in the ICCP system.

The experimental variables in the ICCP test include current density and polarization duration. According to NACE SP0290-2007 [28], current densities of 5, 20, 50, and 100 mA/m^2 were applied on specimens in 4 groups, respectively, while the other group was set as a reference group and did not undergo the ICCP test. In each group, two specimens were tested for polarization duration of 4 months, while the other one had a polarization duration of 6 months. The detailed experimental parameters of specimens are listed in Table 3. The specimen identification is defined as I-current density-polarization duration. For example, a specimen named I-5-4M denotes that the current density and polarization duration in the ICCP test are 5 mA/m^2 and 4 months, respectively. Besides, "R" denotes replicated specimens and "RF" represents specimens in the reference group.

2.3. ICCP Test. ICCP tests begun after the specimens were cured in the laboratory environment for 60 days. Before ICCP application, both the steel bar and the CFRP bar extended outside the concrete cubic were polished to ensure a good conductivity at the cathode and anode connection. The schematic view and real picture of the ICCP test system are shown in Figure 5. During the ICCP test, the potential of the steel bar was measured by Ag/AgCl reference electrodes and a digital voltmeter (DVM). Three kinds of potential were recorded: on-potential, instant-off potential, and depolarization potential measured 4 hours after pausing the cathodic protection system. According to the ASTM C876 standard, the relationship between the rebar corrosion potential and the probability of corrosion is as follows: for potentials (ref. electrode: Ag/AgCl) larger than −119 mV, the probability that no steel corrosion occurs is larger than 90%; For potentials (ref. electrode: Ag/AgCl) smaller than −269 mV, the probability that steel corrosion occurs is larger than 90%; for potentials falling between these limits, the corrosion activity of the reinforcing steel is uncertain. Moreover, after the ICCP system lasts for 120 days, linear polarization resistance of the steel bar was measured and the corresponding corrosion current density was obtained by the Stern–Geary relationship [29] to evaluate the corrosion state of the steel bar.

2.4. Uniaxial Pull Out Test. After ICCP operation, pull out tests were conducted on specimens to investigate the bond performance of CFRP bars after galvanostatic anodic polarization. Considering the low shear strength of CFRP bars, an 80 mm long aluminum sleeve was adhered outside the loading end of the bar to prevent it from being damaged by the chuck of the testing machine, as shown in Figure 6.

Table 2: Chemical compositions of nature seawater (in mg/L).

Na^+	K^+	Ca	Mg	F^-	Cl^-	Br^-	SO_4^{2-}	CO_3^{2-}
395.0	422.5	1.24×10^4	1.00×10^3	5.14	2.00×10^4	48.55	1.82×10^3	7.54

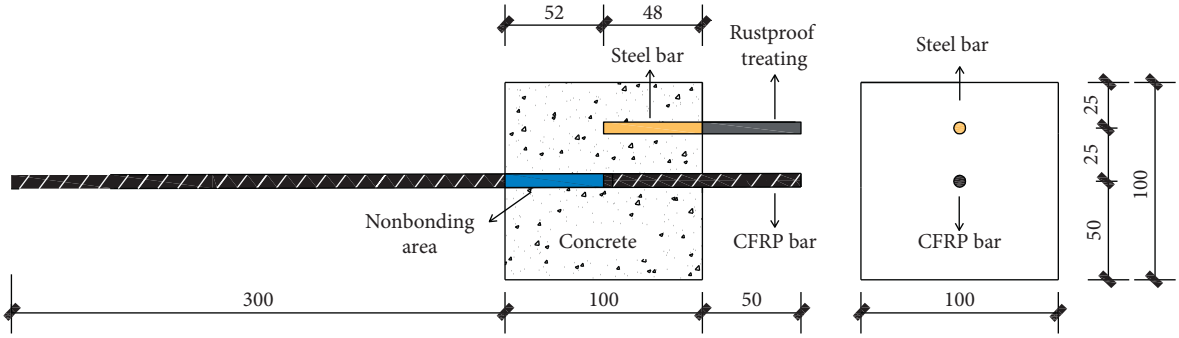

Figure 4: Schematic of the unidirectional pull out specimen (unit: mm).

Table 3: Experimental parameters of specimens.

Specimen no.	Current density (mA/m^2)	Polarization duration (day)
I-0-RF-1	0	0
I-0-RF-2	0	0
I-0-RF-3	0	0
I-5-4M	5	120
I-5-4M-R	5	120
I-5-6M	5	180
I-20-4M	20	120
I-20-4M-R	20	120
I-20-6M	20	180
I-50-4M	50	120
I-50-4M-R	50	120
I-50-6M	50	180
I-100-4M	100	120
I-100-4M-R	100	120
I-100-6M	100	180

The pull out test setup is shown in Figure 7. The pull out tests scheme followed the Chinese standard GB 50152-92 [27]. The tests were conducted with a servo-hydraulic testing machine with a capacity of 300 kN. Extensometers were installed on the loading end and free end of the specimen to measure the slips, and a load cell attached at the bottom of counterforce frame recorded the pull out force. The specimens were tested under the displacement-control mode with a loading rate of 0.05 mm/min. A data acquisition system was used to collect the test data with a sampling frequency of 5 Hz. The average bond stress τ is defined as

$$\tau = \frac{F}{\pi d l_b}, \tag{1}$$

where F is the applied load and d and l_b are the rebar diameter and bond length, respectively.

Moreover, after the pull out test, phenolphthalein solution was sprayed on the bonded area of the split concrete matrix to investigate the acidification condition of the CFRP bar-concrete interface.

3. Test Results and Discussion

3.1. ICCP Test. During the ICCP test, the depolarization potential of the steel bar was monitored since the specimens were cured for 28 days till the pull out test begun. The measured potential, as shown in Figure 8, can be used as an index for reinforcement corrosion monitoring. Based on the evaluation criterion described in Section 2.3, during the natural corrosion stage between 28 and 70 days of curing, the corrosion potentials of all specimens were between -269 mV~−119 mV, indicating an uncertain probability of steel corrosion. After the ICCP test begun, all specimens with ICCP application had corrosion potentials more positive than −119 mV, indicating that the steel passivation appeared and the probability of corrosion is less than 10%. However, for specimens in the reference group without ICCP application, the corrosion potentials continued to decline and were lower than −269 mV after 98 days of curing, which means that the corrosion probability is larger than 90%. The monitoring results showed the effectiveness of the ICCP technique: the corrosion process of reinforcing steel with ICCP protection was inhibited, while steel corrosion continued to develop for specimens without ICCP protection. The measured on-potential histories of specimens during the ICCP test are shown in Figure 9. After the ICCP application, the on-potentials at different current densities stabilized in a certain range and the curves dropped slightly with time increasing. The on-potential became more negative as current density increases.

The measured linear polarization resistance and corresponding corrosion current density of the steel bar at 120 days of ICCP application are listed in Table 4. The results of the polarization resistance measurements show that the specimens without ICCP protection were at a corrosion stage of a high probability, while those with ICCP protection were at a corrosion stage of a low probability. The results of the linear polarization resistance measurement further demonstrate the feasibility and effectiveness of the ICCP protection system with CFRP bar as the anode.

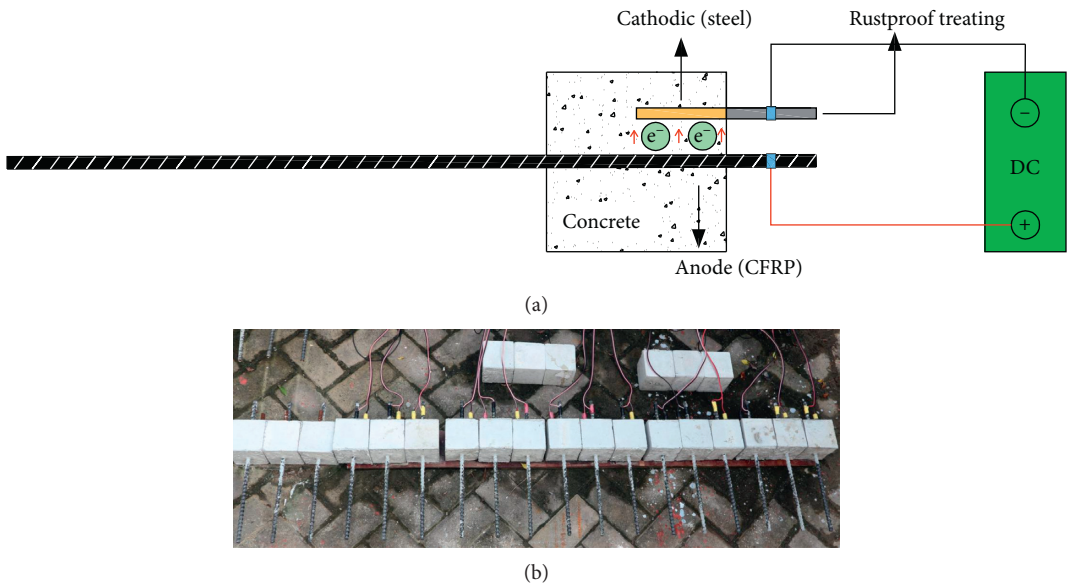

Figure 5: Test setup for ICCP system. (a) Schematic view. (b) Real picture.

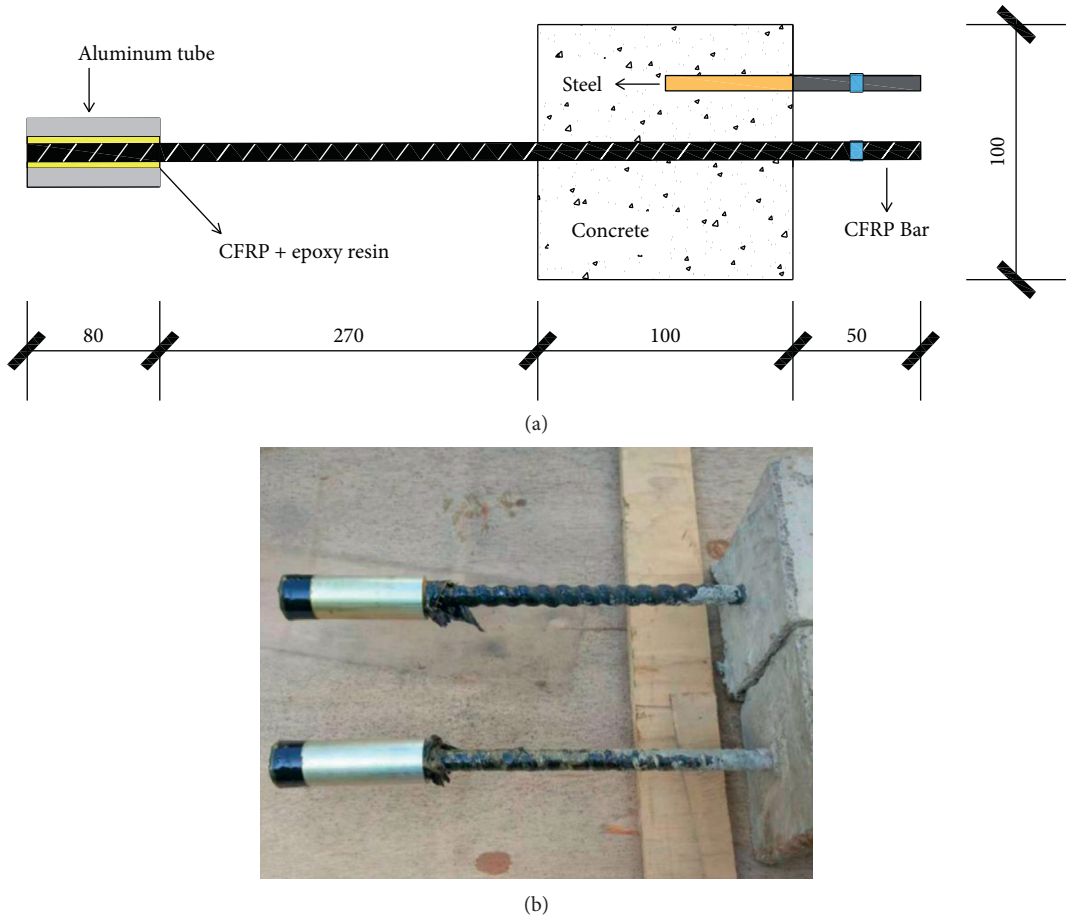

Figure 6: Schematic of the loading end reinforcement. (a) Schematic diagram (unit: mm). (b) Real picture.

3.2. Pull Out Test

3.2.1. Failure Mode. The overall failure mode of all specimens was splitting failure, as shown in Figure 10. During the pull out process, radical cracks first emerged at the free end of the specimen and then propagated toward the side surfaces, eventually splitting the concrete matrix into two or three parts. The indentations caused by CFRP bar ribs were

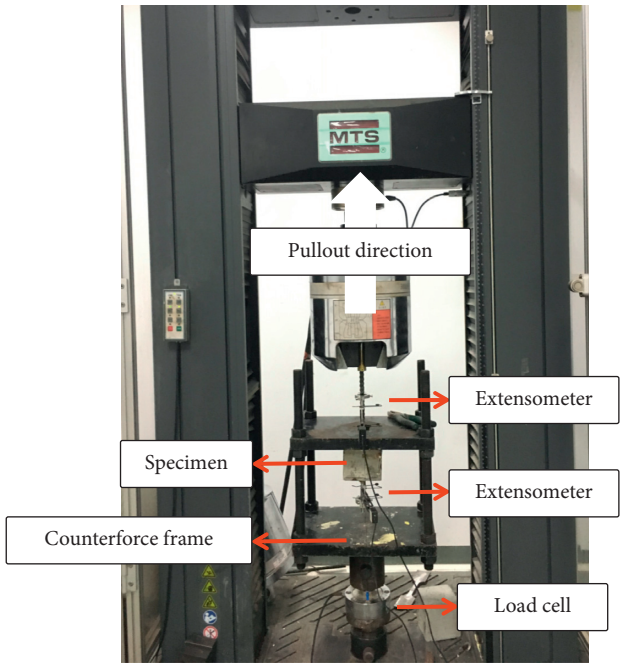

Figure 7: Pull out test setup.

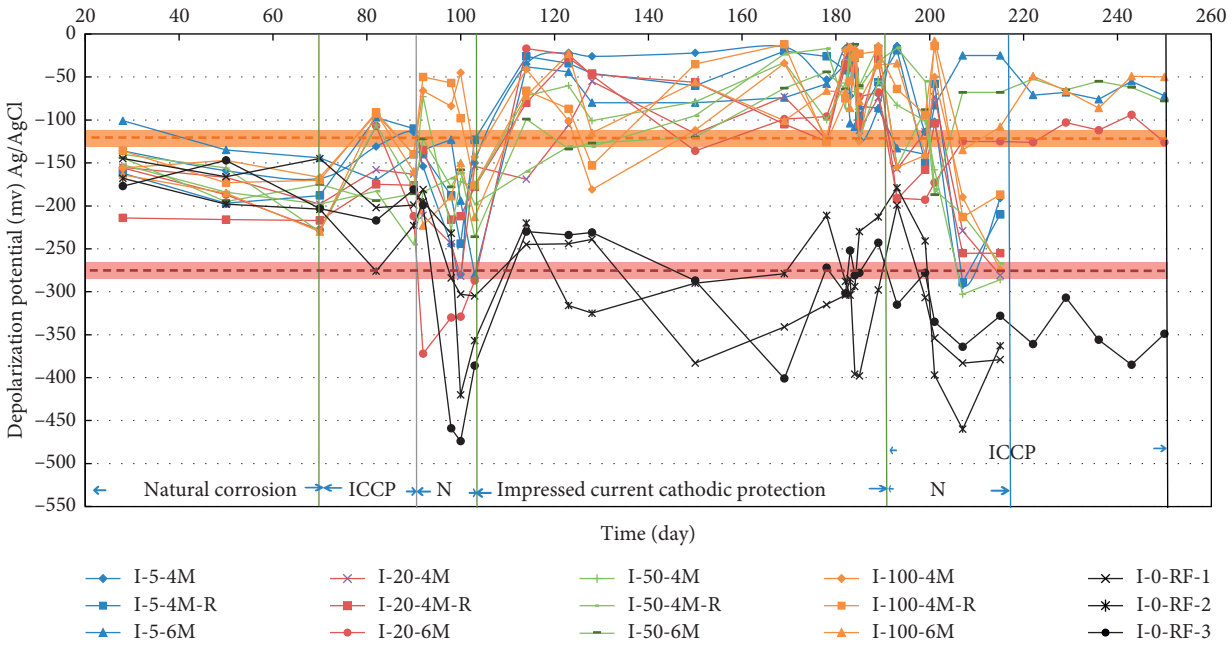

Figure 8: Depolarization potential histories of steel bar during the ICCP tests.

clearly observed on the concrete matrix. The occurrence of splitting failure is caused by a large rib height of the CFRP bar and a relatively small concrete cover thickness. During the pull out process, the inclined ribs of the CFRP bar produced a high radical expansive stress on the concrete matrix, which exceeded the tensile strength of the concrete, leading to the radical cracks and eventually splitting of the matrix.

The local failure modes of the CFRP bar-concrete interface are shown in Figures 11 and 12. For specimens with different ICCP current densities, various failure patterns were observed on the CFRP bar-concrete interface. For I-0-RF specimens, the rib indentations had a close color with the surrounding concrete, and textures created by the surface of the CFRP bar were clearly observed on the concrete interface. The yellow resin adhered to the surface of the CFRP

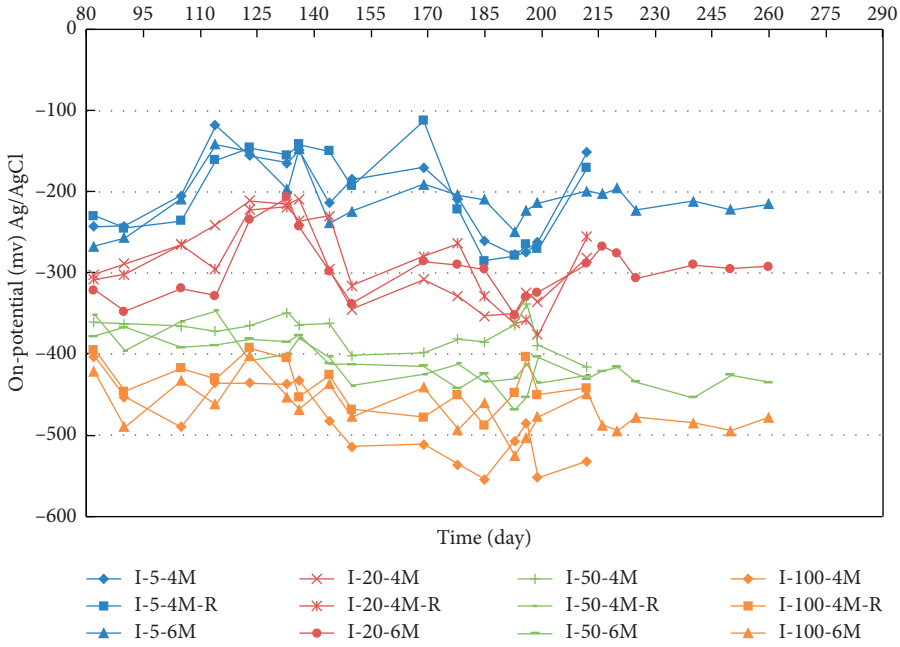

Figure 9: On-potential histories of steel bar during the ICCP tests.

Table 4: Results of the polarization resistance measurements at 120 days of ICCP application.

Specimen No.	ICCP Current density (mA/m^2)	Linear polarization resistance (kOhms)	Corrosion current density ($\mu A/cm^2$)	Corrosion stage
I-0-RF	0	0.367	1.28	High
I-5-4M	5	3.409	0.13	Low
I-20-4M	20	0.963	0.48	Low
I-50-4M	50	3.884	0.12	Low
I-100-4M	100	3.279	0.14	Low

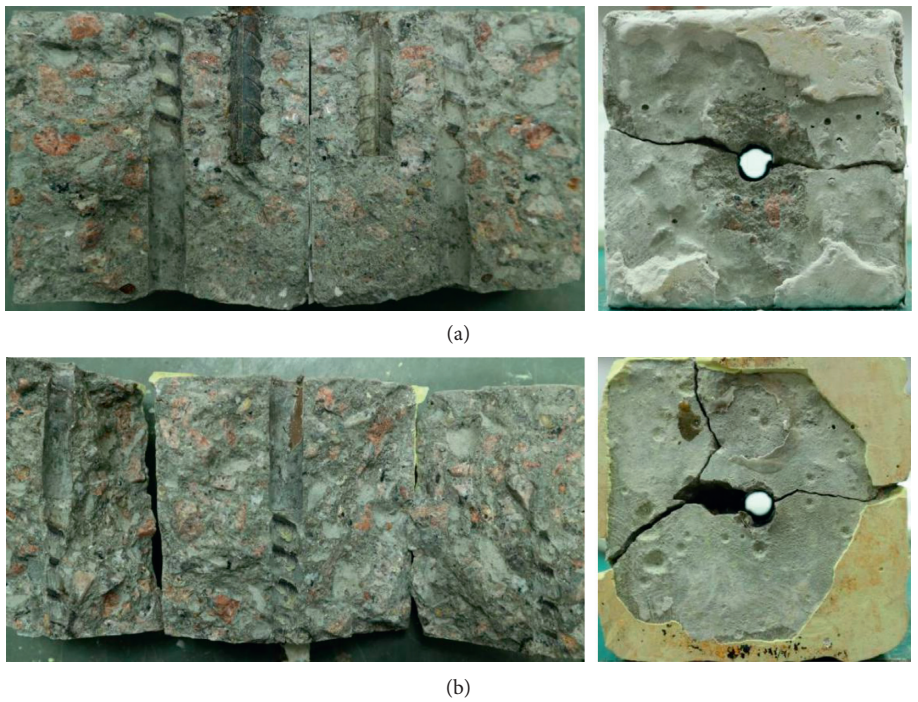

(a)

(b)

Figure 10: Overall bond failure patterns. (a) I-50-4M. (b) I-50-4M-R.

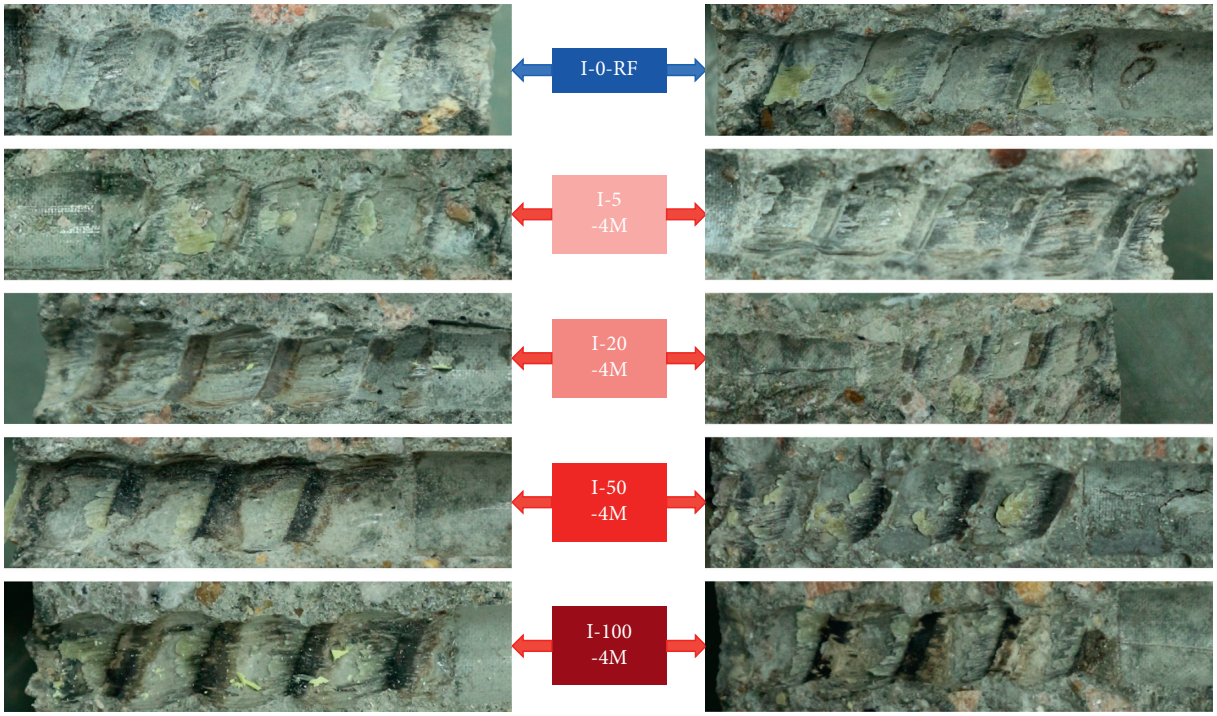

Figure 11: Local failure patterns of concrete in the bonded area.

Figure 12: Local failure patterns of CFRP bar in the bonded area.

bar can be observed in some indentations, which coincides with the local failure pattern of CFRP bar: the ribs of CFRP bar were obviously scratched by the concrete matrix. I-5-4M specimens had a similar local failure pattern with I-0-RF specimens, except that the surface of the CFRP bar underwent more severe scraping. For I-20-4M specimens, the color of the rib indentations on concrete changed to be brown. The specimens in I-50-4M and I-100-4M groups had a deeper color of the rib indentation, and substances with light yellow color were observed on the surface of the CFRP bar, which should be chemical reactions of resins in CFRP bar under galvanostatic anodic polarization. The CFRP fibers on the rebar surface peeled off to some extent and adhered to the rib indentations of the concrete matrix. Generally, with the ICCP current density increased, the chemical reaction accelerated and the degradation of the CFRP bar-concrete interface caused by anodic polarization became more pronounced. Based on the experimental observations, it can be concluded that ICCP application with a current density of $5\,mA/m^2$ did not induce noticeable

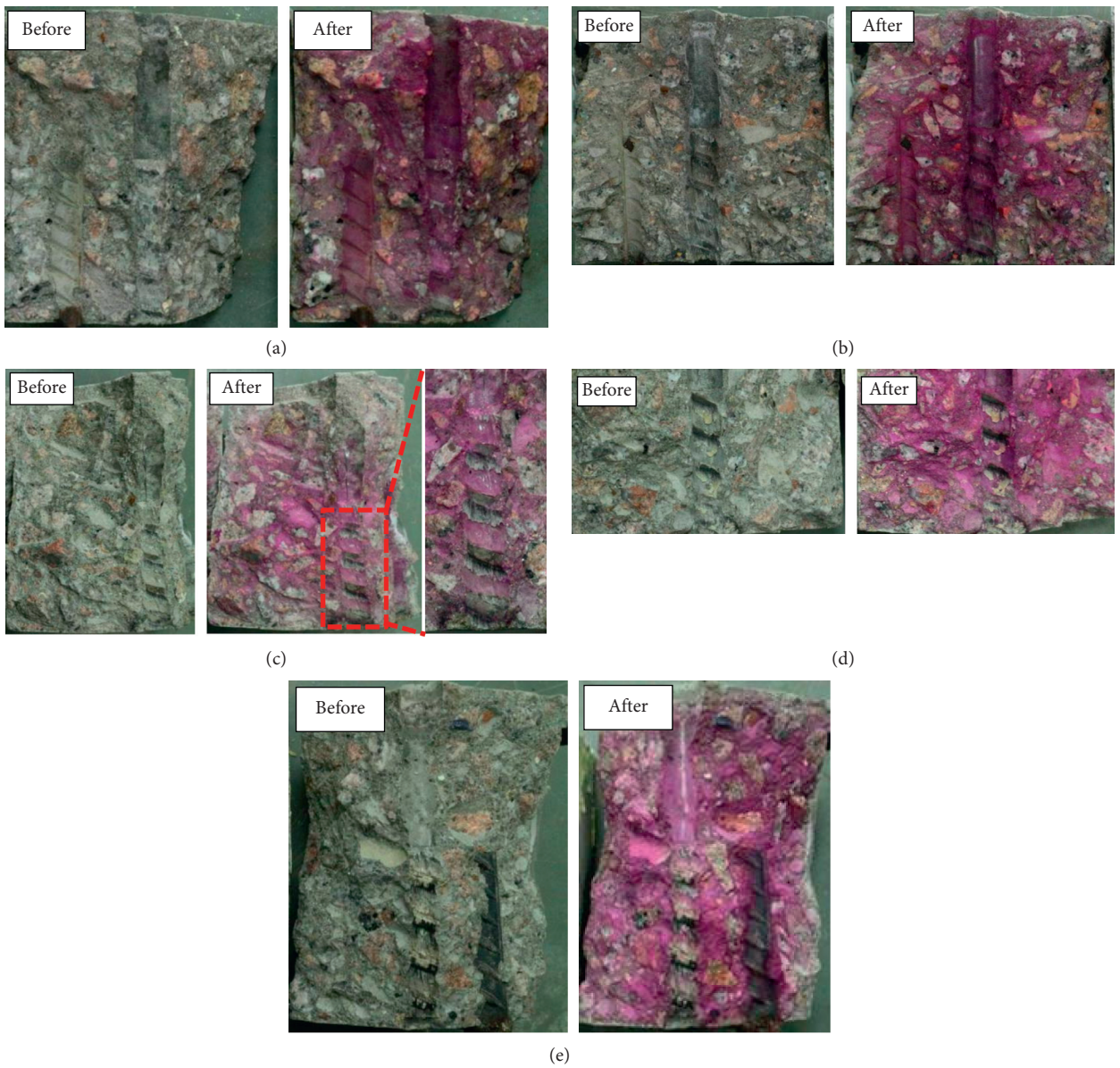

Figure 13: Real pictures of bonded areas before and after spraying phenolphthalein solution. (a) I-0-RF. (b) I-5-4M. (c) I-20-4M. (d) I-50-4M. (e) I-100-4M.

changes to the CFRP bar-concrete interface and that with 20 mA/m^2 had a little influence on the interface. However, ICCP applications with current densities of 50 mA/m^2 and 100 mA/m^2 deteriorated the CFRP bar-concrete interface significantly.

3.2.2. Detection of Acidification of CFRP Bar-Concrete Interface. Figure 13 shows real pictures of bonded areas before and after spraying phenolphthalein solution. For specimens with ICCP current densities of 0 and 5 mA/m^2, the bonded area appeared as red, indicating no acidification occurred on the CFRP bar-concrete interface. For specimens with ICCP current densities of 20, 50, and 100 mA/m^2, the depressed areas of the rebar indentations appeared in red, while the color has not changed in the raised areas of the rebar indentations, indicating that the interface in this area was acidified. The acidification of the interface is mainly due to the oxygen-evolution and chlorine-evolution reactions under the electric field, as shown in equations (2) and (3). The generated Cl_2 further reacts with H_2O to form HClO and HCl, as shown in equation (4). The hydrogen ions produced by these reactions are dissolved in the pore liquid on the interface, leading to the acidification of the interface:

$$2H_2O \longrightarrow O_2 + 2H^+ + 4e^- \quad (2)$$

$$2Cl^- \longrightarrow Cl_2 + 2e^- \quad (3)$$

$$Cl_2 + H_2O \longrightarrow HClO + HCL \quad (4)$$

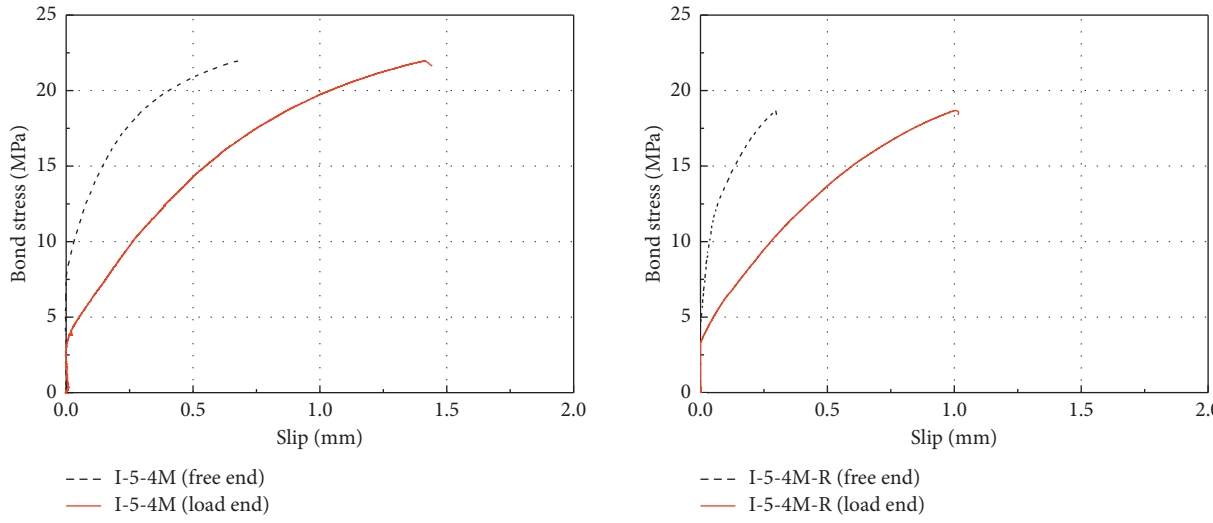

(a)

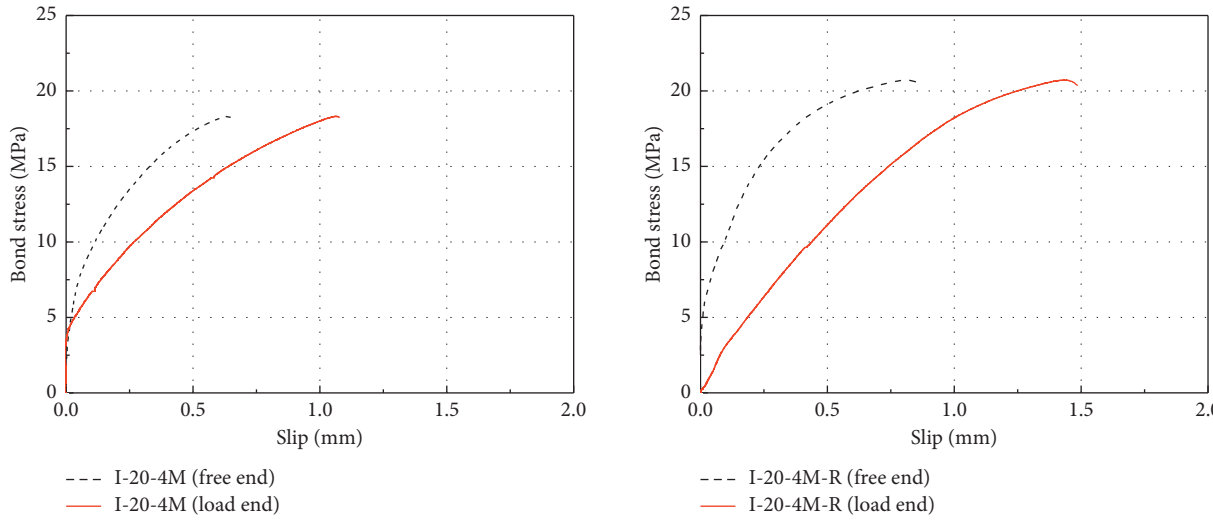

(b)

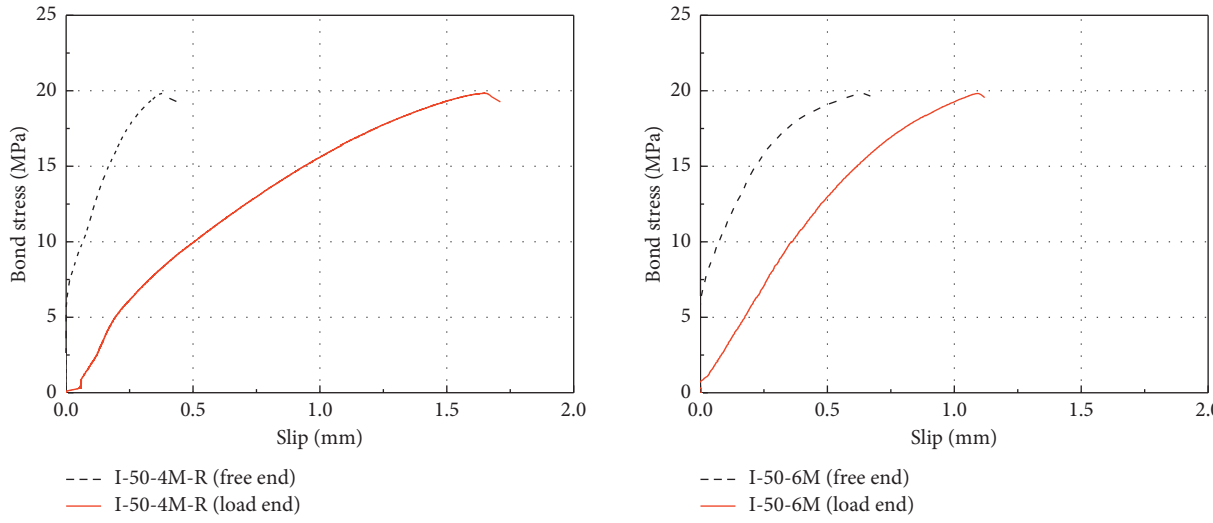

(c)

Figure 14: Continued.

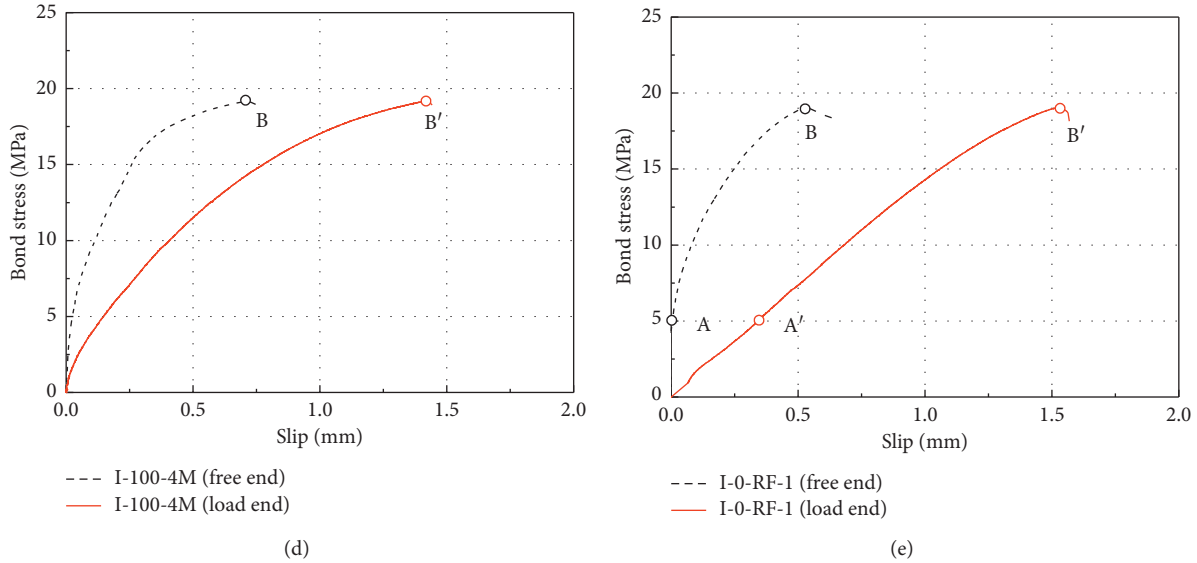

Figure 14: Typical bond-slip curves. (a) I-5. (b) I-20. (c) I-50. (d) I-100. (e) I-0.

Table 5: Summary of pull out test results.

Specimen no.	τ_{max} (MPa)	Average τ_{max} (MPa)	s_{fmax} (mm)
I-0-RF-1	19.03		0.68
I-0-RF-2	17.13	18.96	0.33
I-0-RF-3	20.73		0.74
I-5-4M	21.98	20.33	0.71
I-5-4M-R	18.68		0.32
I-5-6M	20.67	20.67	0.35
I-20-4M	18.32	19.53	0.65
I-20-4M-R	20.73		0.88
I-20-6M	—[a]	—	—
I-50-4M	17.96	18.9	0.44
I-50-4M-R	19.84		0.44
I-50-6M	19.55	19.55	0.68
I-100-4M	19.19	18.68	0.75
I-100-4M-R	18.17		0.49
I-100-6M	17.48	17.48	0.39

[a]Data not measured.

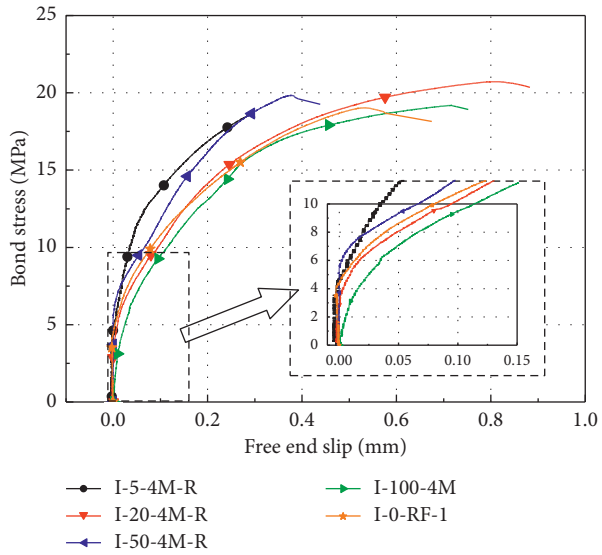

Figure 15: Bond-slip curves at different ICCP current densities.

3.2.3. Bond-Slip Curves. The measured bond-slip curves are shown in Figure 14. Characteristic values of bond-slip curves are summarized in Table 5, where τ_{max} denotes the maximum bond stress and s_{fmax} denotes the slip at free end corresponding to τ_{max}. Table 5 indicates that there is an obvious scattering for the test results of specimens in the same group, which is mainly caused by the deviation of the concrete tensile strength. Therefore, the average τ_{max} is adopted as an index to evaluate the influence of ICCP test parameters on the bond performances. It can be seen from Table 5 that an increase in the ICCP current density results in a slight decrease of the average τ_{max}, while the polarization duration did not show an obvious influence on the average of τ_{max} due to the relatively short duration of all the ICCP tests.

Figure 15 compares bond stress-free end slip curves at different ICCP current densities. For the specimen with a large ICCP current density of 100 mA/m^2, the free end slip emerged at the beginning of the loading. However, for other specimens, the free end began to slip at bond stress around 5 MPa. This phenomenon indicates that a large ICCP current density can change the bond mechanisms of the FRP bar-concrete interface.

3.2.4. Analysis of Bond Mechanisms of CFRP Bar-Concrete Interface after Anodic Polarization. The bond stress between a ribbed bar and concrete is composed of the following parts: (1) chemical adhesion; (2) interlocking of the ribs against the concrete; (3) interface friction induced by circumference confinement of concrete cylinder [30]. For specimens without ICCP protection, the shift progress of three bond mechanisms at different stages of the bond-slip curve is schematically shown in Figure 16. In the initial stage of the

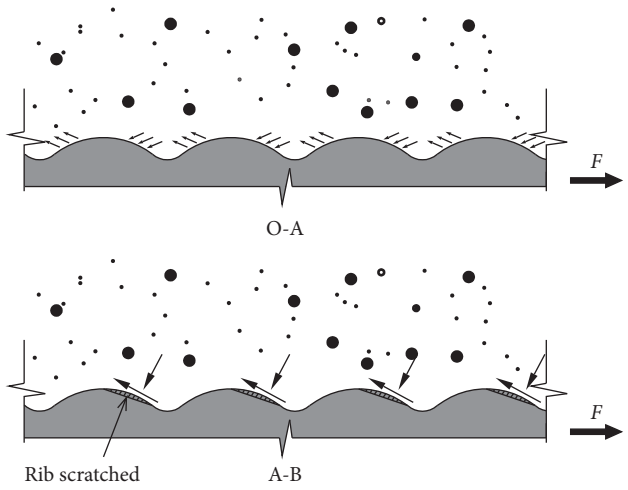

Figure 16: Illustration of bond mechanisms at different stages of the bond-slip curve.

pull out process (O-A stage in Figure 14(e)), the chemical adhesion plays a major role. In this stage, there was no slip at the free end and the slip at the loading end was contributed by the elastic deformation of the concrete matrix, resulting in an elastic bond behavior with large stiffness on the bond-slip curve. With the load continuing to increase, the chemical adhesion interface was broken and the bond was gradually governed by the interlocking of the rebar ribs and the concrete matrix and interface friction. In this stage, the concrete expanded in the radial direction and cracked under the extrusion of inclined ribs, and the outer layer resin was scratched by hard concrete matrix. This nonlinear damage progress led to a nonlinear segment with a decreasing slope of the bond-slip curve (A-B stage in Figure 14(e)). At the peak load (Point B), the radical cracks propagated through the concrete cover, splitting the matrix cylinder into several parts and causing a sudden drop in the bond stress.

However, for specimens with ICCP application of a large current density, the CFRP bar-concrete interface underwent severe anodic polarization, which changed the bond behavior. Figure 14(d) shows that the O-A stage was absent in the bond-slip curve, and the free end of the CFRP bar slipped at the beginning of the loading. Considering that the O-A stage is mainly governed by the chemical adhesive force, it is reasonable to deduce that the anodic polarization of the ICCP test deteriorated the cementation interface and broke the chemical adhesion between CFRP bar and concrete. Therefore, in the pull out test, the bond-slip curve entered into the A-B stage controlled by the interlocking action and interface friction directly, and the following bond behavior was similar to that of specimens without ICCP application.

4. Conclusion

In this paper, the ICCP technique was applied to the hybrid CFRP-steel reinforced concrete structures with the CFRP bar as the anode material and reinforcement. To evaluate the effectiveness of the ICCP system on corrosion protection, the potential of steel bar was monitored during the ICCP test and the linear polarization resistance of steel bar was measured after the ICCP system ran for 120 days. After the ICCP application, pull out tests were conducted to investigate the bond performance of the CFRP bar-concrete interface under anodic polarization. Based on the experimental observation and analysis, the following conclusions can be drawn:

(1) ICCP-CB technique can effectively prevent the steel bar from corrosion for the hybrid CFRP-steel reinforce concrete structure. The ICCP system provided electrons to the steel bar continuously and brought the potential of the steel bar down to the immunity region. The measured linear polarization resistance of the steel bar also showed that the corrosion rate of steel bar under ICCP-CB protection was significantly lower than that without ICCP-CB protection.

(2) The CFRP bar-concrete interface presented acidification under anodic polarization, and the level of acidification increased as the ICCP current density increased. Furthermore, interfacial acidification concentrated in the raised areas of rebar indentations.

(3) The bond stress of the CFRP bar-concrete interface is mainly contributed by the chemical adhesion, the interface friction, and the interlocking action between rebar ribs and concrete matrix. The measured bond-slip curves show that the ICCP system with a large current density of $100\,mA/m^2$ reduced the chemical adhesion significantly, leading to the earlier slip for the free end of the CFRP bar.

(4) The CFRP bar in the ICCP-CB system has a reliable bond performance in short-term. An increase in ICCP current density resulted in a slight decrease in the bond strength, while the polarization duration had an insignificant influence on the bond strength.

Data Availability

All data used to support the findings of this study are available from the corresponding author upon request.

Conflicts of Interest

The authors declare that they have no conflicts of interest.

Acknowledgments

The work described in this paper was financially supported by the National Natural Science Foundation of China (Grants nos. 51878414, 51808345, and 51978412). The authors are grateful for each one of these contributions.

References

[1] A. Poursaee, *Corrosion of Steel in Concrete Structures*, Woodhead Publishing, Sawston, UK, 2016.

[2] K. Bhargava, A. K. Ghosh, Y. Mori, and S. Ramanujam, "Model for cover cracking due to rebar corrosion in RC

structures," *Engineering Structures*, vol. 28, no. 8, pp. 1093–1109, 2006.

[3] C. Jiang, Y.-F. Wu, and M.-J. Dai, "Degradation of steel-to-concrete bond due to corrosion," *Construction and Building Materials*, vol. 158, pp. 1073–1080, 2018.

[4] H. Fang, Y. Bai, W. Liu, Y. Qi, and J. Wang, "Connections and structural applications of fibre reinforced polymer composites for civil infrastructure in aggressive environments," *Composites Part B: Engineering*, vol. 164, pp. 129–143, 2019.

[5] B. Hu, Y. Zhou, F. Xing, L. Sui, and M. Luo, "Experimental and theoretical investigation on the hybrid CFRP-ECC flexural strengthening of RC beams with corroded longitudinal reinforcement," *Engineering Structures*, vol. 200, Article ID 109717, 2019.

[6] Z. Wang, X.-L. Zhao, G. Xian et al., "Long-term durability of basalt- and glass-fibre reinforced polymer (BFRP/GFRP) bars in seawater and sea sand concrete environment," *Construction & Building Materials*, vol. 139, pp. 467–489, 2017.

[7] S. El-Gamal, B. Benmokrane, E. El-Salakawy, P. Cousin, and A. Wiseman, "Durability and structural performance of carbon fibre reinforced polymer—reinforced concrete parking garage slabs," *Canadian Journal of Civil Engineering*, vol. 36, no. 4, pp. 617–627, 2009.

[8] H. A. Abdalla, "Evaluation of deflection in concrete members reinforced with fibre reinforced polymer (FRP) bars," *Composite Structures*, vol. 56, no. 1, pp. 63–71, 2002.

[9] T. H. Almusallam, "Analytical prediction of flexural behavior of concrete beams reinforced by FRP bars," *Journal of Composite Materials*, vol. 31, no. 7, pp. 640–657, 1997.

[10] R. Masmoudi, M. Theriault, and B. Benmokrane, "Flexural behavior of concrete beams reinforced with deformed fiber reinforced plastic reinforcing rods," *ACI Structural Journal*, vol. 95, no. 6, pp. 665–676, 1998.

[11] Y. F. Wu, "Ductility demand of compression yielding fiber-reinforced polymer-reinforced concrete beams," *ACI Structural Journal*, vol. 105, no. 1, pp. 104–110, 2008.

[12] S.-B. Kang, K. H. Tan, and E.-H. Yang, "Progressive collapse resistance of precast beam-column sub-assemblages with engineered cementitious composites," *Engineering Structures*, vol. 98, pp. 186–200, 2015.

[13] N. Krstulovic-Opara, K. A. Watson, and J. M. Lafave, "Effect of increased tensile strength and toughness on reinforcing-bar bond behavior," *Cement and Concrete Composites*, vol. 16, no. 2, pp. 129–141, 1994.

[14] D. Lau and H. J. Pam, "Experimental study of hybrid FRP reinforced concrete beams," *Engineering Structures*, vol. 32, no. 12, pp. 3857–3865, 2010.

[15] E. Dehghani, F. Daneshjoo, A. A. Aghakouchak, and N. Khaji, "A new bond-slip model for adhesive in CFRP-steel composite systems," *Engineering Structures*, vol. 34, no. 1, pp. 447–454, 2012.

[16] W. Ge, J. Zhang, D. Cao, and Y. Tu, "Flexural behaviors of hybrid concrete beams reinforced with BFRP bars and steel bars," *Construction and Building Materials*, vol. 87, pp. 28–37, 2015.

[17] Y. Zhou, H. Fu, P. Li, D. Zhao, L. Sui, and L. Li, "Bond behavior between steel bar and engineered cementitious composite (ECC) considering lateral FRP confinement: test and modeling," *Composite Structures*, vol. 226, Article ID 11206, 2019.

[18] D. Zhao, W. Yi, and S. K. Kunnath, "Shear mechanisms in reinforced concrete beams under impact loading," *Journal of Structural Engineering, ASCE*, vol. 143, no. 9, Article ID 04017089, 2017.

[19] L. Bertolini, F. Bolzoni, P. Pedeferri, L. Lazzari, and T. Pastore, "Cathodic protection and cathodic preventionin concrete: principles and applications," *Journal of Applied Electrochemistry*, vol. 28, no. 12, pp. 1321–1331, 1998.

[20] P. Pedeferri, "Cathodic protection and cathodic prevention," *Construction and Building Materials*, vol. 10, no. 5, pp. 391–402, 1996.

[21] R. B. Polder, G. Leegwater, D. Worm, and W. Courage, "Service life and life cycle cost modelling of cathodic protection systems for concrete structures," *Cement and Concrete Composites*, vol. 47, no. 47, pp. 69–74, 2014.

[22] R. B. Polder and W. H. A. Peelen, "Service life aspects of cathodic protection of concrete structures," in *Concrete Repair. A practical guide*, CRC Press, Boca Raton, FL, USA, 2011.

[23] F. Lee-Orantes, A. A. Torres-Acosta, M. Martínez-Madrid, and C. lópez-cajún, "cathodic protection in reinforced concrete elements, using carbon fibers base composites," *ECS Transactions*, vol. 3, no. 3, pp. 198–201, 2007.

[24] S. Gadve, A. Mukherjee, and S. N. Malhotra, "Corrosion protection of fiber-reinforced polymer-wrapped reinforced concrete," *ACI Materials Journal*, vol. 107, no. 4, pp. 349–356, 2010.

[25] P. Lambert, C. Van Nguyen, P. S. Mangat, F. J. O'Flaherty, and G. Jones, "Dual function carbon fibre fabric strengthening and impressed current cathodic protection (ICCP) anode for reinforced concrete structures," *Materials and Structures*, vol. 48, no. 7, pp. 2157–2167, 2015.

[26] C. Van Nguyen, P. Lambert, P. S. Mangat, F. J. O'Flaherty, and G. Jones, "Near-surface mounted carbon fibre rod used for combined strengthening and cathodic protection for reinforced concrete structures," *Structure & Infrastructure Engineering*, vol. 12, no. 3, pp. 1–10, 2015.

[27] Ministry of Housing and Urban-Rural Development of the People's Republic of China, *Standard Methods for Testing of Concrete Structures*, Ministry of Housing and Urban-Rural Development of the People's Republic of China, Beiijng, China, 1992.

[28] NACE SP0290-2007, *Impressed Current Cathodic Protection of Reinforcing Steel in Atmospherically Exposed Concrete Structures*, NACE International, Houston, TX, USA, 2007.

[29] M. Stern and A. L. Geaby, "Electrochemical polarization," *Journal of the Electrochemical Society*, vol. 104, no. 1, pp. 56–63, 1957.

[30] J. A. den Uijl and A. J. Bigaj, "A bond model for ribbed bars based on concrete confinement," *Heron*, vol. 41, no. 3, pp. 201–226, 1996.

Hindawi
Advances in Polymer Technology
Volume 2020, Article ID 7573848, 16 pages
https://doi.org/10.1155/2020/7573848

Research Article

Elliptical FRP-Concrete-Steel Double-Skin Tubular Columns under Monotonic Axial Compression

Bing Zhang,[1] **Gui-Sen Feng**,[1,2] **Yan-Lei Wang**,[3] **Cong-Cong Lai**,[1] **Chen-Chen Wang**,[1] **and Xia-Min Hu**[1]

[1]*College of Civil Engineering, Nanjing Tech University, Nanjing, China*
[2]*Shandong Tong Yuan Design Group, Jinan, China*
[3]*School of Civil Engineering, Dalian University of Technology, Dalian, China*

Correspondence should be addressed to Bing Zhang; zhangb@njtech.edu.cn

Received 14 September 2019; Accepted 15 October 2019; Published 24 January 2020

Guest Editor: Tianyu Xie

Hybrid FRP-concrete-steel double-skin tubular columns (hybrid DSTCs) are a novel form of hollow columns consisting of an outer FRP tube, an inner steel tube, and an annular layer of concrete between the two tubes. Due to the effective confinement of the two tubes, the concrete in hybrid DSTCs is well confined, leading to excellent ductility and strength enhancement. Hybrid DSTCs also have excellent corrosion resistence due to the effective protection of the outer FRP tube. However, existing studies mainly focused on hybrid DSTCs with a circular cross-section. When subjecting to different loads in the two horizontal directions, elliptical columns are preferred as they can provide different bending stiffness and moment capacity around two axes of symmetry without significantly reducing the confining effect of the FRP tube. This paper extends the existing work on circular DSTCs to elliptical DSTCs with a particular focus on four issues: the effect of elliptical aspect ratio (i.e., the ratio of the major axis to the minor axis of the outer elliptical cross-section), the effect of the FRP tube thickness, the effect of void area ratio (i.e., the ratio of the area of concrete void to the area of the outer elliptical section), and the effect of the cross-section of the inner steel tube (i.e., both rectangular and elliptical steel tubes were used). Experimental results show that, the averaged peak stress of the confined concrete in elliptical DSTCs increases with the increase in the elliptical aspect ratio, whereas the elliptical aspect ratio has no obvious effect on the ultimate axial strain; the cross-section shape of the inner steel tube has significant effect on the axial stress-strain behavior of the confined concrete in elliptical DSTCs; elliptical DSTCs with an elliptical steel tube exhibit much better ductility and strength enhancement than those specimens with a rectangular steel tube. A simple stress-strain model of confined concrete was proposed for elliptical DSTCs to account for the effects of the elliptical aspect ratio, the inner void, and the shape of the inner steel tube, which can provide reasonably accurate but conservative predictions.

1. Introduction

Fiber-reinforced polymer (FRP) composites have many advantages compared with traditional building materials (i.e., concrete and steel), such as high strength-weight ratio and excellent corrosion resistance. FRP composites have found increasing applications in civil engineering, both in the retrofitting of existing reinforced concrete structures (e.g., bonding FRP composites to concrete beams to enhance their bending strength or shear strength; wrapping FRP composites on concrete columns to improve their ductility under seismic loading) and in the construction of new structures incorporating with FRP (e.g., FRP decks for footbridges; FRP domes for radar equipment; concrete-filled FRP tubes as bridge piles) [1–3]. Extensive studies have been conducted to explore the possibilities of constructing new structures using FRP composites [4–7], in which traditional materials (e.g., concrete and steel) are combined with FRP composites to create novel hybrid structures. The word *hybrid* rather than *composite* is used here to indicate the combined use of traditional materials and FRP composites to prevent any confusion or misunderstanding as FRP itself is a composite material consisting of both fibers and resin matrix.

Hybrid FRP-concrete-steel double-skin tubular columns (hybrid DSTCs), which combine concrete, steel, and FRP composites in an optimal manner, were invented at the Hong Kong

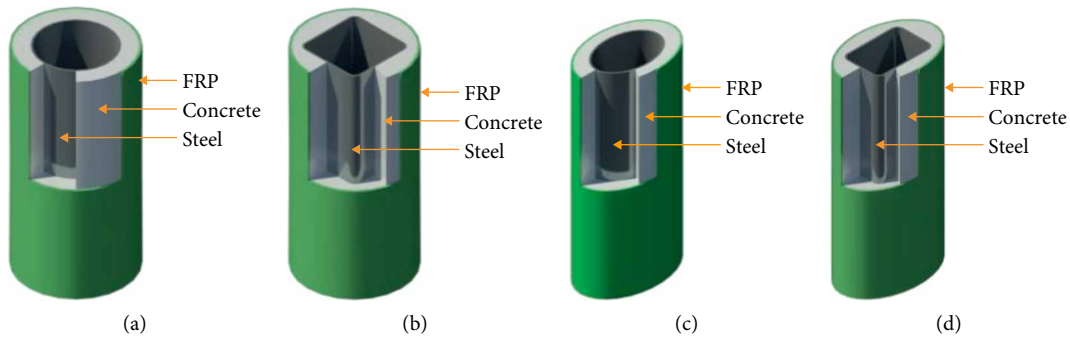

FIGURE 1: Hybrid DSTCs. (a) Circular DSTCs with a circular steel tube. (b) Circular DSTCs with a square steel tube. (c) Elliptical DSTCs with an elliptical steel tube. (d) Elliptical DSTCs with a rectangular steel tube.

Polytechnic University in 2004 [8, 9]. Hybrid DSTCs consist of an inner steel tube, an annular layer of concrete, and an outer FRP tube (Figure 1(a)). The inner steel tube provides the main longitudinal reinforcement for hybrid DSTCs and also prevents the concrete from inward spalling during the earthquake. The outer FRP tube usually consists of fibers oriented in the hoop direction or close to the hoop direction to confine the concrete and to enhance the seismic performance of the member. To reduce the construction cost, the outer FRP tube and the inner steel tube could also be used as the in-situ mold for the concrete casting. Hybrid DSTCs are quite suitable for structural members in harsh environments due to their excellent corrosion resistance, which is enabled by the use of the outer FRP tube. Hybrid DSTCs are also particularly attractive for use in seismic regions due to their excellent energy dissipation ability under earthquake loading.

Teng et al. [8, 9] presented the first-ever experimental study on hybrid DSTCs under axial compression and explained the rationale and advantages of hybrid DSTCs in detail. Since then, hybrid DSTCs have received extensive research attention from researchers. Existing research on hybrid DSTCs mainly covers the following aspects: (1) hybrid DSTCs under monotonic axial compression [8–16]; (2) hybrid DSTCs under cyclic axial compression [17–19]; (3) hybrid DSTCs under eccentric compression [20, 21]; (4) hybrid DSTCs subjected to combined axial compression and cyclic lateral loading [22–25]; (5) hybrid DSTCs under lateral impact loading [26, 27]. Yu [10] presented the first systematic study of hybrid DSTCs under axial compression, in which small-scale specimens with normal strength concrete (NSC) were tested. Yu's [10] work confirmed the concrete in hybrid DSTCs is very effectively confined by the two tubes, and the local buckling of the inner steel tube is either delayed or suppressed by the surrounding concrete, leading to a very ductile response. Hybrid DSTCs constructed with high strength concrete (HSC) was first reported in Zhang et al. [12], which confirmed that hybrid DSTCs still possess excellent ductility if the FRP tube has sufficient confinement stiffness and sufficient rupture strain capacity. Zhang et al. [16] conducted a study on large-scale hybrid DSTCs subjected to combined axial compression and cyclic lateral loading, which indicates that hybrid DSTCs possess excellent ductility and seismic resistance even when high strength concrete with a cylinder compressive strength of around 120 MPa is used. Wang et al. [26] tested hybrid DSTCs under lateral impact loading using a drop hammer testing facility and confirmed the excellent energy dissipation ability of hybrid DSTCs. Some variations of hybrid DSTCs were also investigated experimentally, including (1) use of light-weight concrete [28]; (2) use of recycled aggregate concrete [29]; (3) use of ribbed steel tubes [30]; (4) use of high-strength steel tubes [31]; (5) use of large-rupture-strain FRP tubes [32].

Existing studies, however, are mostly focused on hybrid DSTCs with a circular cross-section (i.e., the cross-section of the outer FRP tube is circular) (Figures 1(a) and 1(b)). Although circular DSTCs are attractive as bridge piers, elliptical DSTCs are preferred when the column is subjected to different loads in the two horizontal directions. Elliptical DSTCs can provide different bending stiffness and moment capacity around two axes of symmetry without significantly reducing the confining effect of the FRP tube [33]. To extend the existing study on hybrid DSTCs, the present study presents an experimental study of elliptical DSTCs under monotonic axial compression with a particular focus on four issues: the effect of elliptical aspect ratio ρ_A (i.e., the ratio of the major axis to the minor axis of the outer elliptical cross-section), the effect of the FRP tube thickness t_{frp}, the effect of the void area ratio φ_A (i.e., the ratio of the area of the concrete void to the area of the outer elliptical section), and the effect of the cross-section of the inner steel tube (i.e., both rectangular and elliptical steel tubes were used, Figures 1(c) and 1(d)).

2. Experimental Program

2.1. Specimen Details. In the present study, elliptical DSTCs with a height of 600 mm were fabricated and tested. These specimens could be divided into two groups based on the cross-section of steel tubes: (1) elliptical DSTCs with an elliptical inner steel tube (referred to as EE-DSTCs) (Figure 2); (2) elliptical DSTCs with a rectangular inner steel tube (referred to as ER-DSTCs) (Figure 3). Specimen details are summarized in Table 1 and cross-sectional configurations are shown in Figures 2 and 3. For all specimens, the major axis 2a of the outer elliptical cross-section was 300 mm, while the minor axis $2b$ was 300, 250, or 200 mm, leading to three different elliptical aspect ratios $\rho_A = 2a/2b$ (i.e., 1.0, 1.2, or 1.5). Specimens which have an elliptical aspect ratio ρ_A of 1.0 are circular DSTCs (i.e., EC1-ec1-F6 and EC1-rc1-F6 as

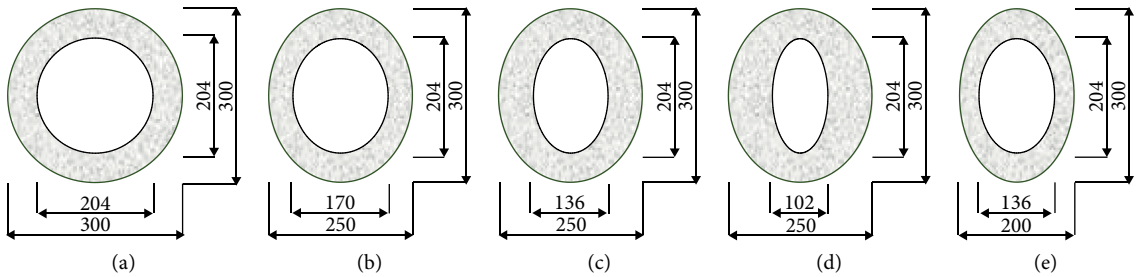

Figure 2: Elliptical DSTCs with an elliptical steel tube. (a) EC1-ec1-F6. (b) EC2-ec2-F3 and EC2-ec2-F6. (c) EC2-ec3-F6. (d) EC2-ec4-F6. (e) EC3-ec3-F3 and EC3-ec3-F6.

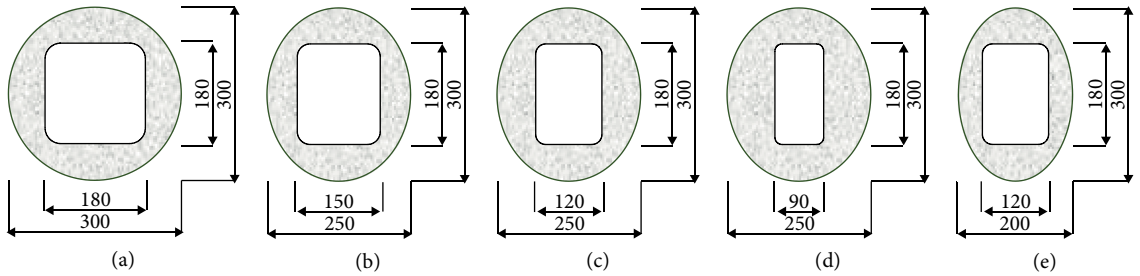

Figure 3: Elliptical DSTCs with a rectangular steel tube. (a) EC1-rc1-F6. (b) EC2-rc2-F3 and EC2-rc2-F6. (c) EC2-rc3-F6. (d) EC2-rc4-F6. (e) EC3-rc3-F3 and EC3-rc3-F6.

Table 1: Specimen details.

Specimen	Outer elliptical dimensions			Type of inner steel tube	FRP thickness t_{frp} (mm)	Void area ratio φ_A
	2a (mm)	2b (mm)	ρ_A = 2a/2b			
EC1-ec1-F6	300	300	1.0	ec1	2.10	0.46
EC2-ec2-F3	300	250	1.2	ec2	1.05	0.46
EC2-ec2-F6	300	250	1.2	ec2	2.10	0.46
EC2-ec3-F6	300	250	1.2	ec3	2.10	0.37
EC2-ec4-F6	300	250	1.2	ec4	2.10	0.28
EC3-ec3-F3	300	200	1.5	ec3	1.05	0.46
EC3-ec3-F6	300	200	1.5	ec3	2.10	0.46
EC1-rc1-F6	300	300	1.0	rc1	2.10	0.46
EC2-rc2-F3	300	250	1.2	rc2	1.05	0.46
EC2-rc2-F6	300	250	1.2	rc2	2.10	0.46
EC2-rc3-F6	300	250	1.2	rc3	2.10	0.37
EC2-rc4-F6	300	250	1.2	rc4	2.10	0.28
EC3-rc3-F3	300	200	1.5	rc3	1.05	0.46
EC3-rc3-F6	300	200	1.5	rc3	2.10	0.46

shown in Figure 2(a) and 3(a), respectively). For EE-DSTCs, four types of elliptical steel tubes were used, which had the same length of major axis $2a_s$ (i.e., 204 mm), but four different minor axes $2b_s$ (i.e., 204, 170, 136 and 102 mm) (Figure 2, Table 2). For RE-DSTCs, four types of rectangular steel tubes were used, which had the same corner radius of 20 mm, the same breadth l_s of the steel rectangular cross-section (i.e., 180 mm), but four different widths w_s (i.e., 180, 150, 120 and 90 mm) (Figure 3, Table 3).

For ease of reference, each specimen is given a name (Table 1), which consists of three parts: (1) the first part "EC1", "EC2" and "EC3" indicate the elliptical aspect ratio ρ_A to be "1.0", "1.2" and "1.5", respectively; (2) the second part starts with "ec" or "rc" to indicate the cross-sectional shape of the steel tube to be elliptical or rectangular, followed by a digit to indicate the steel tube type as described in Tables 2

Table 2: Details of elliptical steel tubes.

Type	$2a_s$ (mm)	$2b_s$ (mm)	a_s/b_s	f_y (MPa)	E_s (GPa)	f_u (MPa)
ec1	204	204	1.0	302.6	201.0	441
ec2	204	170	1.2			
ec3	204	136	1.5			
ec4	204	102	2.0			

Table 3: Details of rectangular steel tubes.

Type	l_s (mm)	w_s (mm)	l_s/w_s	f_y (MPa)	E_s (GPa)	f_u (MPa)
rc1	180	180	1.0	308.0	200.3	459
rc2	180	150	1.2			
rc3	180	120	1.5			
rc4	180	90	2.0			

and 3; (3) the third part has a letter "F" and one digit to indicate the fiber sheet layers of the FRP tube. The nominal thickness of each layer fiber sheet was 0.35 mm, leading to two FRP tube thicknesses for these specimens (i.e., 1.05 mm and 2.10 mm).

All elliptical and rectangular steel tubes in the present study had the same thickness (i.e., 4.5 mm). The FRP tube of all specimens was formed by wrapping continuous unidirectional glass/epoxy laminates on the hardened concrete surface with the fibers oriented in the hoop direction. For each FRP tube, there was an overlapping zone spanning a circumferential distance of 150 mm (Figure 4). Additional FRP strips with a width of 40 mm were provided near the two ends of the specimens to prevent premature failure there. Compared with FRP-confined solid columns, hybrid DSTCs can save concrete significantly due to the inner void, which could be indicated by the void area ratio φ_A (i.e., the ratio of the area of the concrete void to the area of the outer elliptical section). Two groups of elliptical DSTCs were prepared to investigate the effect of the void area ratio φ_A (i.e., EC2-rc2-F6, EC2-rc3-F6, and EC2-rc4-F6; EC2-ec2-F6, EC2-ec3-F6, and EC2-ec4-F6). To investigate the effect of the cross-section shape of the inner steel tube, for each elliptical DSTC with an elliptical inner steel tube, there was a companion elliptical DSTC with a rectangular inner steel tube, which had the same aspect ratio, the same FRP tube thickness, and the same void area ratio (e.g., EC2-rc2-F6 and EC2-ec2-F6 are a pair of elliptical DSTCs for comparison).

2.2. Material Properties

2.2.1. Concrete. Self-compacting concrete (SCC) was adopted to ensure the quality of the concrete casting. Three plain concrete cylinders (150 mm in diameter and 300 mm in height) were prepared and tested under a displacement-controlled loading rate of 0.18 mm/mm to obtain the compressive properties of unconfined concrete according to ASTM C39/C39M [34]. The elastic modulus E_c, the peak stress f_{co}, and the axial strain at peak stress ε_{co} averaged from these concrete cylinder tests are 33.6 GPa, 50.4 MPa, and 0.26%, respectively.

2.2.2. FRP. To determine the material properties of the FRP tube for these specimens, tensile tests were conducted on six flat coupons according to ASTM D3039/D3039M [35]. The FRP coupon, which contained two layers of fiber sheets, was fabricated using the same wet-layup technique as the FRP tube for elliptical DSTCs. The elastic modulus E_{frp}, the ultimate strength and the ultimate strain averaged from these FRP flat coupon tests are 80.1 GPa, 1836.2 MPa, and 2.29%, respectively.

2.2.3. Steel Tube. As mentioned above, there were four types of elliptical steel tubes and four types of rectangular steel tubes for elliptical DSTCs (Tables 2 and 3). All elliptical steel tubes were fabricated using the same batch of raw materials, whereas all rectangular steel tubes were manufactured using another batch of raw materials. All these steel tubes were manufactured following four steps: (1) cutting a flat steel plate to designed dimensions; (2) bending the flat steel plate to form half part of a steel tube; (3) welding two identical half parts together by two longitudinal welds; (4) milling the two ends of each steel tube to achieve flat ends which are perpendicular to its axis. Tensile tests on five steel coupons were conducted following BS 18 [36] for elliptical steel tubes and rectangular steel tubes, respectively. Test results showed the tensile stress-strain curves of these steel coupons had a long yield plateau and then a hardening branch before the final rupture. The average elastic modulus E_s, the average yield stress f_y and the average ultimate tensile strength f_u are shown in Tables 2 and 3.

In addition, for each type of these steel tubes, two hollow steel tubes, which had the same height as those used in elliptical DSTCs (i.e., 600 mm), were tested under monotonic axial compression. On the outer surface of each steel tube, four hoop strain gauges and four axial strain gauges with a gauge length of 20 mm were installed at the midheight uniformly distributed along the circumferential direction. Four LVDTs were installed to measure the overall axial shortening of each steel tube. The failed steel tubes after axial compression tests and the axial stress-axial strain curves are all shown in Figures 5 and 6, with the axial strain being obtained from LVDTs. As shown in Figure 5, steel tube ec1 showed an elephant foot buckling failure mode which is typical for circular steel tubes, whereas other elliptical steel tubes showed local buckling failures near the midheight of the steel tube. The axial stress-strain curves of elliptical steel tubes exhibited an ascending branch and a slowly descending branch. As shown in Figure 6, all rectangular steel tubes showed local inward/outward buckling failure, and their axial stress-strain curves exhibited a linear ascending branch and then a descending branch after the peak stress point. As shown in Figures 5 and 6, the peak stresses of these steel tubes were much lower than the ultimate tensile strength f_u obtained from the flat steel coupon tests, which was mainly due to the local buckling failure of these steel tubes.

2.3. Experimental Setup and Instrumentation. Figure 4 shows the experimental setup and instrumentation for all specimens. Six LVDTs were installed to measure the axial deformation of each specimen. Of the six LVDTs, four (i.e., LVDT-300) were used to measure the shortening of the 300-mm midheight region, while the other two (i.e., LVDT-600) were used to measure the total shortening of the specimen. For the outer FRP tube, four axial strain gauges were installed at the midheight of the specimen uniformly distributed along the circumference of the elliptical cross-section; in addition, ten hoop strain gauges were also installed at the midheight as shown in Figure 4(a). At the midheight of the inner steel tube

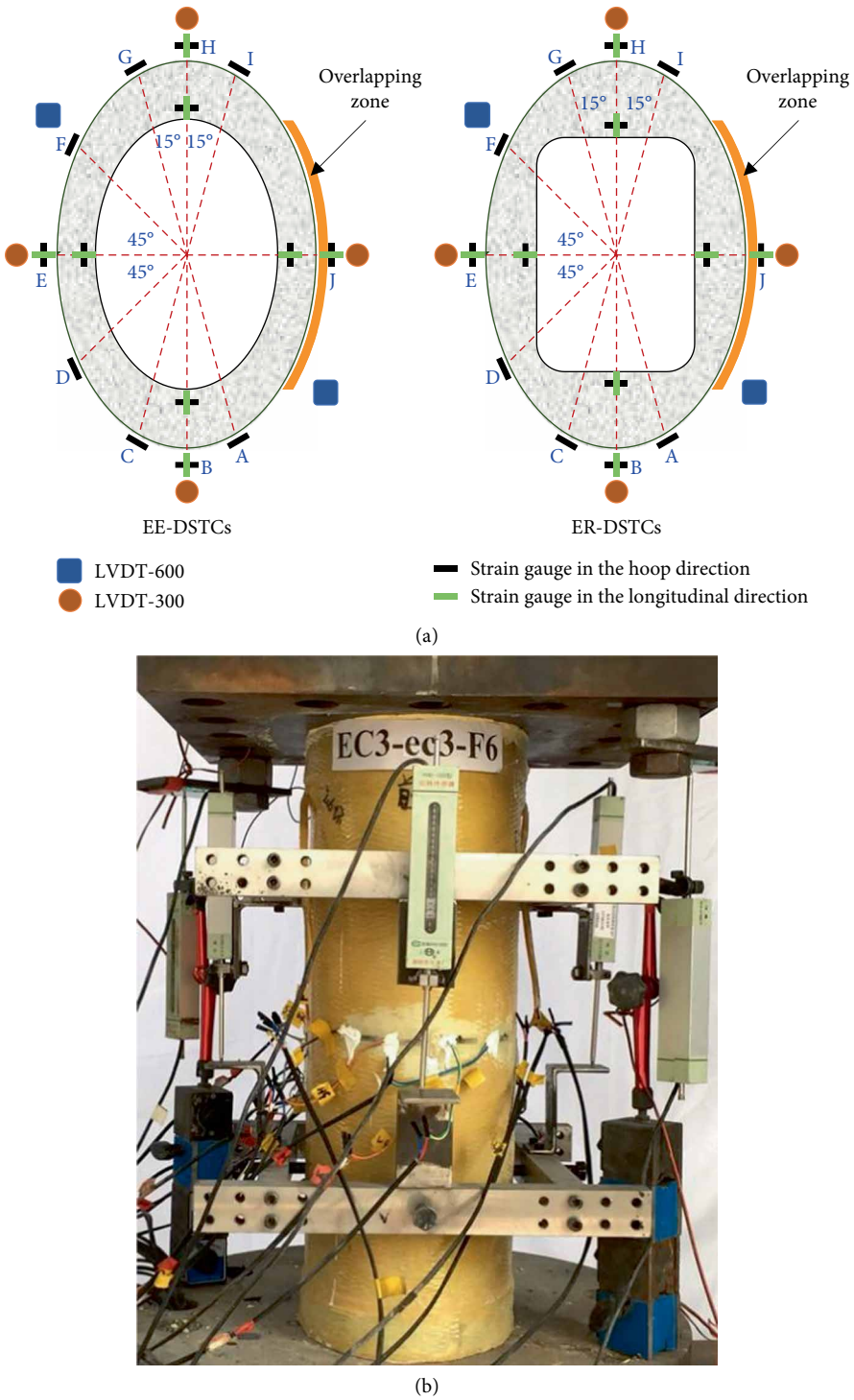

Figure 4: Experimental set-up and instrumentation. (a) Planar view of strain gauges and LVDTs. (b) Experimental set-up.

of elliptical DSTCs, four hoop strain gauges and four axial strain gauges with a gauge length of 20 mm were installed and distributed evenly over the circumference. A large column testing facility (maximum capacity of 10,000 kN) was used to conduct axial compression tests with a displacement control rate of 0.36 mm/min. All the test data, including strains, loads, and displacements, were recorded simultaneously by a data acquiring system.

3. Test Results and Discussions

3.1. General. A small preload was applied to each specimen to check the concentric loading condition and then was removed before the axial compression test. At the initial stage of the loading test, readings of the four axial strains on the FRP tube were quite uniform, and there was no obvious phenomenon on the outer FRP tube. When the axial strain readings exceeded

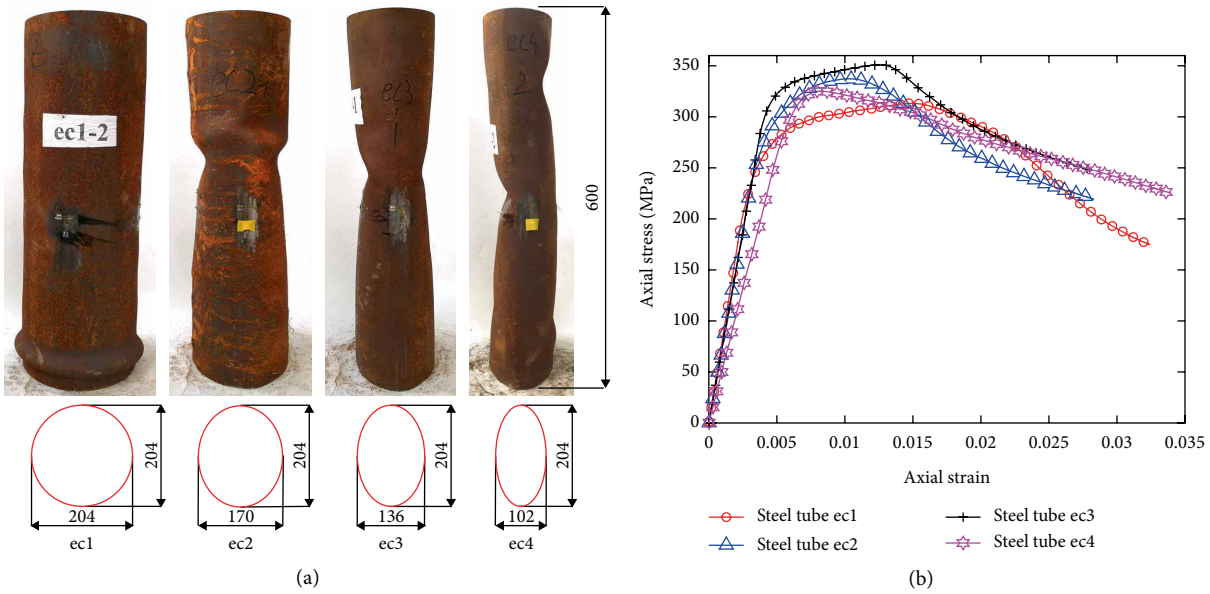

FIGURE 5: Axial compression test of elliptical hollow steel tubes. (a) Elliptical hollow steel tubes. (b) Axial stress–strain curves.

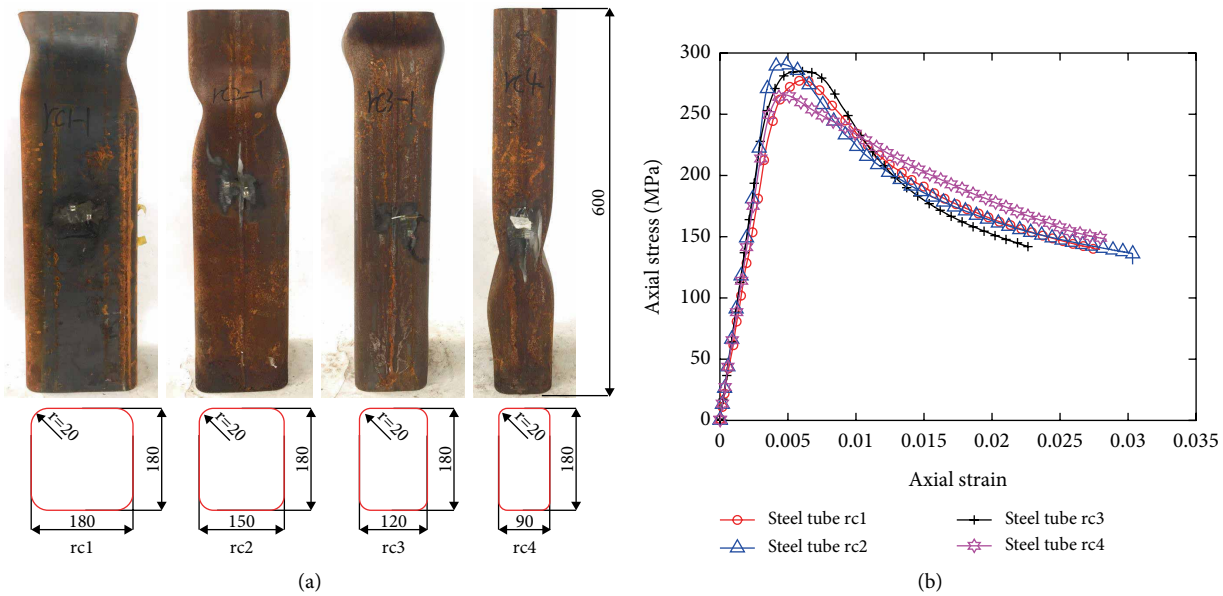

FIGURE 6: Axial compression test of rectangular hollow steel tubes. (a) Rectangular hollow steel tubes. (b) Axial stress-strain curves.

around 0.03%, a loud noise was noticed emitting from the specimens, suggesting that severe damage had occurred in the concrete. As the loading process progressed, the hoop strain readings of these strain gauges near the ends of the major axis of elliptical cross-section (i.e., strain gauges A, B, C, G, H, I in Figure 4(a)) generally increased faster than the rest hoop strain gauges, indicating the FRP tube provided more effective confinement there. Before the rupture of the FRP tube, noticeable damages were observed on the outer surface of the FRP tube, which were generally close to the ends of the major axis of the elliptical cross-section. At the final stage of the loading test, progressive snapping noise of fibers was noticed and finally, the explosive rupture of FRP tube occurred associated with a big noise.

After the test, the damage of the FRP tube and the inner steel tube was carefully examined (Figure 7). The ruptures of the FRP tube, which was mainly due to the hoop tension induced by the dilation of the inner concrete, were generally close to the ends of the major axis of the elliptical cross-section. As expected, the concrete layer also suffered severe crushing at the locations where FRP ruptures occurred. Severe inward deformation and local buckling, which was generally close to the localized damage of the FRP tube, was noticed for the inner steel tubes. It is evident that the inward buckling of rectangular steel tubes was much severe than that of elliptical steel tubes (Figure 7).

3.2. Axial Load–Axial Strain Curves. As the axial strain gauges were on the outer surface of the FRP tube and the

steel tube, their readings may not closely reflect the strain state of the confined concrete especially after the development of significant localized damage on the FRP tube and the local buckling of the steel tube. The axial strain obtained from the LVDTs cover the total height of the specimen (i.e., LVDT-600) may not reflect the strain state of the confined concrete especially at the early stage of the axial compression as there may be initial gaps between the loading plates and the two ends of the specimen. In this paper, the axial strain found from LVDT-300, which reflects the average axial strain of the 300-mm midheight region, is used to represent the axial strain of these specimens. Axial load–axial strain curves of all specimens are shown in Figure 8 in two groups. As shown in Figure 8(a), the axial load–axial strain curves of EE-DSTCs exhibit an ascending linear branch and a smooth curve transition at the axial strain of around 0.3%, then followed by a second ascending branch. In contrast, the second branch of ER-DSTCs is approximately a plateau with a staled load (Figure 8(b)). For some ER-DSTCs (e.g., specimens EC1-rc1-F6 and EC2-rc2-F6), the second branch is a slightly descending curve.

3.3. Key Test Results. As introduced above, the elliptical FRP tubes of these elliptical DSTCs only had fibers oriented in the hoop direction. Therefore, the direct load contribution of the FRP tube is ignored in the present study. For elliptical DSTCs, the direct load contribution of inner steel tubes should be considered when obtaining the axial load resisted by the concrete. The axial load resisted by the concrete in elliptical DSTCs is assumed to be equal to the axial load resisted by the specimen subtracted by the axial load resisted by the inner steel tube at the same axial strain. The axial load carried by the inner steel tube was assumed to be the same as the hollow steel tubes under axial compression (Figures 5 and 6). The axial loads of the specimen, the concrete, and the steel tube are illustrated for two typical elliptical DSTCs in Figure 9. The average axial stress of the confined concrete in elliptical DSTCs is obtained as the load resisted by the concrete divided by the cross-section area of the concrete.

The key test results of all specimens are summarized in Table 4. $P_{\max}$ is the peak axial load of the specimen obtained from the test. f_{cc} is the peak axial stress of the confined concrete. ε_{cu} is the ultimate axial strain of the specimen when the FRP tube ruptured. $\varepsilon_{\text{hrup}}$ is the rupture strain of the FRP tube averaged from the hoop strain gauges outside of the overlapping zone. Some of the hoop strain gauges, which failed to work before the rupture of the FRP tube, were excluded from the calculation of the average hoop rupture strain $\varepsilon_{\text{hrup}}$. $\varepsilon_{\text{hrup,max}}$ is the maximum hoop rupture strain found from the ten hoop strain gauges on the midheight of the FRP tube. The planar location of the hoop strain gauge with the maximum hoop rupture strain $\varepsilon_{\text{hrup,max}}$ could be found in Figure 4(a) and Table 4. It is evident that the maximum hoop rupture strain $\varepsilon_{\text{hrup,max}}$ mostly occurred near the ends of the major axis of the elliptical cross-section. f_{cc}/f_{co} and $\varepsilon_{cu}/\varepsilon_{co}$ is the strength enhancement ratio and the strain enhancement ratio of the confined concrete, respectively.

3.4. Effect of Elliptical Aspect Ratio. As shown in Figure 10, axial stress-strain curves of the confined concrete of elliptical DSTCs are examined to evaluate the effect of the elliptical aspect ratio. Elliptical DSTCs in each subfigure had the same FRP tube thickness (i.e., the nominal thickness of FRP tube is 2.10 mm) and the same void area ratio (i.e., 0.46), but different elliptical aspect ratios. As shown in Figure 10, the averaged stress of the confined concrete increases with the increase in the elliptical aspect ratio, whereas the elliptical aspect ratio has no obvious effect on the ultimate axial strain. For an elliptical DSTC with a larger aspect ratio, the concrete at region A of the elliptical cross-section (i.e., the region of the concrete between the FRP tube and the steel tube along the direction of the major axis of the elliptical section) is under more effective confinement due to the larger local curvature of the FRP tube, leading to higher strength enhancement there (Figure 10).

3.5. Effect of FRP Tube Thickness. As shown in Figure 11, four pairs of elliptical DSTCs, which have the same elliptical aspect ratio, the same void ratio but a different FRP tube thickness, are compared to investigate the effect of FRP tube thickness. It is well known that the response of concrete confined by FRP is significantly affected by the confinement stiffness and the hoop rupture strain of the FRP tube. A thicker FRP tube generally has larger strength enhancement and ductility improvement. As shown in Table 4, the strength enhancement ratio f_{cc}/f_{co} and the strain enhancement ratio $\varepsilon_{cu}/\varepsilon_{co}$ of these specimens with a 6-layer FRP tube are much higher than those of companion specimens with a 3-layer FRP tube. It is evident that FRP tube thickness has a significant effect on the axial stress-strain curves of Elliptical DSTCs: a thicker FRP tube leads to higher peak stress and larger ultimate axial strain for the confined concrete in elliptical DSTCs. For EE-DSTCs, it is also evident that a thicker FRP tube leads to a higher stiffness for the second portion of the axial stress-strain curve of the confined concrete (Figures 11(a) and 11(b)).

3.6. Effect of Void Area Ratio. The effect of the void ratio can be examined by comparing the stress-strain curves of two groups of elliptical DSCTs. EE-DSTCs [i.e., EC2-ec2-F6 (φ_A = 0.46), EC2-ec3-F6 (φ_A = 0.37) and EC2-ec4-F6 (φ_A = 0.28)] are compared in Figure 12(a) while ER-DSTCs [i.e., EC2-rc2-F6 (φ_A = 0.46), EC2-rc3-F6 (φ_A = 0.37) and EC2-rc4-F6 (φ_A = 0.28)] are compared in Figure 12(b). As shown in Figure 12(a) for EE-DSTCs, specimen EC2-ec2-F6 (φ_A = 0.46) has the largest peak axial stress and the largest ultimate axial strain, while specimen EC2-ec3-F6 (φ_A = 0.37) has the smallest peak axial stress and the smallest ultimate axial strain. However, the effect of the void area ratio is quite the opposite for ER-DSTCs as shown in Figure 12(b). Nevertheless, within the range examined the void area ratio does not have a significant effect on either the ultimate axial strain or the peak axial stress of the confined concrete. A further experimental study is needed to clarify the effect of the void ratio.

3.7. Effect of Cross-Section of the Steel Tube. Six pairs of elliptical DSTCs are compared in Figure 13 to evaluate the effect of the cross-section shape of the inner steel tube. For elliptical DSTCs with an elliptical inner steel tube, the axial stress-strain curves exhibit a typical bilinear ascending shape with a smooth transition curve connecting the two linear

Figure 7: Typical specimens after test. (a) EC1-ec1-F6. (b) EC2-ec2-F6. (c) EC3-ec3-F6. (d) EC1-rc1-F6. (e) EC2-rc2-F6. (f) EC3-rc3-F6.

portions (Figure 13). The axial stress-strain curve of specimen EC1-ec1-F6 has a small descending portion when the axial strain exceeds 0.032, which is believed to be attributed to the local inward buckling of the inner steel tube. In contrast, elliptical DSTCs with a rectangular inner steel tube display axial stress-strain curves with a linear ascending curve and

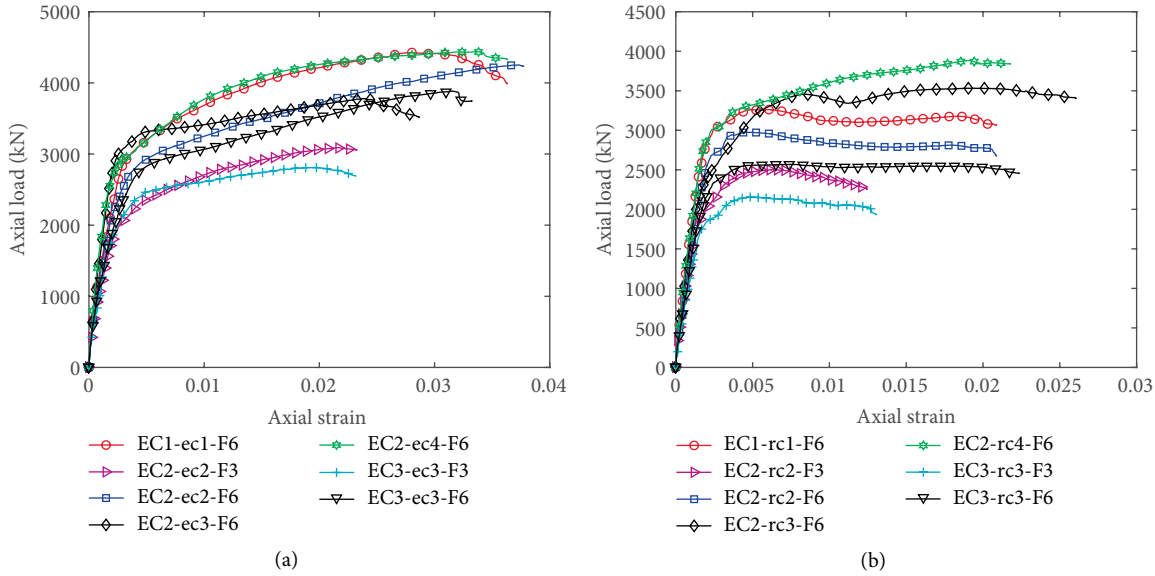

Figure 8: Axial load–axial strain curves. (a) EE-DSTCs. (b) ER-DSTCs.

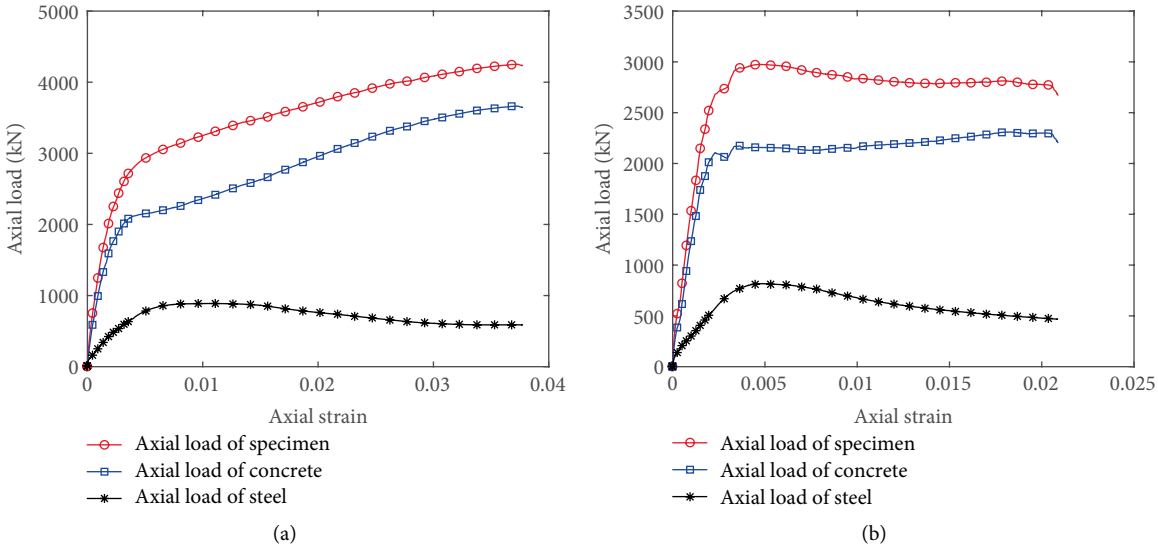

Figure 9: Axial load taken by the concrete and the steel tube. (a) EC2-ec2-F6. (b) EC2-rc2-F6.

an approximately linear curve with almost constant stress (Figure 13). As shown in Figure 7, the inward buckling of rectangular steel tubes was much severe than that of elliptical steel tubes. Therefore, the confinement effect of ER-DSTCs is much less efficient than that of EE-DSTCs, especially after the development of severe buckling. It is evident that the second portion of the axial stress-strain curves of EE-DSTCs has much larger stiffness due to the effective confinement of both the elliptical FRP tube and the elliptical inner steel tube. However, the second portion of the axial stress-strain curves of ER-DSTCs has a very small stiffness which was mainly due to the severe inward buckling of the inner rectangular steel tube as shown in Figure 7. It is evident that the cross-section shape of the inner steel tube has a significant effect on the axial stress-strain behavior of the confined concrete in elliptical DSTCs. As illustrated in Figure 7 and Table 4, elliptical DSTCs with an elliptical steel tube generally failed at much larger ultimate axial strains and had much large strain enhancement ratios and strength enhancement ratios than corresponding elliptical DSTCs with a rectangular steel tube. Therefore, elliptical DSTCs with an elliptical steel tube exhibit much better ductility and strength enhancement than those specimens with a rectangular steel tube.

4. Stress–Strain Model

4.1. Yu et al.'s Model for Circular DSTCs with a Circular Steel Tube. Yu et al. [11] proposed a simple stress-strain model for the confined concrete of circular DSTCs with a circular steel tube (Figure 1(a)), which was based on Teng et al.'s [37] stress-strain model for circular FRP-confined solid concrete

Table 4: Key test results.

Specimen name	P_{max} (kN)	f_{cc} (MPa)	ε_{cu} (%)	ε_{hrup} (%)	$\varepsilon_{hrup,max}$ (%)/Location*	f_{cc}/f_{co}	$\varepsilon_{cu}/\varepsilon_{co}$
EC1-ec1-F6	4424	101.9	3.64	1.74	1.91/H	2.02	14.0
EC2-ec2-F3	3090	76.2	2.33	1.34	1.61/B	1.51	8.96
EC2-ec2-F6	4253	115.5	3.78	1.35	2.33/H	2.29	14.5
EC2-ec3-F6	3778	86.0	2.87	1.43	2.30/F	1.71	11.0
EC2-ec4-F6	4438	92.3	3.64	1.43	2.05/B	1.83	14.0
EC3-ec3-F3	2811	85.8	2.32	1.21	1.48/I	1.70	8.92
EC3-ec3-F6	3883	131.7	3.33	1.26	1.69/F	2.61	12.8
EC1-rc1-F6	3262	65.6	2.09	1.00	1.09/B	1.30	8.05
EC2-rc2-F3	2500	53.8	1.25	0.98	1.29/C	1.07	4.80
EC2-rc2-F6	2974	71.5	2.09	0.95	1.29/C	1.42	8.03
EC2-rc3-F6	3532	82.5	2.61	1.53	2.38/C	1.64	10.0
EC2-rc4-F6	3883	79.1	2.18	1.49	2.19/H	1.57	8.39
EC3-rc3-F3	2156	56.2	1.31	1.29	1.94/A	1.12	5.03
EC3-rc3-F6	2568	81.3	2.24	1.20	1.50/I	1.61	8.61

*The planar location of the hoop strain gauge with the maximum hoop rupture strain $\varepsilon_{hrup,max}$ can be found in Figure 4(a).

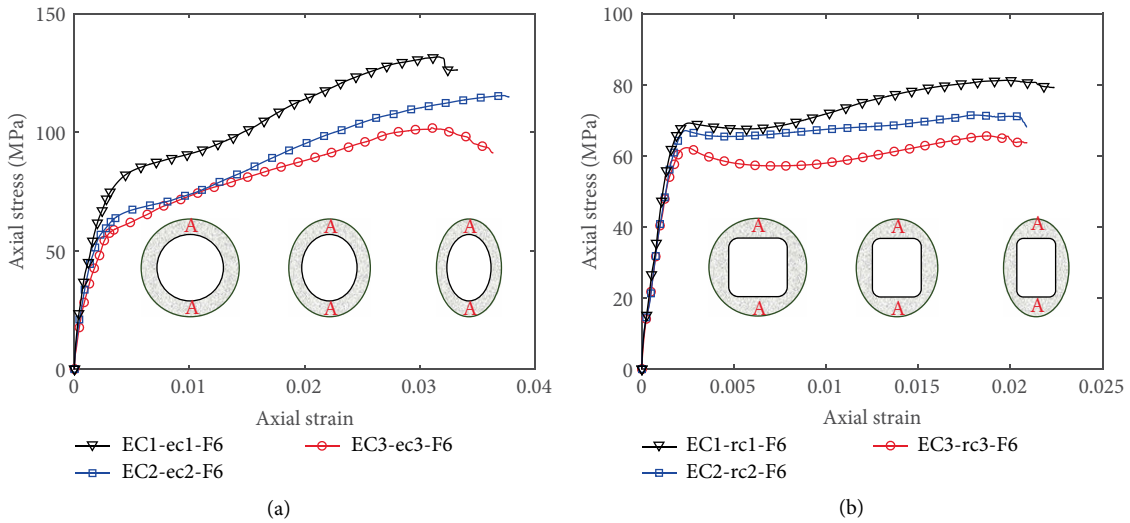

Figure 10: Effect of cross-sectional aspect ratio. (a) EE-DSTCs. (b) ER-DSTCs.

columns. Based on Yu et al.'s [11] study, the inner void of circular DSTCs had a negligible effect on the axial stress of the confined concrete. Yu et al.'s [11] model includes modifications to Teng et al.'s [37] model to consider the effect of an inner void on the ultimate axial strain of the confined concrete in circular DSTCs. Yu et al.'s [11] model consists of a parabolic first portion followed by a linear second portion with a smooth transition between the two portions. Equations of Yu et al.'s [11] model are as follows:

$$\sigma_c = E_c\varepsilon_c - \frac{(E_c - E_{2c})^2}{4f_o}\varepsilon_c^2, \quad 0 \le \varepsilon_c \le \varepsilon_t, \tag{1}$$

$$\sigma_c = f_o + E_{2c}\varepsilon_c, \quad \varepsilon_t \le \varepsilon_c \le \varepsilon_{cu}, \tag{2}$$

$$\varepsilon_t = \frac{2f_o}{E_c - E_{2c}}, \tag{3}$$

$$E_{2c} = \frac{f'_{cc} - f_o}{\varepsilon_{cu}}, \tag{4}$$

$$\frac{f'_{cc}}{f'_{co}} = \begin{cases} 1 + 3.5(\rho_K - 0.01)\rho_\varepsilon & \rho_K \ge 0.01 \\ 1 & \rho_K < 0.01, \end{cases} \tag{5}$$

$$\frac{\varepsilon_{cu}}{\varepsilon_{co}} = 1.75 + 6.5\rho_K^{0.8}\rho_\varepsilon^{1.45}(1-\varphi)^{-0.22}, \tag{6}$$

$$\frac{f_l}{f'_{co}} = \frac{E_{frp}t_{frp}\varepsilon_{h,rup}}{f'_{co}R} = \rho_K\rho_\varepsilon, \tag{7}$$

$$\rho_K = \frac{E_{frp}t_{frp}}{E_{seco}R}, \tag{8}$$

$$\rho_\varepsilon = \frac{\varepsilon_{h,rup}}{\varepsilon_{co}}, \tag{9}$$

$$E_{seco} = \frac{f'_{co}}{\varepsilon_{co}}, \tag{10}$$

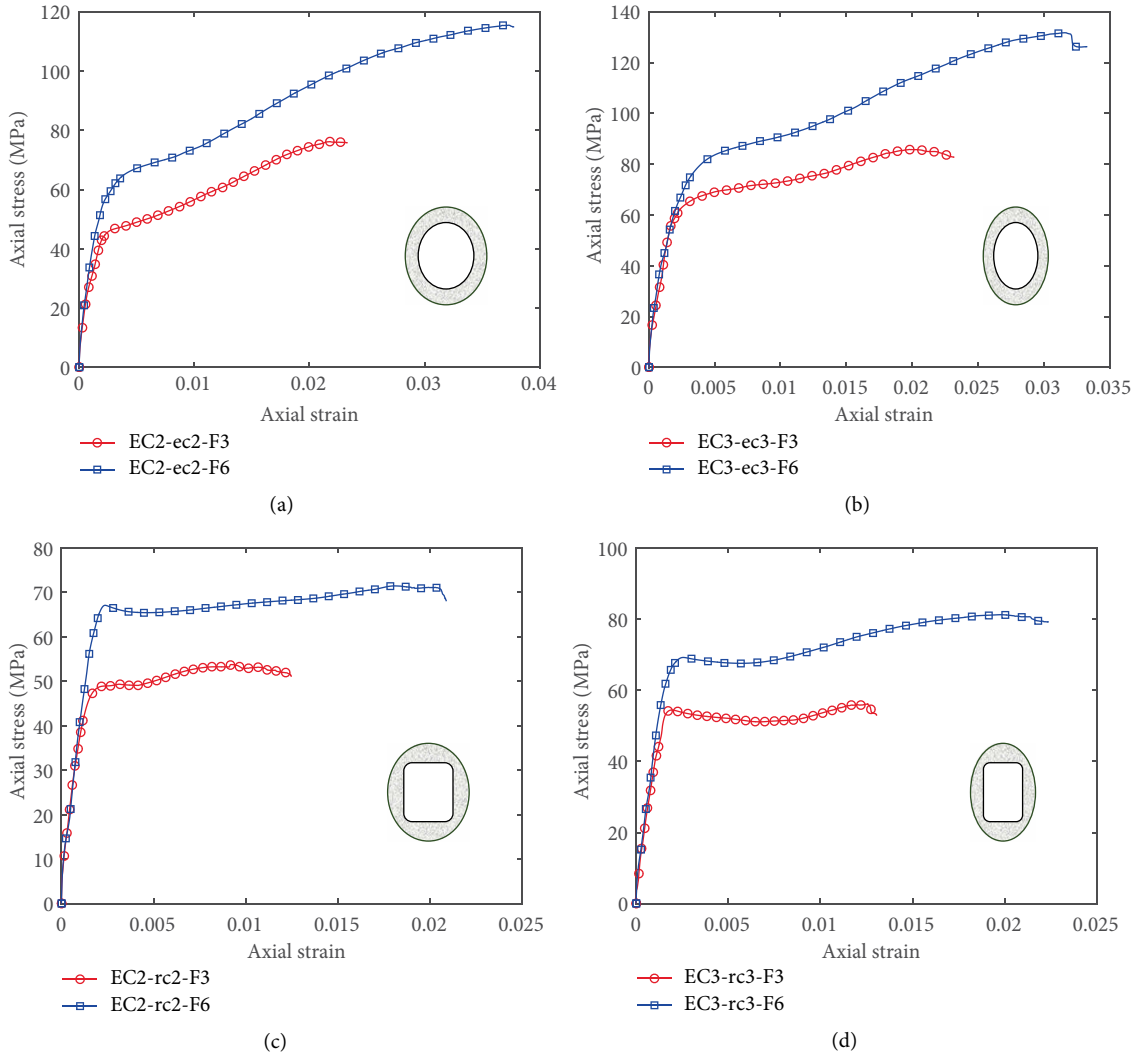

Figure 11: Effect of FRP thickness. (a) EE-DSTCs, $\rho_A = 1.2$. (b) EE-DSTCs, $\rho_A = 1.5$. (c) ER-DSTCs, $\rho_A = 1.2$. (d) ER-DSTCs, $\rho_A = 1.5$.

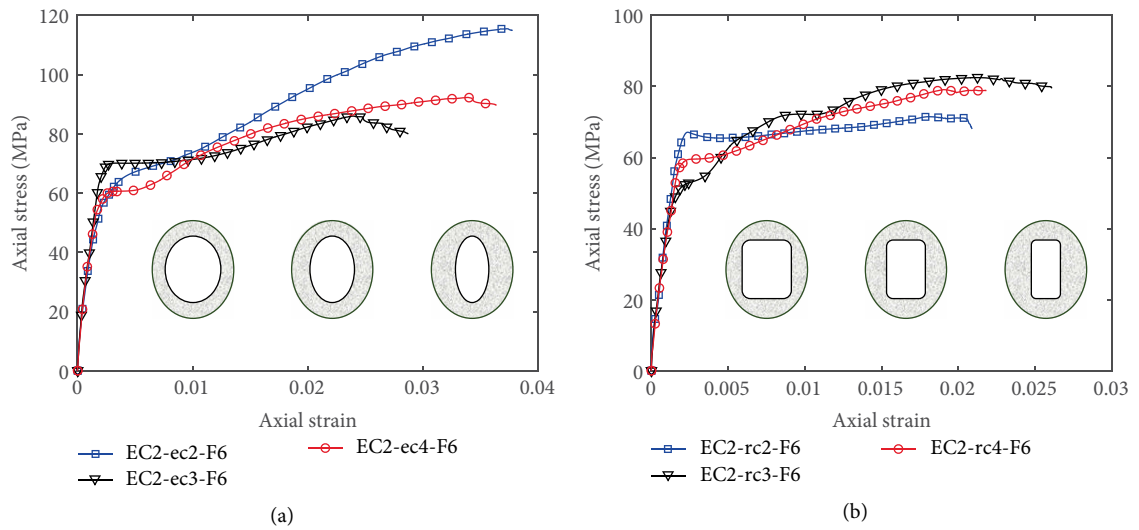

Figure 12: Effect of void area ratio. (a) EE-DSTCs. (b) ER-DSTCs.

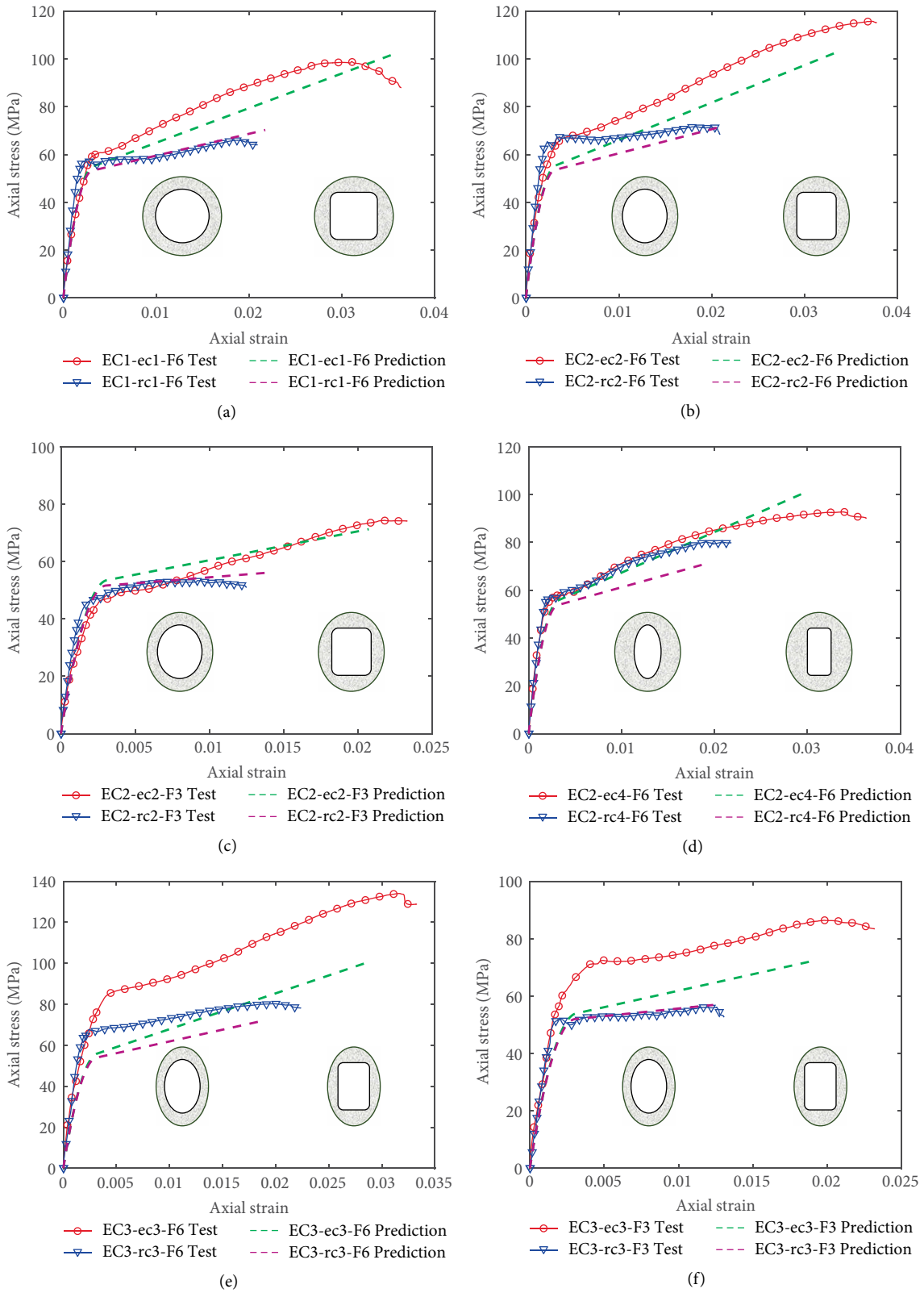

Figure 13: Effect of inner steel tubes.

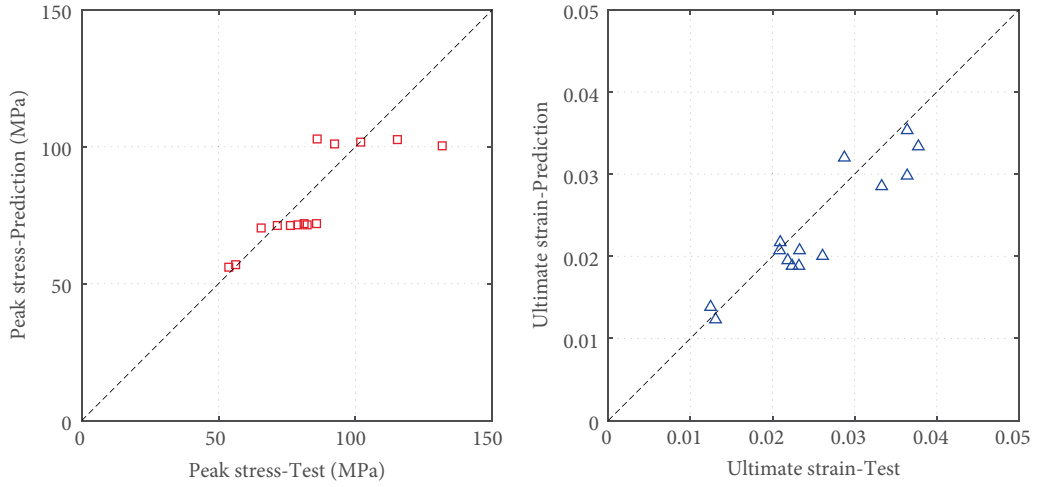

Figure 14: Predictions of the proposed model. (a) Peak stress. (b) Ultimate strain.

where:

σ_c and ε_c are the axial stress and the axial strain of confined concrete, respectively;

f'_{cc} and ε_{cu} are the compressive strength and the ultimate axial strain of confined concrete, respectively;

f'_{co} and ε_{co} are the compressive strength and the axial strain at peak axial stress of unconfined concrete, respectively;

f_o is the intercept of the stress axis by the linear second portion, which is taken to be f'_{co};

E_c is the initial elastic modulus of confined concrete;

E_{2c} is the slope of the linear second portion of the stress-strain curve;

E_{seco} is the secant modulus of unconfined concrete;

ε_t is the axial strain at the smooth transition point where the parabolic first portion meets the linear second portion;

ρ_K and ρ_ε are the confinement stiffness ratio and the strain ratio, respectively;

E_{frp} is the elastic modulus of FRP in the hoop direction;

t_{frp} is the thickness of the FRP tube;

$\varepsilon_{\text{h,rup}}$ is the hoop strain of FRP at the rupture of the tube due to hoop tensile stresses;

R and D_c is the outer radius and the outer diameter of the annular concrete section, respectively;

φ is the ratio between the outer diameter of the steel tube d_s and the outer diameter of the annular concrete section D_c.

4.2. Teng et al.'s Model for Elliptical FRP-Confined Solid Concrete Columns. Teng et al. [38] proposed a simple stress-strain model for the confined concrete of elliptical FRP-confined solid concrete columns, which was also based on Teng et al.'s [37] stress-strain model for circular FRP–confined solid columns. The effect of elliptical aspect ratio on the compressive strength of confined concrete was considered in Teng et al.'s [38] model, which consists Equations (1), (3), (4), (9), and the following equations:

$$\sigma_c = \begin{cases} f'_{co} + E_{2c}\varepsilon_c & \rho_K \geq 0.01 \\ f'_{co} & \rho_K < 0.01, \end{cases} \quad \varepsilon_t \leq \varepsilon_c \leq \varepsilon_{cu}, \tag{11}$$

$$\frac{f'_{cc}}{f'_{co}} = 1 - K(\rho_K)\rho_\varepsilon, \tag{12}$$

$$K(\rho_K) = \begin{cases} -3.5(\rho_K - 0.01) & \rho_K \geq 0.01 \\ 0 & \rho_K < 0.01, \end{cases} \tag{13}$$

$$\frac{\varepsilon_{cu}}{\varepsilon_{co}} = 1.75 + 6.5\rho_K^{0.8}\rho_\varepsilon^{1.45}, \tag{14}$$

$$\rho_{\text{FRP}} = \frac{1.5(a+b) - \sqrt{ab}}{ab} t_{\text{frp}}, \tag{15}$$

$$\rho_K = \frac{\rho_{\text{FRP}} E_{\text{frp}} \varepsilon_{co}}{2f'_{co}}, \tag{16}$$

$$\varepsilon_{\text{h,rup}} = k_s k_\varepsilon \varepsilon_{fu}, \tag{17}$$

$$k_s = 0.5\left(3 - \frac{a}{b}\right), \tag{18}$$

where:

ρ_{FRP} is the FRP volumetric ratio for elliptical FRP-confined solid concrete column;

ρ_K is the confinement stiffness ratio with the effect of elliptical aspect ratio considered;

a and b are half of the major axis and the half of the minor axis of elliptical cross-section;

ε_{fu} is the ultimate tensile strain of FRP from tensile coupon tests;

k_ε is the FRP strain efficiency ratio accounting for the discrepancy between the FRP jacket rupture strain obtained from an FRP-confined concrete column test and that obtained from the flat coupon test; k_ε is taken as 0.70 in Teng et al. (2009);

k_s is the shape factor accounting for the effect of cross-sectional shape on the jacket rupture strain for the equivalent circular column.

4.3. Proposed Model. Yu et al.'s [11] model was proposed for circular DSTCs with a circular inner steel tube, whereas Teng et al.'s [38] model was proposed for elliptical FRP-confined solid concrete columns. Both models were proposed based on Teng et al.'s [37] stress–strain model for circular FRP-confined solid columns. The effect of the elliptical aspect ratio could not be reflected in Yu et al.'s [11] model, while the effect of inner void in elliptical DSTCs could neither be considered in Teng et al.'s [38] model. Based on the experimental results in the present study, Equations (19) and (20), which are derived through a trial and error process, are proposed to account for the effects of the elliptical aspect ratio, the inner void, and the cross-section shape of the inner steel tube for elliptical DSTCs.

$$\frac{\varepsilon_{cu}}{\varepsilon_{co}} = 1.75 + 6.5\rho_K^{0.8}\rho_\varepsilon^{1.45}\left(1 - \sqrt{\varphi_A}\right)^{-0.22}, \tag{19}$$

$$\rho_{\text{FRP}} = \frac{1.5(a+b) - \sqrt{ab}}{ab} t_{\text{frp}} k_t, \tag{20}$$

where:

φ_A is the void area ratio, which the ratio between the area of the concrete void and the area of the outer elliptical section of concrete;

k_t is the shape factor of the inner steel tube; k_t is taken to be 1.0 and 0.5 for an elliptical inner steel tube and a rectangular inner steel tube, respectively.

To summarize, the proposed stress-strain model for confined concrete in elliptical DSTCs includes Equations (19) and (20) proposed in the present study and Equations (1), (3), (4), (9), (11)–(13), (16)–(18). The void area ratio φ_A in Equation (19) (i.e., the ratio between the area of the concrete void and the area of the outer elliptical section of concrete), is different from the void ratio φ in Equation (6) of Yu et al.'s [11] model which is defined as the ratio between the outer diameter of the steel tube d_s and the outer diameter of the annular concrete section D_c. Equation (19) is degraded to Equation (6) for circular DSTCs. k_t is the shape factor of the inner steel tube. k_t is taken to be 1.0 for an elliptical inner steel tube, but is 0.5 for a rectangular inner steel tube to account for the negative effect of the significant inward buckling of the rectangular steel tube. For elliptical FRP-confined solid concrete columns, Equations (19) and (20) are degraded to Equations (14) and (15), respectively.

The axial stress-axial strain curves of experimental results are compared with predictions of the proposed model in Figure 13. The FRP rupture strain obtained from the flat coupon test was used in all predictions following Equation (17) as suggested in Teng et al.'s [38] model. It is evident that the proposed model produces approximately bilinear axial stress-strain curves for the confined concrete of elliptical DSTCs which are in close agreement with the experimental stress-strain curves. The predicted peak stress and ultimate strain of the confined concrete in elliptical DSTCs are compared with the predictions of the proposed model in Figure 14. It is evident, the proposed model is capable of providing reasonably accurate but generally conservative predictions.

5. Conclusions

This paper presents an experimental study on elliptical DSTCs under monotonic axial compression. The test results and discussions allow the following conclusions to be drawn:

(1) The elliptical aspect ratio has no obvious effect on the ultimate axial strain of the confined concrete in elliptical DSTCs, whereas the averaged peak stress increases with the increase of the elliptical aspect ratio.

(2) Elliptical DSTCs with an elliptical steel tube exhibit much better ductility and strength enhancement than those elliptical DSTCs with a rectangular steel tube.

(3) Elliptical DSTCs with a thicker FRP tube generally have higher averaged peak stress and larger ultimate axial strain of the confined concrete.

(4) Within the range examined the void area ratio does not have a significant effect on either the ultimate axial strain or the peak axial stress of the confined concrete.

(5) Based on Yu et al.'s model for circular DSTCs with a circular inner steel tube and Teng et al.'s model for elliptical FRP-confined solid concrete columns, a simple stress-strain model of confined concrete was proposed for elliptical DSTCs, which can provide reasonably accurate but generally conservative predictions.

Data Availability

The experimental data presented in the paper is obtained by the authors. All the test data is available by sending an email to the corresponding author.

Conflicts of Interest

The authors declare that they have no conflicts of interest.

Acknowledgments

The authors are grateful for the financial support received from the National Natural Science Foundation of China (Grant Nos. 51608263, 51778102), and the Natural Science Foundation of Jiangsu Province (Grant No. BK20160998).

References

[1] L. C. Hollaway and J. G. Teng, *Strengthening and Rehabilitation of Civil Infrastructures Using Fibre Reinforced Polymer (FRP) Composites*, Woodhead Publishing, Cambridge, UK, 2008.

[2] M. Motavalli and C. Czaderski, "FRP composites for retrofitting of existing civil structures in Europe: state-of-the-art review," in *Proceedings, International Conference of Composites and Polycon*, pp. 1–10, American Composites Manufacturers Association, Tampa, FL, USA, 2007.

[3] L. C. Bank, *Composites for Construction: Structural Design with FRP Materials*, John Wiley & Sons, West Sussex, UK, 2006.

[4] J. J. Xu, Z. P. Chen, Y. Xiao, C. Demartino, and J. H. Wang, "Recycled aggregate concrete in FRP-confined columns: a review of experimental results," *Composite Structures*, vol. 174, pp. 277–291, 2017.

[5] H. Nordin and B. Taljsten, "Testing of hybrid FRP composite beams in bending," *Composites Part B: Engineering*, vol. 35, no. 1, pp. 27–33, 2004.

[6] J. G. Teng, "New-material hybrid structures," *China Civil Engineering Journal*, vol. 51, no. 12, pp. 1–11, 2008.

[7] Y. L. Wang, G. H. Cai, Y. Y. Li, D. Waldmann, A. S. Larbi, and K. D. Tsavdaridis, "Behavior of circular fiber-reinforced polymer-steel-confined concrete columns subjected to reversed cyclic loads: experimental studies and finite-element analysis," *Journal of Structural Engineering*, vol. 145, no. 9, Article ID 04019085, 2019.

[8] J. G. Teng, T. Yu, and Y. L. Wong, "Behaviour of hybrid FRP-concrete-steel double-skin tubular columns," in *Proceedings, Second International Conference on FRP Composites in Civil Engineering*, pp. 811–818, Adelaide, Australia, 2004.

[9] J. G. Teng, T. Yu, Y. L. Wong, and S. L. Dong, "Hybrid FRP-concrete-steel tubular columns: concept and behavior," *Construction and Building Materials*, vol. 21, no. 4, pp. 846–854, 2007.

[10] T. Yu, *Behavior of Hybrid FRP-concrete-steel double-skin tubular columns [PhD Thesis]*, The Hong Kong Polytechnic University, Hong Kong, 2007.

[11] T. Yu, J. G. Teng, and Y. L. Wong, "Stress-strain behavior of concrete in hybrid FRP-concrete-steel double-skin tubular columns," *Journal of Structural Engineering*, vol. 136, no. 4, pp. 379–389, 2010.

[12] B. Zhang, T. Yu, and J. G. Teng, "Axial compression tests on hybrid double-skin tubular columns filled with high strength concrete," in *Proceedings, Third International Postgraduate Conference on Infrastructure and Environment*, pp. 171–176, Hong Kong, China, 2011.

[13] B. A. L. Fanggi and T. Ozbakkaloglu, "Compressive behavior of aramid FRP-HSC-steel double-skin tubular columns," *Construction and Building Materials*, vol. 48, pp. 554–565, 2013.

[14] J. N. Zheng and T. Ozbakkaloglu, "Sustainable FRP-recycled aggregate concrete-steel composite columns: behavior of circular and square columns under axial compression," *Thin-Walled Structures*, vol. 120, pp. 60–69, 2017.

[15] B. Zhang, *Hybrid FRP-concrete-steel double-skin tubular columns under static and cyclic loading [PhD Thesis]*, The Hong Kong Polytechnic University, Hong Kong, 2014.

[16] B. Zhang, J. G. Teng, and T. Yu, "Compressive behavior of double-skin tubular columns with high-strength concrete and a filament-wound FRP tube," *Journal of Composites for Construction*, vol. 21, no. 5, p. 04017029, 2017.

[17] T. Yu, B. Zhang, Y. B. Cao, and J. G. Teng, "Behavior of hybrid FRP-concrete-steel double-skin tubular columns subjected to cyclic axial compression," *Thin-Walled Structures*, vol. 61, pp. 196–203, 2012.

[18] T. Ozbakkaloglu and E. Akin, "Behavior of FRP-confined normal-and high-strength concrete under cyclic axial compression," *Journal of Composites for Construction*, vol. 16, no. 4, pp. 451–463, 2012.

[19] T. Ozbakkaloglu and B. A. L. Fanggi, "FRP-HSC-steel composite columns: behavior under monotonic and cyclic axial compression," *Materials and Structures*, vol. 48, no. 4, pp. 1075–1093, 2013.

[20] P. Xie, *Behavior of large-scale hybrid FRP-concrete-steel double-skin tubular columns subjected to concentric and eccentric compression [PhD Thesis]*, The Hong Kong Polytechnic University, Hong Kong, 2018.

[21] T. Yu, Y. L. Wong, and J. G. Teng, "Behavior of hybrid FRP-concrete-steel double-skin tubular columns subjected to eccentric compression," *Advances in Structural Engineering*, vol. 13, no. 5, pp. 961–974, 2010.

[22] L. H. Han, Z. Tao, F. Y. Liao, and Y. Xu, "Tests on cyclic performance of FRP-concrete-steel double-skin tubular columns," *Thin-Walled Structures*, vol. 48, no. 6, pp. 430–439, 2010.

[23] B. Zhang, J. G. Teng, and T. Yu, "Experimental behavior of hybrid FRP-concrete-steel double-skin tubular columns under combined axial compression and cyclic lateral loading," *Engineering Structures*, vol. 99, pp. 214–231, 2015.

[24] I. A. Omar, M. A. ElGawady, G. Ahmed, A. Sujith, and A. Mohanad, "Seismic performance of innovative hollow-core FRP-concrete-steel bridge columns," *Journal of Bridge Engineering*, vol. 22, no. 2, Article ID 04016120, 2017.

[25] Y. Idris and T. Ozbakkaloglu, "Behavior of square fiber reinforced polymer-high-strength concrete-steel double-skin tubular columns under combined axial compression and reversed-cyclic lateral loading," *Engineering Structures*, vol. 118, pp. 307–319, 2016.

[26] R. Wang, L. H. Han, and Z. Tao, "Behavior of FRP–concrete–steel double skin tubular members under lateral impact experimental study," *Thin-Walled Structures*, vol. 95, pp. 363–373, 2015.

[27] I. A. Omar and M. A. ElGawady, "Performance of hollow-core FRP–concrete–steel bridge columns subjected to vehicle collision," *Engineering Structures*, vol. 123, pp. 517–531, 2016.

[28] Y. W. Zhou, X. M. Liu, F. Xing, D. W. Li, Y. C. Wang, and L. L. Sui, "Behavior and modeling of FRP-concrete-steel double-skin tubular columns made of full lightweight aggregate concrete," *Construction and Building Materials*, vol. 139, pp. 52–63, 2017.

[29] J. J. Zeng, J. F. Lv, G. Lin, Y. C. Guo, and L. J. Li, "Compressive behavior of double-tube concrete columns with an outer square FRP tube and an inner circular high-strength steel tube," *Construction and Building Materials*, vol. 184, pp. 668–680, 2018.

[30] K. D. Peng, T. Yu, N. S. Muhammad, and L. Huang, "Compressive behavior of hybrid double-skin tubular columns with a rib-stiffened steel inner tube," *Composite Structures*, vol. 204, pp. 634–644, 2018.

[31] L. Zeng, L. J. Li, Z. Su, and F. Liu, "Compressive test of GFRP-recycled aggregated concrete-steel tubular long columns," *Construction and Building Materials*, vol. 176, pp. 295–312

[32] T. Yu, S. Zhang, S. L. Huang, and C. W. Chan, "Compressive behavior of hybrid double-skin tubular columns with a large rupture strain FRP tube," *Composite Structures*, vol. 171, pp. 10–18, 2017.

[33] B. Zhang, G. Feng, S. W. Wei, N. Y. Zhang, Q. B. Zhang, and X. M. Hu, "Behavior of elliptical GFRP-concrete-steel double-skin tubular columns under axial compression," *Journal of Building Structures*, 2019.

[34] ASTM C39/C39M, *Standard test method for compressive strength of cylindrical concrete specimens*, American Society for Testing and Materials, Philadelphia, PA, USA, 2008.

[35] ASTM D3039/D3039M, *Standard test method for tensile properties of polymer matrix composite materials*, American Society for Testing and Materials, Philadelphia, PA, USA, 2017.

[36] BS 18, *Tensile Testing of Metals (Including Aerospace Materials)*, British Standards Institution, London, UK, 1987.

[37] J. G. Teng, T. Jiang, L. Lam, and Y. Z. Luo, "Refinement of a design-oriented stress-strain model for FRP-confined concrete," *Journal of Composites for Construction*, vol. 13, no. 4, pp. 269–278

[38] J. G. Teng, J. Y. Wu, S. Casalboni, Q. G. Xiao, and Y. Zhao, "Behavior and modeling of fiber-reinforced polymer-confined concrete in elliptical columns," *Advances in Structural Engineering*, vol. 19, no. 9, pp. 1359–1378, 2016.